

ESTIMATION OF EXTREME RESPONSE AND
FAILURE PROBABILITIES OF WIND TURBINES
IN NORMAL OPERATION BY CONTROLLED
MONTE CARLO SIMULATION

AALBORG UNIVERSITY 2009
MASTER THESIS
SØREN SØRENSEN
JACOB JØRGENSEN
JONAS NISSEN

**The Faculties of Engineering,
Science and Medicine**

Department of Civil Engineering
Sohngårdsholmsvej 57
9000 Aalborg
<http://www.civil.aau.dk/>

Title:

Estimation of extreme response and failure probabilities of wind turbines in normal operation using controlled Monte Carlo simulation.

Abstract:

The purpose of the thesis is to test alternative methods for estimating the extreme response for wind turbines under normal operation. Currently, different extrapolation methods are used for determining the extreme responses by extracting maxima from a few simulations of normally 10 minutes. These extrapolation methods are associated with unknown statistical uncertainties. In the first part of the thesis, the extrapolation method suggested by the IEC-61400 standard is described and the associated uncertainties and problems are clarified and the extrapolation method is tested for determining the extreme response for a wind turbine model. Afterwards two simple structural systems are presented, a simple shear frame and a simple wind turbine model, which will be the basis for evaluation of the alternative methods presented. The alternative methods Russian Roulette and Splitting with Distance Control (RR&S), Importance Sampling (IS) and RESTART are presented as alternatives to the present extrapolation methods. The latter of the three does not provide promising results, whereas RR&S and IS provide promising results on both of the simple structural systems reducing the computational time significantly. Finally, the RR&S algorithm is implemented on the aero-elastic code FAST. The algorithm provides promising results for estimating the extreme responses if disabling the wind turbine control system and no significant improvements if the control system is enabled.

Supervisors:

Dr. Techn. Søren R.K. Nielsen
Prof. John D. Sørensen

Authors:

Søren Sørensen
Jonas Nissen
Jacob Jørgensen

Term: Master Thesis - September 2008 to June 2009
Ended: 15th of June, 2009

Copies: 7
Pages: 186

Preface

The present thesis was prepared as a Master Thesis on the 3rd and 4th semester of the MSc Civil Engineering education under the Department of Civil Engineering at Aalborg University. The project was written as a preliminary investigation for the research project "Estimation of extreme responses of wind turbines under normal operations by means of controlled Monte Carlo". The thesis was written in the period from September 2008 to June 2009.

We wish to thank our supervisors Prof. Dr. Techn. Søren R.K. Nielsen and Prof. John D. Sørensen for their guidance throughout the project period. We would also like to thank PhD Fellow Mahdi Teimouri Sichani for providing the basics of many of the turbulence models used throughout the project and Bo Juul Pedersen for his advice during meetings at Aalborg University and at LAC Engineering.

The thesis contains a main part and appendices. The appendices are referenced from the main part where applicable. The bibliography is cited by the Harvard method, using the form [Author, year]. If multiple citations exist for the same author and year, a letter is added after the year in the citations.

Aalborg University, June 2009

Søren Sørensen

Jonas Nissen

Jacob Jørgensen

Contents

1	Introduction	1
1.1	Determination of loads on wind turbine	2
1.2	Thesis description	3
2	Determination of extreme loads using the IEC61400-1 standard	5
2.1	Description of extrapolation method	5
2.2	Extrapolation of loads on 5MW wind turbine	7
2.3	Conclusion	12
3	Alternative methods for determination of low exceedance probabilities	13
4	Two storey shear frame exposed to horizontal earthquake excitation	15
4.1	Structural system	15
4.2	Ground Surface Acceleration Models	17
4.3	Numerical time integration	20
4.4	Parameter analysis	21
5	Two bladed wind turbine exposed to a turbulent wind field	27
5.1	Structural system	27
5.2	Calibration of model	31
5.3	Loads on the system	32
5.4	Results	35
6	Crude Monte Carlo simulations	39
7	Importance Sampling	43
7.1	Implementation on two storey shear frame exposed to a turbulent wind field	49
7.2	Implementation on two bladed wind turbine exposed to a turbulent wind field	57
7.3	Conclusion	64
8	Russian Roulette & Splitting with Distance Control	67
8.1	RR&S algorithm	67
8.2	Choice of distance variable	75
8.3	Implementaion on two dof shear frame exposed to earthquake	77
8.4	Implementation on three dof wind turbine	80
8.5	Implementation on 5MW reference wind turbine	83
8.6	Conclusion	88
9	RESTART	91
9.1	Description of the method	91
9.2	Implementation on two node tandem network	93
9.3	Conclusion	95
10	Comparison of RR&S and IS with the POT method.	97
11	Conclusion	99
	Bibliography	101

Appendices	105
A FAST	105
A.1 Basic description of the FAST code	105
B Turbulence simulation	107
B.1 Turbulence simulation using TurbSim	110
B.2 Turbulence simulation using moving average model	112
B.3 Turbulence simulation using state space ARMA model	114
C Description of 5MW reference wind turbine	115
D Analysis of wind turbine response Gaussianity	119
E Load extrapolation	121
E.1 Extrapolation results and observations by LE ³	121
E.2 Amendment to IEC61400-1:2005 - draft for voting	124
F Extremes of stationary Gaussian processes	127
G Modal analysis of plane n storey shear frame exposed to a horizontal earthquake excitation	131
H Assessments of the Broken Line Process	139
I RR&S	141
I.1 Implementation on one dof oscillator	141
I.2 Implementation on two dof shear frame exposed to earthquake, static load & carrier wave	143
I.3 Non-uniform distribution of realisations	154
I.4 Mechanical energy oscillations	157
I.5 Parameter analysis	158
J Importance Sampling	167
J.1 Stochastic differential equations	167
J.2 Multi-modal sampling simulation methods	174
J.3 Scalar diffusion with a constant drift	175
J.4 Importance sampling applied to a single dof linear oscillator	178
K Poisson approximation	183

Chapter 1

Introduction

In modern society, electricity is one of the most important power sources. With the increased attention on sustainability and green energy, electricity from wind turbines has become popular in the recent years and with an annual growth of more than 30% in the last years wind energy is the fastest growing of the sustainable energy sources today [World Resources Institute, 2008].

Traditionally wind turbines have been placed onshore in windy locations but in the last decade offshore wind energy has increased because of the obvious advantages; more wind, more space and no nearby neighbours to take into consideration. The market for the offshore wind industry is expected to be fast-growing in the coming years - from 2009 to 2010 the installed offshore wind turbine capacity is expected to increase more than 100% [Holmager, 2008].

The large growth in the wind energy demand is accompanied with a demand of improved wind turbine efficiency and requires larger wind turbines to satisfy customers; normally energy companies or governments. The reason for constructing larger wind turbines is that the expenses for e.g. grid connection, foundation and control system is smaller for a larger wind turbine than for a comparable number of smaller wind turbines. Figure 1.1 shows the development of wind turbine sizes over the last 20 years. It is seen that both rotor diameter and tower heights have increased significantly.

The wind industry has traditionally been using a lower reliability level than for normal buildings and structures. The annual probability of failure is around 10^{-4} to 10^{-3} for wind turbines and around 10^{-6}

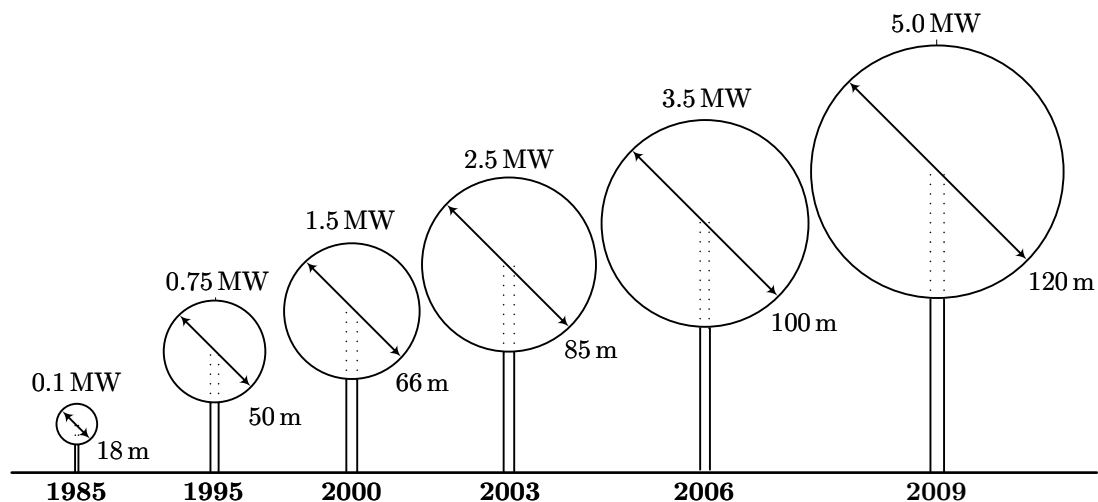


Figure 1.1: Historical development of wind turbine rotor diameter and tower heights. [Sandia National Laboratories, 2008]

to 10^{-5} for normal buildings and structures [Stensgaard and Sørensen, 2008]. The knowledge gained from numerous similar structures and the smaller possibility of loss of life compared to buildings and structures are some of the reasons for using a lower reliability for wind turbines. With the increase in wind turbine size the knowledge gained from smaller wind turbines is getting less relevant and instead theoretical models for documentation of the reliability are needed.

By increasing the size of the structure without increasing the stiffness of the structure proportionally an increased sensitivity to dynamic loads may be expected and more accurate statistical methods and structural models for determining extreme loads on the critical parts of the wind turbines are required. Determining the low-probability extreme responses in the chosen lifetime of the wind turbine should be performed with a great certainty to make sure that the calculated extreme stresses or strains are not exceeded within the lifetime.

The methods being used by the wind turbine industry today is described in the following to clarify problems and uncertainties. Also, an example of determination of extreme loads is carried through in the forthcoming chapter to clarify the uncertainties in choosing different parameters and probability distribution functions in the *extrapolation method*.

1.1 Determination of loads on wind turbine

The IEC61400-1 standard prescribes minimum design requirements for wind turbines of different sizes and is used by wind turbine manufacturers internationally [International Electrotechnical Commission, 2005]. The standard is published by the International Electrotechnical Commission and describes several design situations to take into consideration when designing wind turbines; design situations under normal or extreme external conditions, fault design situations and design conditions under transportation, installation and maintenance are some examples. The different design situations described in the standard should all be examined when designing a wind turbine.

In the standard wind turbine classes I, II and III are defined to categorise wind turbines designed to withstand a predefined climate. The different climates are characterised by a reference average wind speed at hub height in 10 minutes having a *recurrence period* of 50 years, i.e. the expected first passage time is equal to 50 years, corresponding to an annual probability of failure of 2%. For example wind turbine class I characterised by a 10 minutes mean wind speed of 50 m/s at hub height. In addition to the wind speed, the turbulence characteristics are of great importance and are specified by different turbulence intensities $I \in [0.1, 0.2]$ corresponding to the site turbulence level. The wind turbine classes are not applicable on offshore wind turbine design.

By using the turbine class and turbulence intensity of a given wind turbine, different wind conditions is to be taken into consideration. The standard specifies a dozen of different wind conditions that is to be examined. Some of the design wind conditions are stated below.

Normal wind profile model: Average wind speed varying over height - no turbulence.

Normal turbulence model: Turbulence model using a representative 90% quantile turbulence intensity for the hub height wind speed.

Extreme wind speed model: Steady and turbulent wind model with extreme wind speed.

Extreme operating gust: Extreme gust with recurrence period of 50 years.

Extreme turbulence model: Normal wind profile with extreme turbulence intensity.

Extreme direction change: Normal wind profile with extreme direction change over 6 s.

Extreme coherent gust with direction change: Rise of gust and direction change over 10 s.

Extreme wind shear: Extreme horizontal and vertical shear gradients of mean wind field in the rotor plane.

For each of the wind conditions the standard states whether the wind condition should be used to analyse the wind turbine ultimate loads or fatigue loads. For each of the design load cases appropriate partial safety factors are given. Some examples of design load situations are given below.

- 1) Power production: Ultimate loads and fatigue loads on structural parts are examined by using an *extrapolation method* to determine extreme responses during the wind turbine life time.
- 2) Power production and fault: Examples are control system faults, loss of electrical network or protection system fault. The faults are combined with different wind conditions and the ultimate strengths or fatigue loads are determined.
- 3+4) Start up and shut down: Conditions at start up and shut down combined with different wind conditions. Fatigue loads and ultimate loads are considered.
- 5) Emergency shut down: Ultimate loads at emergency shut down using normal turbulence model wind conditions.
- 6) Parked condition: Using 50-year and 1-year recurrence periods of the mean wind speed and extreme wind speed model the ultimate loads are examined under different conditions.
- 7) Parked and fault condition: Ultimate loads are examined under extreme wind speed.
- 8) Transport, assembly, maintenance and repair: Ultimate loads are examined under different wind conditions.

If it is not obvious what wind speeds or turbulence levels that are most critical, different wind speeds and turbulence levels should be analysed. For each of the analyses described the structural responses are not easily calculated because of the rather complicated dynamic system. Some of the loads that are to be considered are aerodynamic, gravitational, inertia and control loads. Obviously these loads influence one another which is important to take into consideration when designing the wind turbine. It is obvious that designing a wind turbine is not a simple task and that sophisticated tools and methods are required.

Also other environmental effects that could have an impact on safety should be taken into consideration, e.g. temperature, humidity, earthquake, snow and ice. Other site specific conditions are also to be taken into account.

Beside the structural parts of the wind turbine the reliability of the control systems and mechanical systems are of great importance. Equally important is the assembly, installation, operation and maintenance that is also considered in the standard. Despite this fact this thesis will focus only on the structural parts and other parts of wind turbines will not be treated.

1.2 Thesis description

Thesis statement

The method for determining extreme loads on wind turbines in the IEC standard assumes a known distribution for the response peaks. Though measured data is available for verification of the distribution, this data is confined to the central part of the probability distribution for which reason the accuracy of the tail fit is unknown. Assuming exact models for wind loads and turbine structure, the exact distribution can be estimated by so-called crude or standard crude Monte Carlo simulation. But for low probabilities of failures crude Monte Carlo simulation results in unacceptable large variances

on the estimate with the capabilities of present computational resources. For this reason it is desirable to apply so-called variance reduction methods or controlled Monte Carlo methods on wind turbines which can improve the estimate of the failure probability estimates.

Methods

The goal of this thesis is to adapt known variance reduction methods and apply them on wind turbines. The methods to investigate are chosen in cooperation with the thesis supervisors and is based on methods that have previously been applied on dynamic systems or systems in civil engineering that resembles the dynamic system of a wind turbine.

To verify the application and implementation of the methods, results from chosen articles are firstly reproduced. The methods are subsequently applied to the same simple two storey shear frame, to investigate their relative capability on simple structural systems. Verification of the accuracy of the methods are performed by either crude Monte Carlo simulations or analytical approximations. The method(s) that are found usable based on these investigations are next tested on a wind turbine model.

For simulating wind loads and wind turbine responses the aero-elastic code FAST is used. The FAST code uses a spectral model for simulating wind fields and employs a combined modal and multi body dynamics formulation for the structural analysis. For simulations in FAST using variance reduction methods a state formulation of the turbulence is needed. The state formulation should be implemented with the only input being Gaussian white noise, either by an ARMA vector model or a filter model defined by an impulse response matrix. A state space formulation of an ARMA model for simulating turbulence is implemented in the FAST code.

Thesis boundaries

Due to limited time only three variance reduction methods are considered. The obtained results are compared only with simulated data and no comparison with measurements are performed. Thus, it is the probabilistic method rather than the structural model of the wind turbine which is assessed. The only considered load case is load case 1.1 in the IEC61400-1 standard. This corresponds to determining the response event which has a recurrence period of 50 years.

Chapter 2

Determination of extreme loads using the IEC61400-1 standard

In the following an introduction and discussion on the methods currently used for determining *extreme responses* on wind turbines under power production will be given. In section 2.1 the extrapolation method is described and the problems, limitations and uncertainties are clarified. In section 2.2 the method is utilised for determination of the characteristic extreme responses for a wind turbine.

Determination of extreme responses corresponds to load situation 1.1 using a normal turbulence model as described in section 1.1. The current method is based on the guidance given in Annex F in the IEC61400-1 standard. Only the design situation when producing power under normal operation is taken into account by the method described in Annex F, i.e. the method only accounts for windspeeds; $V_{in} < V < V_{out}$ where V , V_{in} and V_{out} are the wind speed at hub height, cut-in wind speed and cut-out wind speed, respectively.

The IEC61400-1 standard prescribes that the design value of the material resistance should be larger than the design value of the response corresponding to a 50 year recurrence period for each component in the wind turbine where ultimate strength analysis is appropriate. The calculation of extreme values shall include at least the blade in-plane moment and out-of-plane moments and the blade tip deflections. The design value of the response is determined by dividing the characteristic response corresponding to a 50 year recurrence period by a predefined partial safety factor. Only the tower fore-aft moment and the blade out-of-plane moment have been considered in the following.

In the following the method from annex F in the standard is described. The following is based on the IEC61400-1 standard, Annex F [International Electrotechnical Commission, 2005].

2.1 Description of extrapolation method

To determine the extreme response of e.g. the moment at the blade roots or tower base moments the *extrapolation method* is used. Firstly the wind speeds from V_{in} to V_{out} are divided into a number of *wind speed bins*, defined as a class of e.g. 2 m/s in the interval $[V_{in}, V_{out}]$. The wind direction for all wind speeds are assumed to be the same because variations on wind direction are assumed not to happen in 10 minute periods and then has no influence on the calculated loads. For each of the wind speed bins a number of turbulent wind fields with different seeds are generated and the required response is extracted from the considered dynamic structure model. In practise between 6 and 12 turbulence wind fields are generated and the response for each turbulence wind field is calculated. For each wind speed bin a number of extreme values for each turbulence wind field is extracted and a probability distribution function for extreme values in the wind speed bin is fitted. Assuming that all extracted extreme values are statistically independent the exceedance probability of the extreme response M_{ext} in a certain position of the turbine during the observation period T on condition of $V = v$ can be written as

$$P(M_{ext} \geq m|v, T) = 1 - (F_{max}(m|v))^{E(n|v, T)} \quad (2.1)$$

where $F_{max}(m|v)$ is the probability distribution function for the maximum response and $E(n|v, T)$ is the expected number of maxima in the period T on condition of $V = v$. The unconditional exceedance probability is given as

$$P(M_{ext} \geq m|T) = \int_{V_{in}}^{V_{out}} P(M_{ext} \geq m|v, T) f_V(v) dv \quad (2.2)$$

where $f_V(v)$ is the probability density function for the hub-height wind speed.

In practice M_{ext} corresponding to a 50-year recurrence period is determined by fitting parameters in candidate distributions for the exceedance probabilities $P(M_{ext} \geq m|v, T)$ in all wind speed bins. The fitted distribution parameters is used in determination of $P(M_{ext} \geq m|v, T)$ in (2.2).

When the probability distribution functions for all wind speed bins are known, the unconditional probability of exceedance in the period $T = 600$ s is determined. Assuming statistical independence between observation intervals, the following relation between the exceedance probability in $T = 600$ s and the exceedance probability in the recurrence period T_r applies

$$P(M_{ext} > m|T_r) = 1 - (1 - P(M_{ext} > m|T))^{T_r/T} \quad (2.3)$$

$$\cong \frac{T_r}{T} P(M_{ext} > m|T) \quad (2.4)$$

By assuming that $P(M_{ext} > m|T_r) \lesssim 1$ the following relation is found with $T = 600$ s and $T_r = 50$ years

$$P(M_{ext} > m|T) = \frac{T}{T_r} \approx 3.8 \cdot 10^{-7} \quad (2.5)$$

Next the characteristic load is determined by insertion of (2.2) into (2.5) and solving with respect to the characteristic load $m = m_c$. The functional relation is non-linear and iterations are needed.

An example of utilisation of this method is given in chapter 2.2.

2.1.1 Problems, limitations and uncertainties

In this section the problems, limitations and uncertainties in the method from the IEC61400-1 standard will be discussed. Independence of extracted extreme response values, extraction of extreme values, choice of candidate distribution function and other steps in the method are discussed. The uncertainties in the method have been investigated by and IEC subcommittee, the so-called LE³ committee, see appendix E.1.

One of the problems in the above described method is that an unknown number of extreme values for each wind speed bins should be extracted to determine $P(M_{ext} \geq m|T)$. The extreme values have to be independent i.e. the extreme values should originate from different wind gusts and be independent of previous wind gusts. For a given response time series it should be tested statistically that the extracted values are independent. The period of wind gusts varies with time which makes it difficult to determine if extracted values are independent. A possible solution is to set a minimum time separation between successive maxima.

One method of extracting extreme values is the method of global maxima. The approach is to only extract one maximum value for each simulated wind field, which means that the number of realisations required to obtain a reliable fit of parameters in the candidate distribution functions is relatively high. Another available method is the peak-over-threshold method (POT) that includes a procedure of extracting multiple extreme values over a given threshold for each simulated wind field. The IEC standard suggests to extract extreme values using the POT method by extracting successive upcrossings of $\mu_M + 1.4\sigma_M$, where μ_M is the mean value and σ_M is the standard deviation of the response, and then assume that all extracted values are independent. Other studies show that the threshold can not be determined beforehand but that the optimum should be determined for each wind speed bin by trying different thresholds and choosing the threshold that fits best to a chosen distribution function [Ragan and Manuel, 2008]. This requires the optimum choice of distribution function to be specified beforehand - but this is also an uncertainty in the method.

If the process, e.g. the blade out-of-plane moment is Gaussian the distribution function of the local maxima within a given interval on condition of a given threshold is approximately independent of the chosen threshold, see appendix F. This means that the choice of threshold should not affect the fitted local distribution function for the wind speed bins. It is shown in appendix D that the response is not Gaussian and that the influence from choosing different thresholds might influence the fit of candidate probability distribution function.

Choosing the distribution function that fits the extreme values best is also an important matter in the extrapolation method. In the IEC standard the 3-parameter Weibull and the Gumbel probability distribution functions are suggested as candidates. For Gaussian processes it is known that the extreme values are normally distributed for broadbanded processes whereas they are Rayleigh distributed for narrowbanded processes. A Weibull distribution is able to model both a Rayleigh and a normal distribution by choosing the right parameters, which makes it a good choice if the loads are Gaussian. In the example in the next section a 3-parameter Weibull and a Gumbel distribution have been used as examples. The probability distribution functions for the 3-parameter Weibull and Gumbel are given in (2.6) and (2.7) respectively.

$$F_M(m) = 1 - \exp\left(-\left(\frac{m - u_0}{a}\right)^k\right) \quad (2.6)$$

$$F_M(m) = \exp\left(-\exp\left(\frac{x - u_0}{a}\right)\right) \quad (2.7)$$

where u_0 , a and $k > 0$ are location, scale and shape parameters, respectively.

2.2 Extrapolation of loads on 5MW wind turbine

The method from the IEC standard is used to extrapolate the tower fore-aft bending moment and the blade out-of-plane moments for the "NREL offshore 5-MW baseline wind turbine" described in appendix C. The structural model used to determine the loads is the aeroelastic code FAST. The 10 minutes wind fields used in the simulations are created by TurbSim which was setup to use recommendations from the IEC standard. A description of the FAST model and input parameters used for simulations are given in appendix A and a description of turbulence simulation in TurbSim is given in appendix B. In the following extrapolations the annual mean wind speed at hub height is set to 10 m/s and the wind speeds are assumed to be Rayleigh distributed according to the standard turbine classes in the IEC61400-1 standard.

The extrapolation to a load corresponding to a recurrence period of 50 years is calculated by solving (2.2) and setting $P(M_{ext} > m|T) = 3.8 \cdot 10^{-7}$ corresponding to a reference period of 10 minutes. The short-term probability distribution functions for each wind speed bin is calculated by fitting candidate probability distribution functions to extreme data extracted by the POT method. For each wind speed bin 10 time series with different seeds are simulated. Using only 10 time series could induce a significant statistical uncertainty in the estimated extreme loads and other studies of the method show that increasing the number of time series lead to lower predictions of the extreme values as shown in figure E.1.

2.2.1 Choice of threshold

The choice of threshold might have a great impact on the extrapolated load if the response process $\{M(t)\}$ is not Gaussian. The differences between choosing a threshold of $\mu_M + 1.4\sigma_M$ as suggested in the IEC standard and a threshold of $\mu_M + 3\sigma_M$ is shown in figure 2.1 for the blade out-of-plane moment in wind bin 13 – 15 m/s. The distribution function used for the POT data is a 3-parameter Weibull fitted by the methods of moments method as suggested in the IEC61400-1 standard. The non-exceedance probability is assigned to each extreme value by using a Weibull plotting position formula; $F_i = 1 - i/(n + 1)$, where i is the peak value number when arranging the peak values in descending order and n is the total number of peak values in the bin. The figure clearly shows that different thresholds provide significantly different fits for the local probability distribution functions. The high threshold leads to extraction of 25 peak values whereas the threshold of $\mu_M + 1.4\sigma_M$ leads to extraction of more than 500 peak values. The abscissas have been normalized with respect to the maximal observed peak m_{max} during all realisations. It is seen that the high threshold provides a better fit to the largest extreme values. Therefore, in fitting the distribution function in the following analyses different thresholds between $\mu_M + 1.4\sigma_M$ and m_{max} are used and the one that provides the best fit in terms of average relative error and provides extraction of at least 10 extreme values is used. The average relative error ϵ is defined as

$$\epsilon = \frac{1}{n} \sum_{i=1}^n \frac{|M_{i,fit} - M_{i,peak}|}{M_{i,peak}} \quad (2.8)$$

where n is the number of peak values in the wind speed bin, $M_{i,fit}$ is the i th fitted value whereas $M_{i,peak}$ is the i th peak value.

The significant differences in distribution functions for the maxima extracted using different thresholds, suggests that the blade out-of-plane moment is not a Gaussian random variable. As described in appendix F the distribution of local maxima for a Gaussian variable should not be dependent on the chosen threshold. An analysis of the Gaussianity of the blade out-of-plane moment in appendix D shows that the response is not Gaussian meaning that the choice of threshold might influence the distribution of the maxima.

The extracted peak values are required to be stochastic independent. A minimum time separation of 5s between peaks have been introduced to enhance possibility that extracted peak values arise from different wind gusts. If multiple peak values over the threshold are found within 5s only the largest peak value is extracted.

2.2.2 Choice of candidate distribution function

The candidate distribution functions 3-parameter Weibull and Gumbel are fitted to the extreme data for each bin to show differences in the extrapolated loads due to the choice of distribution function. The extrapolated loads for tower fore-aft bending moment and blade-out-of-plane moment are shown in figure 2.2 and 2.3, respectively. Abscissas are normalised with respect to the maximum simulated load

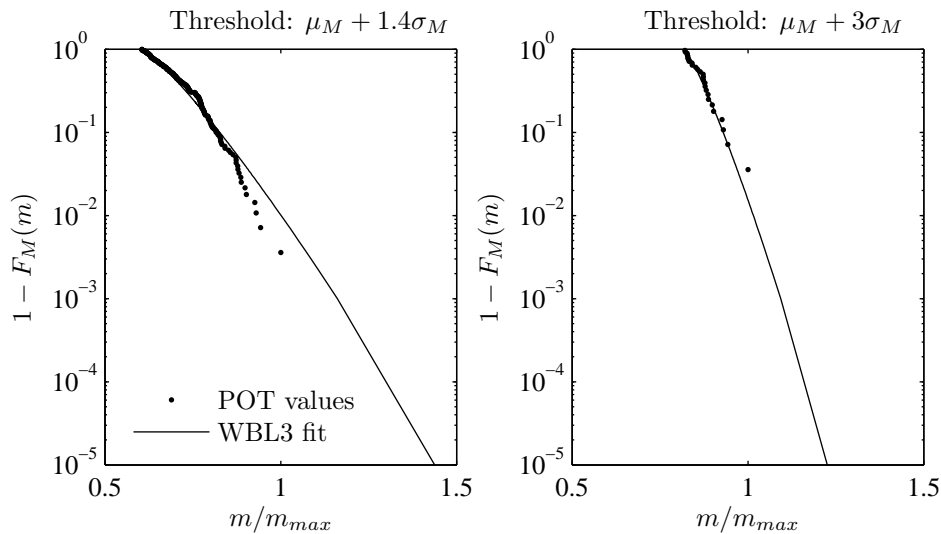


Figure 2.1: Comparison of Weibull fits to POT sample values for blade out-of-plane moment in wind bin 13-15 m/s using thresholds of $\mu_M + 1.4\sigma_M$ and $\mu_M + 3\sigma_M$.

m_{max} . The extrapolated loads from the 3-parameter Weibull distribution and the Gumbel distribution provides very different results. The Gumbel load is larger for both the blade out-of-plane bending moment and the tower fore-aft bending moment. For the blade bending moment the Gumbel fit is 50% larger than the 3-parameter Weibull fit and for the tower bending the Gumbel load is 58% larger at the response corresponding to a recurrence period of 50 years. Similar result have also been obtained by previous studies on extrapolating extreme loads using the Gumbel distribution [Ragan and Manuel, 2008].

The peak values and fitted probability distribution functions for the 3-parameter Weibull and Gumbel distribution functions are shown for all wind speed bins in figures 2.4 and 2.5 respectively. The non-exceedance probability is assigned to each extreme value by using a Weibull plotting position formula. It is seen that the 3-parameter Weibull provides the best fits to the peak values in each bin whereas the Gumbel distribution function consequently overestimates the probability of failure. The average relative error ϵ for the two distribution functions is calculated by (2.8). For the Weibull fits the relative average error is $\approx 2\%$. For the Gumbel fits the average relative error is $\approx 10\%$ for all bins.

The Weibull distribution provided the best fit of the tested candidate distribution functions. Other extreme value distribution functions could also have been used in fitting, i.e. the generalised Pareto distribution, the generalised extreme value function and the logarithmic distribution, see appendix E.1.

Previous studies on the extrapolation method used on measurements from wind turbines also conclude that the 3-parameter Weibull distribution function gives the best fit of the candidate distribution functions that were used in fitting wind turbine extreme loads [Ragan and Manuel, 2008]. However, a comparison with 50 years of measurement or simulations is yet to be performed to show the real deviation for the 50 year extrapolation load.

It should be noted that an amendment for the IEC-61400-1 standard was submitted for voting in January 2009. A brief description of the amendment and its changes to the extrapolation methodology is described in appendix E.2. However, at the end of this thesis the amendment had not been accepted and has therefore not been treated any further.

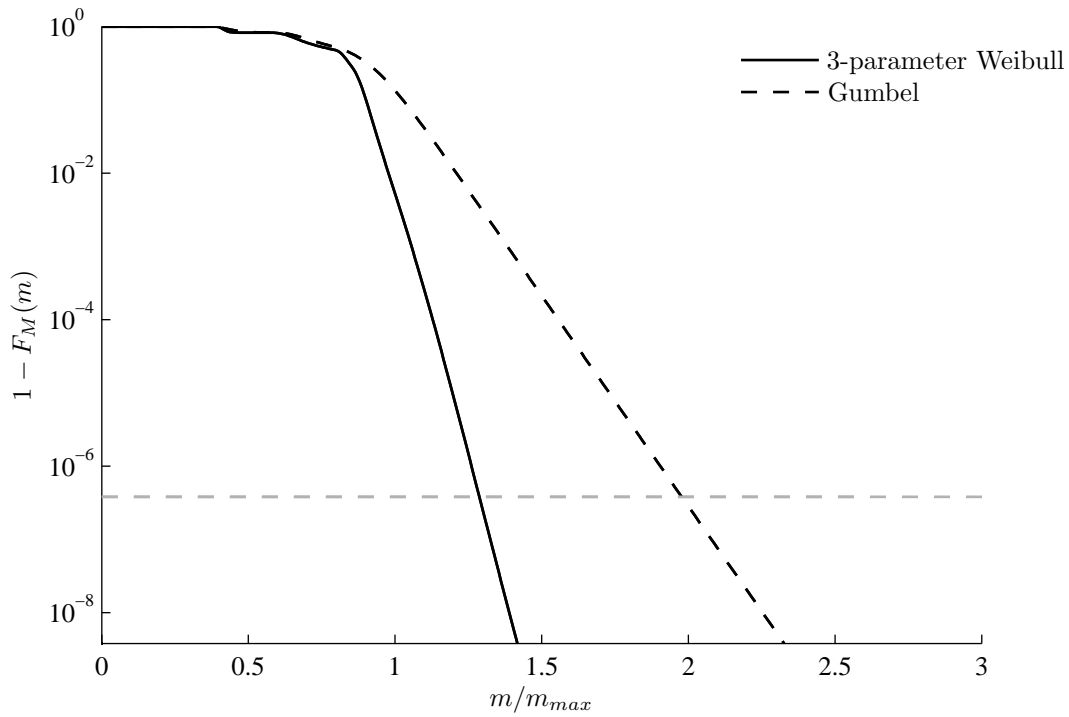


Figure 2.2: Extrapolated blade out-of-plane moment by 3-parameter Weibull and Gumbel distributions.

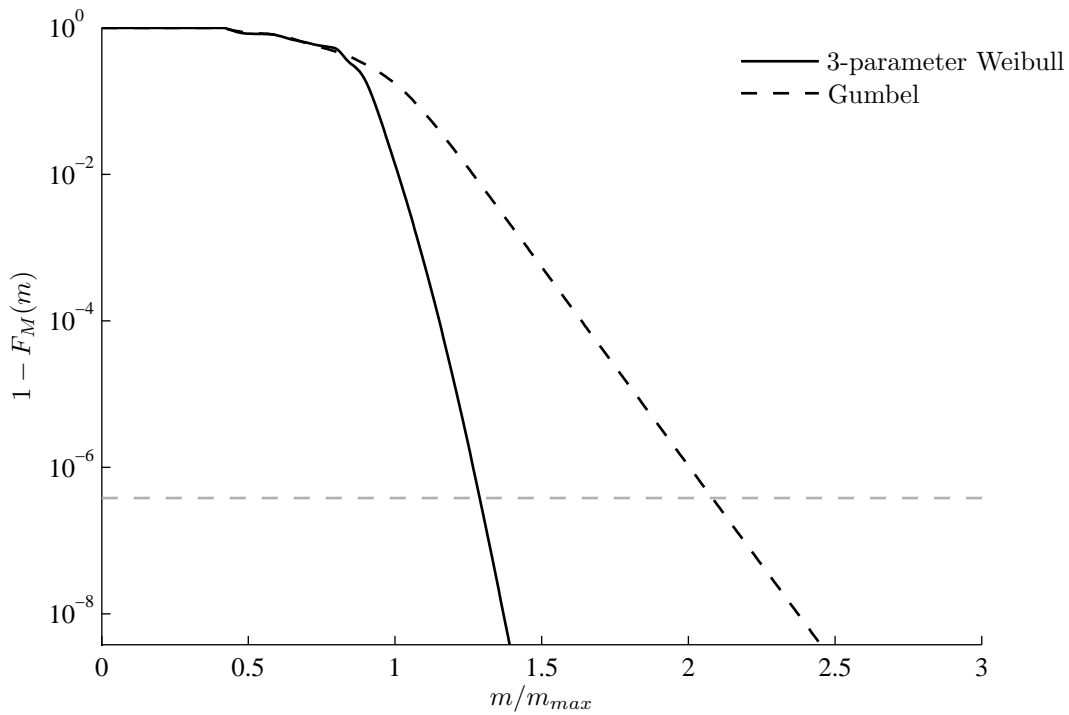


Figure 2.3: Extrapolated tower fore-aft bending moment by 3-parameter Weibull and Gumbel distributions.

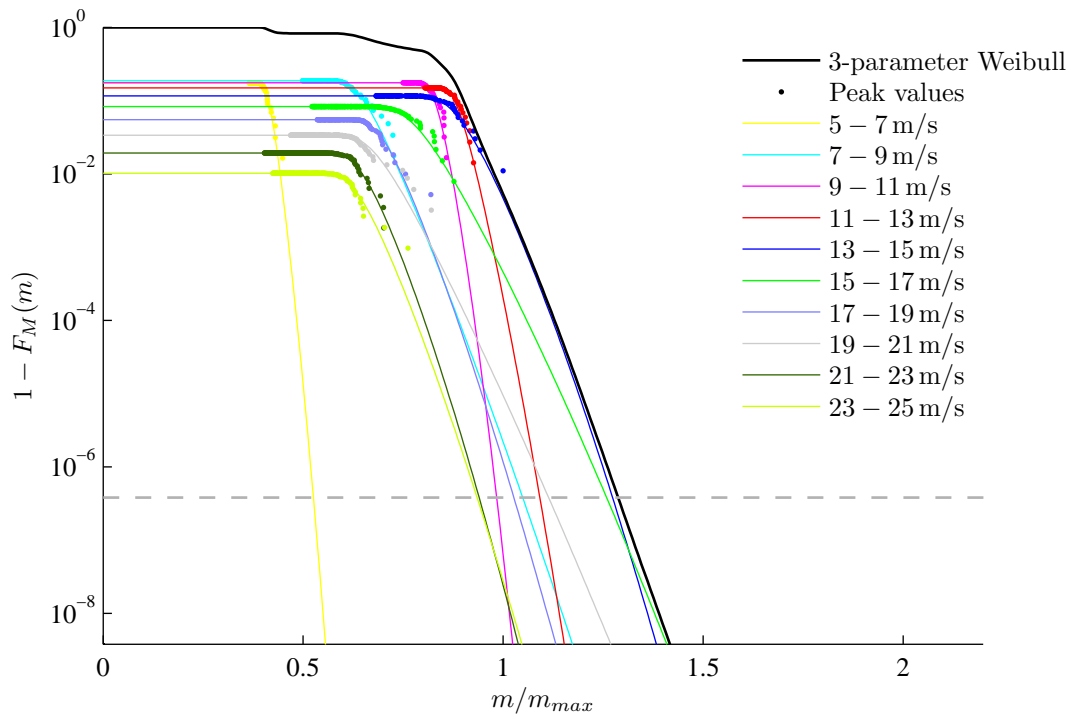


Figure 2.4: Extrapolated Weibull 3-parameter fit for tower fore-aft bending moment with peak values and local probability distribution fits; $P(M_{ext} \geq m|T)$ for each wind speed bin.

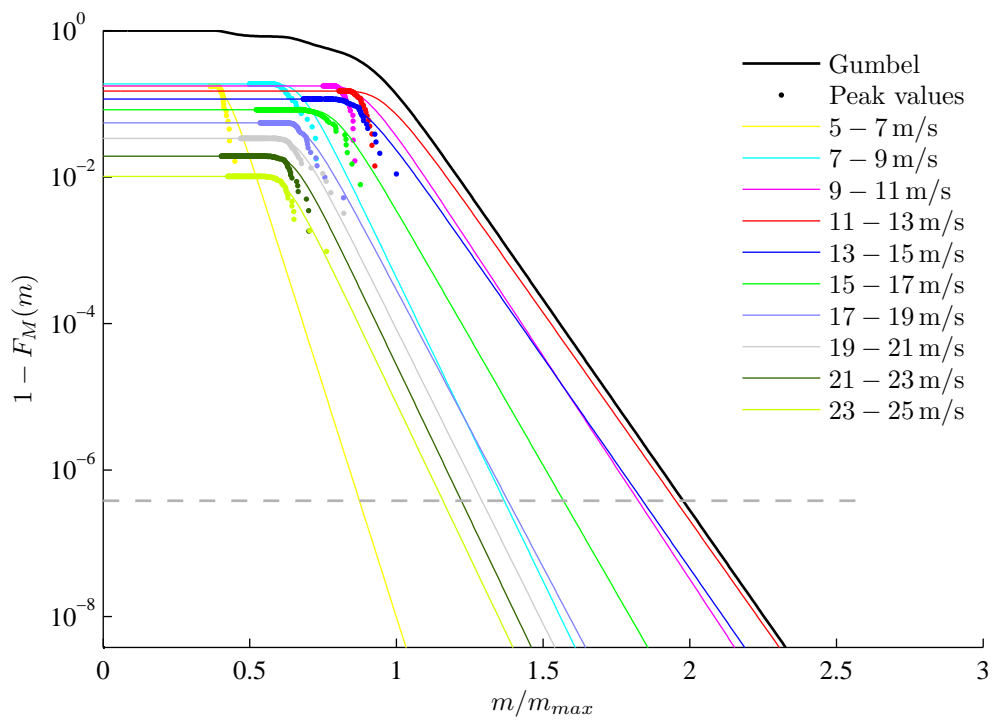


Figure 2.5: Extrapolated Gumbel fit for tower fore-aft bending moment with peak values and local probability distribution fits; $P(M_{ext} \geq m|T)$ for each wind speed bin.

2.3 Conclusion

In this chapter the statistical extrapolation method from the IEC61400-1 standard has been described and the extreme responses corresponding to a 50 year recurrence period for the tower fore-aft moment and the blade out-of-plane moment have been determined.

It was found that the extraction of extremes from a few response realisations in each wind speed bin provides different results when using different thresholds in the POT method. Introduction of a minimum time separation between extraction of peaks combined with choice of a threshold higher than the suggestion in the IEC61400-1 standard provides low dependence between extracted peak values.

The candidate probability distribution functions suggested in the IEC61400-1 standard, Gumbel and 3-parameter Weibull, have been compared for extrapolation. The 3-parameter Weibull distribution function provided the lowest average error when fitting to the local probabilities in each wind speed bin and produced estimates of the response corresponding to a 50 year recurrence period significantly smaller than the Gumbel probability distribution function.

It is concluded that the statistical extrapolation method suggested in the IEC61400-1 standard introduces a statistical uncertainty of unknown size and significance.

Chapter 3

Alternative methods for determination of low exceedance probabilities

It might be possible to overcome some of the limitations and uncertainties described in the previous chapter by introducing alternative simulation methods. The reason for choosing the currently used method is simplicity and the short computational time because only a limited number of 10 minute load series are used. The accuracy of the extrapolation is not certain because the real distribution is neither a Weibull, generalised extreme value distribution or a Pareto distribution [Ragan and Manuel, 2008]. The real distribution is something in between and an analytical solution might be impossible to find.

One method that could be proposed is a crude Monte Carlo simulation. By doing 10^9 or more simulations one could achieve a good estimate of the exceedance probability of a threshold corresponding to a 50 year recurrence load. The 10^9 simulations would generate around 25 time series failing. The problem is the calculation time which would be more than 10 years on a modern processor, taking a time-speed ratio of approximately 5 into consideration, implying that simulation of 10 minutes real time would require 2 minutes of processor time. Of course multi processor environments could speed up calculation but such a solution is not desirable.

Other methods of interest are controlled Monte Carlo simulation methods. By doing simulations in the same way as when using traditional Monte Carlo and using methods to control the weight and importance of each realisation it is possible to get better estimates of the failure probability using a limited number of simulations. In this project controlled Monte Carlo techniques "Russian Roulette and Splitting with Distance Control" and "RESTART" will be examined for use in determination of extreme loads on wind turbines.

Importance Sampling is another method that can be useful for sampling low probability events. The idea is to concentrate the sampling space around the part of the sample space that has greatest influence on the probability of failure. The problem regarding the method is choosing a sampling function that moves the samples close to the areas that has a great contribution to the probability of failure. For multidimensional systems this can be difficult and in some cases impossible. Several tests will be performed to check whether the method is usable in the purpose of this project.

In the following chapters the above mentioned methods will be examined on a simple structure to gather information on complexity compared to the effectiveness in extracting low exceedance probabilities. By using a simple structures in validating and studying the different methods it is expected to be easier to discover the limitations and drawbacks. The simple structures are further analysed in chapters 4 and 5 to choose load modelling technique and a numerical solvers.

Chapter 4

Two storey shear frame exposed to horizontal earthquake excitation

In this chapter a two storey shear frame exposed to horizontal earthquake excitation is analysed for testing the different failure probability simulations techniques mentioned in chapter 3. Three techniques for generating the acceleration process by equivalent white noise processes with finite variance are explained. The techniques are denoted the *random phase process*, the *broken line process* and the *impulse response excitation method*. A Newmark algorithm is used as numerical solver for the dynamic system, when exposed to the random phase process and the broken line process. At last it is investigated which of the three techniques is the fastest for simulating the response of the frame. Before evaluating the computational time of the three techniques, a parameter study of the three methods is carried out to estimate parameters which will result in identical accuracy for the three methods.

4.1 Structural system

The system consists of a two storey plane shear frame exposed to a horizontal earthquake excitation as shown in figure 4.1. The storey beams are assumed to be infinite rigid in bending and axial deformation, with a local mass m . The columns are linear elastic with the shear stiffness k , massless and fixed to the foundation. The energy dissipation in the columns are modelled as a viscous damper with the damping constant c .

The equations of motion for the system formulated in the relative storey displacements $Y_1(t)$ and $Y_2(t)$ are given by

$$\mathbf{M}\ddot{\mathbf{Y}} + 2\zeta_0\omega_0\mathbf{k}\dot{\mathbf{Y}} + \omega_0^2\mathbf{k}\mathbf{Y} = -\mathbf{b}\ddot{Y}_0(t) \quad (4.1)$$

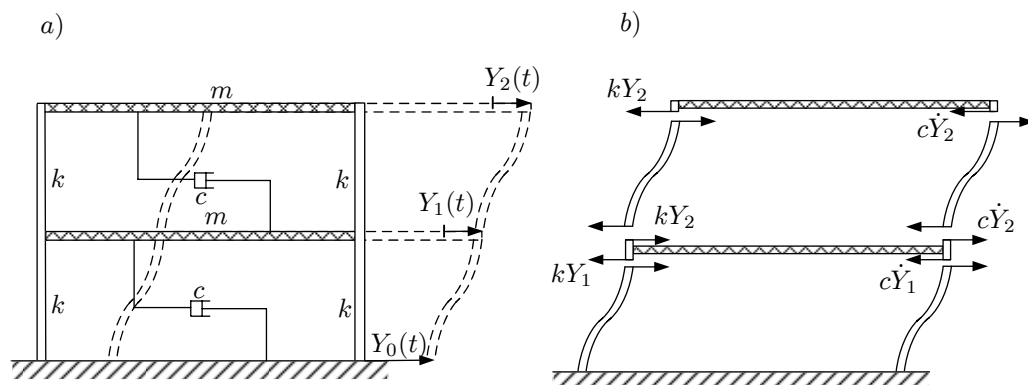


Figure 4.1: a) Two storey shear frame exposed to horizontal earthquake excitation. b) Forces acting on the free storey beams.

where

$$\mathbf{Y}(t) = \begin{bmatrix} Y_1(t) \\ Y_2(t) \end{bmatrix}, \quad \mathbf{M} = \begin{bmatrix} 1 & 0 \\ 1 & 1 \end{bmatrix}, \quad \mathbf{k} = \begin{bmatrix} 1 & -1 \\ 0 & 1 \end{bmatrix}, \quad \mathbf{b} = \begin{bmatrix} 1 \\ 1 \end{bmatrix}$$

The parameters ω_0 and ζ_0 are given as

$$\omega_0 = \sqrt{\frac{k}{m}}, \quad \zeta_0 = \frac{c}{2\sqrt{mk}} \quad (4.2)$$

A modal analysis of the system is carried out in appendix G. The undamped angular eigenfrequencies and the modal damping ratios are given by

$$\left. \begin{array}{l} \omega_1 \\ \omega_2 \end{array} \right\} = \sqrt{\frac{3 \mp \sqrt{5}}{2}} \omega_0 \quad (4.3)$$

$$\left. \begin{array}{l} \zeta_1 \\ \zeta_2 \end{array} \right\} = \sqrt{\frac{3 \mp \sqrt{5}}{2}} \zeta_0 \quad (4.4)$$

The first angular eigenfrequency and the first damping ratio is set to $\omega_1 = 1$ rad/s and $\zeta_1 = 0.01$ respectively. Thus by (4.3) and (4.4)

$$\begin{aligned} \omega_0 &= 1.618 \text{ rad/s}, & \omega_2 &= 2.618 \text{ rad/s} \\ \zeta_0 &= 0.01618, & \zeta_2 &= 0.0262 \end{aligned}$$

The frequency response function for the two storeys are given by, cf. appendix G.

$$H_1(\omega) = \frac{P_1(i\omega)}{Q(i\omega)}, \quad H_2(\omega) = \frac{P_2(i\omega)}{Q(i\omega)} \quad (4.5)$$

where

$$P_1(z) = -z^2 - 4\zeta_0\omega_0 z - 2\omega_0^2$$

$$P_2(z) = -2\zeta_0\omega_0 z - \omega_0^2$$

$$Q(z) = \prod_j^4 (z - z_j)$$

z_j denotes the poles of the system and are given by

$$\left. \begin{array}{l} z_1 \\ z_2 \end{array} \right\} = \omega_1 \left(-\zeta_1 \pm i\sqrt{1 - \zeta_1^2} \right) \quad (4.6)$$

$$\left. \begin{array}{l} z_3 \\ z_4 \end{array} \right\} = \omega_2 \left(-\zeta_2 \pm i\sqrt{1 - \zeta_2^2} \right) \quad (4.7)$$

The frequency response functions $H_i(\omega)$ will later on be used to calculate the auto-covariance function of each relative storey displacement response.

4.2 Ground Surface Acceleration Models

The ground surface acceleration is modelled by a white noise process $\{\ddot{Y}_0(t), t \in \mathbb{R}\}$, which is a zero-mean homogeneous Gaussian process with the auto-covariance function given by

$$E[\ddot{Y}_0(t)\ddot{Y}_0(t+\tau)] = 2\pi S_0 \delta(\tau) \quad (4.8)$$

where S_0 is the spectral intensity and $\delta(\tau)$ is the Dirac delta function. Next, the three mentioned techniques for generating an equivalent white noise process are investigated.

Random Phase Process

An upper cut-off frequency ω_m is specified, which is above all angular eigenfrequencies in the system. The frequency range $[0, \omega_m]$ is discretised in N equidistant intervals, with a bandwidth of $\Delta\omega$ as shown in figure 4.2. Then the white noise process is replaced with an equivalent sum of random phase processes defined by

$$\ddot{Y}_0(t) = \sum_{j=1}^N a_j \cos(\omega_j t + \Phi_j) \quad (4.9)$$

$$E[\ddot{Y}_0(t)] = 0 \quad (4.10)$$

$$E[\ddot{Y}_0(t)\ddot{Y}_0(t)] = \sum_{j=1}^N \frac{1}{2} a_j^2 \quad (4.11)$$

a_j and ω_j are real constants and Φ_j are mutual independent uniformly distributed random variables in the interval $[0, 2\pi]$. a_j is calibrated so that the variance contribution from the band width with center frequency ω_j is equal to the area under $S_{\ddot{Y}_0\ddot{Y}_0} = S_0$. The variance contribution of each harmonic component is given by

$$\begin{aligned} \sigma_{\ddot{Y}_0,j}^2 &= \frac{1}{2} a_j^2 = 2S_0 \Delta\omega \Rightarrow \\ a_j &= \sqrt{4S_0 \Delta\omega} \end{aligned} \quad (4.12)$$

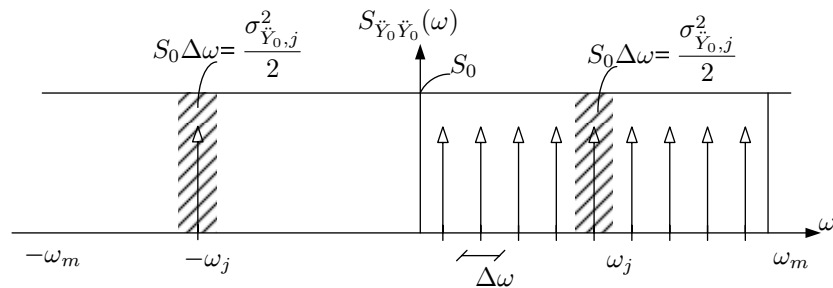


Figure 4.2: Discretisation of the double sided auto spectral density function $S_{\ddot{Y}_0\ddot{Y}_0}(\omega)$.

The random phase process will converge towards a white noise process for $N \rightarrow \infty$ and $\omega_m \rightarrow \infty$. Since an infinite number of harmonic components is not possible, a convergence study is carried out in section 4.4.

Broken Line Process

Another approach for simulating a band-limited white noise process is a so-called broken line process $\{\tilde{O}(t)\}$, which is illustrated in figure 4.3. The process is determined by interpolating between identical distributed independent random variables $O_j \sim N(0, \sigma_O)$ placed at equidistant instants of time T_0, T_1, \dots as given by

$$\tilde{O}(t) = O_i + (O_{i+1} - O_i) \frac{t - T_i}{\Delta t_{bl}} \quad , \quad t \in [T_i, T_i + \Delta t_{bl}[\quad (4.13)$$

$$T_i = i \cdot \Delta t_{bl} \quad , \quad i = 0, 1, \dots, T/\Delta t_{bl} - 1$$

where Δt_{bl} is the interval between the time T_i and T_{i+1} . α is a random variable uniformly distributed in the interval $[0, 1]$, which is suppose to secure a stationary \tilde{O} -process, cf. figure 4.3. σ_O and Δt_{bl} are determined so that the auto-spectral density function given by (4.14) remains flat within the frequency band $[0, \omega_m]$. [Clough and Penzien, 1982]

$$S_{\tilde{O}\tilde{O}}(\omega) = \frac{\sigma_O^2 \Delta t_{bl}}{2\pi} \left(\frac{\sin(\frac{1}{2}\omega \Delta t_{bl})}{\frac{1}{2}\omega \Delta t_{bl}} \right)^4 \quad (4.14)$$

σ_O and Δt_{bl} is determined by presuming that the spectrum is flat within 99% of the value of the requested auto-spectral density S_0 at the angular frequency ω_m . ω_m is selected well above all angular eigenfrequencies of the structure related to modes of the importance for the global dynamic response. Hereby the following criteria must be fulfilled

$$\Delta t_{bl} \leq \frac{0.2455}{\omega_m} \quad (4.15)$$

$$\sigma_O = \sqrt{\frac{2\pi}{\Delta t_{bl}}} S_0 \quad (4.16)$$

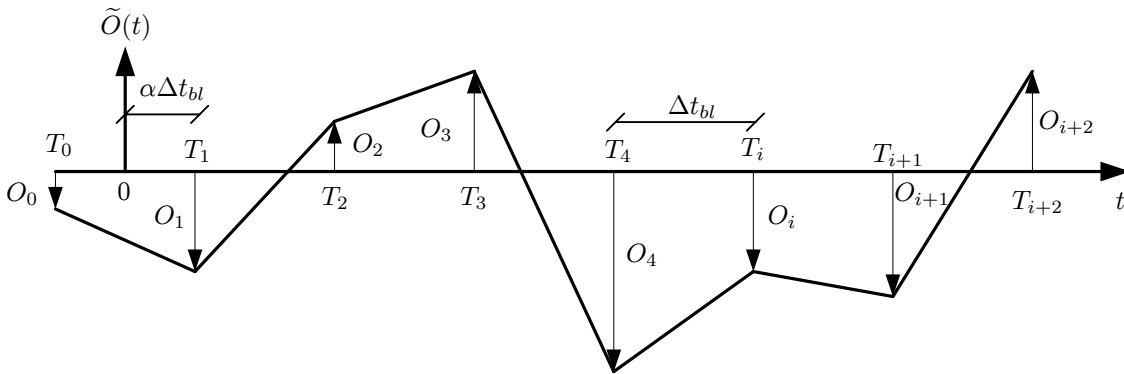


Figure 4.3: Realization of a broken line process.

When generating the \tilde{O} -process, problems can occur if $t - (1 - \alpha)\Delta t_{bl}$ is a integer-multiplier r of Δt_{bl} , because the interpolation point $(t - T_i)$ becomes deterministic for each realisation of α cf. appendix H. This is overcome by choosing r as a irrational number.

Impulse response excitation method

This section explains how the so-called Franklin's method can be used to simulate the response process if the equations of motion of the system is formulated as an equivalent stochastic differential equation. The method relies on the system being linear in which case it may be written on the state vector form

$$\left. \begin{aligned} \frac{d}{dt}\mathbf{Z}(t) &= \mathbf{A}\mathbf{Z}(t) + \mathbf{B}\mathbf{W}(t) \quad , \quad t > t_0 \\ \mathbf{Z}(t_0) &= \mathbf{Z}_0 \end{aligned} \right\} \quad (4.17)$$

where \mathbf{A} and \mathbf{B} are real constant matrices of dimension $n \times n$ and $n \times m$, respectively. Then, the Itô and Stratonovich formulation are equivalent, see appendix J.1. For the structural system described in section 4.1, \mathbf{A} and \mathbf{B} are given by

$$\mathbf{A} = \begin{bmatrix} \mathbf{0} & \mathbf{I} \\ -\omega_0^2 \mathbf{k} & -2\zeta_0 \omega_0 \mathbf{k} \end{bmatrix} \quad , \quad \mathbf{B} = \begin{bmatrix} \mathbf{0} \\ -\mathbf{b} \end{bmatrix} \quad (4.18)$$

$\mathbf{Z}(t), t \in [t_0, \infty[$ is an n -dimensional state vector $\mathbf{Z} = [Y_1, \dots, Y_n, \dot{Y}_1, \dots, \dot{Y}_n]^T$ with initial values \mathbf{Z}_0 , and $\mathbf{W}(t), t \in]t_0, \infty[$ is an m -dimensional excitation process for which the component processes are independent white noise processes. A numerical solution to (4.17) is given on the discrete form, [Nielsen, 2007b]

$$\mathbf{Z}_{j+1} = e^{\mathbf{A}\Delta t} \mathbf{Z}_j + \mathbf{R} \quad (4.19)$$

where \mathbf{R} can be simulated by, [Nielsen, 2007b]

$$\mathbf{R} = \mathbf{C}_{\mathbf{RR}}^{\frac{1}{2}} \mathbf{\Xi} \quad (4.20)$$

where $\mathbf{\Xi}$ is a n -dimensional vector $\mathbf{\Xi}^T = [\Xi_1, \dots, \Xi_n]^T$ in which all entries are mutually independent normal variables distributed as $\Xi \sim N(0, 1)$. $\mathbf{C}_{\mathbf{RR}}$ is the covariance matrix of \mathbf{R} and determined by, [Nielsen, 2007b]

$$\mathbf{C}_{\mathbf{RR}} = 2\pi S_0 \int_0^{\Delta t} (e^{\mathbf{A}u} \mathbf{B})(e^{\mathbf{A}u} \mathbf{B})^T du \quad (4.21)$$

The matrix exponential function $e^{\mathbf{A}u}$ is calculated as

$$e^{\mathbf{A}u} = \mathbf{\Psi} e^{\mathbf{\Lambda}u} \mathbf{\Psi}^{-1} \quad (4.22)$$

where

$$\Psi = [\Psi^{(1)} \dots \Psi^{(n)}] \quad (4.23)$$

$$\Lambda = \begin{bmatrix} \lambda_1 & & \\ & \ddots & \\ & & \lambda_n \end{bmatrix} \quad (4.24)$$

and $(\lambda_j, \Psi^{(j)})$ denotes the eigenvalues and eigenvectors of the eigenvalue problem

$$\mathbf{A}\Psi^{(j)} = \lambda_j\Psi^{(j)} \quad (4.25)$$

Realisations of the response process \mathbf{Z} is now generated by use of (4.19). The method is stable and exact for arbitrary time steps Δt .

4.3 Numerical time integration

The equations of motion of the shear frame are solved numerically by an unconditional stable Newmark algorithm free of numerical damping corresponding to the integration parameters $(\beta, \gamma) = (\frac{1}{4}, \frac{1}{2})$. In order to calculate the response properly, the integration time step Δt_I is set to $\frac{1}{20}$ of the first fundamental eigenperiod T_1 . The largest time step is then given by

$$\Delta t_I \leq \frac{1}{20}T_1 = \frac{1}{20} \frac{2\pi}{\omega_1} \Rightarrow \Delta t_I \leq 0.31s \quad (4.26)$$

However, if utilising the broken line process for modelling the ground surface acceleration, the upper boundary for the integration time Δt_I step is governed by the broken line time step Δt_{bl} given by (4.15) as the condition $\Delta t_I \leq \Delta t_{bl}$ should be fulfilled.

Auto-Covariance function

The stationary variance of the system exposed to a white noise acceleration process is determined by an ergodic sampling. The corresponding analytical solution for the autocovariance function $\kappa_{Y_i Y_i}(\tau)$ for the relative displacement of storey i is given by, [Nielsen, 2007b]

$$\kappa_{Y_i Y_i}(\tau) = -\pi S_0 \sum_{j=1}^s \frac{e^{z_j|\tau|}}{z_j} \frac{P_i(z_j)P_i(-z_j)}{\prod_{\substack{k=1 \\ k \neq j}}^s (z_k^2 - z_j^2)}, \quad i = 1, 2 \quad (4.27)$$

$P_i(z)$ is the numerator in the rational frequency response function, (4.5) and z_j are the poles of the denominator polynomial given by (4.6) and (4.7). The order of the denominator polynomial Q is $s = 4$. For a spectral intensity $S_0 = 1$ the variance $\sigma_{Y_i}^2$ is found at $\tau = 0$

$$\sigma_{Y_1}^2 = 82.5149 \quad , \quad \sigma_{Y_2}^2 = 32.0731$$

To evaluate the performance of different acceleration processes, an ergodic sampling of the response is carried out. The sampling interval T is divided in n subintervals of the length Δt and assuming that the mean value is zero an estimate of $\sigma_{\hat{Y}_i}^2$ is determined by

$$\hat{\sigma}_{Y_i}^2 = \frac{1}{n} \sum_{j=1}^n Y_i^2(j \cdot \Delta t) \quad (4.28)$$

4.4 Parameter analysis

Before the different equivalent white noise models are evaluated, a parameter analysis is carried out. First of all the transient phase and the minimum value for the upper cut-off frequency ω_m of the flat spectra are evaluated. Hereafter the parameters for the two equivalent white noise models are evaluated. The important parameters for the random phase process are the discretisation increment of the load spectra $\Delta\omega$ and the integration time step Δt_I . For the broken line process the magnitude of the integration time step Δt_I in proportion to the time step Δt_{bl} in the broken line process is the important parameters.

4.4.1 Transient phase

To simulate a stationary process from the start, the initial condition has to be modelled as a stochastic variable belonging to the same population as the displacement and velocity response in the stationary state. This is in general difficult, but is possible in the present simple case. Despite this possibility the initial conditions are set to the deterministic values

$$\mathbf{Y}(t_0) = \begin{bmatrix} 0 \\ 0 \end{bmatrix}, \quad \dot{\mathbf{Y}}(t_0) = \begin{bmatrix} 0 \\ 0 \end{bmatrix} \quad (4.29)$$

The transient phase is estimated from the eigenvibrations of $\{\mathbf{Y}, t \in [0, \infty]\}$ and the initial condition given by

$$\mathbf{Y}(t_0) = \begin{bmatrix} 1 \\ 1 \end{bmatrix}, \quad \dot{\mathbf{Y}}(t_0) = \begin{bmatrix} 0 \\ 0 \end{bmatrix} \quad (4.30)$$

From figure 4.4 it is shown that after $50T_1$ the displacements are less than 5% of the initial displacement by which it is assumed that the initial condition can be neglected for $t > 50T_1$. Notice that the modal damping ratios in the present case have been selected as $\zeta_1 = \zeta_2 = 0.01$.

In the following parameter analysis, the variance will be determined from an ergodic sampling after the 50 fundamental eigenperiods.

4.4.2 Cut-off frequency

The maximum frequency is chosen in a way, so the eigenfrequencies of the structure are contained within the band. In the evaluation of the upper band limit, the acceleration process is modelled by a random phase process.

As it emerge from figure 4.5 the estimate of the standard deviation of the 1st storey displacement $\sigma_{\hat{Y}_1}$ converge when $\omega_m > \omega_1$. Note that σ_{Y_1} denote the analytical solution for the stationary standard

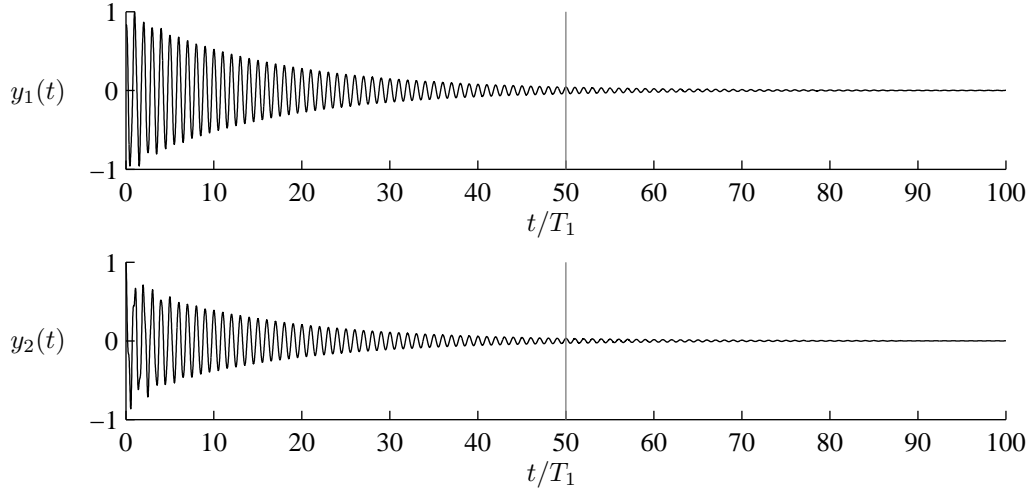


Figure 4.4: Damped eigen vibration of \mathbf{Y} given the initial condition (4.30).

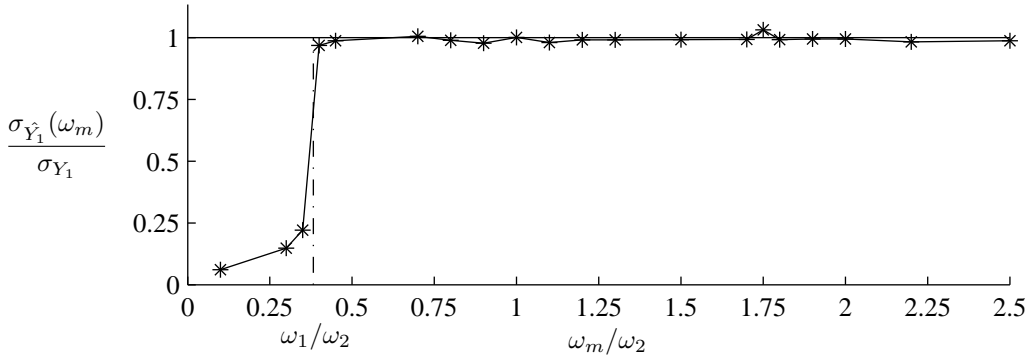


Figure 4.5: Convergence study of the cut-off frequency. Random Phase Process: $\Delta t_I = T_1/30$, $N = 1000$ and $T = 1000T_1$.

deviation of $Y_1(t)$, obtained from (4.27). The reason why the criteria $\omega_m > \omega_1$ is sufficient to obtain convergence of σ_{Y_1} is that influence on the response from the second mode is negligible.

The low influence of the second mode is also seen in the frequency response functions of the system, figure 4.6. For this reason only $\sigma_{\hat{Y}_1}$ is evaluated in the following parameter analysis, as the standard deviation of the second storey is almost proportional.

4.4.3 Integration time step

Based on the random phase process a convergence study of the integration time step Δt_I in the Newmark algorithm is carried out. Previously a least 20 time steps per fundamental eigenperiod T_1 was proposed. This proposition is verified in figure 4.7.

4.4.4 Random phase process

Next, the influence on the estimate of σ_{Y_1} as a function of the number of harmonic components N is evaluated. The cut-off frequency ω_m is kept fixed, so the frequency band $\Delta\omega = \omega_m/N$ varies. Convergence of the estimate as a function of N is shown in figure 4.8.

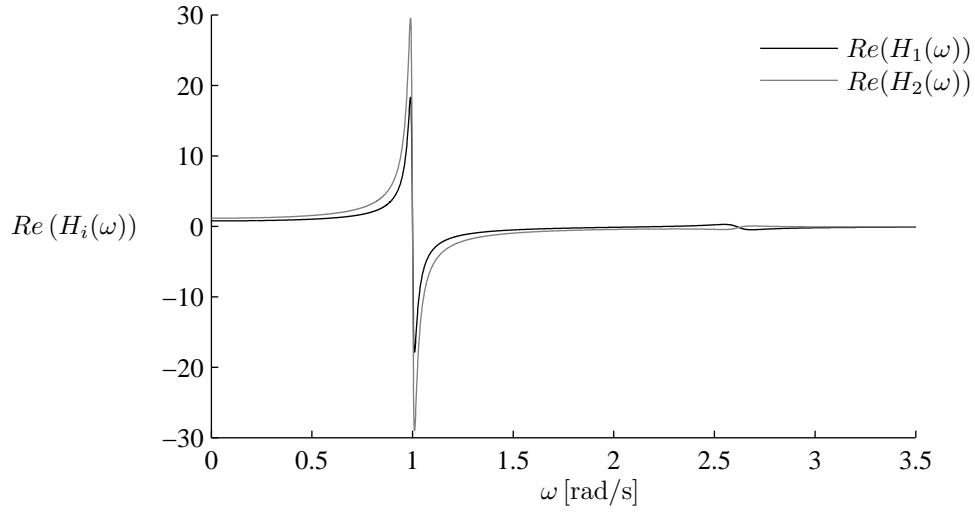


Figure 4.6: Real part of the response functions $H_i(\omega)$ for the reference frame.

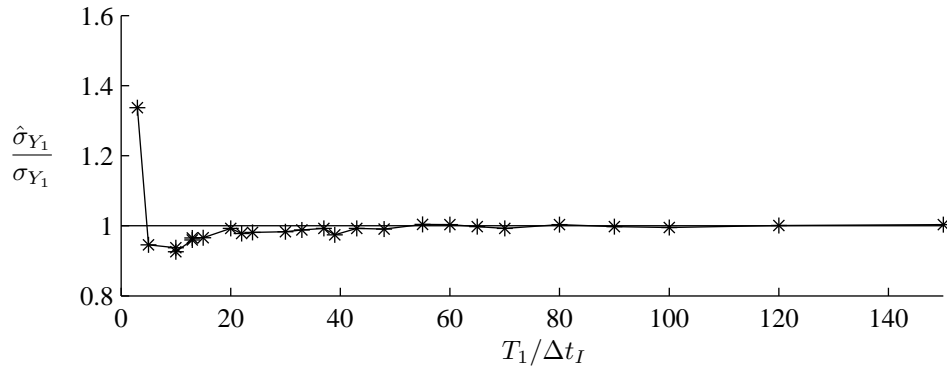


Figure 4.7: Convergence study of Δt_I per T_1 . Random Phase process: $\omega_m = 2\omega_2$, $N = 400$ and $T = 1000T_1$.

As it is seen in figure 4.8 $\hat{\sigma}_{Y_1}$ has converged with sufficient accuracy for approximately $N \geq 400$.

4.4.5 Broken line process

To establish a flat spectra within the band-limit an upper limit for the incremental time step of the process generation is given by (4.15). In the same way as for the random phase process the ground surface acceleration is determined at the instants of time $t = t_i$, where

$$t_i = i \cdot \Delta t_I \quad , \quad i = 0, 1, \dots, n \quad (4.31)$$

n is the number of integration steps. Next, a convergence study of $\Delta t_{bl}/\Delta t_I$ is carried out.

As seen in figure 4.9 the estimate of the variance process do converge for $\Delta t_{bl}/\Delta t_I > 1$. It is also seen that the response has increased intensity when $\Delta t_I > \Delta t_{bl}$, whereby the following criteria must be fulfilled

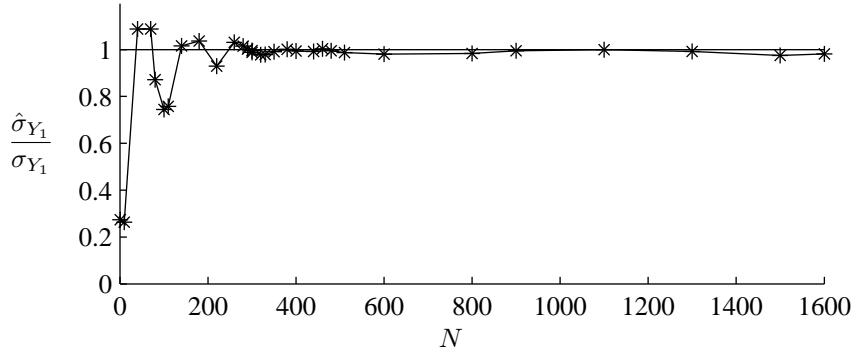


Figure 4.8: Convergence study of N . The following parameters are used: $\Delta t_I = T_1/30$, $T = 1000T_1$. \dot{Y}_0 is modelled as a random phase process.

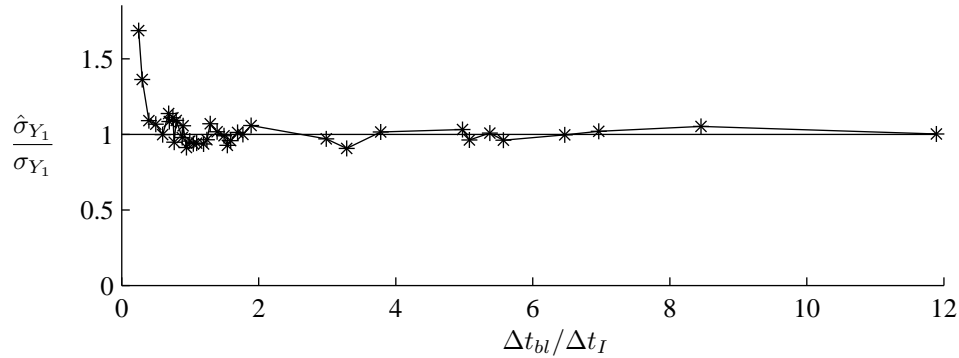


Figure 4.9: Convergence study of $\Delta t_{bl}/\Delta t_I$. The following parameters are used: $\Delta t_{bl} = 0.0782$, $T = 1000T_1$.

$$\Delta t_{bl} > \Delta t_I \quad (4.32)$$

A consequence of (4.32) is that the time step Δt_I must be decreased significantly, resulting in an increase in the calculation time. Δt_{bl} can be increased by reducing the criteria of the flatness of the spectra.

4.4.6 Evaluation of the ground surface acceleration processes

Based on the parameter analysis, the three load models will be evaluated with respect to the used computational time for achieving a certain accuracy of the variance estimate. The parameters used in the comparison are given table 4.1.

-	Random phase process	Broken line process	Impulse response exiation
ω_m	3.14 rad/s	3.14 rad/s	-
N	400	-	-
Transient phase	$50 T_1$	$50 T_1$	$50 T_1$
Δt_{bl}	-	0.0782 s	-
Δt_I	$\frac{2\pi}{20}$ s	$\frac{2\pi}{135}$ s	$\frac{2\pi}{20}$ s

Table 4.1: Parameters used in the evaluation of the three ground acceleration processes.

The parameters are selected so they will give the lowest possible computational time and still converge. The computational time for the different ground surface accelerations is shown in table 4.2.

-	Random phase process	Broken line process	Impulse response excitation
Computational time	1.1 s	5.1 s	0.1 s

Table 4.2: Computational time used to calculate the response of the shear frame for 1000 periods.

From table 4.2 it emerge that the random phase process is 5 times faster than the broken line process. The reason for this is that the number of time steps required by the broken line process is increased by a factor 6.75 compared to the random phase process. The broken line process might be more useful for systems with smaller fundamental eigenperiod, as the time step is determined by the system.

Chapter 5

Two bladed wind turbine exposed to a turbulent wind field

In the following a simple model of a wind turbine will be set up, on which the IS method and RR&S algorithm will be implemented to obtain the extreme response value corresponding to a recurrence period of 50 years. The mass and stiffness of the wind turbine will be calibrated so the deflections and eigenvibrations correspond to the 5-MW reference wind turbine described in appendix C. The damping of the system will be modelled by using the damping ratios of the 5 MW reference wind turbine. The wind load acts only on the blades and consists of a mean wind speed of 15 m/s and a time-varying turbulence, modelled by the state space representation of an ARMA model described in appendix B.3.

5.1 Structural system

The wind turbine consists of a tower, a nacelle and two blades. The tower and blades are modelled as beams which only deflect in the mean wind direction as shown in figure 5.1. Furthermore, the blades perform rigid body rotation around the nacelle in the clockwise direction as seen from an upwind direction and are fixed in all other directions. The nacelle is fixed to the end of the tower beam and is modelled as a point mass.

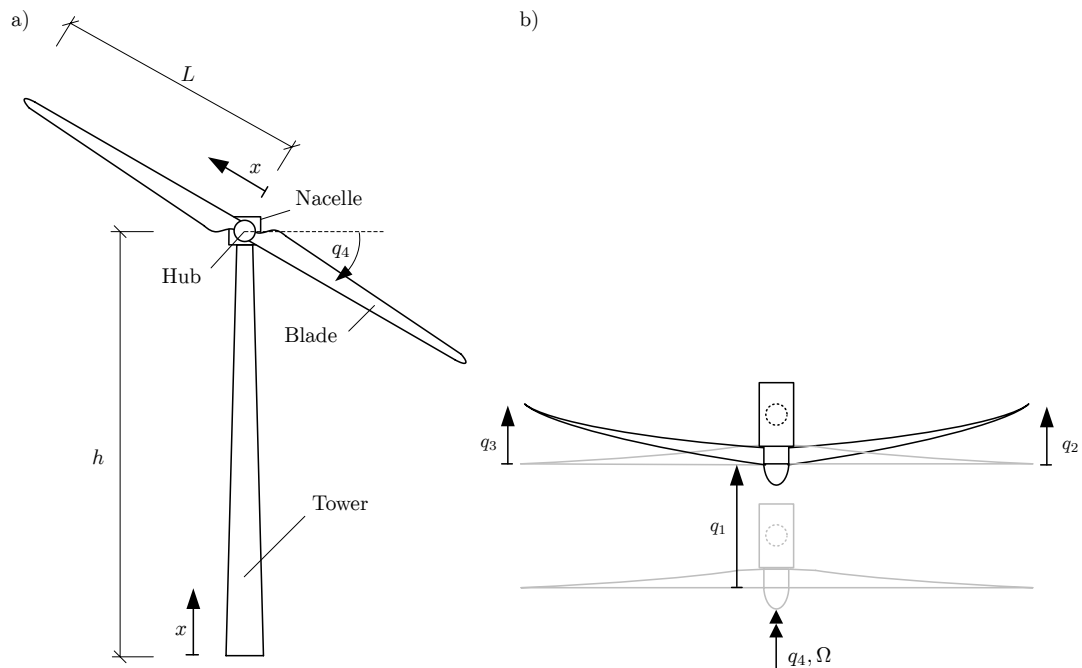


Figure 5.1: a) Two bladed wind turbine seen from the front. b) Two bladed wind turbine seen from the top.

5.1.1 System reduction

The continuous beam element of each substructure is modelled by single degree-of-freedom models. Only motions in the mean wind direction is considered for which reason no gyroscopic forces (save the centripetal inertial forces) are present.

Let $y_1(x, t)$ denote the displacement of the tower in the mean wind direction where $x \in [0, h]$ is measured from the foundation and h is the height of the nacelle above the ground surface. Further let $y_2(x, t)$ and $y_3(x, t)$ denote the displacement fields of the blades relative to the hub in the same direction where $x \in [0, L]$ is measured from the hub and L is the length of the blades. The indicated displacement fields will be modelled by merely a single degree of freedom $q_1(t)$, $q_2(t)$ and $q_3(t)$ corresponding to the representations

$$\left. \begin{aligned} y_1(x, t) &\simeq \Phi_0(x)q_1(t) \\ y_2(x, t) &\simeq \Phi(x)q_2(t) \\ y_3(x, t) &\simeq \Phi(x)q_3(t) \end{aligned} \right\} \quad (5.1)$$

$\Phi_0(x)$ and $\Phi(x)$ are mode shapes which fulfil the kinematic boundary conditions at the foundation and at the hub, i.e.

$$\left. \begin{aligned} \Phi_0(0) &= \frac{d\Phi_0(0)}{dx} = 0 \\ \Phi(0) &= \frac{d\Phi(0)}{dx} = 0 \end{aligned} \right\} \quad (5.2)$$

All mode shapes are assumed to be normalized to 1 at the other end, i.e. $\Phi_0(h) = \Phi(L) = 1$.

The blades are modelled as Bernoulli-Euler beams with the bending stiffness $EI(x)$ and the mass per unit length $\mu(x)$. The tower is also modelled as a Bernoulli-Euler beam with the bending stiffness $EI_0(x)$. The mass per unit length is formally written as

$$\bar{\mu}_0(x) = \mu_0(x) + M_0\delta(x - h) \quad (5.3)$$

where $\mu_0(x)$ denotes the continuous mass distribution, M_0 is the mass of the nacelle and $\delta(\cdot)$ is Dirac's delta function. The dynamic load per unit length on the tower in the mean wind direction is denoted $p_1(x, t)$. Correspondingly, the load on the two blades in the same direction are denoted $p_2(x, t)$ and $p_3(x, t)$.

The drive train is modelled as a single rotational degree-of-freedom q_4 by assuming infinitive stiff driveshaft and no elastic deformation in the gear, whereby the following kinematic relation emerge

$$q_4 = Nq_g \quad (5.4)$$

where N is the gear ratio and q_g is the rotational speed of the generator, cf. figure 5.2. Furthermore, the mass moment of inertia of the gear wheels and the connected shafts are included into the mass moment of inertia J_r and J_g of the rotor and the generator rotor, respectively.

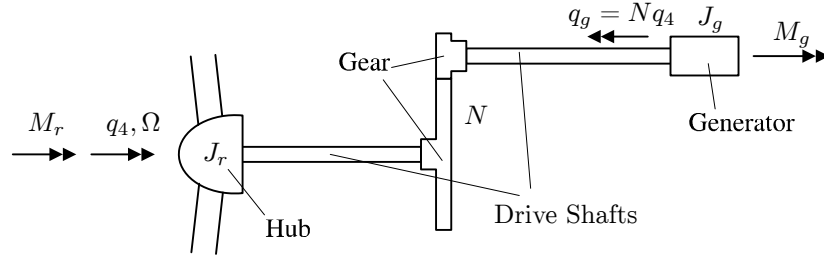


Figure 5.2: Single degree-of-freedom representation of drive train.

The kinetic energy of the structure becomes

$$\begin{aligned}
 \mathcal{T}(\dot{q}_1, \dot{q}_2, \dot{q}_3, \dot{q}_4) &= \int_0^{h^+} \frac{1}{2} \bar{\mu}_0(x) \dot{y}_1^2(x, t) dx + \int_0^L \frac{1}{2} \mu(x) (\dot{y}_1(h) + \dot{y}_2(x, t))^2 dx + \\
 &\quad \int_0^L \frac{1}{2} \mu(x) (\dot{y}_1(h) + \dot{y}_3(x, t))^2 dx + \frac{1}{2} (J_0 + N^2 J_g) \dot{q}_4^2 \\
 &= \frac{1}{2} m_0 \dot{q}_1^2(t) + \frac{1}{2} m \dot{q}_2^2(t) + \frac{1}{2} m \dot{q}_3^2(t) + m_1 \dot{q}_1(t) \dot{q}_2(t) + m_1 \dot{q}_1(t) \dot{q}_3(t) + J \dot{q}_4^2
 \end{aligned} \tag{5.5}$$

where

$$\left. \begin{aligned}
 m_0 &= \int_0^h \mu_0(x) \Phi_0^2(x) dx + M_0 + 2 \int_0^L \mu(x) dx \\
 m &= \int_0^L \mu(x) \Phi^2(x) dx \\
 m_1 &= \int_0^L \mu(x) \Phi(x) dx
 \end{aligned} \right\} \tag{5.6}$$

m_0 and m are the generalised masses related to the degrees of freedom $q_1(t)$ and $q_2(t)$, $q_3(t)$. m_1 is a coupling parameter and J is the generalised mass moment of inertia related to the rigid body degree of freedom $q_4(t)$ given as

$$J = J_r + N^2 J_g \tag{5.7}$$

The potential energy becomes

$$\begin{aligned}
\mathcal{U}(q_1, q_2, q_3, q_4) &= \int_0^L \frac{1}{2} EI_0(x) \left(\frac{d^2 y_1}{dx^2} \right)^2 dx + \int_0^L \frac{1}{2} EI(x) \left(\frac{d^2 y_2}{dx^2} \right)^2 dx + \\
&\quad \int_0^L \frac{1}{2} EI(x) \left(\frac{d^2 y_3}{dx^2} \right)^2 dx - \int_0^h y_1(x) p_1(x, t) dx - \\
&\quad \int_0^L (y_1(h) + y_2(x, t)) p_2(x, t) dx - \int_0^L (y_1(h) + y_3(x, t)) p_3(x, t) dx + \\
&\quad q_4(t)(-M_0 + NM_g) \\
&= \frac{1}{2} k_0 q_1^2 + \frac{1}{2} k q_2^2 + \frac{1}{2} k q_3^2 - q_1 F_1(t) - q_2 F_2(t) - q_3 F_3(t) - q_4 F_4(t)
\end{aligned} \tag{5.8}$$

where the generalised stiffness coefficients are given as

$$\left. \begin{aligned} k_0 &= \int_0^h EI_0(x) \left(\frac{d^2 \Phi_0}{dx^2} \right)^2 dx \\ k &= \int_0^h EI(x) \left(\frac{d^2 \Phi}{dx^2} \right)^2 dx \end{aligned} \right\} \tag{5.9}$$

The generalised external dynamic loads become

$$\left. \begin{aligned} F_1(t) &= \int_0^h \Phi_0(x) p_1(x, t) dx + \int_0^L (\Phi(x) p_2(x, t) + \Phi(x) p_3(x, t)) dx \\ F_2(t) &= \int_0^L \Phi(x) p_2(x, t) dx \\ F_3(t) &= \int_0^L \Phi(x) p_3(x, t) dx \\ F_4(t) &= -M_0 + NM_g \end{aligned} \right\} \tag{5.10}$$

where M_r is the rotor torque and M_g is the generator torque. Next the Lagrangian is formed as

$$\mathcal{L}(\mathbf{q}, \dot{\mathbf{q}}) = \mathcal{T}(\dot{\mathbf{q}}) - \mathcal{U}(\mathbf{q}) \tag{5.11}$$

where

$$\mathbf{q}(t) = \begin{bmatrix} q_1(t) \\ q_2(t) \\ q_3(t) \\ q_4(t) \end{bmatrix} \tag{5.12}$$

Lagrange's equations of motion then provides [Juang and Phan, 2001]

$$\frac{d}{dt} \left(\frac{\partial \mathcal{L}}{\partial \dot{q}_i} \right) - \frac{\partial \mathcal{L}}{\partial q_i} = F_{d,i} \quad , \quad i = 1, 2, 3, 4 \quad (5.13)$$

where $F_{d,i}$ represents the generalized non-conservative loads. These stem from structural and aerodynamic damping in the tower and blades and frictional damping in the bearings and gear in the transmission system, which are all modelled as linear viscous. Insertion of (5.11) in (5.13) provides the following matrix equations of motion

$$\mathbf{M}\ddot{\mathbf{q}} + \mathbf{C}\dot{\mathbf{q}} + \mathbf{K}\mathbf{q} = \mathbf{F}(t) \quad (5.14)$$

$$\mathbf{M} = \begin{bmatrix} m_0 & m_1 & m_1 & 0 \\ m_1 & m & 0 & 0 \\ m_1 & 0 & m & 0 \\ 0 & 0 & 0 & J \end{bmatrix} \quad (5.15)$$

$$\mathbf{K} = \begin{bmatrix} k_0 & 0 & 0 & 0 \\ 0 & k & 0 & 0 \\ 0 & 0 & k & 0 \\ 0 & 0 & 0 & 0 \end{bmatrix} \quad (5.16)$$

$$\mathbf{C} = \begin{bmatrix} 2\zeta_0\omega_0 m_0 & 0 & 0 & 0 \\ 0 & 2\zeta\omega m & 0 & 0 \\ 0 & 0 & 2\zeta\omega m & 0 \\ 0 & 0 & 0 & \eta M_r \end{bmatrix} \quad (5.17)$$

$$\mathbf{F} = \begin{bmatrix} F_1(t) \\ F_2(t) \\ F_3(t) \\ F_4(t) \end{bmatrix} \quad (5.18)$$

In the above equations of motion ω and ζ denote the eigenfrequency and damping ratio of the blades, when these are fixed to the hub. Correspondingly ω_0 and ζ_0 denote the eigenfrequency and damping ratio of the lowest mode of the wind turbine. η in (5.17) denotes the loss factor of the transmission system, which typically is a few percent. Most of the loss is taken place in the gear.

5.2 Calibration of model

In the following, the parameters in the equations of motion are calibrated to provide motions corresponding to the motions of the 5MW NREL wind turbine when applying a given load. The masses, mode shapes and eigenfrequencies of the wind turbine are given in appendix C. The modal masses m_0 , m and m_1 are calculated by (5.6) using the eigenmodes of the tower and blades as shape function.

$$m_0 = 386000 \text{ kg}$$

$$m = 870 \text{ kg}$$

$$m_1 = 3500 \text{ kg}$$

The lower angular eigenfrequency ω_0 and the fixed bay eigenfrequency of the blades ω are given by

$$\begin{aligned}\omega_0 &= 2.1 \text{ rad/s} \\ \omega &= 4.6 \text{ rad/s}\end{aligned}$$

The modal stiffnesses of the blades are then estimated by

$$\omega^2 = \frac{k}{m} \quad (5.19)$$

thus

$$\begin{aligned}k_0 &= 1.7 \cdot 10^6 \text{ N/m} \\ k &= 18.5 \cdot 10^3 \text{ N/m}\end{aligned}$$

The structural damping ratio of the blades and tower are set to 0.01, but due to aeroelastic damping the damping ratio of the blades are set to 0.2. The energy dissipation in the drive train is neglected, thus the following damping ratios and coefficients are used

$$\begin{aligned}\zeta_0 &= 0.01 \\ \zeta &= 0.2\end{aligned}$$

5.3 Loads on the system

The loads on the turbine are generated from the wind and the rotating blades. The load distributions on the tower $p_1(x, t)$ is neglected whereas the loads on the blades $p_2(x, t)$ and $p_3(x, t)$ are assumed to be linearly distributed with zero load at $x = 0$ and maximum load at $x = L$ as shown in figure 5.3. Further, stationary operational conditions are assumed, where the rotor is rotating with the constant rotational speed $\Omega_r = \dot{q}_4$ so $\eta M_r \dot{q}_4 = M_r - N M_g$. The load on the blade is given as

$$p_i(x, t) = p_{tip}(t) \frac{x}{L} \quad , \quad x \in [0, L] \quad , \quad i = 2, 3 \quad (5.20)$$

The load normal to the rotor plane on the tip airfoil is given by

$$p_{tip}(t) = \frac{1}{2} \rho c C_N V_r^2(t) \quad (5.21)$$

where ρ is the air mass density, c is the mean chord length of the outer 1/3 of the blade, set to 2.5 m. C_L and C_D are the lift and drag coefficient and C_N is the normal coefficient, which depends on the angle of attack relative to the zero-line of the airfoil. It is assumed that the pretwist of the blade is so that $C_N = 0.9$ all along the blade. V_r is the resulting wind speed acting on the i th blade. In reality a

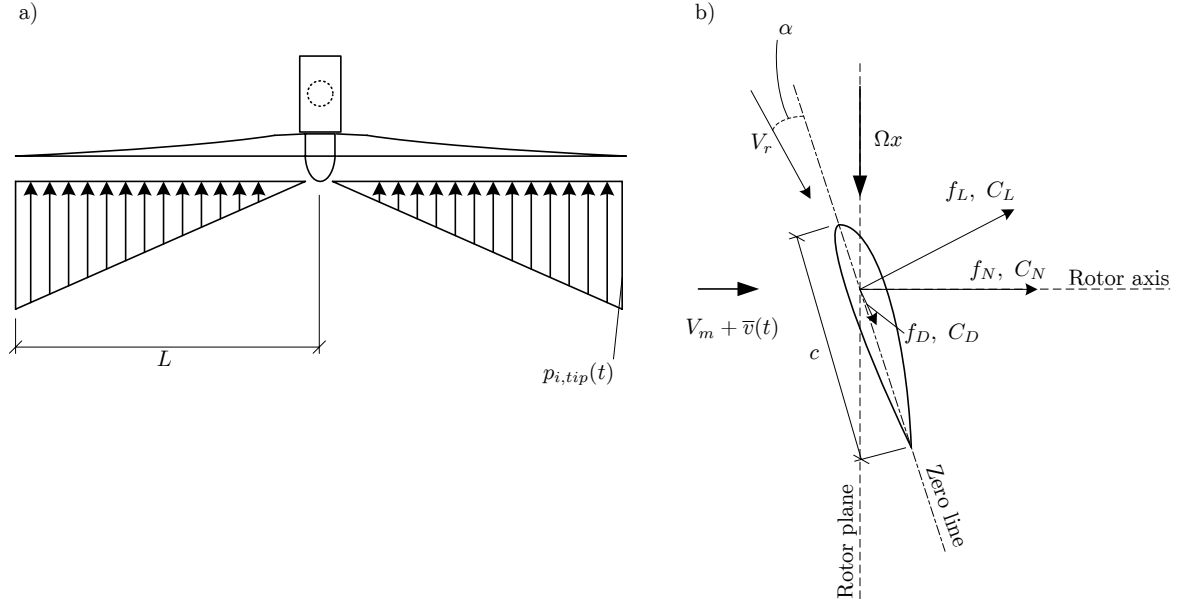


Figure 5.3: a) Load distribution on the blades. b) Forces on the airfoil.

reduction of the wind speed is introduced due to the induction effect. This effect is neglected whereby the resulting wind speed at the tip is given by

$$V_r^2(t) = (V_m + \bar{v}(t))^2 + (\Omega L)^2 \quad (5.22)$$

where V_m is the 10 min mean wind speed, $\bar{v}(t)$ is the turbulence component in the mean wind direction. The turbulence in the two other directions are neglected. The rotational speed is set to a constant value of 12 rpm or $\frac{2}{5}\pi$ rad/s. For simplicity a linearisation of the resulting wind speed is introduced as

$$V_r^2(t) = V_m^2 + 2V_m\bar{v}(t) + (\Omega L)^2 \quad (5.23)$$

The load vector \mathbf{F} is determined by insertion of $p_1(x, t) = 0$, $p_2(x, t)$ and $p_3(x, t)$ in (5.10). The result may be written on the matrix form

$$\mathbf{F}(t) = \mathbf{b}(\mathbf{f}_s + a_T\bar{\mathbf{v}}(t)) \quad (5.24)$$

where

$$\mathbf{b} = \begin{bmatrix} 0 & 1 & 1 & 0 \\ 0 & 1 & 0 & 0 \\ 0 & 0 & 1 & 0 \\ 0 & 0 & 0 & 0 \end{bmatrix}, \quad \mathbf{f}_s = \begin{bmatrix} 0 \\ f_s \\ f_s \\ 0 \end{bmatrix}, \quad \bar{\mathbf{v}}(t) = \begin{bmatrix} 0 \\ \bar{v}_1 \\ \bar{v}_2 \\ 0 \end{bmatrix} \quad (5.25)$$

The components of \mathbf{f}_s , f_s and the constant a_T are given by the following expressions

$$f_s = \frac{1}{2}\rho C_N \int_0^L c(x)\Phi(x) (V_m^2 + (\Omega L)^2) \frac{x}{L} dx \quad (5.26)$$

$$a_T = \frac{1}{2}\rho C_N \int_0^L c(x)\Phi(x) 2V_m \frac{x}{L} dx \quad (5.27)$$

where $c(x) = c$ is the chord length of the airfoil and $\rho = 1.25 \text{ kg/m}^3$ is the mass density of air.

All simulations are performed using $V_m = 15 \text{ m/s}$ corresponding to $f_s = 108 \cdot 10^3 \text{ N}$ and $a_T = 525 \text{ kg/s}$. Note that a_T is multiplied by 20 to obtain realistic contribution to the response from the dynamic load, whereby $a_T = 10500 \text{ kg/s}$ is used.

5.3.1 Turbulence

The turbulence on the systems is generated by means of the state space representation of the ARMA model (SSM) described in appendix B.3. Since the SSM is derived for fixed spatial points it is not possible to generate the turbulence directly at the rotating tip of the blade, whereby a spacial interpolation between fixed spatial points is needed. Note that only interpolation in the rotor plane is performed. The turbulence is generated at a number of points m on the periphery of the rotor plane as shown in figure 5.4.

To avoid variance reduction of the interpolated turbulence a zero order interpolation method is used. The turbulence component $\bar{v}_i(t)$ at the tip of the i th blade is formally defined

$$\bar{v}_i(t) = \mathbf{N}_i(q_4(t))\mathbf{v}(t) \quad , \quad i = 1, 2 \quad (5.28)$$

where \mathbf{v} is a $m \times 1$ nodal turbulence vector and $\mathbf{N}_i(q_4, t)$ is a $1 \times m$ shape function matrix. The azimuthal location of the i th blade is determined by

$$\theta_i(t) = \Omega t + \theta_{0,i} \quad (5.29)$$

where $\theta_{0,i}$ is the location of the i th blade at $t = 0$. Since $\theta_i(t)$ is repeated with 2π a relative angle of the i th blade is introduced as

$$\theta_{r,i}(t) = \theta_i(t) - 2\pi n \quad , \quad n = \left\lfloor \frac{\Omega L}{2\pi} \right\rfloor \quad (5.30)$$

The j th component of the shape function matrix is then defined by a zero-order interpolation as

$$N_{i,j}(q_4, t) = \begin{cases} 1 & , \quad \theta_{r,i} \in [\theta_j - \frac{\Delta\theta}{2} \quad \theta_j + \frac{\Delta\theta}{2} [\\ 0 & , \quad \text{else} \end{cases} \quad (5.31)$$

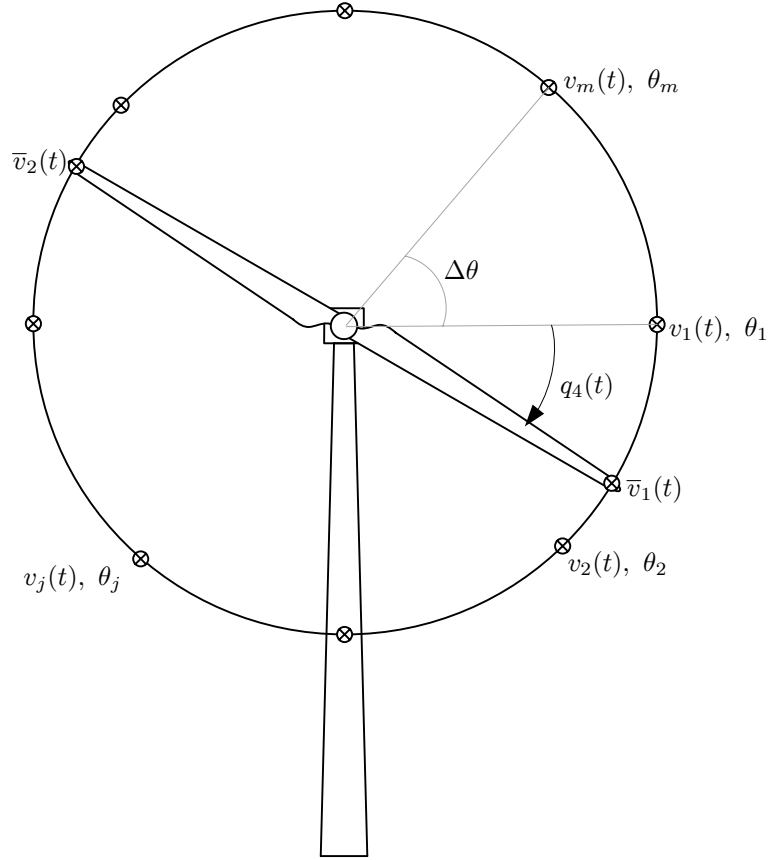


Figure 5.4: Turbulence grid on the rotor plane.

where θ_j is the angle associated with the j th grid point, cf. figure 5.4.

The turbulence vector $\bar{\mathbf{v}}(t)$ may be written on the matrix form

$$\bar{\mathbf{v}}(t) = \mathbf{N}(q_4(t)) \mathbf{v}(t) = \begin{bmatrix} 0 & 0 & \dots & 0 \\ N_{1,1} & N_{1,2} & \dots & N_{1,m} \\ N_{2,1} & N_{2,2} & \dots & N_{2,m} \\ 0 & 0 & \dots & 0 \end{bmatrix} \mathbf{v}(t) \quad (5.32)$$

5.4 Results

In the following a sample of the turbulence and the corresponding response is given. A sample response of the three dofs are given in figure 5.5 where as a sample of the turbulence v_1 is given in figure 5.6.

The turbulence is simulated from an empiric spectral representation. The simulated turbulence is verified by comparing the analytical one sided auto-spectral density function S_{v_i} with the one sided auto-spectral density function for the simulated turbulence \hat{S}_{v_i} . Also, the auto-spectral density function for the simulated interpolated turbulence at the blade tip $\hat{S}_{\bar{v}_i}$ is compared to the analytical auto-spectral density function. The auto-spectral density functions of the simulated turbulence is obtained by a Fourier analysis using $T = 50000T_b$, where T_b is the eigenperiod of the blade. The comparison is shown in figure 5.7. The interpolated turbulence shows peaks at $\omega = 2/5\pi$, $\omega = 4/5\pi\dots$

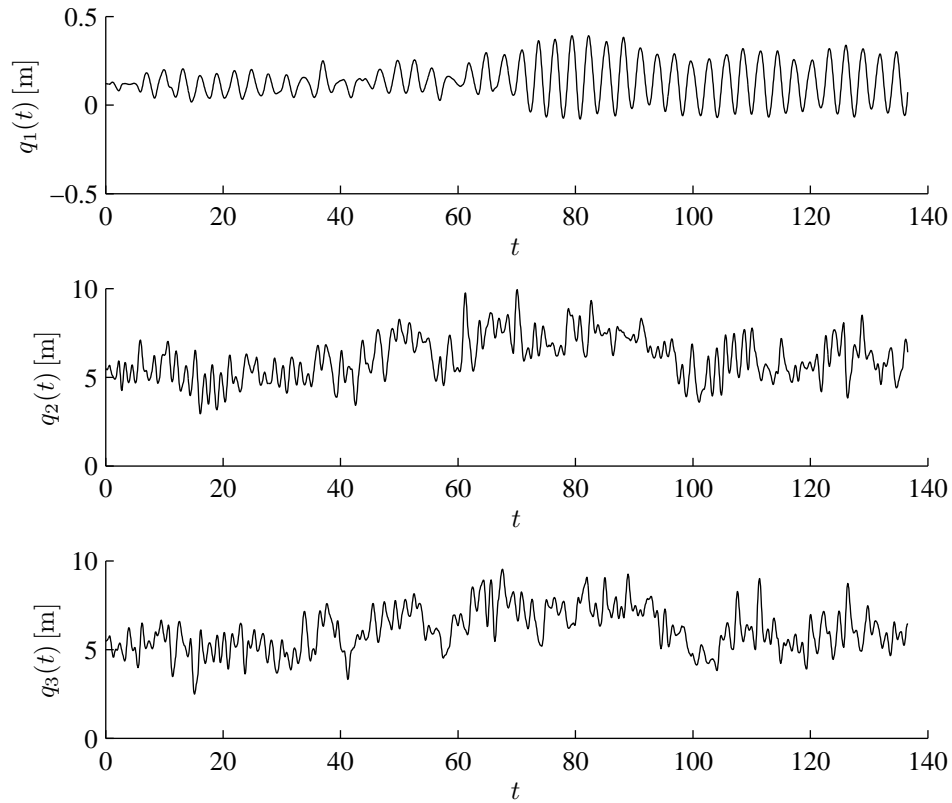


Figure 5.5: Sample response of tower and blades for three dof wind turbine.

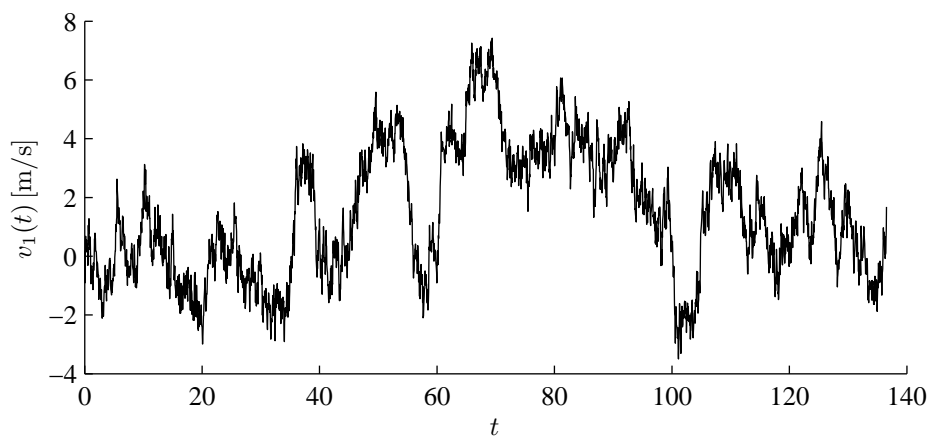


Figure 5.6: Sample of turbulence in fixed spatial point.

corresponding to integer multiple of the rotational angular frequency of the blades $\Omega = 2/5\pi$. The peaks originates in the correlation length of the turbulence. Note that the area under $\hat{S}_{\bar{v}_1}$ and \hat{S}_{v_1} must be the same due to energy conservation. To be able to generate the spectral change, 10 turbulence grid points has been used. In the following only 4 grid points is used.

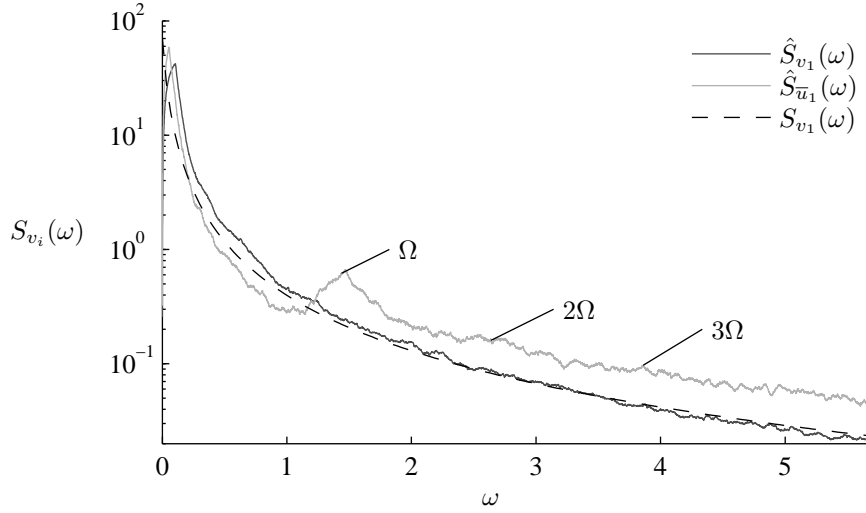


Figure 5.7: Comparison of analytical one sided auto-spectral density function and the one sided auto-spectral density function obtained by Fourier analysis of sample simulation.

In all simulations the mean value and standard deviations of the stationary responses q_1 , q_2 and q_3 are used in determining the barrier levels. The mean values and standard deviations are determined by simulation of 10 sample series of $T = 1000T_b$. The first $100T_b$ are discarded to obtain stationary mean values and standard deviations. The values obtained are shown in table 5.1.

Component	$\hat{\mu}_{q_i}$	$\hat{\sigma}_{q_i}$
Tower, q_1	0.13 m	0.076 m
Blade 1, q_2	5.89 m	1.51 m
Blade 2, q_3	5.89 m	1.51 m

Table 5.1: Estimated mean values and standard deviations of the stationary responses.

Chapter 6

Crude Monte Carlo simulations

In this chapter simulations are performed for crude Monte Carlo (CMC) simulation techniques to gather information on problems, limitations and computational time required for determining failure probabilities for rather low barrier levels. Two different CMC simulation methods denoted "simple" and "ergodic" are used in the following.

In the simple CMC simulation method the failure probability is determined by simulating N time series of length T , e.g. $T = 600$ s for wind turbines, and determine the number of time series that crosses out into the failure domain \mathcal{F} .

The probability of failure $P_f([0, T])$ in the interval $[0, T]$ is in the simple CMC simulation method then determined by

$$P_f([0, t]) = \frac{1}{N} \sum_{i=1}^N I_i \quad (6.1)$$

where I_i is the indicator function for the i th realisation. The indicator function is 1 if the realisation has crossed out in the interval $[0, T]$ and 0 if the realisation has not crossed out in the interval $[0, T]$. The method is applicable to both stationary and non-stationary processes with or without time-constant safe domains.

The ergodic CMC simulation method is based on a single time series. The method is only applicable to stationary processes with a time-constant safe domain. By using ergodic sampling on the time series, estimates of the distribution function of time lengths spent in the safe domain $F_L(l)$, their mean value $E[L]$ and the probability of being in the safe domain initially at time $t = 0$, $P(\mathbf{Y}(0) \in \mathcal{S})$ can be estimated as [Nielsen, 2007b]

$$F_L(l) \simeq \frac{N_{\leq l}}{N} \quad (6.2)$$

$$E[L] \simeq \frac{1}{N} \sum_{j=1}^N L_j \quad (6.3)$$

$$P(\mathbf{Y}(0) \in \mathcal{S}) \simeq \frac{1}{T} \sum_{j=1}^N L_j \quad (6.4)$$

where $N_{\leq l}$ is the number of interval lengths spent in the safe domain \mathcal{S} smaller than l , N is the total number of outcrossings from the safe domain, L is the random variable representing interval lengths spent in the safe domain, T is the total length of the time series and $\mathbf{Y}(0)$ is the displacement vector at the beginning of the time series.

The first-passage time probability density function can then be calculated by [Nielsen, 2007b]

$$f_T(t) = \frac{1}{\mathbb{E}[L]}(1 - F_L(t)) \quad (6.5)$$

As the first passage time probability density function $f_T(t)$ is estimated from a simulated distribution function $F_L(t)$ a smooth curve is obtained.

By insertion of (6.2) and (6.3) into (6.5) and subsequently integrating (6.5) the first passage time distribution function $F_T(t)$ is determined. Then, the probability of failure in a specified time interval $P_f([0, t])$ can be calculated as, [Nielsen, 2007b]

$$P_f([0, t]) = 1 - P(\mathbf{Y}(0) \in \mathcal{S}) + F_T(t)P(\mathbf{Y}(0) \in \mathcal{S}) \quad (6.6)$$

The performance of the two CMC simulation methods for determining the failure probability is evaluated on the 2-dof shear frame described in chapter 4. The applied load is a horizontal white noise earthquake excitation with autospectral density $S_0 = 1$ modelled by a broken line process. Throughout this thesis barrier levels are specified by the non-dimensional parameter α corresponding to the physical barrier level given as

$$y_{c,i} = \mu_{Y_i} + \alpha\sigma_{Y_i} \quad (6.7)$$

where σ_{Y_i} is the stationary standard deviation and μ_{Y_i} is the mean value of the considered response process. In the present case the barrier level is chosen to $\alpha = 3$ and since $\mu_{Y_i} = 0$ this corresponds to $y_{c,i} = 3\sigma_{Y_i}$ for the i th storey.

A transient phase of $50T_1$ has been discarded from the simulation to make sure that the initial conditions do not influence the results. Figure 6.1 shows a comparison between the first passage time probability distribution in the interval $[0, 50T_1]$ obtained by a simple CMC simulation and the ergodic CMC simulation method with a time series length of $500000T_1$ corresponding to the same total length as for the simple CMC simulation method. In the simple CMC simulation this corresponds to having 10000 sample curves of each $50T_1$. The first passage time probability distribution function is very smooth for the ergodic CMC simulation, and is also relatively smooth for the simple CMC simulation method because of the high number of sample curves and the low barrier levels used.

A comparison of the convergence of the probability of failure in the two methods is shown in figure 6.2. For the simple CMC simulation method the probability of failure is calculated whenever a simulation is finished, i.e. for every 50 periods. For the ergodic CMC simulation method the probability of failure is calculated at each outcrossing. It is seen that the failure probability converges at approximately same speed for both methods even when using a small barrier level providing a rather large probability of failure. The failure probability equal to the estimated first passage time probability distribution function at $T = 50T_1$ of the two different simulation methods converge towards values between 0.22 and 0.24. None of the methods can be concluded to be superior to the other as they converge at the same speed.

To test whether the same results are obtained for higher barrier levels, i.e. smaller probability of failures, the same simulation is performed for the barrier level $\alpha = 4$. The comparison of the first passage time probability distribution function for the barrier level $\alpha = 4$ is shown in figure 6.3 and shows a very smooth curve for the ergodic CMC simulation method and a more irregular curve for the simple CMC simulation method which was also seen for $\alpha = 3$.

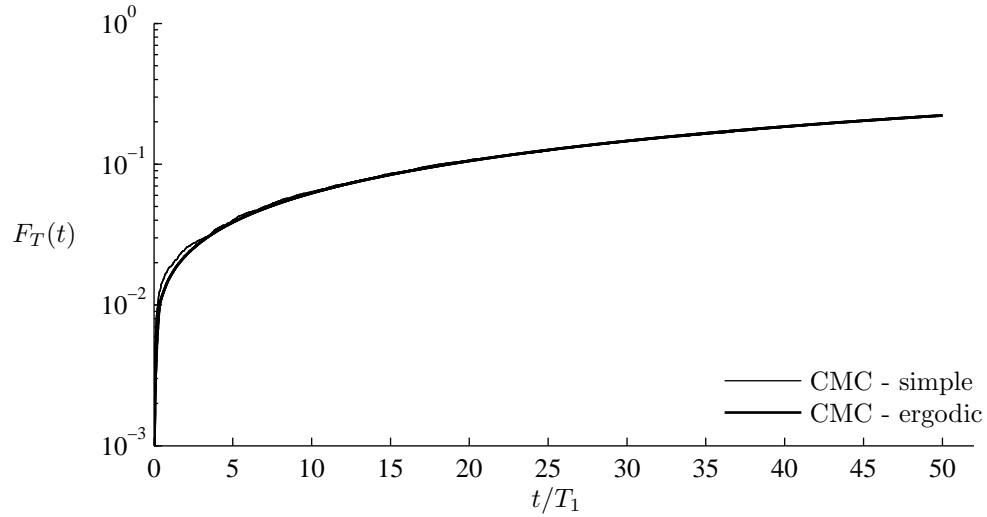


Figure 6.1: First passage time probability distribution function for CMC methods, $\alpha = 3$.

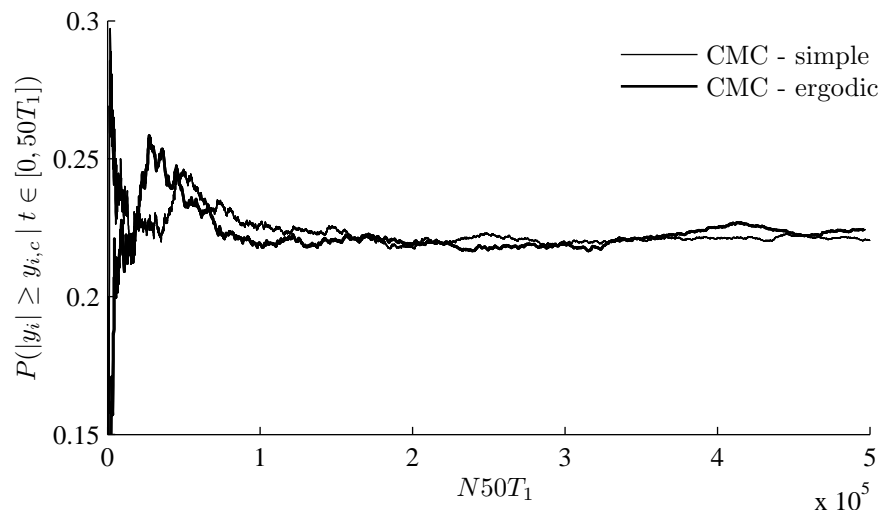


Figure 6.2: Convergence of probability of failure for CMC simulation methods as a function of simulation time, $\alpha = 3$.

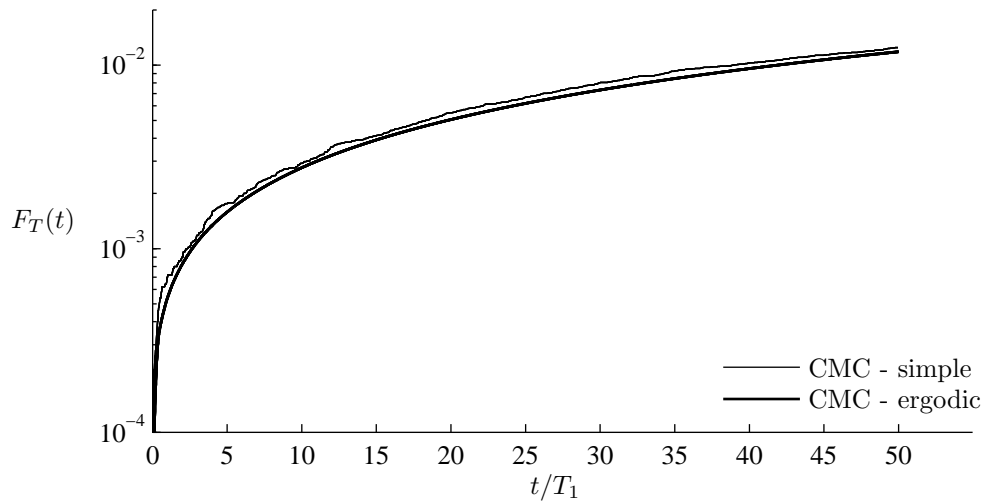


Figure 6.3: First passage time probability distribution function for CMC methods, $\alpha = 4$.

Convergence for the probability of failure within a time interval of $50T_1$ in the two methods and a barrier level $\alpha = 4$ is shown in figure 6.4. Again, none of the methods can be concluded to be superior to the other. The computational time of the methods shows that the ergodic CMC simulation method is around 20% faster than the simple CMC simulation method for the tested cases which means that it is preferable. The differences in computational time is mainly due to the transient phase which is simulated N times for the simple Monte Carlo method, but only once for the ergodic version.

Because of the slow convergence and demanding computational time required even for rather low barrier levels other methods are needed, which will be studied further in the following chapters.

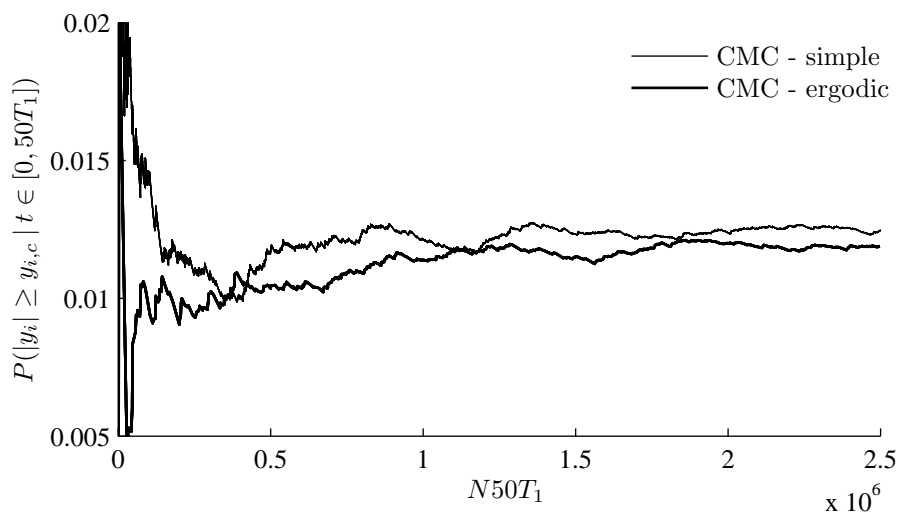


Figure 6.4: Convergence of probability of failure for CMC simulation methods as a function of simulation time, $\alpha = 4$.

Chapter 7

Importance Sampling

In this chapter the variance reduction Monte Carlo simulation method known as Importance Sampling (IS) is investigated for possible use for determining extreme responses of wind turbines. The basic idea of this method is to generate samples close to the failure surface and to reduce the statistical weight so the consistency is preserved. The result of this approach is more outcrossings with fewer simulations, and thereby a faster convergence. First, a short description of the IS method is given.

Given a failure function $g(\mathbf{w})$ and a failure surface defined by $g(\mathbf{w}) = 0$ cf. figure 7.1 then the related failure domain is defined as

$$\mathcal{F} = \{\mathbf{w} \mid g(\mathbf{w}) \leq 0\} \quad (7.1)$$

where \mathbf{w} denotes samples of an M -dimensional stochastic vector \mathbf{W} with the joint probability density function $f_{\mathbf{W}}(\mathbf{w})$.

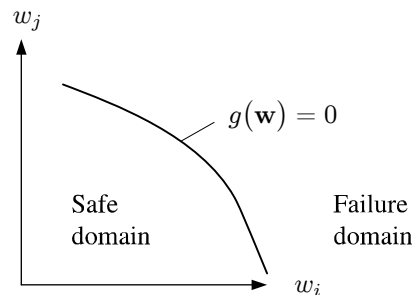


Figure 7.1: Failure and safe domain separated by the failure surface.

Then, the probability of failure is given as

$$P_f = \int_{\mathcal{F}} f_{\mathbf{W}}(\mathbf{w}) d\mathbf{w} = \int_{\mathbb{R}^M} I(\mathbf{w}) f_{\mathbf{W}}(\mathbf{w}) d\mathbf{w} = \mathbb{E}[I(\mathbf{W})] \quad (7.2)$$

where $I(\mathbf{w})$ is an indicator function defined as

$$I(\mathbf{w}) = \begin{cases} 1 & , \quad \mathbf{w} \in \mathcal{F} \\ 0 & , \quad \mathbf{w} \in \mathcal{S} \end{cases} \quad (7.3)$$

The probability measure $P_{\mathbf{W}}(\mathcal{B})$ relates a probability to any sub-domain \mathcal{B} of \mathbb{R}^M . The probability of samples in a differential volume $d\mathbf{w}$ around a sample point \mathbf{w} has the measure

$$dP_{\mathbf{W}}(\mathbf{w}) = f_{\mathbf{W}}(\mathbf{w})d\mathbf{w} \quad (7.4)$$

Next, another M -dimensional stochastic vector $\tilde{\mathbf{W}}$ with the probability measure $P_{\tilde{\mathbf{W}}}(\mathcal{B})$ and the joint probability density function $f_{\tilde{\mathbf{W}}}(\tilde{\mathbf{w}})$ is introduced. Then, (7.2) may be written as

$$P_f = \int_{\mathbb{R}^M} I(\mathbf{w}) \frac{f_{\mathbf{W}}(\mathbf{w})d\mathbf{w}}{f_{\tilde{\mathbf{W}}}(\mathbf{w})d\mathbf{w}} f_{\tilde{\mathbf{W}}}(\mathbf{w}) d\mathbf{w} = \int_{\mathbb{R}^M} I(\mathbf{w}) \frac{dP_{\mathbf{W}}(\mathbf{w})}{dP_{\tilde{\mathbf{W}}}(\mathbf{w})} f_{\tilde{\mathbf{W}}}(\mathbf{w}) d\mathbf{w} = E \left[I(\tilde{\mathbf{W}}) \frac{dP_{\mathbf{W}}(\tilde{\mathbf{W}})}{dP_{\tilde{\mathbf{W}}}(\tilde{\mathbf{W}})} \right] \quad (7.5)$$

The fraction $\frac{dP_{\mathbf{W}}(\mathbf{w})}{dP_{\tilde{\mathbf{W}}}(\mathbf{w})}$ is known as the *Radon-Nikodym derivative* of the measure $P_{\mathbf{W}}(\mathbf{w})$ with respect to the measure $P_{\tilde{\mathbf{W}}}(\mathbf{w})$ at the sample point \mathbf{w} . The expectations in (7.2) and (7.5) are evaluated with respect to the joint probability density functions $f_{\mathbf{W}}(\mathbf{w})$ and $f_{\tilde{\mathbf{W}}}(\mathbf{w})$, respectively.

The expectation in (7.2) forms the basis for CMC simulation of the failure probability. Given N samples $\mathbf{w}_1, \mathbf{w}_2, \dots, \mathbf{w}_N$ of the random vector \mathbf{W} , an unbiased estimate \hat{P}_f of the failure probability is given as

$$\hat{P}_f = \frac{1}{N} \sum_{j=1}^N I(\mathbf{w}_j) \quad (7.6)$$

The expectation in (7.5) forms the basis for IS of the failure probability. Given N samples $\tilde{\mathbf{w}}_1, \tilde{\mathbf{w}}_2, \dots, \tilde{\mathbf{w}}_N$ of the random vector $\tilde{\mathbf{W}}$, an unbiased estimate of \hat{P}_f of the failure probability is given as

$$\hat{P}_f = \frac{1}{N} \sum_{j=1}^N I(\tilde{\mathbf{w}}_j) \frac{dP_{\mathbf{W}}(\tilde{\mathbf{w}}_j)}{dP_{\tilde{\mathbf{W}}}(\tilde{\mathbf{w}}_j)} \quad (7.7)$$

7.0.1 Sample density function

Ideally, the sampling measure $P_{\tilde{\mathbf{W}}}(\mathbf{w})$ should have its probability mass concentrated near the failure surface as illustrated for the marginal distribution of the i th component of \mathbf{w} in figure 7.2. $f_{\mathbf{W}}(\mathbf{w})$ is very small in the area around $g(\mathbf{w}) = 0$, whereas $f_{\tilde{\mathbf{W}}}(\mathbf{w})$ is of relatively large magnitude in this area.

In order to determine the sample measure, the system of interest needs to be modelled. The IS method used in this project takes its basis in the *Itô stochastic differential equation*

$$d\mathbf{Z}(t) = \boldsymbol{\mu}(t, \mathbf{Z})dt + \boldsymbol{\sigma}(t, \mathbf{Z})d\mathbf{W}(t) \quad (7.8)$$

where $\mathbf{Z}(t)$ is the n -dimensional system state vector, $\boldsymbol{\mu}(t, \mathbf{Z})$ is a n -dimensional drift vector, $\boldsymbol{\sigma}(t, \mathbf{Z})$ is a $n \times m$ -dimensional diffusion matrix and $d\mathbf{W}(t)$ is a m -dimensional incremental Wiener vector process with mutual independent component processes with zero mean and the variance dt . (7.8) can be solved directly by means of any predictor based numerical integration scheme as long as the diffusion

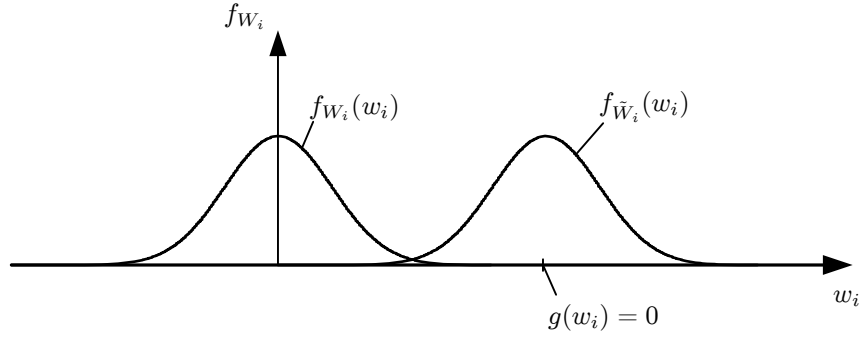


Figure 7.2: Marginal probability density function for $\tilde{\mathbf{W}}$ and \mathbf{W} .

term is state vector independent. In cases where the diffusion matrix is state dependent numerical solution may still be obtained by the Euler scheme with forward increments or the impulse response method (4.19) for drift vectors which depends linearly on the drift vector. If higher order integration schemes relies on future state vectors in the time-interval a so-called *Wong-Zakai correction* must be applied cf. appendix J.1. For simplicity and generality a forward Euler scheme is used in what follows

$$\left. \begin{aligned} \mathbf{Z}_{i+1} &= \mathbf{Z}_i + \boldsymbol{\mu}(t_i, \mathbf{Z}_i)\Delta t + \boldsymbol{\sigma}(t_i, \mathbf{Z}_i)\Delta \mathbf{W}_i \\ t_i &= \Delta t \cdot i \quad , \quad \Delta t = \frac{T}{M} \quad , \quad i = 0, 1, \dots, M-1 \end{aligned} \right\} \quad (7.9)$$

where $\mathbf{Z}_i = \mathbf{Z}(t_i)$. In order to establish an effective IS, the samples are generated near the failure surface by utilising a Girsanov transformation of the incremental input process $d\mathbf{W}(t)$. The Girsanov transformation of the Wiener process increments is determined by, cf. appendix J.1.1

$$\Delta \tilde{\mathbf{W}}(t) = \mathbf{u}(t)\Delta t + \Delta \mathbf{W}(t) \quad (7.10)$$

where $\mathbf{u}(t)$ is a so-called control function vector.

Selection of the sample control function

The control function determines the efficiency of the importance measure and is proposed determined by the First Order Reliability Method (FORM) by [Tanaka, 1998]. $\mathbf{u}(t)$ is a deterministic *sample control function* which can be interpreted as the realisation of $\Delta \mathbf{W}$ which has the highest probability of occurring and which also gives failure at the design time t^* . By utilising an optimal sample control function, approximately half of the samples generated under the IS density function is in the failure domain.

Let the failure function of the i th component of the system be defined as

$$g(Y_i(t)) = y_{c,i} - Y_i(t) \quad (7.11)$$

where $Y_i(t)$ is the i th component of $\mathbf{Y}(t)$ which is determined by (7.9) and $y_{c,i}$ is a deterministic barrier function of the i th component defined by (6.7).

A minimal distance β is introduced as the shortest distance from origo to the failure surface in the standard normal distributed space, spanned by the Gaussian vector Ξ cf. figure 7.3. The components of Ξ are mutual independent and identical distributed with zero mean and unit variance. The location of the shortest distance to the failure surface in the Ξ -space is denoted the *design point*. The minimal distance β corresponds to the *reliability index* used in time invariant reliability theory.

In what follows (7.8), due to simplicity is reduced to a single dimensional stochastic differential equation. Note that $\Delta\mathbf{W}$ now is a vector containing the increments $\Delta W_1, \Delta W_2, \dots, \Delta W_M$. The relation between the j th component of $\Delta\mathbf{W}$ and Ξ is given by

$$\Delta W_j = \sqrt{\Delta t} \Xi_j \quad (7.12)$$

The minimal distance β from the failure surface $g_i(\Xi_1, \dots, \Xi_M) = 0$ to the design time $t^* = t_M$ is given by

$$\beta^{(t_M)} = \sqrt{\sum_{j=1}^M (\xi_j^*)^2} \quad (7.13)$$

where ξ_j^* are the coordinates of the design point in the normal distributed space. Next, the control function $u^{(t_M)}(t)$ is determined so the expectation $E_{P_{\tilde{\mathbf{W}}}}[\Delta\tilde{\mathbf{W}}]$ of $\Delta\tilde{\mathbf{W}}$ with respect to the measure $P_{\tilde{\mathbf{W}}}$ becomes equal to zero, i.e. half of the samples of $\Delta\tilde{\mathbf{W}}$ will in average bring the system into the failure domain. From (7.10) follows

$$\begin{aligned} E_{P_{\tilde{\mathbf{W}}}}[\Delta\tilde{W}_j] &= E_{P_{\Delta\tilde{\mathbf{W}}}}[\Delta W_j] + u_j \Delta t = 0 \Rightarrow \\ u_j &= -\frac{E_{P_{\tilde{\mathbf{W}}}}[\Delta W_j]}{\Delta t} = -\frac{E_{P_{\tilde{\mathbf{W}}}}[\Xi_j]}{\sqrt{\Delta t}} \end{aligned} \quad (7.14)$$

By choosing a realisation of the incremental load process ΔW_j with the highest failure probability of \mathbf{Z} at the time t_M , an optimal sampling control function is achieved. This is in fact the deterministic design point ξ_j^* whereby (7.14) becomes

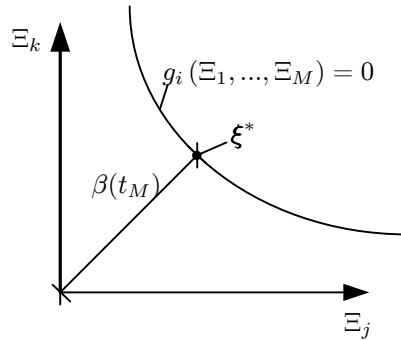


Figure 7.3: Design point at the time t_M .

$$u_j = \frac{-\xi_j^*}{\sqrt{\Delta t}} \quad (7.15)$$

The joint probability density function $f_{\Delta \mathbf{W}}(\Delta \mathbf{w})$ of $\Delta \mathbf{W}$ at $\Delta \mathbf{w} = \Delta \tilde{\mathbf{w}}$ is given by

$$f_{\Delta \mathbf{W}}(\Delta \tilde{\mathbf{w}}) = \frac{1}{(2\pi\Delta t)^{M/2}} \exp\left(-\frac{1}{2\Delta t} \sum_{j=1}^M (\Delta \tilde{w}_j)^2\right) \quad (7.16)$$

Since $\Delta \tilde{W}_j \sim N(u_j \Delta t, \sqrt{\Delta t})$ the joint probability density function $f_{\Delta \tilde{\mathbf{W}}}(\Delta \tilde{\mathbf{w}})$ of $\Delta \tilde{\mathbf{W}}$ at $\Delta \tilde{\mathbf{w}}$ is given by

$$f_{\Delta \tilde{\mathbf{W}}}(\Delta \tilde{\mathbf{w}}) = \frac{1}{(2\pi\Delta t)^{M/2}} \exp\left(-\frac{1}{2\Delta t} \sum_{j=1}^M (\Delta \tilde{w}_j - u_j \Delta t)^2\right) \quad (7.17)$$

whereby the *Radon-Nikodym derivative* at the sample point $\Delta \tilde{\mathbf{W}}$ is determined by

$$\frac{f_{\Delta \mathbf{W}}(\Delta \tilde{\mathbf{w}})}{f_{\Delta \tilde{\mathbf{W}}}(\Delta \tilde{\mathbf{w}})} = \exp\left(-\frac{1}{2} \sum_{j=1}^M u_j^2 \Delta t - \sum_{j=1}^M u_j \Delta w_j\right) \quad (7.18)$$

By using the design point ξ^* it is possible to determine a control function $u(t)$ so the highest likelihood of the event $Y_i(t) > y_{c,i}$, $t \in [t_0, T]$ is achieved. This kind of approximation fits systems which are dominated by a single exit time as for instance crack growth problems. The method has successfully been applied for a scalar diffusion process in appendix J.3, which verifies that the approximation is valid for single exit-time systems. The expectation of the exit time is typically found at $t = T$, whereby the design point is found at $t^* = T$.

However, first passage time probability of oscillatory systems are generally not dominated by a single exit time, since the contribution to the first passage time probability is determined by several exit times [Olsen, 2006]. A method to overcome this problem is proposed by [Macke and Bucher, 2002] and described in the following.

Multi-modal sampling density

As the system is not dominated by a single exit time there is a considerable contribution to the failure probability from other exit times different from $t^* = T$ by which (7.18) is inadequate. A way to overcome this is by introducing a so-called multi-modal sample density function where samples are generated around M design points, where the region around a design point is emphasised in proportion to the probability density function at that design point. An illustration of the method is given in figure 7.4.

The emphasising of the design points is achieved by attaching the following weights to each of the design points

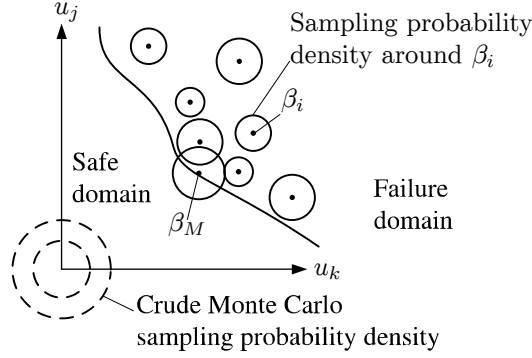


Figure 7.4: CMC and multi-modal IS probability density function

$$\mathcal{W}_i = \frac{\Phi(-\beta^{(i)})}{\sum_{j=1}^M \Phi(-\beta^{(j)})} \quad (7.19)$$

The weights \mathcal{W}_i are proposed by [Macke and Bucher, 2002]. Then, the multi-modal sampling probability density function $h_{\Delta\tilde{\mathbf{w}}}$ is defined as

$$h_{\Delta\tilde{\mathbf{w}}}(\Delta\tilde{\mathbf{w}}^{(l)}) = \sum_{i=1}^M \mathcal{W}_i f_{\Delta\tilde{\mathbf{w}}}^{(i)}(\Delta\tilde{\mathbf{w}}^{(l)}) \Rightarrow \quad (7.20)$$

$$h_{\Delta\tilde{\mathbf{w}}}(\Delta\tilde{\mathbf{w}}^{(l)}) = \frac{1}{\sum_{s=1}^M \Phi(-\beta^{(s)})} \sum_{i=1}^M \left(\frac{\Phi(-\beta^{(i)})}{(2\pi\Delta t)^{2/M}} \exp\left(-\frac{1}{2\Delta t} \sum_{j=1}^M (\Delta\tilde{w}_j^{(l)} - u_j^{(i)}\Delta t)^2\right) \right) \quad (7.21)$$

where $f_{\Delta\tilde{\mathbf{w}}}^{(i)}(\Delta\tilde{\mathbf{w}})$ is the original sample density with the mean shifted to $u_j^{(i)}$ which is the control function at the time $j\Delta t$ for the design point $\beta^{(i)}$. $\Delta\tilde{w}_j^{(l)}$ is a realisation of $\Delta\tilde{W}_j$ determined from (7.10) with the mean $u^{(l)}(t)$ which is the control function corresponding to the design point $\beta^{(l)}$. The Radon-Nikodym derivative used in (7.7) is derived in appendix J.2 and given by

$$\frac{f_{\Delta\mathbf{w}}(\Delta\tilde{\mathbf{w}}^{(l)})}{h_{\Delta\tilde{\mathbf{w}}}(\Delta\tilde{\mathbf{w}}^{(l)})} = \mathcal{R}^{(l)} \quad (7.22)$$

where

$$\frac{1}{\mathcal{R}^{(l)}} = \frac{1}{\sum_{s=1}^M \Phi(-\beta^{(s)})} \sum_{i=1}^M \left(\Phi(-\beta^{(i)}) \exp\left(\sum_{j=1}^M u_j^{(i)} \Delta w_j + \frac{1}{2} \sum_{j=1}^M u_j^{(i)} (2u_j^{(l)} - u_j^{(i)}) \Delta t\right) \right) \quad (7.23)$$

whereby an estimate of the failure probability is determined from

$$\hat{P}_f = \frac{1}{N} \sum_{l=1}^N I(\tilde{\mathbf{w}}^{(l)}) \mathcal{R}^{(l)} \quad (7.24)$$

For systems described by a multi dimension stochastic differential equation e.g. (7.8), is (7.23) given by

$$\frac{1}{\mathcal{R}^{(l)}} = \frac{1}{\sum_{s=1}^M \Phi(-\beta^{(s)})} \sum_{i=1}^M \left(\Phi(-\beta^{(i)}) \exp \left(\sum_{k=1}^m \left(\sum_{j=1}^M u_k^{(i)}(j) \Delta w_k(j) + \frac{1}{2} \sum_{j=1}^M u_k^{(i)}(j) (2u_k^{(l)}(j) - u_k^{(i)}(j)) \Delta t \right) \right) \right) \quad (7.25)$$

where $u_k(j)$ and $w_k(j)$ is the k th entry in the m -dimensional vectors $\mathbf{u}(t)$ and $\Delta \mathbf{w}(t)$, at the j th time increment.

In what follows is P_f in (7.24) equal to the first passage time distribution function F_T , since all realisation belongs to the safe domain at $t = 0$.

The method has successfully been applied to a single dof linear oscillator exposed to a unit white noise, cf. appendix J.4. In section 7.1 the method will be applied to the two dof shear frame exposed to a turbulent stationary wind load process with correlated load components.

7.1 Implementation on two storey shear frame exposed to a turbulent wind field

In the following example the multi-modal IS method will be applied to the two storey shear frame described in chapter 4, where the load process is changed from a single input earthquake to a two dimensional stationary stochastic wind load vector, with correlated components acting on the storey beams. The equations of motion given in a state space formulation becomes

$$\left. \begin{aligned} \frac{d}{dt} \mathbf{Z}(t) &= \mathbf{A} \mathbf{Z}(t) + \mathbf{B} \mathbf{V}(t) \quad , \quad t > t_0 \\ \mathbf{Z}(t_0) &= \mathbf{Z}_0 \end{aligned} \right\} \quad (7.26)$$

where

$$\underset{(4 \times 4)}{\mathbf{A}} = \begin{bmatrix} \mathbf{0} & \mathbf{I} \\ -\omega_0^2 \mathbf{k} & -2\zeta_0 \omega_0 \mathbf{k} \end{bmatrix} \quad , \quad \underset{(4 \times 2)}{\mathbf{B}} = \begin{bmatrix} \mathbf{0} \\ \mathbf{I} \end{bmatrix} \quad , \quad \underset{(4 \times 1)}{\mathbf{Z}} = \begin{bmatrix} \mathbf{Y} \\ \dot{\mathbf{Y}} \end{bmatrix} \quad (7.27)$$

The turbulence load process $\{\mathbf{V}(t), t \in [0, \infty]\}$ acts on the storey beams and is determined by the turbulence vector process described in appendix B.2, which in a discrete form is determined by the causal convolution integral

$$\mathbf{V}(l) = \sqrt{4\pi} \sum_{k=0}^{\infty} \tilde{\mathbf{h}}(k) \Delta \mathbf{W}(l-k) \quad , \quad j = 0, 1, \dots \quad (7.28)$$

(2×1) (2×4) (4×1)

where the abbreviated notation $\mathbf{V}(l) = \mathbf{V}(l \cdot \Delta t)$ and $\Delta \mathbf{W}(l) = \Delta \mathbf{W}(l \cdot \Delta t)$ is used. The stochastic sequence $\{\Delta \mathbf{W}(l), l = 0, \pm 1 \pm 2, \dots\}$ consists of independent and identical distributed stochastic vectors $\Delta \mathbf{W}(l)$. Furthermore, all components of $\Delta \mathbf{W}(l)$ are mutual independent, zero mean Gaussian variables with the variance Δt . $\tilde{\mathbf{h}}(k)$ is an impulse response matrix. (7.28) corresponds to the Moving Average part of an ARMA model, where the upper limit in (7.28) is set to a finite value, which corresponds to the Nyquist frequency. Note that the turbulence vector $\mathbf{V}(t)$ is used directly as the force on the storey beams. This means that the displacements are measured from the static deformation of the frame caused by the static wind load. In this case an analytical solution of the control function can be achieved.

The solution of (7.26) may be written as

$$\mathbf{Z}(t) = e^{\mathbf{A}t} \mathbf{Z}(0) + \int_0^t e^{\mathbf{A}(t-\tau)} \mathbf{B} \mathbf{V}(\tau) d\tau \quad (7.29)$$

where the matrix exponential may be evaluated as indicated by (4.22). Upon discretisation of (7.29) the following numerical solution is achieved

$$\mathbf{Z}(j) = \mathbf{h}^0(j) \mathbf{Z}(0) + \sum_{l=0}^j \mathbf{h}^s(j-l) \mathbf{V}(l) \quad , \quad j = 1, 2, \dots \quad (7.30)$$

where

$$\mathbf{h}^0(j) = e^{\mathbf{A}j\Delta t} \quad (7.31)$$

$$\mathbf{h}^s(j) = e^{\mathbf{A}j\Delta t} \mathbf{B} \Delta t \quad (7.32)$$

By inserting (7.28) into (7.30) the solution to (7.26) is given on the form

$$\mathbf{Z}(j) = \mathbf{h}^0(j) \mathbf{Z}(0) + \sqrt{4\pi} \sum_{l=0}^j \mathbf{h}^s(j-l) \sum_{k=0}^q \tilde{\mathbf{h}}(k) \Delta \mathbf{W}(l-k) \quad , \quad j = 0, 1, \dots \quad (7.33)$$

In order to determine the design point (7.33) is rewritten on matrix form

$$\mathbf{Z}(j) = \mathbf{h}^0(j) \mathbf{Z}(0) + \sqrt{4\pi} \mathcal{H} \mathcal{G} \Delta \mathcal{V} \quad (7.34)$$

where

$$\begin{aligned} \mathcal{H}_{(4 \times 2 \cdot j)} &= [\mathbf{h}^s(j) \quad \mathbf{h}^s(j-1) \quad \dots \quad \mathbf{h}^s(0)] \\ \mathcal{G}_{(2 \cdot j \times 4(q+j))} &= \begin{bmatrix} \tilde{\mathbf{h}}(q) & \dots & \tilde{\mathbf{h}}(0) & \mathbf{0} & \dots & \mathbf{0} & \mathbf{0} \\ \mathbf{0} & \tilde{\mathbf{h}}(q) & \dots & \tilde{\mathbf{h}}(0) & & \vdots & \vdots \\ & \mathbf{0} & & \ddots & & \mathbf{0} & \\ \vdots & \vdots & & \tilde{\mathbf{h}}(q) & \dots & \tilde{\mathbf{h}}(0) & \mathbf{0} \\ \mathbf{0} & \mathbf{0} & \dots & \mathbf{0} & \tilde{\mathbf{h}}(q) & \dots & \tilde{\mathbf{h}}(0) \end{bmatrix} \\ \Delta \mathcal{V}_{(4(q+j) \times 1)} &= \begin{bmatrix} \Delta \mathbf{W}(-q) \\ \dots \\ \Delta \mathbf{W}(j) \end{bmatrix} \end{aligned}$$

The the failure function g_r of the r th storey at the design time $t^* = j$ for a deterministic barrier function $y_{c,r}$ is given by

$$g_r = y_{c,r} - \mathbf{h}_{(r)}^0(j) \mathbf{Z}(\mathbf{0}) + \sqrt{4\pi} \mathcal{H}^{(r)} \mathcal{G} \Delta \mathcal{V} \quad (7.35)$$

where subscript (r) denotes the r th row, corresponding to the r th storey. The safety margin \mathcal{M} is then given in the standard normal distributed space by

$$\mathcal{M} = y_{c,r} - \mathbf{h}_{(r)}^0(j) \mathbf{Z}(\mathbf{0}) + \sqrt{4\pi} \mathcal{H}^{(r)} \mathcal{G} \Xi \sqrt{\Delta t} \quad (7.36)$$

where it has been used that $\mathcal{V} = \sqrt{\Delta t} \Xi$. As seen in (7.36), $\mathcal{M} = 0$ is a plane hyper-surface in $\mathbb{R}^{4(q+j)}$, whereby the mean value and the standard deviation of the safety margin \mathcal{M} is determined directly as

$$\mu_{\mathcal{M}} = y_{c,r} - \mathbf{h}_{(r)}^0(j) \mathbf{Z}(\mathbf{0}) \quad , \quad \sigma_{\mathcal{M}} = \left| \sqrt{4\pi \Delta t} \mathcal{H}_{(r)} \mathcal{G} \right| \quad (7.37)$$

The minimal distance $\beta^{(j)}$ and the normal vector at the failure surface $\boldsymbol{\alpha}^{(j)}$ found at the design time $t^* = j$ is then determined as

$$\beta^{(j)} = \frac{\mu_{\mathcal{M}}}{\sigma_{\mathcal{M}}} = \frac{y_{c,r} - \mathbf{h}_{(r)}^0(j-1) \mathbf{Z}(\mathbf{0})}{\sqrt{4\pi} \left| \sqrt{\Delta t} \mathcal{H}_{(r)} \mathcal{G} \right|} \quad , \quad \boldsymbol{\alpha}^{(j)} = \frac{-\sqrt{4\pi} (\mathcal{H}_{(r)} \mathcal{G})^T \sqrt{\Delta t}}{\sqrt{4\pi} \left| \sqrt{\Delta t} \mathcal{H}_{(r)} \mathcal{G} \right|} \quad (7.38)$$

whereby the design point becomes

$$\boldsymbol{\xi}^{*(j)}_{(4(q+j) \times 1)} = \beta^{(j)} \boldsymbol{\alpha}^{(j)} = \frac{-\left(y_c - \mathbf{h}_{(r)}^0(j-1) \mathbf{Z}(\mathbf{0})\right) (\mathcal{H}_{(r)} \mathcal{G})^T}{\sqrt{4\pi} \left| \mathcal{H}_{(r)} \mathcal{G} \right|^2 \sqrt{\Delta t}} \quad (7.39)$$

By using (7.15) a transformation back to the original $\Delta\mathcal{V}$ -space is achieved

$$\mathbf{u}^{(j)}_{(4(q+j)\times 1)} = \frac{\left(y_c - \mathbf{h}_{(r)}^0(j-1)\mathbf{Z}(\mathbf{0})\right) (\mathcal{H}_{(r)}\mathcal{G})^T}{\sqrt{4\pi} |\mathcal{H}_{(r)}\mathcal{G}|^2 \Delta t} \quad (7.40)$$

IS of the response process $\tilde{\mathbf{Z}}(t)$ is now achieved by utilising the transformed Wiener process $\Delta\tilde{\mathbf{W}}$ and the control function given in (7.40)

$$\tilde{\mathbf{Z}}(i) = \mathbf{h}_0(i)\tilde{\mathbf{Z}}(0) + \sqrt{4\pi} \sum_{l=0}^i \mathbf{h}^s(i-l) \sum_{k=0}^q \tilde{\mathbf{h}}(k) \Delta\tilde{\mathbf{W}}^{(j)}(l-k) \quad , \quad i = 0, 1, \dots \quad (7.41)$$

where $\Delta\tilde{\mathbf{W}}^{(j)}(i)$ is the transformed incremental Wiener process at time $t = i$ with the mean value $\mathbf{u}^{(j)}(i)$.

7.1.1 Results

The sample control functions corresponding to a design time $t^* = T = 35$ eigenperiods is shown in figure 7.5

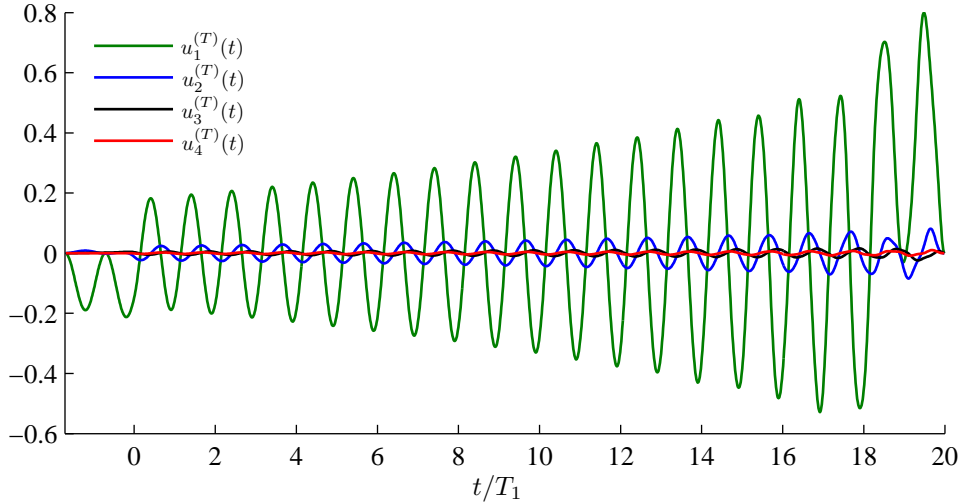


Figure 7.5: The control functions for the four input processes.

As seen in figure 7.5 the sample control functions of the system is non-zero for $t < 0$, since the turbulence model is determined from the white noise process before $t = 0$ cf. (7.28). The control function has a relative small intensity for the time $t < 0$, where after the intensity increases and the control function oscillates in phase with the first mode of the frame. This is so because the response is dominated by the first mode. This resonance behavior of the sampling control functions seems to be general for oscillating systems that only are dominated by a single mode.

The minimal distance β determined from (7.13) is shown in figure 7.6.

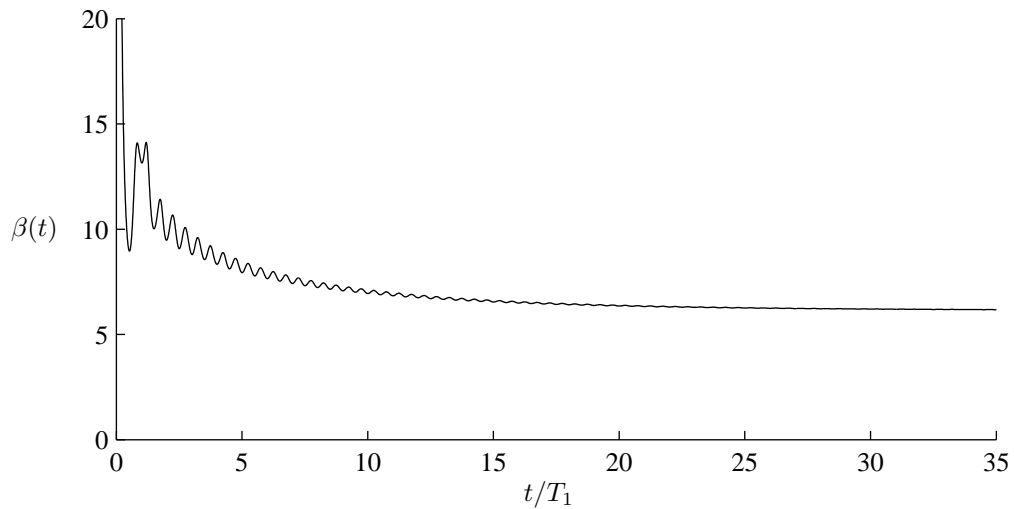


Figure 7.6: β function.

It appears that the β function is oscillating and local extremes emerge, which signifies the need of the multi-modal IS method. An unexpected behavior is seen in the time interval $t = [0, 2T_1]$, where the β function attains a lower value than in the following time interval. This is not to be expected since the system is quiescent at $t = 0$, whereby it must be concluded that an inaccurate estimate of the beta function in the first two eigenperiods occur. This issue is not a problem for time series larger than 10 eigenperiods, since the outcrossing probability during the first two periods is negligible compared to the total outcrossing probability. This is evident when considering the weight function given by (7.19) since it is zero in the first periods, cf. figure 7.7.

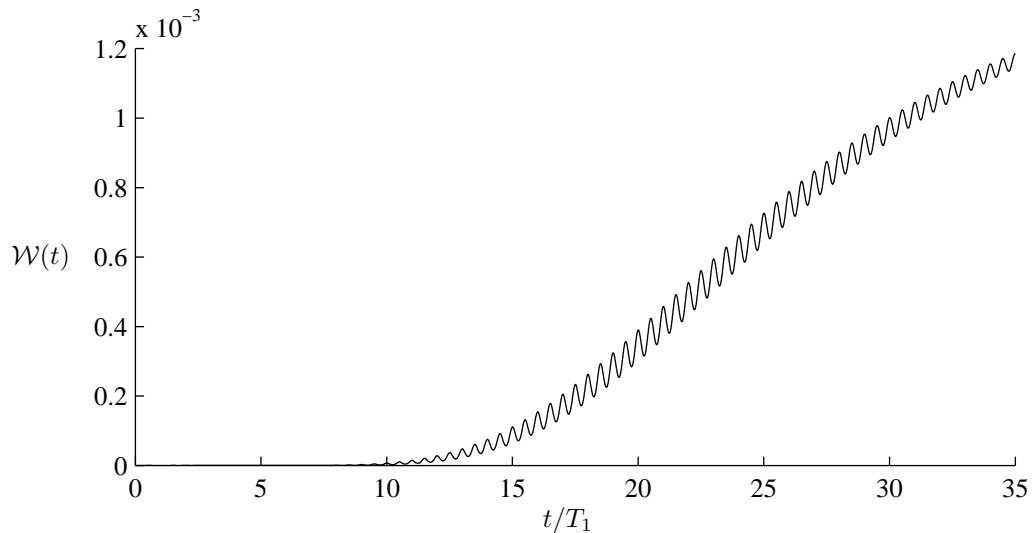


Figure 7.7: Weight function.

The response of the first storey of the structure exposed to the turbulent vector process with and without utilisation of the control function is shown in figure 7.8. The same seed has been used for the two trajectories, whereby only the control function causes the deviation. As seen in figure 7.8 the

control function is dominating the response almost from the beginning, which differs from systems exposed to a white noise process cf. appendix J.4.

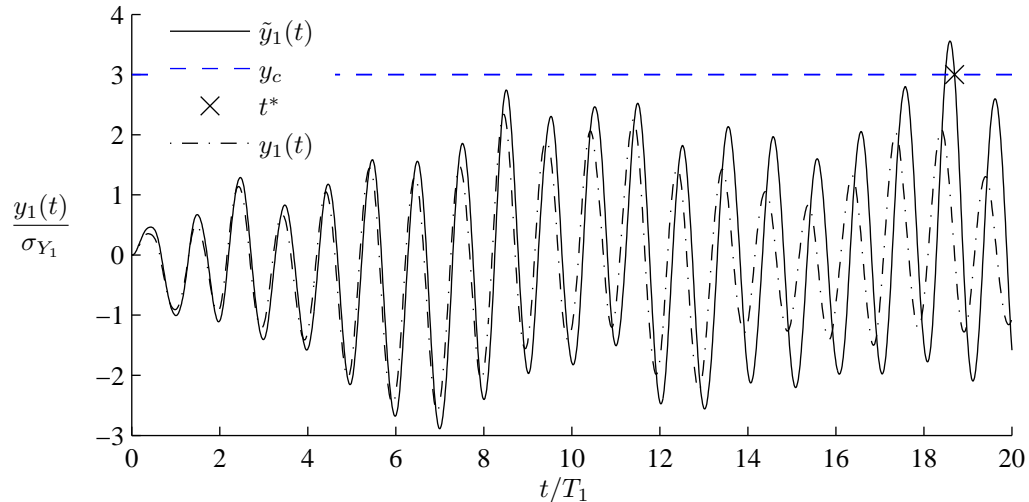


Figure 7.8: Response of the first storey with and without the control function.

The probability of failure for different barrier levels, estimated with the IS method and the CMC method, is shown in figure 7.9. For each barrier and exit-time, three estimates are calculated to give an idea of the standard deviation.

As seen in figure 7.9 the multi-modal IS method gives a good and effective estimates of the first passage time distribution function determined from a deterministic initial state. In the following, the recurrence period and the barrier corresponding to a given recurrence period are determined for the stationary case.

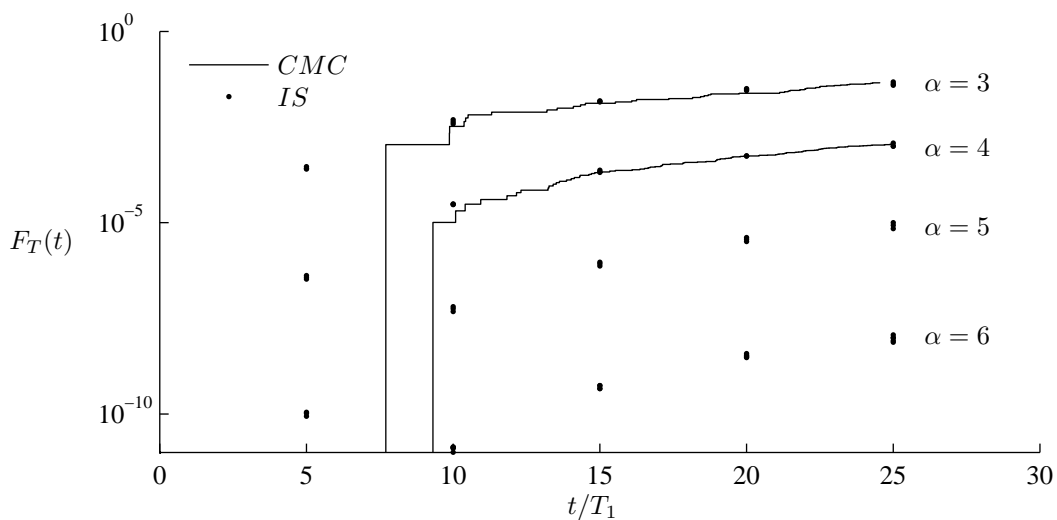


Figure 7.9: The first passage time probability distribution function for different barrier levels α . 10^4 and 10^5 simulation are used for the CMC simulation for $\alpha = 3$ and $\alpha = 4$, respectively. 500 simulations are used for all IS simulations.

7.1.2 Characteristic extreme responses

In the previous section, IS was used to estimate first passage time for responses with deterministic initial condition, i.e. non-stationary responses. In this section it is shown how IS can also be used to estimate failure probabilities for stationary responses. The reason for considering stationary responses is that characteristic extreme responses for wind turbines are determined from stationary responses.

There are two ways by which IS can be used to estimate first passage times for stationary responses. The first way is to include the distribution of the initial stationary state vector $\mathbf{Z}(t_0)$ in the safety margin. Since the distribution of the initial state in general is difficult to determine, this approach is not preferred.

The second way is to determine the first passage time probability from an estimated hazard rate of the stationary response.

Firstly, let the deterministic initial state belong to the safe domain $\mathbf{z}(t_0) \in \mathcal{S}$, then the first passage time distribution is determined by [Nielsen, 2007b]

$$F_T(t) = 1 - \exp\left(-\int_0^t \lambda(\tau, y_c) d\tau\right) \quad (7.42)$$

where $\lambda(t, y_c)$ is the hazard rate. By assumed excursions from the safe domain are independent of previous outcrossings, the hazard rate is approximated by the outcrossing intensity, thus

$$\lambda(t, y_c) \simeq \nu^+(t, y_c) \quad (7.43)$$

For a stationary process $\{Y(t)\}$ with a constant safe domain, the outcrossing intensity is constant, whereby $F_T(t)$ becomes

$$F_T(t) \simeq 1 - \exp(-\nu^+(y_c)t) \quad (7.44)$$

For small arguments the approximation $\exp(\epsilon) \approx 1 + \epsilon$ holds, whereby (7.44) becomes

$$F_T(t) \simeq \nu^+(y_c)t \quad (7.45)$$

From (7.45) it is evident that the outcrossing intensity $\nu^+(y_c)$ of the stationary response is equal to the slope of a linear fitted line through the first passage time probabilities found after a transient phase. For the two storey shear frame exposed to a turbulent wind field it is assumed that the stationary response is obtained after 25 eigenperiods, whereby the outcrossing intensity ν^+ of the barrier level $\alpha = 6.1$ is determined as the slope of the fitted line shown in figure 7.10.

Using the same approach as shown in figure 7.10, an estimate of $\nu^+(y_c)$ is made for the barrier levels $\alpha = [3, 4, 5, 6, 6.1]$. From these five estimates of $\nu^+(y_c)$ an estimate of the first passage time probability of the stationary response within 600 s $P(y_1 \geq y_{c,1} | T = 600 \text{ s})$ is made.

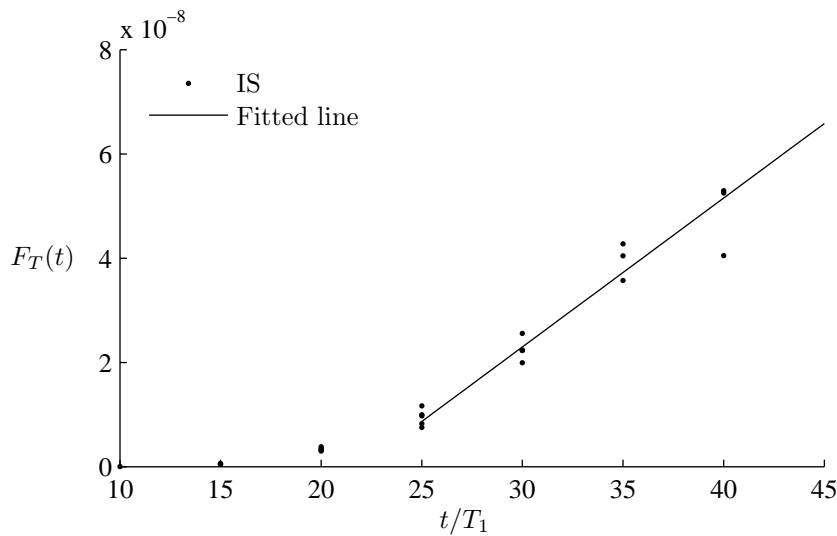


Figure 7.10: Linear fit of $F_T(t)$ after a transient phase of 25 eigenperiods. Barrier level $\alpha = 6.1$.

In the following the first passage time probability obtained by IS method by the above described method is compared with the corresponding failure probability obtained by using the POT extrapolation method described in section 2.1. The obtained failure probability for the IS method is obtained by 500 simulations using $T = 600$ s. The extrapolated failure probability is obtained by 100 simulations using $T = 600$ s. Extraction of extreme responses are performed using the POT method. Extreme values over a threshold $\mu_{Y_1} + 3\sigma_{Y_1}$ are extracted and 3-parameter Weibull and Gumbel probability distribution functions are fitted to the extreme values. Different thresholds are tested and threshold which provides the smallest average relative error is chosen. Figure 7.11 shows the comparison of the results by importance sampling and extrapolation.

The comparison shows that the extrapolation method using a 3-parameter Weibull probability distribution function estimates a response value with a 50 year recurrence period that is around 7%

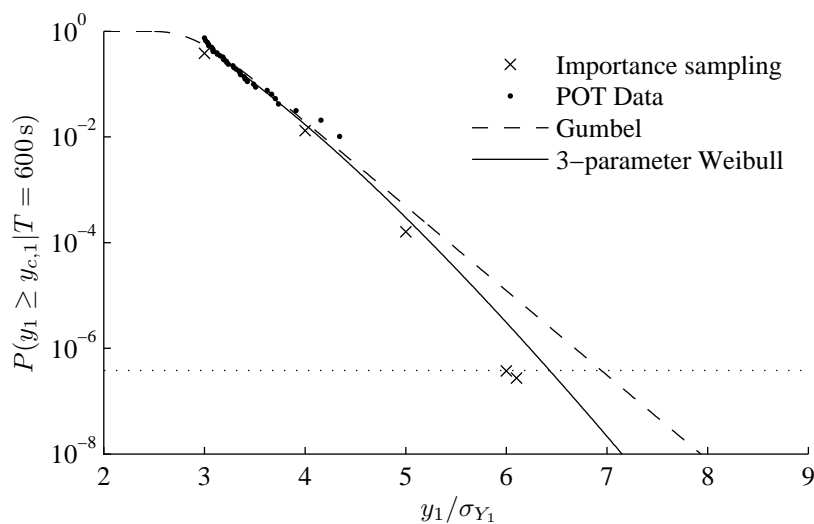


Figure 7.11: Comparison of probabilities of failure for IS and extrapolation methods using Gumbel and 3-parameter Weibull distribution functions.

larger than the response determined by the IS method, whereas the Gumbel probability distribution function estimates a response value that is around 15% larger than the IS estimate. The difference either originates from inaccuracies in the IS method, the assumption that the outcrossing rate is constant for the barriers tested or inaccuracies in the extrapolation method. The extrapolation method is expected to be the largest source of error, since other comparisons have shown that the IS method can simulate correct failure probabilities for barriers $y_c = 3\sigma_{Y_1}$ and $y_c = 4\sigma_{Y_1}$ when comparing with CMC simulations.

As seen in figure 7.11 it is possible to determine the characteristic load on a linear two dof shear frame exposed to a turbulent wind field with the IS method. Using only a few hundred simulations a good estimate of the failure probabilities is achieved. It is hereby concluded that the method is very suitable for simple linear systems exposed to a turbulent wind field. Determination of the control function is the time consuming part of the Multi-modal IS method. Especially the calculations of the load process is very time consuming, by which improvements can be made. In that connection, the state space representation of the ARMA model will be implemented. Furthermore the Multi-modal IS method will be implemented on a system that resembles, the structural behavior of a wind turbine more.

7.2 Implementation on two bladed wind turbine exposed to a turbulent wind field

In the following the multi-modal IS method will be applied to the simple two bladed wind turbine exposed to a turbulent wind field as described in chapter 5. The equations of motion on a state space formulation is given as

$$\left. \begin{aligned} \frac{d}{dt}\mathbf{Z}(t) &= \mathbf{A}\mathbf{Z}(t) + \mathbf{B}\mathbf{F}(\mathbf{Z}(t), t) \quad , \quad t > t_0 \\ \mathbf{Z}(t_0) &= \mathbf{Z}_0 \end{aligned} \right\} \quad (7.46)$$

where \mathbf{A} , \mathbf{B} and $\mathbf{Z}(t)$ are given by

$$\mathbf{A}_{(8 \times 8)} = \begin{bmatrix} \mathbf{0} & \mathbf{I} \\ -\mathbf{M}^{-1}\mathbf{K} & -\mathbf{M}^{-1}\mathbf{C} \end{bmatrix}, \quad \mathbf{B}_{(8 \times 4)} = \begin{bmatrix} \mathbf{0} \\ -\mathbf{M}^{-1}\mathbf{b} \end{bmatrix}, \quad \mathbf{Z}(t)_{(8 \times 1)} = \begin{bmatrix} \mathbf{q}(t) \\ \dot{\mathbf{q}}(t) \end{bmatrix} \quad (7.47)$$

$\mathbf{F}(\mathbf{Z}(t), t)$ is the load normal to the rotor plane at the tip of the blades and given by (5.24). The state dependency of $\mathbf{F}(\mathbf{Z}(t), t)$ is due to the interpolation of the turbulence at the fixed grid. The SSM described in appendix B.3 is used to generate the turbulence in the fixed grid.

By reformulating the SSM to a convolution integral the turbulence is given as a sum of uncorrelated normal distributed stochastic variables, thus

$$\mathbf{V}(l) = \sum_{i=1}^l \mathbf{G}(l-i)\Delta\mathbf{W}(i) \quad (7.48)$$

where $\Delta\mathbf{W}(i)$ is a discrete incremental Wiener vector process and $\mathbf{G}(i)$ is the turbulence impulse response matrix given by

$$\begin{aligned}
\mathbf{G}(0) &= \mathcal{D} \\
\mathbf{G}(1) &= \mathcal{C}\mathcal{B} \\
\mathbf{G}(2) &= \mathcal{C}\mathcal{A}\mathcal{B} \\
&\vdots \\
\mathbf{G}(n) &= \mathcal{C}\mathcal{A}^{n-2}\mathcal{B}
\end{aligned}$$

where \mathcal{A} , \mathcal{B} , \mathcal{C} and \mathcal{D} are the state vector matrices in (B.34) and the matrix multiplication notation $\mathcal{A}^n = \mathcal{A}\mathcal{A}\mathcal{A}\dots$ has been used.

A solution to (7.47) may be determined from (7.29), whereby the solution on a discrete form is given as

$$\mathbf{Z}(j+1) = \mathbf{h}^0(j)\mathbf{Z}(0) + \sum_{l=0}^j \mathbf{h}^s(j-l) \left(\mathbf{f}_s + \mathbf{N}(l)a_T \sum_{k=0}^l \mathbf{G}(k)\Delta\mathbf{W}(l-k) \right), \quad j = 0, 1, \dots, M \quad (7.49)$$

where $\mathbf{N}(t)$ is defined in (5.32) and a_T , \mathbf{f}_s in (5.24).

In order to determine the design point, (7.49) is rewritten on a matrix form

$$\mathcal{Z} = \mathcal{H}^0\mathbf{Z}_0 + \mathcal{H}^s\mathbf{f}_s + a_T\mathcal{H}\mathcal{N}\mathcal{G}\Delta\mathcal{V} \quad (7.50)$$

where

$$\begin{aligned}
\underset{(8M \times 1)}{\mathcal{Z}} &= \begin{bmatrix} \mathbf{Z}(0) \\ \vdots \\ \mathbf{Z}(M) \end{bmatrix}, \quad \underset{(8M \times 8)}{\mathcal{H}^0} = \begin{bmatrix} \mathbf{h}^0(0) \\ \vdots \\ \mathbf{h}^0(M) \end{bmatrix}, \quad \underset{(8M \times 1)}{\mathcal{H}^s} = \begin{bmatrix} \sum_{l=0}^0 \mathbf{h}^s(l)\mathbf{f}_s \\ \vdots \\ \sum_{l=0}^M \mathbf{h}^s(l)\mathbf{f}_s \end{bmatrix} \\
\underset{(4M \times 1)}{\Delta\mathcal{V}} &= \begin{bmatrix} \Delta\mathbf{W}(0) \\ \vdots \\ \Delta\mathbf{W}(M) \end{bmatrix}, \quad \underset{(8M \times 4M)}{\mathcal{H}} = \begin{bmatrix} \mathbf{h}^s(0) & \mathbf{0} & \dots & \mathbf{0} \\ \mathbf{h}^s(1) & \mathbf{h}^s(0) & \ddots & \vdots \\ \vdots & \ddots & \ddots & \mathbf{0} \\ \mathbf{h}^s(M) & \dots & \mathbf{h}^s(1) & \mathbf{h}^s(0) \end{bmatrix} \\
\underset{(4M \times 4M)}{\mathcal{N}} &= \begin{bmatrix} \mathbf{N}(0) & \mathbf{0} & \dots & \mathbf{0} \\ \mathbf{0} & \mathbf{N}(1) & \ddots & \vdots \\ \vdots & \ddots & \ddots & \mathbf{0} \\ \mathbf{0} & \dots & \mathbf{0} & \mathbf{N}(M) \end{bmatrix}, \quad \underset{(4M \times 4M)}{\mathcal{G}} = \begin{bmatrix} \mathbf{G}(0) & \mathbf{0} & \dots & \mathbf{0} \\ \mathbf{G}(1) & \mathbf{G}(0) & \ddots & \vdots \\ \vdots & \ddots & \ddots & \mathbf{0} \\ \mathbf{G}(M) & \dots & \mathbf{G}(1) & \mathbf{G}(0) \end{bmatrix}
\end{aligned}$$

The failure function of the r th element at the design time $t^* = j$ is given as

$$g_r = q_{c,r} - \mathcal{Z}_{(j,r)} = q_{c,r} - \mathcal{H}_{(j,r)}^0 \mathbf{Z}_0 - \mathcal{H}_{(j,r)}^s \mathbf{f}_s - a_T \mathcal{H}_{(j,r)} \mathcal{N} \mathcal{G} \Delta \mathcal{V} \quad (7.51)$$

where (j, r) denotes the r th entry in the j th matrix row and $q_{c,r}$ is the critical displacement of the r th element. The safety margin is then given as

$$\mathcal{M} = q_{c,r} - \mathcal{H}_{(j,r)}^0 \mathbf{Z}_0 - \mathcal{H}_{(j,r)}^s \mathbf{f}_s - a_T \mathcal{H}_{(j,r)} \mathcal{N} \mathcal{G} \Xi \sqrt{\Delta t} \quad (7.52)$$

Where it has been used that $\Delta \mathcal{V} = \sqrt{\Delta t} \Xi$. The mean value and the standard deviation of the safety margin \mathcal{M} is given as

$$\mu_{\mathcal{M}} = q_{c,r} - \mathcal{H}_{(j,r)}^0 \mathbf{Z}_0 - \mathcal{H}_{(j,r)}^s \mathbf{f}_s \quad , \quad \sigma_{\mathcal{M}} = \left| a_T \sqrt{\Delta t} \mathcal{H}_{(j,r)} \mathcal{N} \mathcal{G} \right| \quad (7.53)$$

The minimal distance function $\beta^{(j)}$ and failure surface normal $\boldsymbol{\alpha}^{(j)}$ is found at the design time $t^* = j$

$$\beta^{(j)} = \frac{q_{c,r} - \mathcal{H}_{(j,r)}^0 \mathbf{Z}_0 - \mathcal{H}_{(j,r)}^s \mathbf{f}_s}{\left| a_T \sqrt{\Delta t} \mathcal{H}_{(j,r)} \mathcal{N} \mathcal{G} \right|} \quad , \quad \boldsymbol{\alpha}^{(j)} = \frac{-a_T \sqrt{\Delta t} (\mathcal{H}_{(j,r)} \mathcal{N} \mathcal{G})^T}{\left| a_T \sqrt{\Delta t} \mathcal{H}_{(j,r)} \mathcal{N} \mathcal{G} \right|} \quad (7.54)$$

whereby the design point becomes

$$\boldsymbol{\xi}^{(j)} = \frac{-q_{c,r} + \mathcal{H}_{(j,r)}^0 \mathbf{Z}_0 + \mathcal{H}_{(j,r)}^s \mathbf{f}_s}{a_T \sqrt{\Delta t} \left| \mathcal{H}_{(j,r)} \mathcal{N} \mathcal{G} \right|^2} \cdot (\mathcal{H}_{(j,r)} \mathcal{N} \mathcal{G})^T \quad (7.55)$$

By using (7.15) a transformation back to the original $\Delta \mathcal{V}$ -space is achieved

$$\mathbf{u}^{(j)} = \frac{q_{c,r} - \mathcal{H}_{(j,r)}^0 \mathbf{Z}_0 - \mathcal{H}_{(j,r)}^s \mathbf{f}_s}{a_T \Delta t \left| \mathcal{H}_{(j,r)} \mathcal{N} \mathcal{G} \right|^2} \cdot (\mathcal{H}_{(j,r)} \mathcal{N} \mathcal{G})^T \quad (7.56)$$

IS of the response $\mathbf{Z}(t)$ is generated by using the transformed Wiener process $\Delta \tilde{\mathbf{W}}$.

7.2.1 Results

In the following the results from implementing the multi-modal IS method on the two bladed wind turbine are presented. The structural parameters for the wind turbine model are given in section 5.2 and the turbulence is discretised with four nodes on the periphery of the rotor plane. To minimize the transient phase the initial displacement is set to the estimated mean value of the stationary response cf. table 5.1.

The following results are obtained by “aiming” for failure in the tower, where failure occurs when $q_1 \geq q_{c,1} = 4\sigma_{q_1} + \mu_{q_1}$ which corresponds to barrier level $\alpha = 4$.

The minimal distance function $\beta(t)$ is shown in figure 7.12.

The minimal distance function $\beta(t)$ is oscillating which is also observed for the two dof shear frame exposed to a turbulence wind field cf. section 7.1. The oscillations are more irregular since the response of the tower is affected by all modes. After 30s the beta function is oscillating around a constant value which corresponds to a constant outcrossing rate. The response is therefore dominated by several exit-times, thus there is indeed a need for a multi-modal sampling density function.

The set of sample control functions that in mean drive the tower to failure at the design time $t^* = 70$ s is shown in figure 7.13.

The sample control functions consists of a number of discontinuous intervals where every second interval acts in phase with the tower mode. The control functions is chopped in to discontinuous intervals which corresponds to a blade passing by at that node, which is illustrated for $u_1(t)$ in figure 7.14.

If $\Delta\tilde{\mathbf{W}}(t) = \mathbf{u}(t)\Delta t$ is used in (7.50) failure occurs exactly at the design time t^* as seen in figure 7.15. The response of the blades is not affected by the sample control functions in the same manner as the tower, thus only failure of the tower is estimated when aiming at the tower. The first passage time probability of the entire system requires aiming for all subcomponents.

The first passage time probability distribution function $F_T(t)$ of the rotating wind turbine with a static load is estimated by means of the CMC method and by means the IS method, cf. figure 7.16. 5000 and 20000 time series are used in the CMC method for the barrier levels $\alpha = [3, 4]$, respectively and 500 are used in the IS method for the barrier levels $\alpha = [3, 4, 5, 6]$. By a visual evaluation of the two methods it is evident that the IS method is very effective.

The results shown in figure 7.16 are calculated for a deterministic start and therefore $F_T(t)$ is not directly applicable for estimating the failure probability of the stationary response, which is needed for determining the characteristic extreme response value. As described in section 7.1.2 it is reasonable to assume a constant outcrossing rate for the stationary response and by applying the Poisson

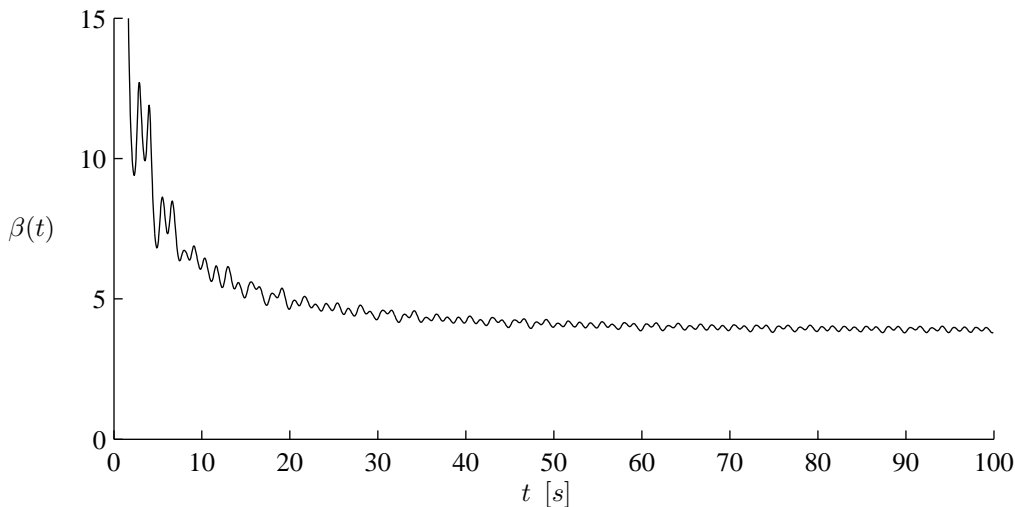


Figure 7.12: The minimal distance function for the barrier level $\alpha = 4$.

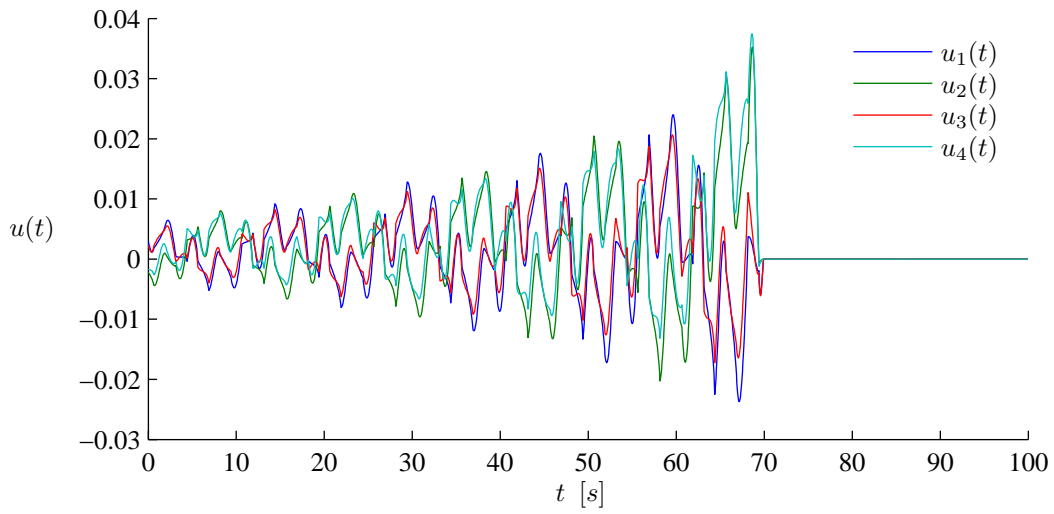


Figure 7.13: The set of sample control functions that in mean drive the system to failure at $t^* = 70$ s.

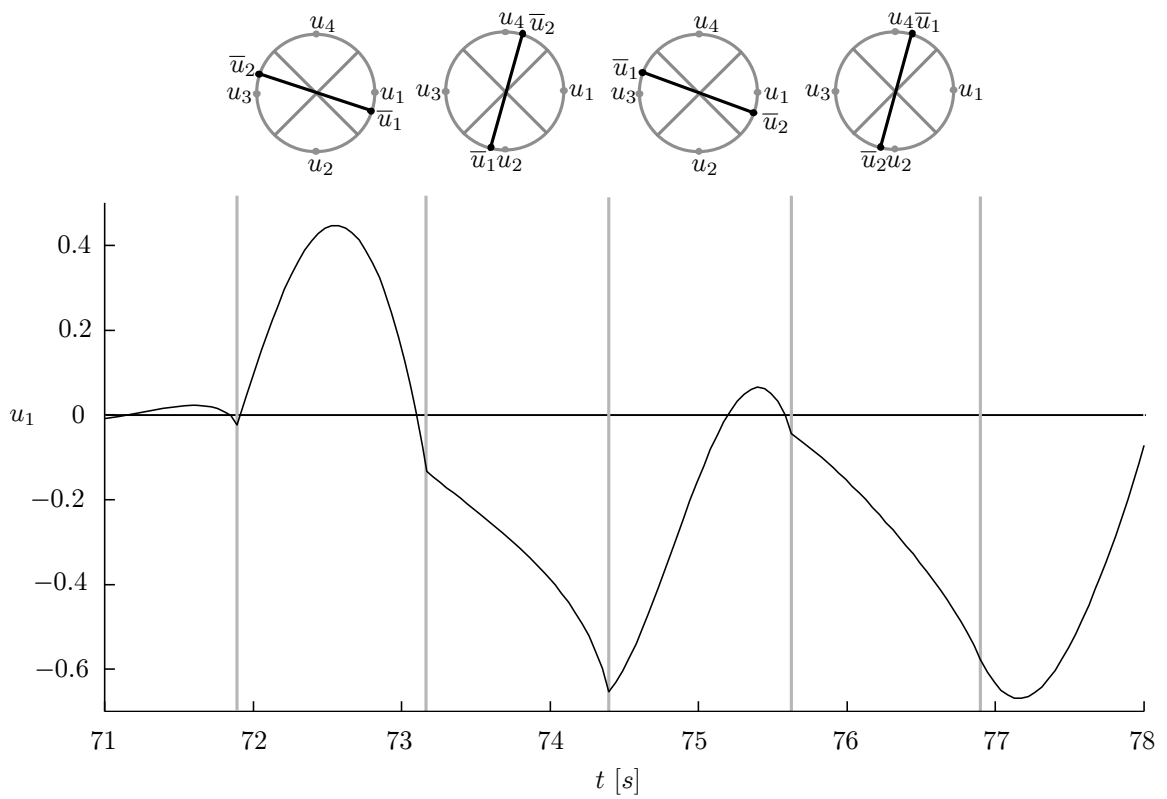


Figure 7.14: The discontinuous sample control function for different location of the blades.

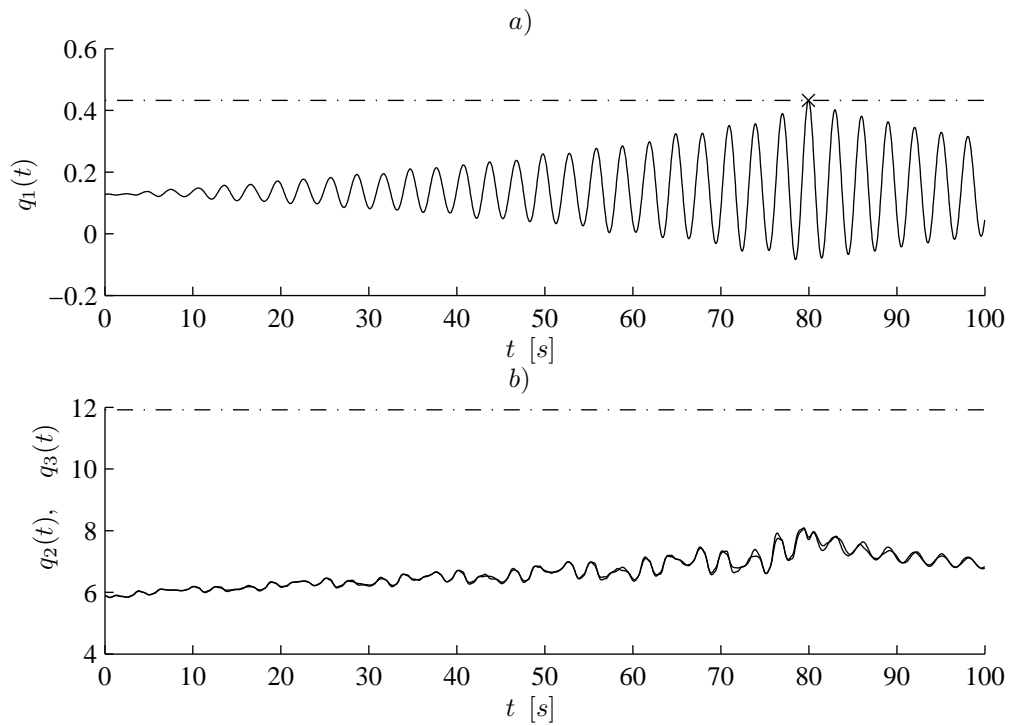


Figure 7.15: Response of the wind turbine components where only the sample control function is applied as load. *a)* is the response of the tower. *b)* is the response of the two blades.

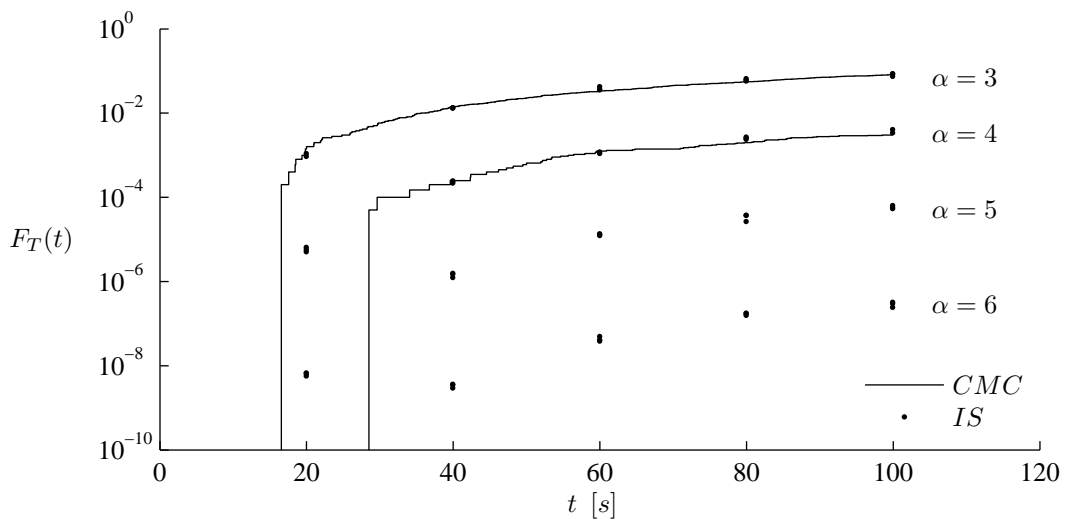


Figure 7.16: The first passage time probability distribution function estimated by means of the IS method and the CMC method for different barrier levels.

assumption the estimates of the first passage time probability distribution function of the stationary response is determined by (7.45). The response is assumed to be stationary after 40 s whereafter the outcrossing rate is estimated as the slope of the best fitted line through the estimated first passage time probabilities as shown in figure 7.17 for the barrier level $\alpha = 6$.

Several points are used to achieve a good estimate by which the calculation time is increased. The increased calculation time is however not substantial since the time consuming part of the IS is the calculation of the sample control functions. The accuracy of the outcrossing rate estimate is increased compared to the estimated first passage time probabilities, but due extrapolation when estimating the first passage time probabilities of the stationary response the accuracy of the final estimate is reduced. The estimated outcrossing rates for the different barrier levels are shown in figure 7.18.

To evaluate the estimated characteristic extreme response value with a 50 year recurrence period on condition of a wind speed of 15 m/s. The extreme response is estimated by means of the POT method where a Gumbel and a 3-parametric Weibull distribution is used as candidate distribution, cf. 2.1. 600 s are used as reference frame for determination of the characteristic extreme response, whereby the characteristic extreme response value with a 50 year recurrence period corresponds to $F_T(600) = 3.8 \cdot 10^{-7}$. 100 time series of 600 s are used to generate the local maxima used in the POT method. The first passage time probability during a time period of 600 s, estimated by means of the POT method and the IS method is shown in figure 7.19.

By a comparison of the candidate distributions it emerge that there is a 20 % deviation in the estimated characteristic extreme response with a 50 year recurrence period. It seems like the extreme response distribution estimated with the IS method is not linear in a logarithmic scale and whereby it does not constitute a Gumbel distribution. The Gumbel distribution deviates 6% from the results by the IS method at the 50 year recurrence period whereas the Weibull distribution deviates 11 %. Therefore it must be concluded that the Gumbel distribution gives the best estimate of the characteristic extreme response with a 50 year recurrence period at the 15 m/s wind bin, assuming that the IS method provides the more accurate extreme response value.

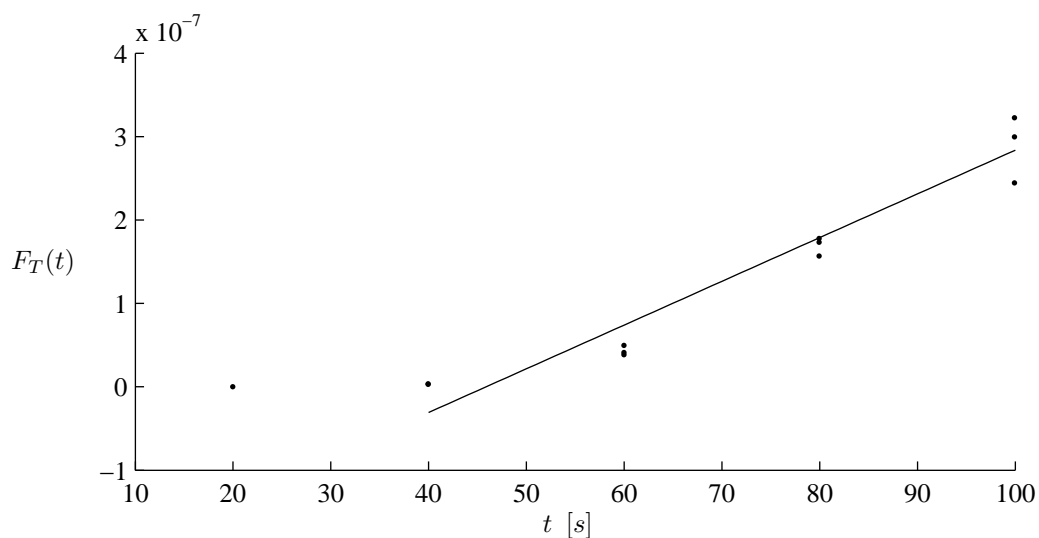


Figure 7.17: Estimation of the outcrossing rate for the barrier level $\alpha = 6$.

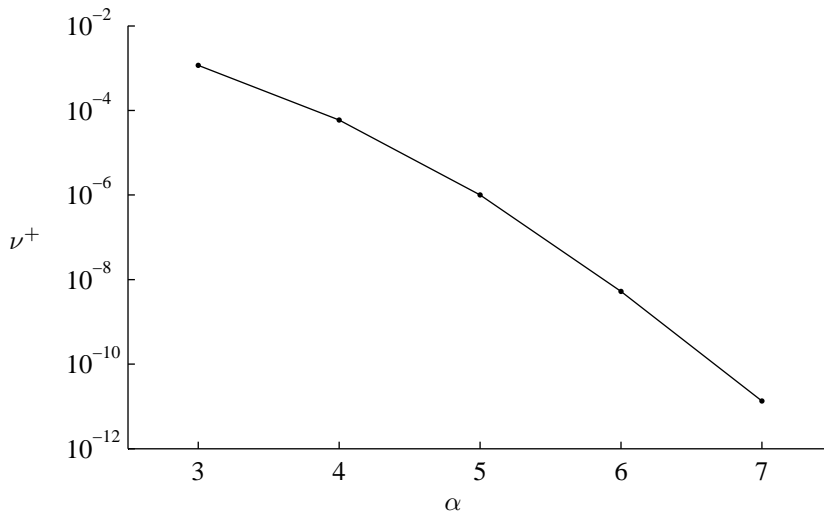


Figure 7.18: Estimated outcrossings rates ν^+ as function of the barrier level α .

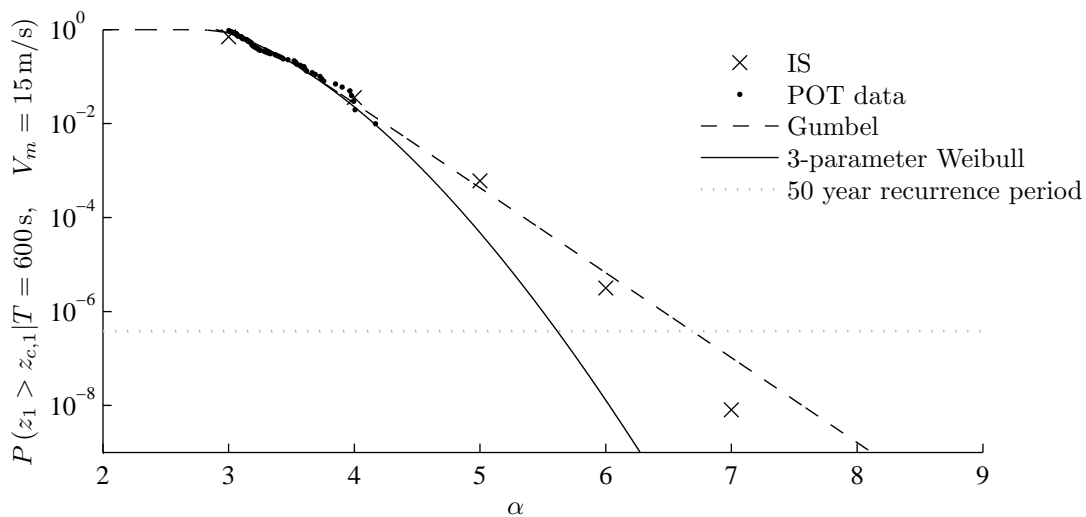


Figure 7.19: Extreme response distribution estimated by means of the POT and IS.

7.3 Conclusion

The IS method has been implemented on the following systems

- Scalar diffusion process with a constant drift
- Single dof oscillator exposed to white noise
- The two storey shear frame exposed to a turbulent wind field
- Two bladed wind turbine exposed to a turbulent wind field

The IS method has successfully been implemented on a scalar diffusion process with a constant drift term. The nature of a diffusion process indicates that the first passage time probability is dominated by a single exit time, whereby an effective importance measure is determined by means of the Girsanov transformation and a sample control function obtained by use of the FORM.

For oscillating systems the first passage time probability is not dominated by a single exit time, whereby a multi-modal importance measure is needed, to include the first passage time probability from all exit times. Again, an effective importance measure is obtained by means of the Girsanov transformation, but to incorporate the effect from all exit times the need of multiple sample control functions is evident. The multi-modal IS method has successfully been implemented on a linear single dof oscillator exposed to a Gaussian white noise.

Since the scope of this project is to evaluate the use of alternative statistical simulation methods to determine extreme loads on wind turbines, it is necessary to incorporate a turbulence model in the considered systems. In that connection the IS method has successfully been implemented on a two storey shear frame exposed to a turbulent wind field, which is obtained through a filter model. The incorporated filter model increases the calculation time of the sample control function significantly due to the long memory of the filter model.

Finally, the multi-modal IS method has successfully been applied to a linear four degree of freedom wind turbine where the turbulence on the turbine is determined by interpolating on a fixed turbulence grid. To increase the accuracy of the turbulence model and decrease the calculation time a State Space representation of the ARMA turbulence model has been used. Again, the time consuming part of the simulation, is the calculation of the sample control function and especially the total number of time steps is very crucial for the calculation time, since a set of sample control functions are calculated for each time step.

The first passage time distribution function estimated by the IS method determined for deterministic initial states, whereby the characteristic extreme response is not determined directly. An estimate of the hazard rate of the stationary response is calculated, whereafter the first passage time probability distribution function of the stationary response is determined. The standard error of the estimated hazard rate is amplified when extrapolating the first passage time probabilities of the stationary response. The uncertainties connected with estimation of the hazard rate need to be investigated further.

7.3.1 New challenges

The control system in wind turbines which needs to be incorporated when calculating the sample control functions, has not been treated in this project. A way to evaluate the applicability of the IS method on systems with active control is to include a control system on the simple two bladed wind turbine addressed in this project.

Only the first passage time probability distribution function of the tower has been determined. In general the nature of controlled simulation methods, is that only the first passage time probability of a single component is estimated. The combined first passage time probability of all components can be estimated by the IS method by including all components when establishing the multi-modal sample density function. A further investigating of this is needed to evaluate the effectiveness.

Generally, the dependency of the number of state space variables in the IS method determines the limitation of the method. In that sense implementing the IS method on the FAST code might be difficult, since the turbulence grid used in FAST is discretised into 61 nodes, thus 61 sample control functions are needed for each time step. The number of sample control functions needed to establish an effective importance measure can be reduced, which corresponds to reducing the total number of sample points, which samples are generated around.

Chapter 8

Russian Roulette & Splitting with Distance Control

This chapter describes the variance reduction method "Russian Roulette & Splitting with Distance Control" (RR&S) and presents the results achieved for estimating first passage times for different systems with the algorithm. The systems which the algorithm is implemented on are

- a one dof non-linear oscillator
- a two dof shear frame - earthquake
- a two dof shear frame - earthquake, static load & carrier wave
- a three dof wind turbine
- a 24 dof wind turbine modelled in FAST

The 1-dof non-linear oscillator is used for verifying that the RR&S algorithm has been implemented correctly. The verification is performed by comparing results for first passage time distribution functions $F_T(t)$ for the 1-dof oscillator with results obtained by [Pradlwarter and Schuëller, 1999]. The 1-dof oscillator and the comparison of the results is presented in appendix I.1.

Next, the RR&S algorithm is implemented on the 2-dof shear frame described in chapter 4. At first the 2-dof shear frame is exposed only to a horizontal earthquake acceleration process modelled by a broken line process, see section 4.2. The achieved results are presented in section 8.3.

Hereafter, an intermediate step is taken to investigate the efficiency of different so-called *distance variables* in the case where the two dof shear frame is exposed to also a static load and a carrier wave. From this investigation a distance variable is chosen for use in simulation of the three dof wind turbine and the 24-dof wind turbine. The investigation is presented in appendix I.2.

After having chosen a distance variable from the above mentioned investigation, the RR&S algorithm is implemented on the three dof wind turbine described in section 5. The achieved results are presented in section 8.4.

Lastly, the RR&S algorithm is implemented on the FAST code which models a wind turbine with up to 24 dofs. The achieved results are presented in section 8.5.

Based on the obtained results on these systems, a conclusion is finally made regarding the potential of the RR&S algorithm for simulating low failure probabilities for wind turbines.

8.1 RR&S algorithm

In this section the RR&S algorithm is described and the parameters of the algorithm are defined. The description is based on [Pradlwarter and Schuëller, 1999].

The method overall consists of the two concepts "Russian Roulette & Splitting" and "Distance Control". "Russian Roulette & Splitting" takes care of replacing "unimportant" realisations with "important" ones, and "Distance Control" determines the importance of each realisation and works toward a uniform density of realisations within a chosen sub-space of the state vector space. A uniform density of realisations is supposed to increase the probability of rare realisations to occur. Already at this point it is clear that the performance of the method depends on the selection of a proper sub-space for distance control. RR&S is claimed to be applicable for multi-dimensional dynamic state vector processes, [Pradlwarter and Schuëller, 1999]. In this respect the dynamic system is represented by an arbitrary M -dimensional state vector process $\{\mathbf{Z}(t) \in \mathbb{R}^M\}$.

In figure 8.1 it is illustrated how the RR&S algorithm redistributes the samples. As the samples moves through space some of them are killed, while others are splitted to replace the ones which are killed.

The advantage of RR&S simulation compared to CMC simulation is illustrated by first considering how N realisations can be used to describe the joint probability density function of $\mathbf{Z}(t)$ using CMC simulation. Afterwards it is explained how RR&S simulation can be used to describe the same probability density function more accurately using the same amount of realisations. In this procedure it is seen that RR&S simulation is more efficient for estimating the probability of rare events compared to CMC simulation.

Let N stochastic independent realisations of $\mathbf{Z}(\tau_i)$ at a certain instant of time τ_i be denoted $\mathbf{z}_{\tau_i}^{(j)}$, $j = 1, \dots, N$. The components of $\mathbf{z}_{\tau_i}^{(j)}$ are denoted as $z_{\tau_i,k}^{(j)}$, $k = 1, \dots, M$. The probability density function of the k th component $\mathbf{Z}(\tau_i)$ is shown in figure 8.2a.

In a CMC simulation, the joint probability density function of $\mathbf{Z}(\tau_i)$ will be estimated by a discrete distribution. The discrete distribution is given by the discrete set $\{\mathbf{z}_{\tau_i}^{(j)}, w_{\tau_i}^{(j)}\}$, where $w_{\tau_i}^{(j)}$ are the statistical weights associated with the samples. In a CMC simulation all sample weights are identical for any instant of time and given by $w_{\tau_i}^{(j)} = w^{(j)} = 1/N$. A CMC simulation will therefore distribute the realisations so the density of realisations are proportional to the joint probability density function. This implies that CMC will concentrate the samples near the peaks of the probability density function as illustrated in figure 8.2b for the one-dimensional case. Since all realisations have identical weights, high probability areas have high density of realisations, whereas the tails have relatively few realisations. Hence, the low probability areas are not accurately estimated.

The idea of the RR&S algorithm is to adjust the weights $w_{\tau_i}^{(j)}$ in a way that the samples become uniformly distributed in the sample space. Ideally the distribution looks as illustrated in figure 8.2c. In this way relatively more samples are located at the tails, for which reason low probability can be estimated with higher accuracy than is the case for the CMC simulation method. Generally, the realisations may be distributed differently than uniformly, but it is argued in appendix I.3 that this

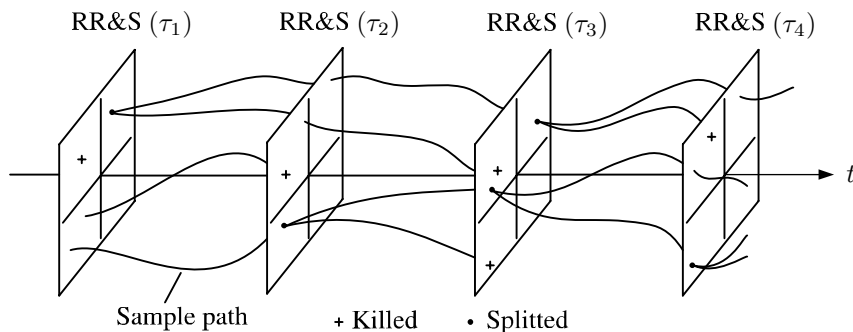


Figure 8.1: Illustration of how samples are killed and splitted at times τ_i , $i = 1, 2, 3, 4$.

may introduce a larger statistical uncertainty. The key to RR&S is therefore to adjust the weights and distribute the samples as shown in figure 8.2c.

The difference between CMC and RR&S simulation is that CMC simulation distributes the samples in a way so the realisation *density* is proportional to the joint probability density function, whereas RR&S simulation distributes the samples in way so the statistical *weights* are proportional to the joint probability density function.

In order to approach a uniform density of realisations in the sample space as shown in figure 8.2c, it is necessary to evaluate the sample set $\{\mathbf{z}_{\tau_i}^{(j)}, w_{\tau_i}^{(j)}\}$ at equidistant time intervals $\Delta\tau$. At each τ_i , where $\tau_i = \Delta\tau \cdot i$ and $i = 1, \dots, T/\Delta\tau$, where T is the length of the simulation, the following steps are performed

1. Ranking of realisations according to an importance measure.
2. Perform Russian Roulette to remove some of the unimportant realisations.
3. Perform Splitting of the most important realisations to keep the same number of realisations.
4. Normalisation of weights to maintain the statistical probability mass 1.
5. Integration of the system forward to next control time τ_{i+1} .

These steps are explained in detail in the following.

Step 1, Ranking of realisations. In order to rank the realisations an *importance measure* is used. The importance measure serves to indicate which samples have a high probability of being killed and which have not. The statistical weight of the samples will then be adjusted according to how important the sample is. The importance measure is a normalised positive scalar quantity associated with each realisation, and is a function of a *distance measure* and a *weight measure*.

In the general case the distance measure is a positive definite function of the D -dimensional vector \mathbf{l} , denoted the *distance variable*. The physical nature of the D components included in \mathbf{l} are combinations of the state variables and may differ from system to system and must be chosen by analysing the nature of the system. For a distance variable to be efficient there should be a clear relation between the value of the distance variable and closeness to failure. What to be aware of when choosing a distance variable will be addressed in section 8.2.

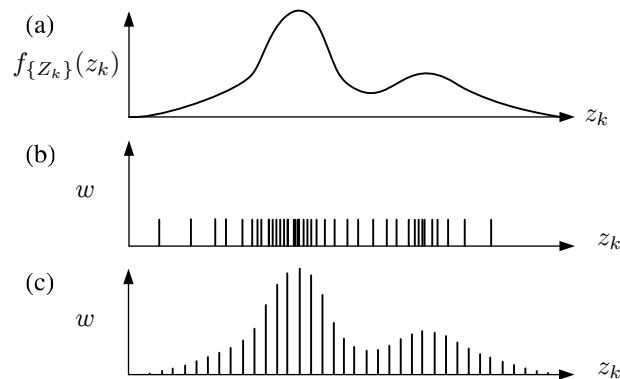


Figure 8.2: a) Probability density function. b) CMC sampling with identical weights. c) RR&S sampling with adjusted weights.

The distance measure serves to distribute the samples uniformly in the D -dimensional subspace in which \mathbf{l} is defined. Obviously, a uniform distribution in the \mathbf{l} -space does not guarantee a uniform distribution in the state space.

Each M -dimensional realisation $\mathbf{z}_{\tau_i}^{(j)}$ is then associated with a D -dimensional vector $\mathbf{l}_{\tau_i}^{(j)}$. To avoid arbitrariness introduced by components of different units, $\mathbf{l}_{\tau_i}^{(j)}$ is generally normalised into an D -dimensional cube $\prod_{h=1}^D [-s_h, +s_h]$. This normalisation is for the D -dimensional case performed by

$$\tilde{l}_{\tau_i,h}^{(j)} = s_h \left(2 \frac{l_{\tau_i,h}^{(j)} - l_{\tau_i,h}^{(\min)}}{l_{\tau_i,h}^{(\max)} - l_{\tau_i,h}^{(\min)} + \epsilon} - 1 \right) \quad , \quad j = 1, \dots, N \quad \wedge \quad h = 1, \dots, D \quad (8.1)$$

where ϵ is a small constant used to avoid a zero denominator in the rather unlikely case where $l_{\tau_i,h}^{(\max)} = l_{\tau_i,h}^{(\min)}$. The amplitudes s_h are next used as weights to augment or lower the importance of components. If the h th entry in $\mathbf{l}_{\tau_i}^{(j)}$ has no importance then $s_h = 0$. The distance measure for the j th realisation is now defined by

$$d_{\tau_i}^{(j)} = \sum_{r=1}^K a_i \|\tilde{\mathbf{l}}_{\tau_i}^{(j_r|j)} - \tilde{\mathbf{l}}_{\tau_i}^{(j)}\| \quad , \quad a_1 > a_2 > \dots > a_K > 0 \quad (8.2)$$

$\|\cdot\|$ denotes the Euclidian norm and $\tilde{\mathbf{l}}_{\tau_i}^{(j_r|j)}$ the r th nearest realisation to $\tilde{\mathbf{l}}_{\tau_i}^{(j)}$ among the other $(N-1)$ realisations, i.e.

$$\|\tilde{\mathbf{l}}_{\tau_i}^{(j_1|j)} - \tilde{\mathbf{l}}_{\tau_i}^{(j)}\| \leq \|\tilde{\mathbf{l}}_{\tau_i}^{(j_2|j)} - \tilde{\mathbf{l}}_{\tau_i}^{(j)}\| \leq \dots \leq \|\tilde{\mathbf{l}}_{\tau_i}^{(j_{N-1}|j)} - \tilde{\mathbf{l}}_{\tau_i}^{(j)}\| \quad (8.3)$$

$d_{\tau_i}^{(j)}$ expresses the "loneliness" of the j th realisation. As only the closest neighbouring realisations provide information on the loneliness of $\mathbf{l}_{\tau_i}^{(j)}$, $d_{\tau_i}^{(j)}$ depends only on the distance to the K closest realisations. Furthermore, the weights a_i provide a tool for weighting the importance of the K closest realisations in a way that the nearest neighbours are weighted most. [Pradlwarter and Schueller, 1999] suggests that the weights a_i are given by

$$a_i = 2^{1-i} \quad (8.4)$$

Although it is demonstrated in appendix I.5 that the influence of these weights may be neglectable and that $a_i = 1$ may provide similar results it is chosen to keep these weights as an option.

In figure 8.3 it is illustrated how the distance between samples are measured in the D -dimensional space. The boundaries of the D -dimensional cube are given by the constants s_h from (8.1).

By (8.2), samples which are located in high density areas will hereby have a small distance measure $d_{\tau_i}^{(j)}$, whereas samples located in low density areas will have a large distance measure.

The weight measure is now introduced. It serves to define the size of the statistical weight of a sample compared to neighbouring samples. The weight measure is not to be confused with the statistical

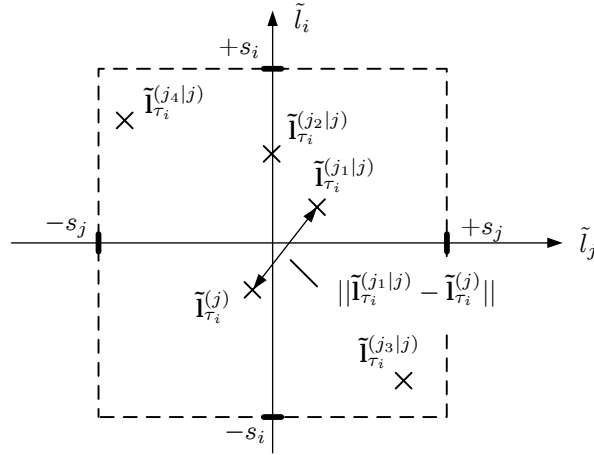


Figure 8.3: Illustration of distance between samples in a 2D-section of the D -dimensional cube.

weight of the sample itself. The statistical weight carries the statistical information for the realisation, whereas the weight measure defines the size of the statistical weight compared to those of neighbouring realisations.

To illustrate the purpose of the weight measure, consider the joint probability density function of \mathbf{L} . In the ideal case the discrete joint probability density function will be approximated in the same manner as figure 8.2c. An illustration which represents an actual realisation better is shown in figure 8.4.

If the sample density in the region of $\mathbf{I}^{(j)}$ and $\mathbf{I}^{(j_1|j)}$ becomes too large, the RR&S algorithm will kill some samples in this region. The most efficient is then to kill samples with small weights as they have negligible influence compared to samples with relatively large weights in the same region. In this way a minimum of samples are used to describe the statistical mass of the region. The weight measure should therefore increase the survival probability more for $\mathbf{I}^{(j_1|j)}$ than for $\mathbf{I}^{(j)}$, as $w^{(j_1|j)}$ is seen in figure 8.4 to be larger than $w^{(j)}$. The weight measure is defined by

$$v_{\tau_i}^{(j)} = 1 + \frac{1}{w_{\tau_i}^{(j)}} \sum_{r=1}^K a_r w_{\tau_i}^{(j_r|j)} \quad , \quad a_1 > a_2 > \dots > a_K > 0 \quad (8.5)$$

where the weights $w_{\tau_i}^{(j_r|j)}$ are associated with the realisation $\tilde{\mathbf{I}}_{\tau_i}^{(j_r|j)}$ in (8.2).

There are now two measures carrying information on the importance of a realisation, namely the

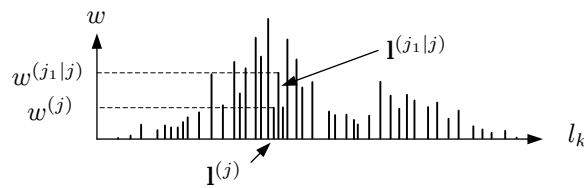


Figure 8.4: Illustration of a realisation of the discrete joint probability density function for the distance variable \mathbf{L} .

distance measure and the weight measure. To obtain one scalar quantity which combines all the information, the distance and weight measure are weighted together into one measure. This measure is denoted the *importance measure* and is an empirical expression suggested by [Pradlwarter and Schuëller, 1999] and is defined by

$$c_{\tau_i}^{(j)} = \frac{d_{\tau_i}^{(j)}}{1 + (\ln(v_{\tau_i}^{(j)}))^{\eta}} \quad (8.6)$$

where η controls how much the weight measure reduces the importance measure. From (8.6) it is seen that samples located in low density areas with relatively large statistical weight, compared to the neighbouring samples, are considered most important. The denominator in (8.6) has a significant influence on the performance of the RR&S algorithm. If the denominator is disregarded and thereby $c_{\tau_i}^{(j)} = d_{\tau_i}^{(j)}$, it will influence the variance adversely.

Now, to specify which realisations are to be splitted and which are to be killed, a survival probability is associated with each realisation. This probability depends on the importance of the sample and is given by

$$p_{\tau_i}^{(j)} = \begin{cases} 1 & \text{if } \tilde{c}_{\tau_i}^{(j)} \geq 1 \\ 1 - P_0(1 - \tilde{c}_{\tau_i}^{(j)}) & \text{if } \tilde{c}_{\tau_i}^{(j)} < 1 \end{cases} \quad (8.7)$$

where $0 < P_0 < 1$ is a constant controlling the probability of unimportant realisations being killed, and $\tilde{c}_{\tau_i}^{(j)}$ is defined as $c_{\tau_i}^{(j)}$ normalised with respect to the mean value of of this quantity among all N realisations

$$\tilde{c}_{\tau_i}^{(j)} = \frac{c_{\tau_i}^{(j)}}{\bar{c}_{\tau_i}}, \quad \bar{c}_{\tau_i} = \frac{1}{N} \sum_{j=1}^N c_{\tau_i}^{(j)} \quad (8.8)$$

Important realisations are then characterised by $\tilde{c}_{\tau_i}^{(j)} \geq 1$, and unimportant by $\tilde{c}_{\tau_i}^{(j)} < 1$. Important realisations are thus the realisations which have the greatest distance to neighbouring realisations as well as the largest weight compared to neighbouring realisations. In order to make the distribution more uniform, it is thus the important realisations that should be splitted.

Before the first evaluation at the time τ_1 the estimate of the joint probability density function will look as figure 8.2b, where all realisations have equal weight. Therefore, at τ_1 only the distance between the realisations have an influence on the importance measure. Thus the realisations in the low density areas will be regarded as important and realisations in the high density area will be regarded as unimportant.

Step 2, Russian Roulette. Russian Roulette is performed according to the realised value of the binary stochastic indicator $I_{R,\tau_i}^{(j)}$ for all unimportant realisations. $I_{R,\tau_i}^{(j)} = 1$ indicates survival, and $I_{R,\tau_i}^{(j)} = 0$ indicates extinction. The probability distribution of $I_{R,\tau_i}^{(j)}$ is given by

$$I_{R,\tau_i}^{(j)} = \begin{cases} P(I_{R,\tau_i}^{(j)} = 0) = 1 - p_{\tau_i}^{(j)} \\ P(I_{R,\tau_i}^{(j)} = 1) = p_{\tau_i}^{(j)} \end{cases} \quad (8.9)$$

To maintain an unbiased estimate all weights are subsequent to the Russian Roulette operation modified by

$$\tilde{W}_{\tau_i}^{(j)} = \frac{I_{R,\tau_i}^{(j)} w_{\tau_i}^{(j)}}{p_{\tau_i}^{(j)}} \quad (8.10)$$

whereby

$$\mathbb{E}[\tilde{W}_{\tau_i}^{(j)}] = w_{\tau_i}^{(j)} \quad (8.11)$$

which is used later to show that the RR&S algorithm produces unbiased estimates.

Step 3, Splitting. To maintain the same number of samples, each killed sample is replaced by a splitting of an important sample. Samples killed by Russian Roulette can be disregarded since their statistical weight are zero after modification by (8.10). Now, the meaning of a splitting is to replace the distance variable $\mathbf{1}_{\tau_i}^{(j)}$ and the state vector $\mathbf{z}_{\tau_i}^{(j)}$ associated with a killed sample with a duplicate of an important sample. To maintain the statistical weight, the weight of the splitted sample, $w_{\tau_i}^{(j)}$, is shared equally between itself and its duplicate. Splitting is always performed in decending order, so that the most important realisations are splitted at first.

In principle an important realisation may be splitted into an arbitrary number of new realisations, but to maintain the same amount of realisations the number of splitted realisations must equal the number of killed realisations. In what follows, important realisations are only splitted into two realisations.

After the splitting procedure the low density areas experience an increase in realisation density, but the distribution of statistical mass is maintained because the weight of the splitted realisation is shared equally between the original realisation and its copy.

After performing splitting and Russian Roulette the set of samples $\{\mathbf{z}_{\tau_i}^{(j)}, w_{\tau_i}^{(j)}\}$ has been modified and is now given by $\{\tilde{\mathbf{z}}_{\tau_i}^{(j)}, \tilde{w}_{\tau_i}^{(j)}\}$. To show that this set still comprise an unbiased representation of the M -dimensional density function $f_{\mathbf{Z}}(\mathbf{x})$ consider the estimator of the distribution function $F_{\mathbf{Z}}(\mathbf{z})$ given by

$$\hat{F}_{\mathbf{Z}}(\mathbf{z}) = \sum_{j=1}^N \tilde{W}_{\tau_i}^{(j)} I_F(\tilde{\mathbf{Z}}_{\tau_i}^{(j)}, \mathbf{z}) \quad (8.12)$$

where $\tilde{\mathbf{Z}}_{\tau_i}^{(j)}, j = 1, \dots, N$ denotes a random sample set of \mathbf{Z} . $\tilde{\mathbf{Z}}_{\tau_i}^{(j)}$ are mutually independent and identical distributed as \mathbf{Z} . The proof of the assertion follows by taking the expectation of (8.12)

$$\mathbb{E}[\hat{F}_{\mathbf{Z}}(\mathbf{z})] = \sum_{j=1}^N \mathbb{E}[\tilde{W}_{\tau_i}^{(j)} I_F(\tilde{\mathbf{Z}}_{\tau_i}^{(j)}, \mathbf{z})] = \quad (8.13)$$

$$\mathbb{E}[\hat{F}_{\mathbf{Z}}(\mathbf{z})] = \sum_{j=1}^N \mathbb{E}[\mathbb{E}[\tilde{W}_{\tau_i}^{(j)} I_F(\hat{\mathbf{Z}}_{\tau_i}^{(j)}, \mathbf{z}) | \tilde{\mathbf{Z}}_{\tau_i}^{(j)}]] = \quad (8.14)$$

$$\mathbb{E}[\hat{F}_{\mathbf{Z}}(\mathbf{z})] = \sum_{j=1}^N w_{\tau_i}^{(j)} \mathbb{E}[\mathbb{E}[I_F(\hat{\mathbf{Z}}_{\tau_i}^{(j)}, \mathbf{z}) | \tilde{\mathbf{Z}}_{\tau_i}^{(j)}]] = \quad (8.15)$$

$$\mathbb{E}[\hat{F}_{\mathbf{Z}}(\mathbf{z})] = \sum_{j=1}^N w_{\tau_i}^{(j)} \mathbb{E}[I_F(\tilde{\mathbf{Z}}_{\tau_i}^{(j)}, \mathbf{z})] = \quad (8.16)$$

$$F_{\mathbf{Z}}(\mathbf{z}) \sum_{j=1}^N w_{\tau_i}^{(j)} = F_{\mathbf{Z}}(\mathbf{z}) \quad (8.17)$$

The latter is seen since $w_{\tau_i}^{(j)} = 1/N$ at the beginning.

Step 4, Normalisation of weights. With the previous steps, the density of realisations has been moved towards a uniform distribution, but in doing so, the statistical mass has been modified in three significant ways. Such modifications calls for a normalisation of the statistical weights of the processes as the sum of the total statistical mass should be unity at all times. The way in which the weights have been modified are firstly, that some important processes have been splitted and in this procedure the weights are splitted as well. Secondly, some unimportant processes have survived the Russian Roulette whereby their weights have been increased by (8.10). Thirdly and most noticeable, some processes have crossed out and subsequently been replaced by splitting an important process.

If no outcrossings has occured in the time interval $t = [0, \tau_i]$, the sum w_t of the weights $w_{\tau_i}^{(j)}$ should be unity as

$$w_t = \sum_{j=1}^N w_{\tau_i}^{(j)} = 1 \quad (8.18)$$

This is illustrated in figure 8.5a where the N processes represents the total statistical mass of 1.

If some processes with a total statistical mass of w_o has crossed out in the time interval $t = [0, \tau_i]$, the sum w_t of the weights $w_{\tau_i}^{(j)}$ should represent the remaining statistical mass which has not crossed out. This is illustrated by figure 8.5b where the N processes represents only the statistical mass which has not crossed out, $w_t = 1 - w_o$.

Therefore, in the general case the weights should be normalised according to

$$\sum_{j=1}^N w_{\tau_i}^{(j)} = 1 - w_o \quad (8.19)$$

Step 5, Step forward. After the normalisation of the weights, the numerical process is continued until τ_{i+1} , where step 1 – 5 are performed again.

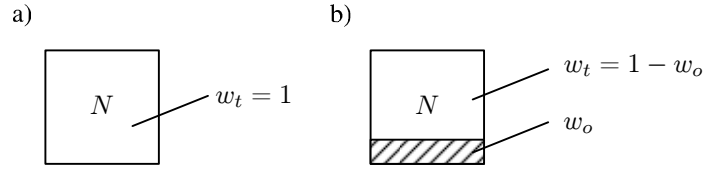


Figure 8.5: a) Illustrates the statistical mass of the N processes in the case where no outcrossings has occurred in the interval $t = [0, \tau_i]$. b) Illustrates the statistical mass of the N processes in the case where some outcrossings with gathered statistical mass of w_o has occurred in the interval $t = [0, \tau_i]$.

This concludes the description of the variance reduction method RR&S. Next, some comments are given on the choice of the distance variable.

8.2 Choice of distance variable

The efficiency of the RR&S algorithm depends highly on which combination of the state vector components is utilised for the distance variable. The distance variable is used to calculate the distance measure (8.2) which again relates to the importance measure through (8.6). The distance variable is thus the main basis for determining the importance measure from which the RR&S algorithm redistributes the realisations. In the following, it is qualitatively assessed what influence the choice of distance variable has for the efficiency of the algorithm. To assess this, temporarily consider the special case where all realisations have the same statistical weight. In this case, the weight measure will not influence the importance measure in (8.6) and the efficiency of the RR&S algorithm solely depends on the choice of distance variable.

To illustrate some undesired effects, three different distance variables are qualitatively described in the following to illustrate what to be aware of when choosing the distance variable. The illustration takes its basis in two simple realisations which both are performing harmonic oscillations but with different amplitudes. The two realisations are shown in figure 8.6. It is seen that realisation B has a larger amplitude than realisation A implying that B is more important than A .

Now, consider three different distance variables for the realisations A and B . The distance variables in question are a two-dimensional distance variable l_1 and two one-dimensional distance variables l_2 and l_3 . More precisely, the distance variables are given by the combinations of the state variables y and \dot{y} given by

- $l_1 = \mathbf{z} = [y, \dot{y}]^T$
- $l_2 = y$
- $l_3 = \frac{1}{2}ky^2 + \frac{1}{2}m\dot{y}^2$

where y is the displacement and \dot{y} is the velocity of the system. Thus, the D -space is two-dimensional for l_1 and one-dimensional for l_2 and l_3 . It is seen that l_1 corresponds to the state vector of the system

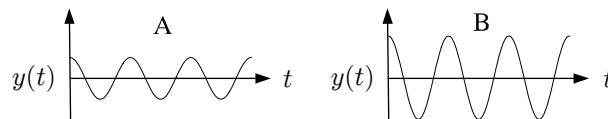


Figure 8.6: Illustration of displacement response A and B .

\mathbf{z} , l_2 corresponds to the displacement of the system and l_3 corresponds to the mechanical energy of the system if k and m are the stiffness and mass of the system, respectively. To illustrate the qualitative difference between the distance variables, consider how the realisations are moving around in their respective D -space. This is illustrated in figure 8.7.

In figure 8.7a the realisations are moving around in the displacement and velocity space given by l_1 . Assuming the realisations are oscillating with an angular frequency of $\omega = 1$, the realisations will orbit clockwise in circles centered at origo. If the two realisations are in phase, the distance between the two realisations at any instant of time will be d_1 whereas the distance between them will be some distance d_2 if there is a phase delay between the two realisations. In the case of harmonic oscillating realisations it is seen that realisations with large oscillations will orbit in circles with large radius. l_1 thus makes a rather clear separation of realisations with large amplitudes and realisations with small amplitudes for any instant of time.

In figure 8.7b the realisations are moving around in only the displacement space. Now, realisation A is oscillating between a_1 and a_2 and realisation B is oscillating between b_1 and b_2 on the y -axis. As the velocity dimension is not included in l_2 it is seen that the realisations are no longer well separated at any instant of time as in the case of l_1 . This can be realised by considering the case where both A and B are located at the same point, e.g. a_1 .

In figure 8.7c the realisations are moving around in the mechanical energy space. As the realisations are performing harmonic oscillations around zero with constant amplitudes, the mechanical energy is constant. The position of realisation A and B is therefore constant in the l_3 space. l_3 thus makes a clear separation of realisations with large amplitudes and realisations with small amplitudes at any instant of time.

From these three examples of distance variables it is seen that there is a qualitative difference in how well the realisations are separated, depending on the choice of distance variable. If the distance variable do not separate the realisations close to failure from those far from failure, the RR&S algorithm will be less efficient. In the simple case of systems oscillating around zero, the mechanical energy seems to provide a clear separation of the realisations as seen in figure 8.7c.

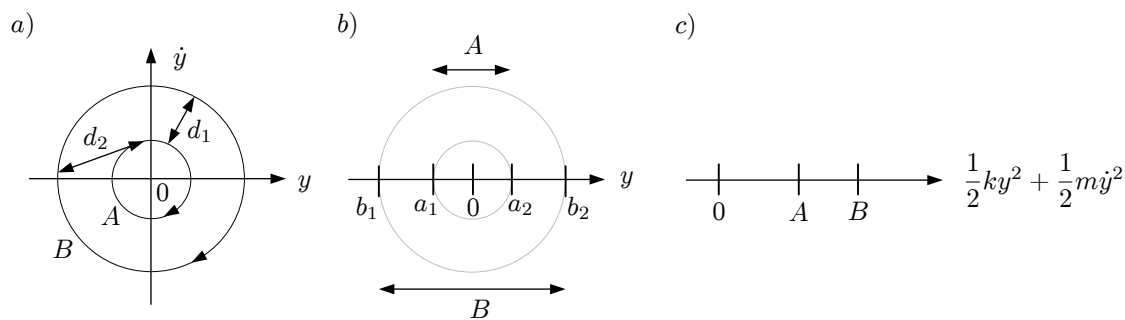


Figure 8.7: a) Illustration of A and B in the velocity and displacement space, l_1 . b) Illustration of realisation A and B in the displacement space, l_2 . c) Illustration of realisation A and B in the mechanical energy space, l_3 .

8.3 Implementaion on two dof shear frame exposed to earthquake

In this section the RR&S algorithm is implemented on the two dof shear frame described in chapter 4. The two dof shear frame is exposed to a horisontal earthquake acceleration process modelled by a broken line process, see section 4.2. Firstly, some comments and assumptions are made on the distance variable and next, the obtained results for the simulation of the first passage time distribution function $F_T(t)$ are presented and commented.

In appendix I.5 a parameter analysis of the RR&S parameters have been performed to investigate the influence of the parameters.

8.3.1 Distance variable

Prior to implementation of the RR&S algorithm on the shear frame it is necessary to choose a distance variable. In section 8.2 it is argued that the mechanical energy may be a good choice of distance variable for systems which performs harmonic oscillations around zero. From figure 8.8a it is seen that the response of the storeys are oscillating around zero, but with varying amplitude. Despite the varying amplitude, the mechanical energy is chosen as distance variable. By comparison of figure 8.8a and 8.8b it is seen that high values of the mechanical energy, denoted E_m , indicates large displacements and thereby also high probability of failure. As only relative displacements are of importance when considering failure of a system, the mechanical energy is calculated from the relative displacements of the system.

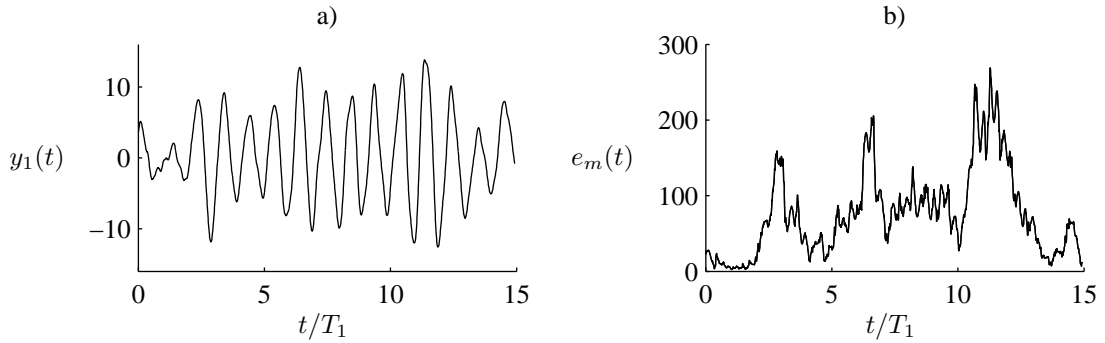


Figure 8.8: a) Realisation of the relative displacement response Y_1 . b) Realisation of the mechanical energy of the two storey frame E_m .

The fuzziness of the mechanical energy is due to the equivalent white noise process used as ground surface acceleration process, which makes the velocity process non-differentiable. e_m could be smoothed by a moving average filter but no significant difference in the performance of the RR&S algorithm has been noticed if such a filtering is performed.

In the following, the mechanical energy is utilised as distance variable whereby the D -dimensional distance variable becomes a scalar $l = e_m$. Now, as the distance variable only has one entry, there is no need to perform the normalisation by (8.1) whereby $\tilde{l} = l$ is used. e_m and thereby \tilde{l} is given by

$$\tilde{l}(t) = e_m(t) = \frac{1}{2} \mathbf{y}(t)^T \mathbf{K} \mathbf{y}(t) + \frac{1}{2} \dot{\mathbf{y}}(t)^T \mathbf{M} \dot{\mathbf{y}}(t) \quad (8.20)$$

where $\mathbf{y}(t)$ is the relative displacement vector of the storeys given by $\mathbf{y}^T(t) = [y_1(t) \ y_2(t)]$ and \mathbf{K} and

\mathbf{M} is the related stiffness and mass matrix, respectively, from section 4. $y_1(t)$ is relative to the ground surface displacement and $y_2(t)$ is relative to $y_1(t)$.

8.3.2 Results

In this section the results obtained when using the RR&S algorithm to simulate first passage times for the two storey frame is presented. The purpose of the results is to estimate the efficiency of the RR&S algorithm. The efficiency \mathcal{P} is measured as the ratio between the computational time for CMC and RR&S simulation. The computational time for simulating the first passage probability distribution function $F_T(t)$ for $t = 600$ s is denoted $F_T(600)$.

Approach

In the following the computational savings are estimated for the barrier levels $\alpha = [4, 5, 6]$. The number of realisations used in the CMC and RR&S simulation, denoted N^{CMC} and $N^{\text{RR\&S}}$, respectively, is adjusted so the estimate of $F_T(600)$, denoted $\hat{F}_T(600)$, has a coefficient of variation (COV) of approximately $COV = 15\%$. The COV will be estimated based on 50 independent trials. Then, the COV is calculated by

$$COV = \frac{\sigma_{\hat{F}_T(600)}}{\mu_{\hat{F}_T(600)}} \quad (8.21)$$

where $\sigma_{\hat{F}_T(600)}$ and $\mu_{\hat{F}_T(600)}$ are the standard deviation and mean value of $\hat{F}_T(600)$, respectively, and given by

$$\mu_{\hat{F}_T(600)} = \frac{1}{50} \sum_{i=1}^{50} \hat{F}_T(600)^i \quad (8.22)$$

$$\sigma_{\hat{F}_T(600)} = \sqrt{\frac{1}{50} \sum_{i=1}^{50} (\hat{F}_T(600)^i - \mu_{\hat{F}_T(600)})^2} \quad (8.23)$$

The standard deviation σ of an estimated probability μ based on N realisations is generally calculated by [Ayyub and McCuen, 1997]

$$\sigma = \sqrt{\frac{\mu(1-\mu)}{N}} \quad (8.24)$$

Substituting $\sigma = \sigma_{\hat{F}_T(600)}$, $\mu = \mu_{\hat{F}_T(600)}$ and $N = N^{\text{CMC}}$, (8.24) is used to determine the number of realisations N^{CMC} needed in a CMC simulation to obtain the same $COV \approx 15\%$. By inserting $\sigma_{\hat{F}_T(600)}$ and $\mu_{\hat{F}_T(600)}$ into (8.24) and subsequently rearranging, N^{CMC} can be determined by

$$\sigma_{\hat{F}_T(600)} = \sqrt{\frac{\mu_{\hat{F}_T(600)}(1-\mu_{\hat{F}_T(600)})}{N^{\text{CMC}}}} \Rightarrow N^{\text{CMC}} = \frac{\mu_{\hat{F}_T(600)}(1-\mu_{\hat{F}_T(600)})}{\sigma_{\hat{F}_T(600)}^2} \quad (8.25)$$

The computational time in an RR&S and CMC simulation are denoted $T_{\text{CPU}}^{\text{RR\&S}}$ and $T_{\text{CPU}}^{\text{CMC}}$, respectively. $T_{\text{CPU}}^{\text{RR\&S}}$ is obtained by measuring it directly during the simulation. $T_{\text{CPU}}^{\text{CMC}}$ is obtained by linear extrapolation of the computational time needed to perform a CMC simulation using 10000 realisations. The reference computational time for 10000 realisations is denoted $T_{\text{CPU}}^{\text{CMC}}(10000)$ and is measured to

$$T_{\text{CPU}}^{\text{CMC}}(10000) = 77s \quad (8.26)$$

Results

The results obtained by the approach described above is given in table 8.1. Second column in table 8.1 shows the efficiency \mathcal{P} for the barrier levels $\alpha = [4, 5, 6]$. \mathcal{P} is defined as

$$\mathcal{P} = \frac{T_{\text{CPU}}^{\text{CMC}}}{T_{\text{CPU}}^{\text{RR\&S}}} \quad (8.27)$$

It is seen that the efficiency of the method increases dramatically as the barrier α increases. At the barrier level $\alpha = 4$ the efficiency \mathcal{P} is seen to be less than one, implying that the RR&S algorithm is more costly in computational time than CMC simulation. This is due to the computational cost related to the RR&S algorithm. At the barrier level $\alpha = 6$ the efficiency has been calculated to 418, implying a computational cost reduction of more than 99%.

The third, fourth and fifth column of table 8.1 shows the mean value, standard deviation and COV calculated by the 50 estimates of $F_T(600)$ by RR&S simulation. The number of realisations N^{CMC} needed for a CMC simulation to produce the COV given in the fifth column of table 8.1 is estimated by inserting values of $\mu_{\hat{F}_T(600)}$ and $\sigma_{\hat{F}_T(600)}$ from table 8.1 into (8.25).

α	\mathcal{P}	$\mu_{\hat{F}_T(600)}$	$\sigma_{\hat{F}_T(600)}$	COV	$N^{\text{RR\&S}}$	N^{CMC}
4	0.6	$2.34 \cdot 10^{-2}$	$33.4 \cdot 10^{-2}$	14.3%	1500	$2.5 \cdot 10^3$
5	12	$3.77 \cdot 10^{-4}$	$58.7 \cdot 10^{-4}$	15.6%	3000	$10.9 \cdot 10^4$
6	418	$1.99 \cdot 10^{-6}$	$28.1 \cdot 10^{-6}$	14.1%	10000	$25.2 \cdot 10^6$

Table 8.1: Results for RR&S for two storey frame.

In figure 8.9 estimates of $F_T(t)$ are shown for barrier levels $\alpha = [4, 5, 6]$. The estimates have been produced by both RR&S and CMC simulations using values of $N^{\text{RR\&S}}$ and N^{CMC} as given in table 8.1. CMC simulation is only performed for $\alpha = [4, 5]$ due to extensive simulation time for $\alpha = 6$. As seen in table 8.1 a CMC simulation for $\alpha = 6$ would require $N^{\text{CMC}} = 25.2 \cdot 10^6$ realisations to produce a $COV \approx 15\%$.

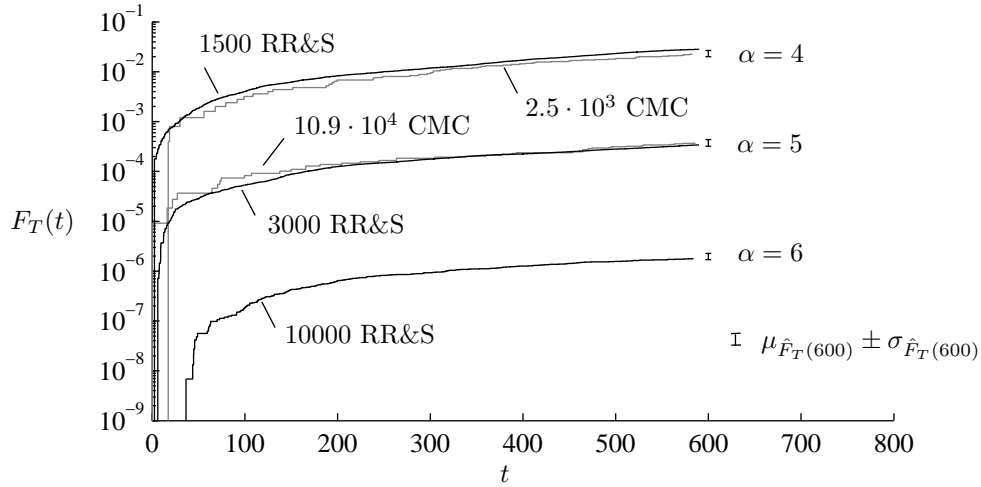


Figure 8.9: Estimates of $F_T(t)$ produced by RR&S and CMC simulation.

The RR&S parameters used to produce the estimates of $F_T(t)$ in figure 8.9 are given in table 8.2.

N	α	$\Delta\tau/T_1$	η	P_0	w_{min}	K	T [s]
1500	4	0.1	0.8	0.5	$1 \cdot 10^{-5}$	10	600
3000	5	0.1	0.8	0.5	$1 \cdot 10^{-7}$	10	600
10000	6	0.1	0.8	0.5	$1 \cdot 10^{-9}$	10	600

Table 8.2: Settings for the RR&S simulations in figure 8.9.

8.3.3 Conclusion

The efficiency of the RR&S algorithm is tested for simulating first passage times for the two dof shear frame presented in chapter 4 exposed to horizontal earthquake. The efficiency \mathcal{P} is measured in terms of savings in the computational time compared to CMC simulation, i.e. $\mathcal{P} = T_{CPU}^{CMC}/T_{CPU}^{RR\&S}$, where T_{CPU}^{CMC} and $T_{CPU}^{RR\&S}$ is the computational time for CMC and RR&S simulation, respectively.

The results show that the efficiency \mathcal{P} depends on the barrier level α . As the barrier level increases, so does the efficiency \mathcal{P} of the RR&S algorithm. The efficiency \mathcal{P} for the barrier levels $\alpha = [4, 5, 6]$ is calculated to $\mathcal{P} = [0.6, 12, 418]$. The highest efficiency $\mathcal{P} = 418$ corresponds to a computational saving of more than 99%.

Generally, the efficiency of the RR&S algorithm seems to depend strongly on the choice of distance variable and implementation of the RR&S algorithm on more complex structures therefore depends on locating such an efficient distance variable.

8.4 Implementation on three dof wind turbine

In the following section the results from the implementation of the RR&S algorithm on the simple wind turbine model described in section 5 are presented. The RR&S algorithm is implemented on the simple turbine to assess the ability of the RR&S algorithm to estimate first passage times for a system which resembles a wind turbine and is exposed to wind load consisting of turbulence and a mean wind velocity. A mean wind velocity of 15 m/s is used and turbulence is generated by the state

space turbulence model described in appendix B.3. As shown in figure 5.4 the turbulence is generated in a number of points on the periphery of the rotor plane. Four grid points have been used in the following and an interpolation of the turbulence is performed as indicated by (5.28).

Now, as it is only possible to aim for failure of one dof at the time a dof has to be chosen. In the following it is chosen to test the RR&S algorithm for simulating first passage times of the tower top displacement q_1 which is illustrated in figure 8.10. Furthermore, only failure of the tower is considered and only the positive barrier is checked.

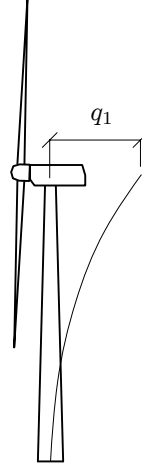


Figure 8.10: Illustration of tower top displacement q_1 .

8.4.1 Barrier

The one sided barrier $q_{c,1}$ which defines failure for the tower is given by (6.7) using μ_{q_1} and σ_{q_1} where μ_{q_1} and σ_{q_1} are the mean value and the stationary standard deviation of the displacement response of q_1 . The values of μ_{q_1} and σ_{q_1} are determined by an ergodic sampling and are given in table 5.1.

8.4.2 Distance variable

To locate an efficient distance variable to use for systems exposed to wind load a number of different distance variables are investigated. The investigation is performed on the 2-dof shear frame exposed to loads which imitates the characteristics of wind load. These characteristics are turbulence and a static wind load. The loads used to imitate these characteristics in the investigation on the 2-dof shear frame is horizontal earthquake, a static load and a carrier wave. The efficiency of the different distance variables are measured by their ability to estimate the first passage time distribution function for the 2-dof shear frame. Out of the seven investigated candidates, candidate 1 turned out as the most efficient and is therefore used in the following investigation of the three dof wind turbine. The investigation of the distance variables is performed in appendix I.2.

Candidate 1 from appendix I.2 corresponds to the mechanical energy calculated after subtracting the static displacement μ_{q_1} . The distance variable is then given by

$$\tilde{l}_1(t) = e_m(t) = \frac{1}{2}k_0(q_1(t) - \mu_{q_1})^2 + \frac{1}{2}m_0\dot{q}_1(t)^2 \quad (8.28)$$

where k_0 and m_0 is the stiffness and mass of the tower given by (5.2) and (5.2), respectively.

8.4.3 Results

In the following the results for estimating the first passage time distribution function $F_T(t)$ are presented. $F_T(t)$ is estimated by CMC and RR&S simulation and a qualitative comparison of the results achieved by the two methods are given in figure 8.11. The parameter values used for the RR&S algorithm to produce the results given in figure 8.11 are shown in table 8.3.

α	$\Delta\tau/T_t$	η	P_0	w_{min}	K	N	T [s]
3	0.2	0.8	0.5	10^{-4}	10	500	600
4	0.2	0.8	0.5	10^{-4}	10	500	600
5	0.2	0.8	0.5	10^{-6}	10	500	600
6	0.2	0.8	0.5	10^{-8}	10	500	600
7	0.2	0.8	0.5	10^{-10}	10	500	600

Table 8.3: Parameter settings for RR&S algorithm for producing results in figure 8.11.

CMC simulation is only used to estimate $F_T(t)$ for the barrier level $\alpha = [3, 4]$ whereas RR&S simulation is used to estimate $F_T(t)$ for the barrier levels $\alpha = [3, 4, 5, 6, 7]$. It is seen in figure 8.11 that CMC and RR&S simulation gives similar results for $\alpha = [3, 4]$ which indicates that RR&S simulation converge toward the same result as CMC simulation. Figure 8.11 shows that the RR&S algorithm is able to estimate failure probabilities far below $1/N$ also for the three dof wind turbine.

The conclusion from the implementation of the RR&S algorithm onto the simple wind turbine model is that clear improvements are achieved when using RR&S simulation for estimating failure probabilities below $1/N$ compared to CMC simulation. This is seen for the barrier levels $\alpha = [5, 6, 7]$ in figure 8.11. Next, the RR&S algorithm is implemented onto the FAST code.

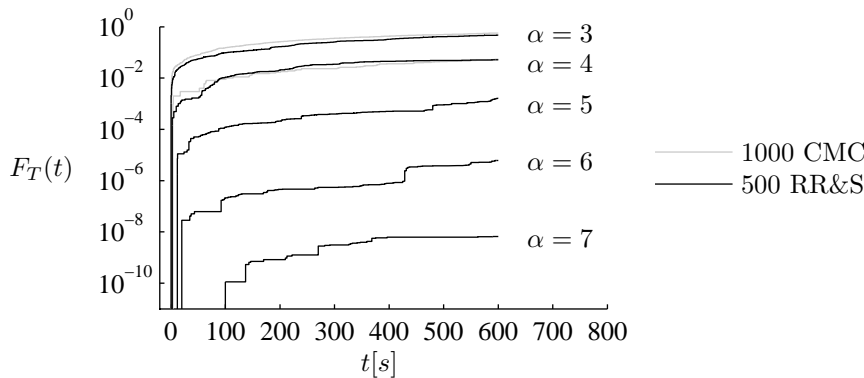


Figure 8.11: Comparison of realisations of $F_T(t)$ produced by RR&S and CMC simulation.

8.5 Implementation on 5MW reference wind turbine

In the following section the results for simulation of the first passage time distribution function $F_T(t)$ for the 5MW reference wind turbine modelled by FAST are presented. The 5MW reference wind turbine is described in appendix C. A mean wind velocity of 15 m/s and turbulence generated by the state space turbulence model described in appendix B.3 is used in the simulation of the 5MW reference wind turbine.

Now, in the same way as described in section 8.4 for the simple three dof wind turbine it is only possible to aim for failure of one dof at the time. As for the simple three dof wind turbine it is chosen to test the RR&S algorithm for simulating first passage times of the tower top displacement y_t which is illustrated in figure 8.12. Again, only failure of the tower is considered.

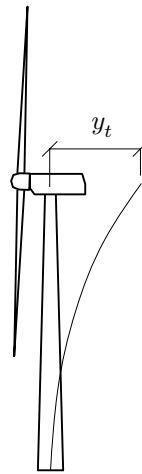


Figure 8.12: Illustration of tower top displacement y_t .

The distance variable used for the RR&S simulation is candidate 1 from section I.2.2 which corresponds to the mechanical energy calculated after subtracting the static displacement. Given that the used distance variable is candidate 1, it will be shown that the RR&S algorithm will only provide improved estimates of $F_T(t)$ if the control system in FAST is disabled. Therefore two different cases are considered for estimating $F_T(t)$. The first case is where the control system is disabled and the second case is where the control system is enabled.

The barrier is defined by (6.7) using μ_{y_t} and σ_{y_t} where μ_{y_t} and σ_{y_t} depends on whether the control system is disabled or enabled. Next, it is shown how the mechanical energy of the tower is calculated and then, the estimates for the first passage time probability distribution function $F_T(t)$ are presented.

8.5.1 Distance variable

The distance measure used for the 5MW reference wind turbine is the same as used for the three dof wind turbine, i.e. candidate 1 from appendix I.2 which corresponds to the mechanical energy of the tower calculated after subtracting the static displacement of the tower μ_{y_t} . FAST uses two modal coordinates q_7 and q_8 to describe the fore-aft displacement of the tower top y_t , see figure A.1. Now, as both first and second eigen mode is normalised to displacement 1 at the tower top, y_t corresponds directly to the sum of the modal coordinates q_7 and q_8 . The modal coordinates and eigen modes for the 1st and 2nd eigen mode of the tower is shown in figure 8.13.

Now, the mechanical energy of the tower calculated as indicated by candidate 1 where the static

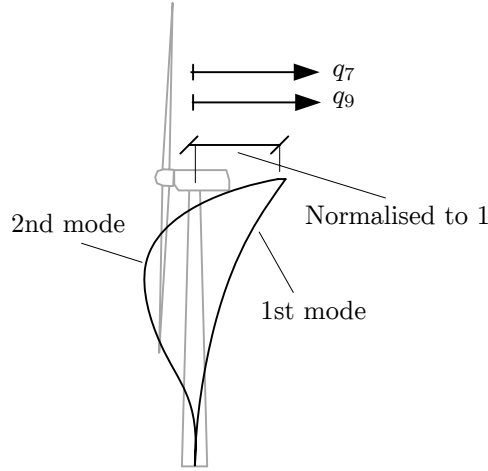


Figure 8.13: Illustration of 1st and 2nd eigen mode with corresponding modal coordinates q_7 and q_8 .

contribution is subtracted, is generally calculated by

$$\tilde{l}_1(t) = e_m(t) = \frac{1}{2}(\mathbf{q}(t) - \mathbf{q}_s)^T(t)\mathbf{K}(\mathbf{q}(t) - \mathbf{q}_s) + \frac{1}{2}\dot{\mathbf{q}}^T(t)\mathbf{M}\dot{\mathbf{q}}(t) \quad (8.29)$$

where $\mathbf{q}(t) = [q_7, q_8]^T$ is the displacement vector, $\mathbf{q}_s = [q_{s,7}, q_{s,8}]^T$ is the static displacement vector where $q_{s,7}$ and $q_{s,8}$ is the static displacement of $q_7(t)$ and $q_8(t)$, respectively. $\dot{\mathbf{q}} = [\dot{q}_7, \dot{q}_8]^T$ is the velocity vector, \mathbf{K} is the modal stiffness matrix and \mathbf{M} is the modal mass matrix. The stiffness and mass matrix which FAST calculates are given by

$$\mathbf{K} = \begin{bmatrix} 1.91 & 2.91 \\ 2.91 & 10244 \end{bmatrix} \cdot 10^6 \text{ [N/m]} \quad , \quad \mathbf{M} = \begin{bmatrix} 4.0 & 0 \\ 0 & 275 \end{bmatrix} \cdot 10^5 \text{ [kg]} \quad (8.30)$$

It is seen that \mathbf{K} includes cross terms which indicates that q_7 and q_8 are not modal coordinates, since \mathbf{K} and \mathbf{M} decouples in the case of a modal description. The cross terms arise due to the approximation of the mode shapes by a 6th order polynomial, whereby the orthogonality condition of the modeshapes is not totally fulfilled. FAST does not calculate the cross terms for \mathbf{M} which is the reason why the mass matrix is shown as decoupled.

Now, concerning the calculation of the mechanical energy of the tower, it will be argued that a good approximation of the mechanical energy is given by

$$\tilde{l}_1(t) = e_m(t) = \frac{1}{2}(q_7(t) - q_{s,7}(t))^2 K_{11} + \frac{1}{2}\dot{q}_7(t)^2 M_{11} \quad (8.31)$$

whereby the contribution arising from the cross terms in \mathbf{K} and mode 2 is disregarded. The approximation holds due to a difference in magnitude of q_7 and q_8 of approximately an order of 5. This difference of magnitude is seen in figure 8.14 which indicates that the response of y_t is carried by the first mode.

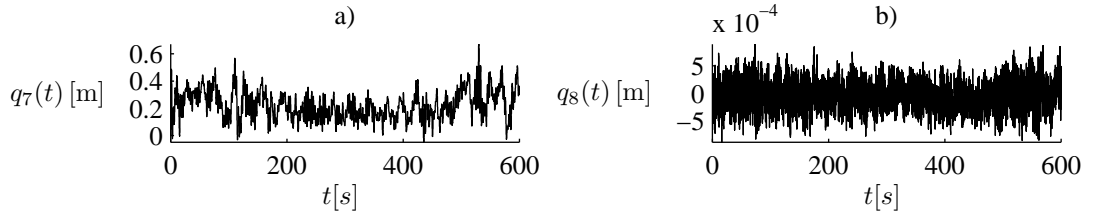


Figure 8.14: a) Realisation of $q_7(t)$. b) Realisation of $q_8(t)$.

In the calculation of the distance measure, the distance variable given by (8.31) is therefore used. In the following (8.31) is used for estimating $F_T(t)$ in the case where the control system is firstly disabled and then enabled.

8.5.2 Disabled control system

In the following the efficiency of RR&S simulation using (8.31) as distance variable is compared with CMC simulation. The control system is disabled and the rotor speed is held constant at approximately 12.1 rpm. Due to the negligible contribution from mode 2 to the displacement, no difference will be made between the response of the tower top $y_t(t)$ and the response of mode 1 $q_7(t)$. The barrier for failure $q_{7,c}$ is calculated by (6.7) using μ_{q_7} and σ_{q_7} where μ_{q_7} and σ_{q_7} are calculated by an ergodic sampling to

$$\mu_{q_7} = 0.225 \text{ m} \quad , \quad \sigma_{q_7} = 0.131 \text{ m} \quad (8.32)$$

The realisation from which μ_{q_7} and σ_{q_7} is determined is shown in figure 8.15 where T_t is the eigenperiod of the tower given by (I.3). A transient phase of 50s is used to damp out the initial conditions, so a stationary response is obtained for the ergodic sampling.

The distance variable is now calculated by (8.31) using $q_{s,7} = \mu_{q_7}$. The results obtained for simulating the first passage time distribution function $F_T(t)$ using CMC and RR&S simulation are shown in figure 8.16. The parameters used for the RR&S simulation is given in table 8.4.

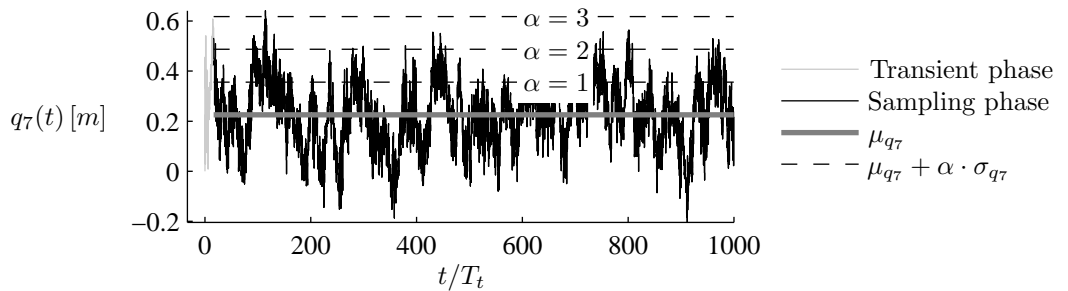


Figure 8.15: Realisation of $q_7(t)$ with control system disabled and constant rotor speed of 12.1 rpm.

α	$\Delta\tau$ [s]	η	P_0	w_{min}	K	N	T [s]
[2, 3]	1.0	0.8	0.5	$1 \cdot 10^{-3}$	10	100	100
4	1.0	0.8	0.5	$5 \cdot 10^{-6}$	10	[100,500]	100

Table 8.4: Parameter settings for RR&S algorithm for results in figure 8.16.

It is seen in figure 8.16 that CMC and RR&S simulation produce comparable results for the barrier levels $\alpha = [2, 3]$. As only one estimate of $F_T(t)$ is produced with CMC and RR&S simulation for each barrier level, the variance is unknown. The number of outcrossings for each estimate of $F_T(t)$ are shown in the figure. Comparison of these numbers shows that the RR&S simulation produce more outcrossings than the CMC simulation for all the barrier levels. For the barrier level $\alpha = 4$ the CMC simulation using 100 time series estimated the failure probability within 100s to 0. RR&S simulation was performed for the barrier level $\alpha = 4$ using both 100 and 500 time series. The RR&S simulation estimated the failure probability within 100s to around 10^{-3} and 10^{-4} using 100 and 500 time series, respectively.

The conclusion is that RR&S simulation seems to provide improved estimates for $F_T(t)$ when simulating failure probabilities below $1/N$ and the control system is disabled.

8.5.3 Enabled control system

In the following the efficiency of RR&S simulation using (8.31) as distance variable is compared with CMC simulation. The control system is enabled and the rotor speed is therefore no longer constant. Again, due to the negligible contribution from mode 2 to the displacement, no difference will be made between the response of the tower top $y_t(t)$ and the response of mode 1 $q_7(t)$. The barrier for failure $q_{c,7}$ is calculated by (6.7) using μ_{q_7} and σ_{q_7} where μ_{q_7} and σ_{q_7} are calculated by an ergodic sampling to

$$\mu_{q_7} = 0.219 \text{ m} \quad , \quad \sigma_{q_7} = 0.100 \text{ m} \quad (8.33)$$

The realisation from which μ_{q_7} and σ_{q_7} is determined is shown in figure 8.17 where T_t is the eigenperiod of the tower given by (I.3). A transient phase of 50s is used to damp out the initial conditions, so a stationary response is obtained for the ergodic sampling.

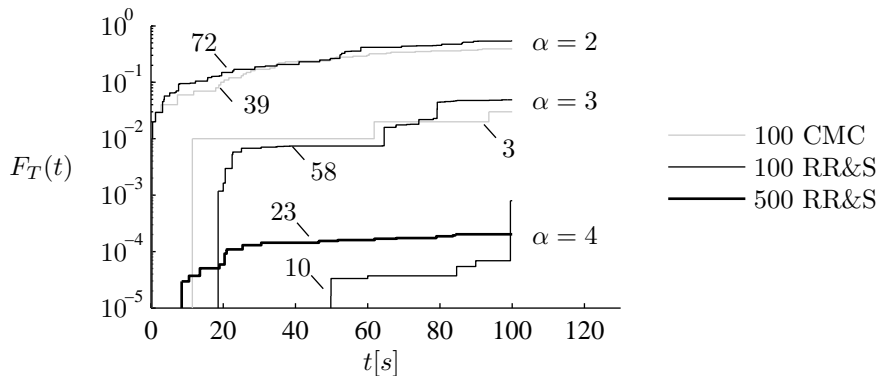


Figure 8.16: Comparison of estimates of $F_T(t)$ produced by RR&S and CMC simulation. RR&S parameters are given in table 8.4. Numbers on plot indicates the achieved number of outcrossings.

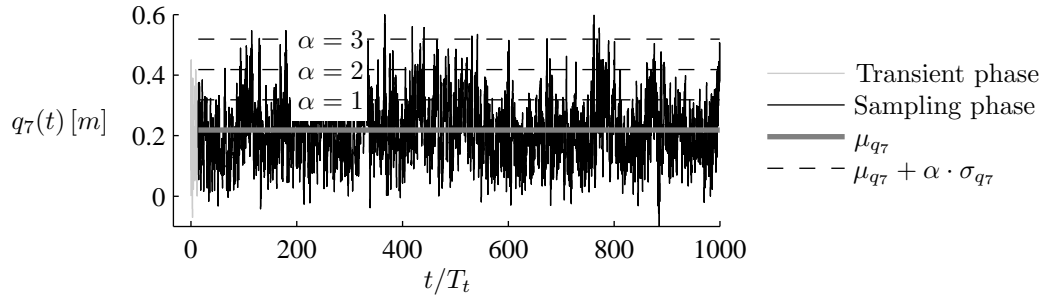


Figure 8.17: Realisation of $q_7(t)$ with mean value and barrier levels.

The distance variable is now calculated by (8.31) using $q_{s,7} = \mu_{q_7}$. The results obtained for simulating the first passage time distribution function $F_T(t)$ using CMC and RR&S simulation is shown in figure 8.18. The parameters used for the RR&S simulation is given in table 8.5.

α	$\Delta\tau$ [s]	η	P_0	w_{min}	K	N	T [s]
[2, 3, 4]	1.0	0.8	0.5	$1 \cdot 10^{-6}$	10	100	100

Table 8.5: Parameter settings for RR&S algorithm for results in figure 8.18.

It is seen in figure 8.18 that CMC and RR&S simulation produce comparable results for the barrier levels $\alpha = [2, 3]$. As only one realisation of $F_T(t)$ is produced with CMC and RR&S simulation for each barrier level, the variance of the estimates of $F_T(t)$ is unknown. The number of outcrossings for each estimate of $F_T(t)$ are shown in the figure. Comparison of these numbers show that the RR&S simulation still produce more outcrossings than the CMC simulation for the barrier levels $\alpha = [2, 3]$. For $\alpha = 4$, one outcrossing was achieved by CMC simulation whereas the RR&S simulation did not produce any outcrossings.

The conclusion is that RR&S simulation does not seem to provide improved estimates for $F_T(t)$ when simulating failure probabilities below $1/N$ and the control system is enabled. This implies that there is a qualitative difference in the efficiency of the mechanical energy as a distance variable depending on whether or not the control system is enabled or disabled.

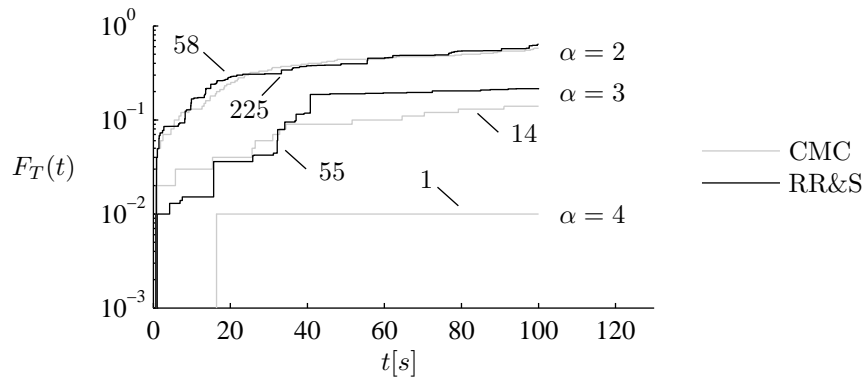


Figure 8.18: Comparison of realisations of $F_T(t)$ produced by RR&S and CMC simulation. RR&S parameters are given in table 8.5. Numbers on plot indicates the achieved number of outcrossings.

8.5.4 Conclusion for RR&S algorithm on wind turbine

The RR&S algorithm was implemented on the FAST code for estimating first passage times of the tower displacement response. Results were produced for the case where the control system was both disabled and enabled. In either case, no conclusion was made on whether the RR&S algorithm improved the estimate of $F_T(t)$ for failure probabilities larger than $1/N$. When the control system was enabled, no improvements were seen for simulating failure probabilities below $1/N$.

When the control system was disabled clear improvements of the estimate of $F_T(t)$ was seen when simulating failure probabilities below $1/N$. Failure probabilities around $5 \cdot 10^{-5}$ was estimated using both 100 and 500 time series. However, the variance of the estimates was not investigated.

In order to produce improvements of $F_T(t)$ when the control system is enabled, more investigations are necessary to determine an efficient distance variable. It is suggested that such a distance variable includes information on the mechanical energy of the system, but also the state of the control system. In this way it may be possible to locate the realisations for which the control system is not able to pitch the blades fast enough to avoid failure.

Finally, it is suggested to investigate the efficiency of RR&S simulation compared to CMC simulation more thoroughly, as the above sections only give a qualitative indication of the efficiency.

8.6 Conclusion

The RR&S algorithm has been tested for estimating first passage times for the five different systems

- a one dof non-linear oscillator
- a two dof shear frame - earthquake exposed
- a two dof shear frame - earthquake, static load & carrier wave
- a three dof three dof wind turbine
- a 24 dof wind turbine modelled in FAST

The 1-dof non-linear oscillator was used for verifying the implementation of the method by comparing the results with results achieved by [Pradlwarter and Schuëller, 1999].

The overall conclusion is that the efficiency of the RR&S algorithm depends highly on locating an efficient distance variable by which it is possible to separate the processes according to their closeness to failure. In section 8.2 it was argued that the mechanical energy seems to provide a reasonable choice of distance variable for separating the realisations according to their closeness to failure.

For the two dof shear frame exposed to earthquake, the mechanical energy turned out to be an efficient choice of distance variable. By use of the mechanical energy, computational savings of more than 99% has been achieved.

For the two dof shear frame exposed to earthquake, static load and a carrier wave, seven different distance variable candidates were suggested to test which one provided the best results for loadings consisting of noise, static load and a carrier wave. The best distance variable turned out to be candidate 1 which was the mechanical energy calculated by subtracting the static displacement. Candidate 1 was therefore the choice for testing the RR&S algorithm on the simple three dof wind turbine.

For the simple three dof wind turbine only qualitative results for the efficiency were produced and the computational saving is therefore unknown. However, RR&S simulation was used to estimate failure probabilities around 10^{-9} using 500 time series which is far below $1/N$.

As for the simple three dof wind turbine only qualitative results were produced for $F_T(t)$ for the 24-dof turbine modelled by FAST. Two different cases were investigated. In the first case the control system was disabled and in the second case it was enabled. In the case where the control system was disabled, failure probabilities around $5 \cdot 10^{-5}$ was estimated for the barrier level $\alpha = 4$ using both 100 and 500 time series. In the case where the control system was enabled, no estimates of $F_T(t)$ were achieved for $\alpha = 4$ which indicates that using the mechanical energy as distance variable is less efficient when the control system is enabled. In order to make the RR&S algorithm efficient for simulating low probabilities for wind turbines, it therefore seems necessary to refine the distance variable. A refinement of the distance variable might be concerned with including information regarding the state of the control system and the load history into the distance variable.

Chapter 9

RESTART

The RESTART algorithm is a so-called accelerated simulation technique that allows evaluation of low probability events. The RESTART method was presented in 1991 [Villén-Altamirano and Villén-Altamirano, 1991] in a one-threshold version and in 1994 it was enhanced to a multiple-threshold version [Villén-Altamirano et al., 1994]. Since then the method has been applied to different applications regarding telecommunication networks and large computing systems. In [Villén-Altamirano et al., 1994] an example of the performance of an ATM multiplexer is described. An estimate of the queue length distribution is calculated using RESTART. In [Villén-Altamirano, 1997] the unreliability of a large computing system with multiple processors and storage disk is determined. The probability of multiple processors of storage disks failing leading to a total failure is presented. In [Villén-Altamirano and Villén-Altamirano, 2006] the RESTART algorithm is used to simulate the queue length distribution of a two node tandem network. None of the articles actually describe the parameters used in the RESTART simulations but states that the method is fitted by running trial simulations that provide an estimate of the optimal parameters. This means that a reproduction of the results might be difficult.

Of the several articles published on the RESTART method all describe use on Markovian systems whereas applications on non-Markovian systems are not available. In [Villén-Altamirano and Villén-Altamirano, 2002], though, it is stated that the estimate of the probability of failure is also unbiased for non-Markovian systems. Further study will have to be performed to clarify assumptions regarding the use on non-Markovian systems.

In the following a general description of the method is firstly given after which a reproduction of the results for the two node tandem network is sought.

9.1 Description of the method

The basics of the RESTART method is to define a number of thresholds where the state vector is splitted and multiple simulations are performed. This leads to a greater confidence and less computational effort in estimation of low probability events because a lower number of simulations are required compared to CMC simulation.

The RESTART method relies on definition of a so-called *importance function* - a non-negative scalar process $\{E(t), t \in [0, T]\}$ for which multiple thresholds e_i describing the importance of a given state of the system are defined. The thresholds are chosen so that thresholds $e_1 \dots e_M$ corresponds to increasing values of the importance function $E(t)$.

The main principle of the method is shown in figure 9.1. When the process upcrosses a threshold e_i the state vector is splitted on R_i identical processes. This means that the weight of each realisation should be modified accordingly. The weight of each new realisation w_{new} can be written as $w_{new} = w_{old}/R_i$, where w_{old} is the weight before splitting. If the R_i new realisations are independent the probability of upcrossing the next threshold is simply increased by R_i .

For a CMC simulation using N realisations the weight of each realisation $w_i = 1/N$ is constant and the probability of failure P_f can be written as a sum of the weights of the N_{out} ourcrossed realisations

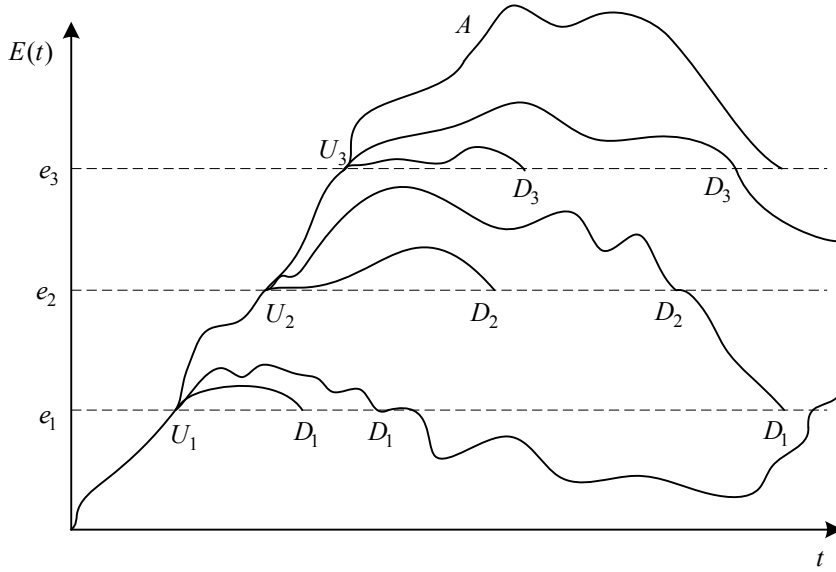


Figure 9.1: Realisations of the importance process showing events in the RESTART method.

$$P_f = \sum_{i=1}^{N_{out}} w_i \quad (9.1)$$

The same applies for the RESTART method using adjusted weights w_i . The weights are adjusted by the number of splittings at each threshold. Hence, the weight $w_i^{(M)}$ of a realisation over M thresholds $e_1 \dots e_M$ is

$$w_i^{(M)} = \frac{1}{N \prod_{i=1}^M R_i} \quad (9.2)$$

The probability of failure for a RESTART simulation using $R_1 \dots R_M$ splittings at M thresholds can be written from (9.2) and (9.1)

$$P_f = \frac{1}{N} \sum_{i=1}^{N_{out}} \frac{1}{\prod_{i=1}^M R_i} \quad (9.3)$$

where N should be interpreted as the number of simulations performed in the interval $[t_0, T]$ - the same interval as for the CMC simulation, i.e. the number of retrials at each threshold does not influence N .

Implementing the method requires definition of events where realisations are splitted and killed. The events of transition from $E < e_i$ to $E \geq e_i$ are defined as events of upcrossings U_i and transitions from $E \geq e_i$ to $E < e_i$ are defined as events of downcrossings D_i . The following procedure is followed when implementing the RESTART method.

- When an event U_i occurs the system state is saved.
- When an event D_i occurs the system state at U_i is restored and the interval U_i to D_i is repeated R_i times.
- When the system state U_i has been restored R_i times, retrial number R_M continues even if crossing down under the threshold e_i and continues until another event U_i occurs or until $t = T$.
- During a retrial of threshold e_i an event U_{i+1} may occur and R_{i+1} retrials of level $i + 1$ is made before the retrial of level i is continued. The simulation of that trial including further retrials of higher levels are continued until an event D_i occurs.

The above described procedure is repeated until all retrials for all thresholds are performed and the simulation reaches $t = T$. An illustration of a realisation of the importance function and transitions are shown in figure 9.1.

In the general formulation of the RESTART method all realisations take initial condition corresponding to an importance function with a value between a lower boundary and e_1 .

In the following section the method is tested on a simple, well-defined system.

9.2 Implementation on two node tandem network

A simple representation of a telecommunication network or a computing system is the two node tandem network. The simple network consists of two random queues in tandem with packets arriving in the first queue according to a stationary Poisson counting process with the arrival rate λ . When packets leave the first queue they arrive in the second queue. The service times of packets in the first queue are exponentially distributed with the rate μ_1 while service of packets in the second queue are exponentially distributed with the service rate μ_2 . The sizes of queues are denoted $Q_1(t)$ and $Q_2(t)$. An illustration of the two node tandem network is shown in figure 9.2.

Different studies have been made on using the RESTART algorithm in estimation of the exceedance probability of the number of packets L in one or more queues in a two node tandem network. In [Villén-Altamirano and Villén-Altamirano, 2006] results are obtained for the method used on a two-queue tandem network for calculating exceedance probabilities of the safety margins $Q_1(t) + Q_2(t) > L$, $Q_2(t) \geq L$ and $\text{Min}(Q_1(t), Q_2(t)) \geq L$. The study includes a description of the general behavior of a two node tandem network, a discussion on optimal choice of parameters in the RESTART algorithm and discussions on simulation cost in RESTART simulations compared to CMC simulations. However, as described in the previous section, specific values of the parameters used in the RESTART algorithm, e.g. number of restarts at each threshold and values of $e_1 \dots e_M$ are not stated.

To reproduce the results, a numerical model for the two node tandem network is formulated and exceedance probabilities for small thresholds are verified by using CMC simulations. In [Villén-Altamirano and Villén-Altamirano, 2006] an exceedance probability when using the mean arrival rate

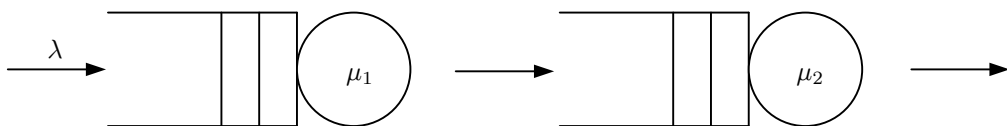


Figure 9.2: Two-queue tandem network.

$\lambda = 1 \text{ s}^{-1}$ and service times $\mu_1 = 1/2 \text{ s}$ and $\mu_2 = 1/3 \text{ s}$ is found to $P(Q_1(t) + Q_2(t) \geq 14) = 1.22 \cdot 10^{-4}$. This result has been reproduced by running 10^6 packet arrivals using CMC simulation. Due to the extensive simulation time using CMC simulation it was not possible to reproduce results obtained for lower exceedance probabilities.

Reproduction of the low-exceedance probabilities obtained in the articles by using the RESTART method is sought by implementing the RESTART algorithm on the two node tandem network. In the RESTART simulations the parameters are chosen to fit the quasi-optimal parameters as defined in [Villén-Altamirano, 1997], i.e. the number of retrials R_i for each threshold and the values of the different thresholds e_i are set according to the quasi-optimal values; the probability of an upcrossing over a given threshold e_{i+1} on condition of an importance function at threshold e_i should be $P(e_{i+1}|e_i) = \exp(1)^{-2}$ and the number of retrials at each threshold should attain the value $R_i = \exp(1)^2$. In practise the probability $P(e_{i+1}|e_i)$ can not be calculated analytically for the system under investigation and is instead fitted by doing trial simulations.

The system state includes the following parameters for the two node tandem network; queue lengths, total time, time to next arrival at queue 1 and time until queue 1 and 2 are finished processing the current packet. One of the important parts of the RESTART algorithm is how to restore the system state when the system reaches a threshold. In the implementation of the algorithm the system state is saved whenever an event U_i occurs. When a retrial is performed the system state is recovered and the simulation is continued. However, restoring the time of occurrence of next arrivals and service times directly, leads to a correlation between retrials $[U_i, D_i]$ and an algorithm taking the previous arrival times and start time of current service into consideration, is used. This means that for each retrial new values for the arrival time and service times are calculated from an exponential distribution having a mean arrival rate of the time until next arrival and finishing of service in the two nodes, respectively. The queue length q_2 has been used as importance measure in the simulations.

The analytical solutions for the probabilities $P(q_2 \geq 20)$ and $P(q_2 \geq 60)$ are shown in table 9.1. In [Villén-Altamirano and Villén-Altamirano, 2006] the authors obtain results within 5% of the analytical solution by using RESTART with a 95% confidence interval of $\pm 10\%$. To reproduce these result, the following parameters are chosen; thresholds are set to $e_1 = 2, e_2 = 4 \dots e_9 = 18$ and the number of retrials for each threshold is set to $R_i = 7$. Using a mean arrival rate $\lambda = 1 \text{ packet/s}$, mean service rates $\mu_1 = 2 \text{ packet/s}, \mu_2 = 3 \text{ packet/s}$ and a total simulation time of $T = 10^6 \text{ s}$ the results obtained are shown in table 9.1. It is seen that the deviations from the results in [Villén-Altamirano and Villén-Altamirano, 2006] are quite large.

It is seen that the RESTART-algorithm overestimate the failure probabilities for both thresholds tested. Also, the standard deviation for the 10 simulations is quite large considering the relatively high number of packet arrivals (more than 10^7 for $L = 60$). Also, the simulation for $q_2 \geq 20$ is performed using $T = 10^7$ to be certain that the simulation time does not give rise to convergence problems. The simulation using $T = 10^6$ does not provide results closer to the analytical solution, hence a larger simulation time does not influence the results.

L	Analytical solution P_f	T	Simulated \hat{P}_f	COV
20	$2.87 \cdot 10^{-10}$	10^6	$7.20 \cdot 10^{-10}$	0.26
60	$2.36 \cdot 10^{-29}$	10^6	$1.32 \cdot 10^{-28}$	0.18

Table 9.1: Comparison of results from RESTART simulations with analytical solutions for the two node tandem network. The table shows the mean probability of 10 RESTART samples \hat{P}_f and the coefficient of variation (COV) for the 10 samples.

9.3 Conclusion

In the following section an attempt was made to reproduce the results from an example in the literature using the RESTART method. Unfortunately the results could not be reproduced which could be the result of using unstable parameters e_i and R_i . In general however, the algorithm should be stable for any value of e_i and R_i which seems not to be the case for the results presented in the previous section.

As the results obtained for the simple case using a two node tandem queue were not satisfactory implementation on the 2-dof shear frame has not been performed. Further study will have to be performed to make the algorithm work on simple systems before implementing it on structural systems. Another problem to consider in the implementation on a structural system is to find and verify the of a suitable non-negative scalar process that can serve as importance process of the system.

Due to the negative outcome of these initial investigations of the RESTART algorithm, the focus of this thesis will be on the methods Importance Sampling and Russian Roulette and Splitting. Both methods will be tested in the application of determining 50-year recurrence period low-probability events for a simple three dof wind turbine.

Chapter 10

Comparison of RR&S and IS with the POT method.

In the following, the estimates of the extreme response distribution for the tower top displacement of the three dof wind turbine estimated by the RR&S, IS and POT methods are compared. The comparison is made to show the potential of using variance reduction methods such as the RR&S and IS method instead of the POT method for determining the characteristic response for wind turbines.

In figure 10.1 the different estimates of the extreme response distribution is shown as the exceedance probability $P(q_1 > q_{c,1} | T = 600 \text{ s}, V_m = 15 \text{ m/s})$. In what follows, the notation $P(q_1 > q_{c,1})$ will be used for $P(q_1 > q_{c,1} | T = 600 \text{ s}, V_m = 15 \text{ m/s})$. The RR&S data points in figure 10.1 corresponds to the estimates of $F_T(600)$ in figure 8.11 and the IS data points corresponds to the data points in figure 7.19.

As described in section 2.1.1 the problems and uncertainties regarding the POT method is that it depends on the extraction of independent maxima from relative few simulations and the choice of the candidate distribution function and that the correct distribution function is unknown. This is also evident in figure 10.1 where it is seen that the estimate of $P(q_1 > q_{c,1})$ produced by the POT method depends on the choice of distribution function, e.g. the 3-parameter Weibull or Gumbel.

The standard error of the IS is expected to be very small, since the only significant contribution to the standard error of the estimate is in the extrapolation of the first passage distribution function, cf 7.2.1. The standard error of the RR&S method is expected to be higher than the IS and especially for the high barriers, due to the rather rough estimate of the first passage time distribution function, cf. figure 10.1. The estimated $P(q_1 > q_{c,1})$ is however considered robust since the most of the estimated points is coinciding with the IS.

The estimates of $P(q_1 > q_{c,1})$ produced by RR&S and IS simulation has a tendency to follow a curved line in the logarithm scale, whereby the extreme response distribution does not constitute a Gumbel distribution. The Weibull distribution represents the curved nature of the extreme response, but is underestimating in the entire interval. The extreme response corresponding to a 50 year recurrence period estimated by the two candidate distributions deviate 6% and 11 % from the value estimated by IS, Gumbel and 3-parameter Weibull, respectively. Eventhough the Gumbel distribution does not constitute the correct extreme response distribution, it is concluded that it gives the best fit of the two candidates. However, as these estimates of $P(q_1 > q_{c,1})$ are calculated for a system which is not effected by a control system, nothing can be said about how well the Gumbel and the 3-parameter Weibull distribution fits the extreme values in the case of a real wind turbine where the response is affected by a control system.

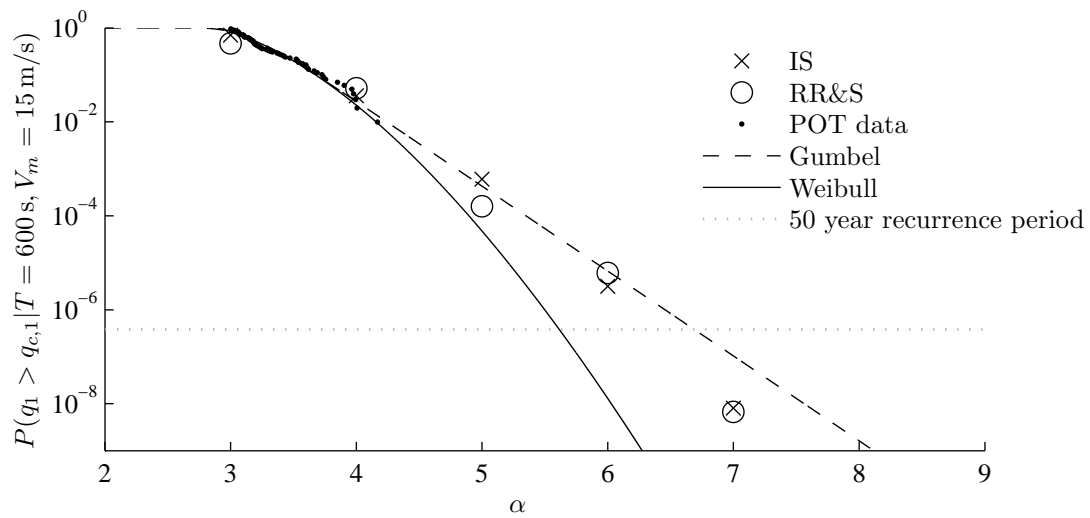


Figure 10.1: Extreme response distribution estimated by means of RR&S, IS and POT using a Gumbel and 3-parametric Weibull distribution.

Neither IS or RR&S has been successfully applied on a wind turbine model with a control system, whereby an evaluation of the applicability on real turbines is not possible.

Chapter 11

Conclusion

In this master thesis the methods currently used for determining extreme loads on wind turbines have been described and tested on a 5MW reference wind turbine. The current method produces a significant variance on the estimate of the extreme response, hence it is desirable to implement so-called variance reduction methods. Three variance reduction methods have been investigated and two of the methods has been found suitable for implementation on structural systems.

In chapter 2 investigations on the extrapolation method from the IEC61400-1 standard has been performed. As only a few simulations are performed in each wind speed bin the main issues have been found to be the extraction of a sufficient number of statistical independent peak values. The peak over threshold method has been tested in chapter 2.2 and seen to provide differing results when comparing it for different thresholds. The candidate probability distribution functions suggested in the standard have been compared and found to estimate extreme responses with a recurrence period of 50 years deviating more than 50% when comparing the 3-parameter Weibull and Gumbel probability distribution functions.

Two of the three variance reduction methods have been evaluated on simple structural systems in the form of a simple two dof shear frame and a simple model of a three dof wind turbine. The models used for modelling the turbulence have been described in appendix B.

The importance sampling method has been evaluated on two different structural systems. To establish an effective importance measure, the Girsanov transformation has been used to apply a mean value to the zero-mean Gaussian input process. The mean value, referred to as the sample control function is obtained by means of the First Order Reliability Method and can be interpreted as an underlying process, that in mean drives the response process of the system to failure at a given design time. The first passage time probability of oscillating systems is dominated by several exit times whereby it is necessary to use a multi modal sample density function, where samples are generated around several design points. The method has successfully been applied for the three dof wind turbine and first passage time probabilities of the order of magnitude 10^{-10} has been estimated with only 500 simulations. The first passage time probability distribution function estimated by the importance sampling method is determined for deterministic initial states, whereby the characteristic extreme response is not determined directly. An estimate of the hazard rate of the stationary response is calculated, whereafter the first passage time probability distribution function of the stationary response is determined. Some uncertainties are introduced when calculating the hazard rate, which needs to be clarified. Also, incorporating a stochastic initial state might be worth considering in future research.

Before anything can be concluded on the applicability of the importance sampling on “real” wind turbines the control systems need to be incorporated in the sample control functions. Further, the number of state variables is crucial for the calculation time of the sample control functions. However this is merely a programming optimisation problem.

In chapter 8 the variance reduction method Russian Roulette & Splitting with Distance Control (RR&S) has been described and results obtained on four different systems has been presented. Overall, the algorithm is highly dependent on the choice of a so-called distance variable. This is indicated in section 8.2 and in appendix I.2 where qualitative and quantitative investigations of different distance variables has been performed. The investigations show that the mechanical energy calculated after

subtracting a possible static displacement is generally a reasonable choice of distance variable and this is used throughout the investigations.

In section 8.3 and 8.4 the results obtained on the preliminary simple systems has been presented and they have shown that the efficiency of the algorithm compared to CMC simulation increases as the barrier level increases. Computational savings of more than 99% has been achieved in section 8.3 using 10000 time series in the RR&S simulation and in section 8.4 failure probabilities in the order of 10^{-9} has been estimated using 500 time series.

The results from the implementation on to the 5MW reference wind turbine have been presented in section 8.5. The results shows that the control system of the wind turbine effects the results significantly. In section 8.5.2 results are presented for the case where the control system has been disabled and failure probabilities in the order of 10^{-4} has been simulated using 100 time series. As shown in section 8.5.3 no improvements were seen when the control system was enabled. From this it has been concluded that the control system effects the efficiency of the mechanical energy as distance variable and more investigations are therefore needed in order to determine an efficient distance variable for the case where the control system is enabled. It has been suggested that such a distance variable should include information on the mechanical energy but also on the state of the control system.

In chapter 9 RESTART have been investigated for use on structural systems. Difficulties on getting the method to provide promising results on even a simple Markovian system lead to the conclusion that the method was not suitable for use on simple structural systems and therefore not applicable for determining extreme responses for wind turbines.

The results achieved by the RR&S and importance sampling methods suggest that the importance sampling method is the most efficient of the two methods but also the hardest to implement. The conclusion on the thesis is that more work needs to be done before any of the variance reduction methods can be succesfully applied to a wind turbine which includes a control system.

Bibliography

- Arnold, L. *Stochastic Differential equations: theory and applications*. Wiley-Interscience New York, 1974.
- Ayyub, Bilal M. and McCuen, Richard H. *Probability, Statistics, and Reliability for Engineers and Scientists*. CHAPMAN&HALL/CRC, 2nd edition, 1997.
- Clough, R. W. and Penzien, J. *Dynamics of Structures*. McGraw-Hill, 1982.
- Geradin, M. and Rixen, D. *Mechanical Vibrations. Theory and Applications to Structural Dynamics*. John Wiley & Sons, 2nd edition, 1997.
- Girsanov, I.V. On transforming a certain class of stochastic processes by absolutely continuous substitution of measures. *Theory of Probability and its Application*, 5:285–301, 1960.
- Holmager, Morten, editor. *OffshoreBook*. Offshore Center Denmark, 2008 edition, 2008.
- IEC Technical Committee 88. Amendment to the IEC 61400-1:2005 standard. International Electrotechnical Commission, IEC Technical Committee 88: Wind Turbines, 2009.
- International Electrotechnical Commission. 61400-1: Wind turbines - part 1: Design requirements. Technical report, 2005.
- Jonkman, J., Butterfield, S., Musial, W., and Scott, G. Definition of a 5-mw reference wind turbine for offshore system development. Technical report, National Renewable Energy Laboratory, 2009.
- Juang, J. and Phan, M. *Identification and Control of Mechanical Systems*. Cambridge University Press, 2001.
- Karamchandani, A. *New Methods in Systems Reliability*. PhD thesis, Stanford University, May 1990.
- Macke, M. and Bucher, C. Importance sampling for randomly excited dynamical systems. June 2002.
- Moriarty, P., editor. *IEC LE3 Boulder Meeting Presentations*, Boulder, CO, 2007. National Wind Technology Center, IEC.
- Moriarty, P. and Veers, P. Wind energy - special issue: Special issue on design load definition. Online in Wiley Interscience, 2008.
- Nielsen, S. R. K. *Structural Dynamics, Vol. 9. - Computational Dynamics*. Department of Civil Engineering, Aalborg University, 2nd edition, 2007a.
- Nielsen, S. R. K. *Structural Dynamics, Vol. 3. - Linear Stochastic Dynamics*. Department of Civil Engineering, Aalborg University, 5th edition, 2007b.
- Olsen, A. I. *Time-variant reliability of dynamic systems by importance sampling and probabilistic analysis of ice loads*. PhD thesis, Norwegian University of Science and Technology, August 2006.
- Pradlwarter, H.J. and Schuëller, G.I. Assessment of low probability events of dynamical systems by controlled Monte Carlo simulation. *Probabilistic Engineering Mechanics*, 14:213–227, 1999.
- Ragan, P. and Manuel, L. Statistical extrapolation methods for estimating wind turbine extreme loads. *Journal of Solar Energy Engineering*, 130:031011–1 to 031011–15, August 2008.
- Sandia National Laboratories. Can the U.S. achieve 20% wind energy by 2030, 2008. URL: <http://www.eurotrib.com/story/2008/5/14/17425/9803>.

- Shinozuka, M. and Jan, C.M. Digital simulation of random processes and its applications. *Journal of Sound and Vibration.*, 25(1):111–128, 1972.
- Sichani, M.T., PhD Fellow, Pedersen, B.J., and Nielsen, S.R.K. State space modelling of along wind turbulence with application to wind turbines. Department of Civil Engineering, Aalborg University, Unpublished, 2009.
- Stensgaard, H. T. and Sørensen, J. D. Reliability analysis of wind turbines. In *4th ASRANet International Colloquium*. Aalborg University. Department of Civil Engineering, 2008.
- Tanaka, H. Application of an importance sampling method to time-dependent systems reliability analyses using the girzanov transformation. Department of Applied Mathematics and Physics, Kyoto University, Japan, A A BALKEMA PUBLISHERS, SCHIPHOLWEG 107C, PO BOX 447, 2316 XC LEIDEN, NETHERLANDS, 1998.
- Veers, Paul S. Three-dimensional wind simulation. Unlimited release, Sandia National Laboratories, 1988.
- Villén-Altamirano, J. Restart method for the case where rare events can occur in retrials from any threshold. *International Journal of Electronics and Communications*, 52(3):183–189, 1997.
- Villén-Altamirano, M. and Villén-Altamirano, J. Restart: a method for accelerating rare event simulations. In *Proceedings of the 13th International Teletraffic Congress, Copenhagen*, p. 71–76. North Holland, 1991.
- Villén-Altamirano, M. and Villén-Altamirano, J. Analysis of restart simulation: Theoretical basis and sensitivity study. *European Trans. Telecomm*, 13(4):373–385, 2002.
- Villén-Altamirano, M. and Villén-Altamirano, J. On the efficiency of restart for multidimensional state systems. *ACM Transactions on Modeling and Computer Simulation*, 16(3):251–279, 2006.
- Villén-Altamirano, M., Martínez-Marrón, A., Gamo, J., and Fernández-Cuesta, F. Enhancement of the accelerated simulation method restart by considering multiple thresholds. In *Proceedings of the 14th International Teletraffic Conference on The Fundamental Role of Teletraffic in the Evolution of Telecommunications Networks. (ITC'94)*, p. 797–810. Elsevier, 1994.
- Wong, E. and Zakai, M. On the relation between ordinary and stochastic differential equations. *International Journal of Engineering Science*, 3:213–229, 1965.
- World Resources Institute. Booming wind energy market, January 2008. <http://earthtrends.wri.org/updates/node/277>.

Appendices

Appendix A

FAST

A.1 Basic description of the FAST code

In this chapter a basic description of the servo-aero-elastic simulator FAST (Fatigue, Aerodynamics, Structures and Turbulence) is given. FAST is capable of determining extreme- and fatigue loads for two- and three-bladed wind turbines. In the present thesis, FAST has been used to calculate response time series for a three-bladed wind turbine under normal operation. The turbulence given as input to FAST is simulated by TurbSim and a state space representation of an ARMA model, described in appendix B.

The FAST model employs a combined modal and multibody dynamics formulation. When modelling a three-bladed wind turbine, the model has 24 dofs. The first six dofs represent the motions of the support platform, the translational dofs surge q_1 , sway q_2 and heave q_3 and the rotational dofs roll q_4 , pitch q_5 and yaw q_6 . Four dofs account for tower motions, two modes in the fore-aft direction q_7, q_8 and two modes in the side-side direction q_9, q_{10} . Yawing motion of the nacell, generator azimuth angle and compliance in the drivetrain between the rotor and generator are described by the dofs q_{11}, q_{12} and q_{13} . Nine dofs $q_{14} - q_{22}$ define blade motions - three dofs for each blade; two dofs defining out-of-plane motions and one dof defining in-plane motions for each blade. The last two dofs, rotor- and tail furl, are normally not used for larger wind turbines. All dofs, except the dofs for blade 2 and 3, rotor- and tail furl, are shown in figure A.1.

The model relies on a simple representation of the flow stream used to determine the forces on the blades. Each blade is split into elements having well defined aerodynamic properties assuming that the pretwist angle and the position of the blade elements is known. The forces on the blades are then calculated at each element and integrated over the total blade length to determine the total force affecting a blade. The calculation of aero dynamic forces is done by the code AeroDyn, which is bundled with the FAST code.

The equations of motion are solved by a fourth-order Adams-Beshforth predictor method. The predictor estimates displacements and velocities at each time step for all dofs and provides an estimate of the acceleration. The estimated acceleration is used in estimating displacements and velocities over again. This procedure is repeated several times. At last a fourth order Adams-Mounton corrector is used to make final estimates of the accelerations. The first four time steps are solved by a fourth-order Runge-Kutta method as the predictor-corrector method require that the previous four time steps are known.

Several control systems can be activated; blade pitch control, variable-speed generator control, high-speed-shaft brake control, nacelle yaw control and tip brakes. For the wind turbine under study in this thesis, the blade pitch control and variable-speed generator controls are activated by using control systems designed especially for the present wind turbine.

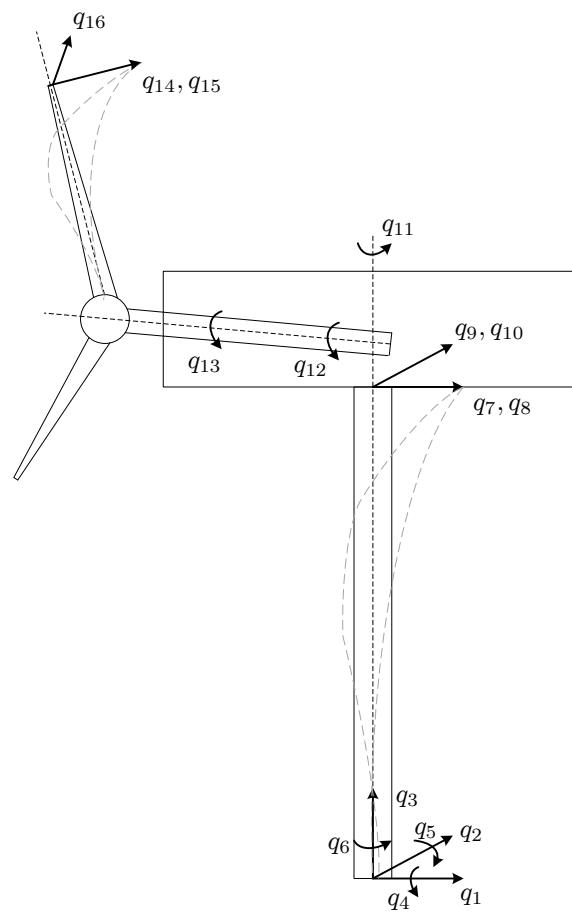


Figure A.1: Sketch of dofs used in FAST.

Appendix B

Turbulence simulation

The turbulence represents the random fluctuations of the incoming wind field around a mean value. The turbulence is modelled as a stochastic Gaussian process $\{v_j(\mathbf{z}, t), (\mathbf{z}, t) \in R^3 \times R\}$ which is homogeneous in the spatial index parameters $\mathbf{z} = (z_1, z_2, z_3)$ and stationary in time t . Hence, the process is uniquely defined by the cross-covariance function $\kappa_{v_j, v_k}(\mathbf{r}, \tau)$ defined as

$$\kappa_{v_j, v_k}(\mathbf{r}, \tau) = E[v_j(\mathbf{z}_1, t_1)v_k(\mathbf{z}_2, t_2)], \quad \mathbf{r} = \mathbf{z}_2 - \mathbf{z}_1, \quad \tau = t_2 - t_1 \quad (\text{B.1})$$

The corresponding cross-spectral density function is defined by the Wiener-Khintchine relation [Nielsen, 2007b]

$$S_{v_j, v_k}(\mathbf{r}, \omega) = \frac{1}{2\pi} \int_{-\infty}^{\infty} e^{i\omega\tau} \kappa_{v_j, v_k}(\mathbf{r}, \tau) d\omega \quad (\text{B.2})$$

The variance of the turbulence in the z_j -direction is given as

$$\sigma_j^2 = \kappa_{v_{(j)}v_{(j)}}(\mathbf{0}, 0) = \int_{-\infty}^{\infty} S_{v_{(j)}v_{(j)}}(\mathbf{0}, \omega) d\omega \quad (\text{B.3})$$

where the parentheses around the index j indicate that summation over the dummy indices is abandoned. Turbulence in shear-flow is non-isotropic for which reason the standard deviations σ_1 , σ_2 and σ_3 are different. Typically the following applies

$$\sigma_2 \simeq 0.7\sigma_1, \quad \sigma_3 \simeq 0.5\sigma_1 \quad (\text{B.4})$$

Further, the turbulence components $v_1(\mathbf{z}, t)$ and $v_3(\mathbf{z}, t)$ at the same position \mathbf{z} and time t are negative correlated. Typically, the correlation coefficients become

$$\rho_{v_1 v_3} = \frac{\kappa_{v_1 v_3}(\mathbf{0}, 0)}{\sigma_1 \sigma_3} \simeq -0.3 \quad (\text{B.5})$$

Empirically, the cross-spectral density function is defined via the coherence function given as

$$\gamma_{v_j, v_k}(\mathbf{r}, \omega) = \frac{S_{v_j, v_k}(\mathbf{r}, \omega)}{\sqrt{S_{v_{(j)}v_{(j)}}(\omega) S_{v_{(k)}v_{(k)}}(\omega)}} \quad (\text{B.6})$$

where $S_{v_{(j)}v_{(k)}}(\omega) = S_{v_{(j)}v_{(k)}}(-\omega)$ is the double-sided auto-spectral density function. Due to the correlation between the turbulence components, $\gamma_{v_j v_k}(\mathbf{r}, \omega) \neq 0, j \neq k$. The coherence function is complex and may be written on the polar form

$$\gamma_{v_j v_k}(\mathbf{r}, \omega) = |\gamma_{v_j v_k}(\mathbf{r}, \omega)| e^{i\Theta(\mathbf{r}, \omega)} \quad (\text{B.7})$$

where $\Theta(\mathbf{r}, \omega)$ is denoted the phase spectrum. Both the modulus $|\gamma_{v_j v_k}(\mathbf{r}, \omega)|$ and the phase spectrum may be modelled by empirical specification. In numerical applications for wind turbines the domain in the vicinity of the rotor is discretized by a 3-dimensional grid with a given spacing $\Delta z_1, \Delta z_2$ and Δz_3 in the coordinate directions. The idea is that turbulence is generated in the grid points. Next, the turbulence components $v_j(\mathbf{z}, t)$ at any point within the discretized domain is obtained by linear interpolation between the turbulence components in the nearest grid points. The $3N$ turbulence components in the N grid points are assembled in the stochastic vector

$$\mathbf{v}(t) = \begin{bmatrix} v_1(\mathbf{z}_1, t) \\ v_2(\mathbf{z}_1, t) \\ v_3(\mathbf{z}_1, t) \\ \vdots \\ v_1(\mathbf{z}_N, t) \\ v_2(\mathbf{z}_N, t) \\ v_3(\mathbf{z}_N, t) \end{bmatrix} \quad (\text{B.8})$$

The corresponding cross-spectral density matrix is denoted $\mathbf{S}_{\mathbf{v}\mathbf{v}}(\omega)$. This is a Hermitian matrix fulfilling the symmetry properties

$$\mathbf{S}_{\mathbf{v}\mathbf{v}}^*(\omega) = \mathbf{S}_{\mathbf{v}\mathbf{v}}^T(\omega) \quad (\text{B.9})$$

where $*$ denotes complex conjugation. A consequence of (B.9) is that all eigenvalues of $\mathbf{S}_{\mathbf{v}\mathbf{v}}(\omega)$ are real for arbitrary frequencies ω . $\mathbf{S}_{\mathbf{v}\mathbf{v}}(\omega)$ admits the eigenvalue decomposition

$$\mathbf{S}_{\mathbf{v}\mathbf{v}}(\omega) = \mathbf{\Psi}(\omega) \mathbf{\Lambda}(\omega) \mathbf{\Psi}^{-1}(\omega) \quad (\text{B.10})$$

where $\mathbf{\Lambda}(\omega)$ is a diagonal matrix with the eigenvalues of $\mathbf{S}_{\mathbf{v}\mathbf{v}}(\omega)$ stored in the main diagonal, and the corresponding eigenvectors are stored columnwise in the modal matrix $\mathbf{\Psi}(\omega)$. Due to the discretization $\mathbf{S}_{\mathbf{v}\mathbf{v}}(\omega)$ is not necessarily positive definite, i.e. some of the eigenvalues may attain small negative values. For this reason $\mathbf{\Lambda}(\omega)$ in (B.10) is replaced by an eigenvalue matrix $\bar{\mathbf{\Lambda}}(\omega)$ where all negative eigenvalues in $\mathbf{\Lambda}(\omega)$ are replaced by 0. Thereby the following modified positive semi-definite cross-spectral density function is defined

$$\bar{\mathbf{S}}_{\mathbf{v}\mathbf{v}}(\omega) = \mathbf{\Psi}(\omega) \bar{\mathbf{\Lambda}}(\omega) \mathbf{\Psi}^{-1}(\omega) \quad (\text{B.11})$$

Then, the following factorization of $\bar{\mathbf{S}}_{\mathbf{v}\mathbf{v}}(\omega)$ is possible [Sichani et al., 2009]

$$\bar{\mathbf{S}}_{\mathbf{v}\mathbf{v}}(\omega) = \mathbf{H}_{\mathbf{v}}^*(\omega)\mathbf{H}_{\mathbf{v}}^T(\omega) \quad (\text{B.12})$$

If the eigenvectors in $\Psi(\omega)$ are normalized to unit length, then [Nielsen, 2007a]

$$\Psi^{-1}(\omega) = \Psi^{*T}(\omega) \quad (\text{B.13})$$

Then, a solution to (B.12) is given as

$$\mathbf{H}_{\mathbf{v}}(\omega) = \Psi^*(\omega)\mathbf{\Lambda}^{\frac{1}{2}}(\omega) \quad (\text{B.14})$$

Alternatively, $\mathbf{H}_{\mathbf{v}}(\omega)$ may be obtained as a lower triangular matrix by Choleski decomposition of $\mathbf{S}_{\mathbf{v}\mathbf{v}}(\omega)$ [Shinozuka and Jan, 1972].

Define a vector process of dimension $3N$ $\{\mathbf{W}(t), t \in R\}$. The component processes $\{W_j(t)\}$ are mutual independent zero-mean Gaussian white noise processes with the double-sided auto-spectral density function $S_{W_{(j)}W_{(j)}}(\omega) \equiv 1$. Then, (B.12) may be written as

$$\mathbf{S}_{\mathbf{v}\mathbf{v}}(\omega) = \mathbf{H}_{\mathbf{v}}^*(\omega)\mathbf{S}_{\mathbf{W}\mathbf{W}}(\omega)\mathbf{H}_{\mathbf{v}}^T(\omega) \quad (\text{B.15})$$

From (B.15) follows that $\mathbf{v}(t)$ may be implemented as a filtration of $\mathbf{W}(t)$ through a linear filter with the frequency response matrix $\mathbf{H}_{\mathbf{v}}(\omega)$. The related impulse response matrix is obtained from [Nielsen, 2007b]

$$\mathbf{h}_{\mathbf{v}}(t) = \frac{1}{2\pi} \int_{-\infty}^{\infty} e^{i\omega t} \mathbf{H}_{\mathbf{v}}(\omega) d\omega \quad (\text{B.16})$$

Then, $\mathbf{v}(t)$ is related to $\mathbf{W}(t)$ via the convolution integral

$$\mathbf{v}(t) = \int_{-\infty}^{\infty} \mathbf{h}_{\mathbf{v}}(t - \tau) \mathbf{W}(\tau) d\tau \quad (\text{B.17})$$

It should be noticed that $\mathbf{h}_{\mathbf{v}}(t)$ is not causal, so the convolution integral (B.17) cannot be truncated at the upper limit $t = \tau$.

Alternatively, $\mathbf{v}(t)$ can be obtained from the spectral representation, [Nielsen, 2007b]

$$\mathbf{v}(t) = \int_{-\infty}^{\infty} e^{i\omega t} \mathbf{H}_{\mathbf{v}}(\omega) d\mathbf{X}(\omega) \quad (\text{B.18})$$

where $d\mathbf{X}(\omega)$ are mutual complex, zero mean, normal distributed independent random increments fulfilling

$$\mathbb{E}[d\mathbf{X}^*(\omega_1)d\mathbf{X}^T(\omega_2)] = \begin{cases} \mathbf{0} & , \omega_1 \neq \omega_2 \\ \mathbf{I}d\omega & , \omega_1 = \omega_2 \end{cases} \quad (\text{B.19})$$

(B.17) form the basis of various filter methods including vector ARMA methods for Monte Carlo simulation of realisations of the vector process $\{\mathbf{v}(t), t \in R\}$. Similarly, (B.18) is the basis for various spectral simulation methods (sum of harmonics). For applications the integrals in (B.17) and (B.18) are replaced by sums.

The requirements for turbulence applied on the wind turbine is described in the IEC-61400 code. The recommended turbulence model is the Mann uniform shear turbulence model. However, the preferred turbulence simulator for use with FAST, TurbSim, does not have the Mann model implemented. Instead a more simple model based on a Kaimal spectrum and exponential coherence is used. Turbulence modelling with TurbSim is described in section B.1.

The basics of the turbulence simulation is a spectral density function. In the IEC-61400 code (Annex B.2) a Kaimal power spectral density function is given [International Electrotechnical Commission, 2005]. The empirical expressions for the double-sided autospectral density function $S_{v_{(i)}v_{(i)}}(\omega)$ is given by

$$S_{v_{(i)}v_{(i)}}(\omega) = \frac{\sigma_i^2}{3V} \frac{6L_i}{(1 + 6|L_i k|)^{5/3}} \quad (\text{B.20})$$

where σ_i is the standard deviation of the turbulence in the z_i direction, V is the mean wind velocity at hub height assumed to be constant over the rotor area, L_i is the correlation length for the z_i direction. The correlation length is given as $L_{z_1} = 8.1\Lambda_1$, $L_{z_2} = 2.7\Lambda_1$ and $L_{z_3} = 0.66\Lambda_1$ for directions z_1 , z_2 and z_3 , respectively. The scale parameter Λ_1 is given as $\Lambda_1 = 0.7h, z \leq 60$ m and $\Lambda_1 = 42$ m, $z \geq 60$ m.

For all simulations, the wind conditions are assumed to be medium turbulence conditions corresponding to a turbulence intensity of $I_{ref} = 0.14$. The standard deviation σ_1 for the normal turbulence model, which is the turbulence model used in this thesis, is determined by

$$\sigma_1 = I_{ref}(0.75V + b) \quad , \quad b = 5.6 \text{ m/s} \quad (\text{B.21})$$

The basics of the turbulence models described in the following is that the turbulence in the longitudinal, lateral and vertical directions are uncorrelated and thereby disregarding the known correlation given by (B.5). The standard deviations for the lateral and upwards directions are given as $\sigma_2 = 0.7\sigma_1$ and $\sigma_3 = 0.5\sigma_1$, respectively.

B.1 Turbulence simulation using TurbSim

TurbSim is a full-field, turbulent-wind simulator developed by NREL built on basic of an older code, SNLWIND. SNLWIND was written by Paul Veers from Sandia National Laboratories (SNL) in 1988 [Veers, 1988] and further developed to SNLWIND-3D and SNwind by different researchers from SNL and NREL in the following 15 years. Today, TurbSim can be used in connection with FAST to generate a full turbulence wind field.

The turbulence is generated by discretising the spectral representation shown in (B.18), [Veers, 1988].

In TurbSIM the rotor plane is discretised into a rectangular grid as shown in figure B.1. Layers in the z_1 -direction can be added. For each time step in FAST the turbulence affecting the blades are determined by bilinear interpolation between the points in the rectangular grid.

The spectral density function (B.20) is used in TurbSim. and as multiple correlated points in space are to be modelled a coherence function is needed. The IEC-61400 code suggests the following exponential coherence model γ_i which is being used in TurbSim

$$\gamma_i(\mathbf{r}, f) = \exp\left(-12\sqrt{(f|\mathbf{r}|/V_{hub})^2 + (0.12|\mathbf{r}|/L_c)^2}\right) \quad (\text{B.22})$$

where f is the frequency in [Hz], r is the individual distance between points in a plane normal to the wind direction and L_c is a coherence scale parameter, $L_c = 8.1\Lambda_1$.

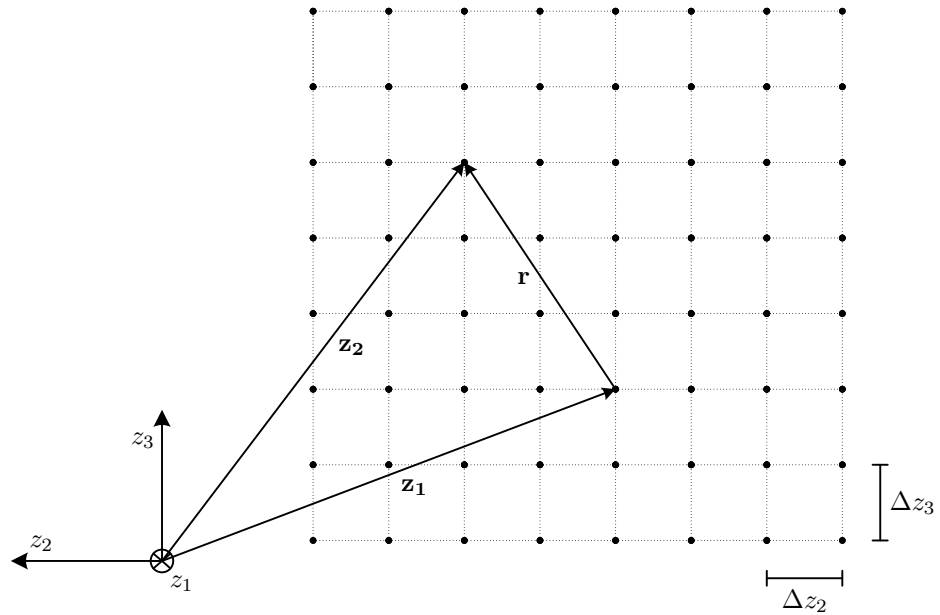


Figure B.1: Rectangular grid used in TurbSim.

B.2 Turbulence simulation using moving average model

When using variance reduction methods such as RR&S and IS the spectral representation of the turbulence used in TurbSim is not applicable. The RR&S algorithm relies on being able to split realisations, which requires the turbulence to develop independently from the time of splitting. This requires, that the turbulence is represented by a Markov state vector, as is the case in the filter method but not for the spectral representation of the turbulence.

A simple model that comply with the above described conditions is a Moving Average vector model. This is merely a reformulation of the discretised version of (B.17), [Sichani et al., 2009] given as

$$\mathbf{v}(j) = \sum_{-N/2}^{N/2} \mathbf{h}_v(l) \Delta \mathbf{W}(j-l) \quad (\text{B.23})$$

where $\mathbf{W}(j-l)$ is a zero mean Gaussian vector with mutually independent random variables with the variance $2\pi\Delta t$. To obtain a causal filter corresponding to (B.23) the following is given for the convolution integral in (B.17)

$$\begin{aligned} \mathbf{v}(t) &= \int_{-\infty}^{\infty} (\mathbf{h}_s(\tau) + \mathbf{h}_a(\tau)) \mathbf{W}(t-\tau) d\tau \\ &= 2 \int_0^{\infty} \mathbf{h}_s(\tau) \mathbf{W}_s(t-\tau) d\tau + 2 \int_0^{\infty} \mathbf{h}_a(\tau) \mathbf{W}_a(t-\tau) d\tau \end{aligned} \quad (\text{B.24})$$

where $\mathbf{h}_s(\tau)$ and $\mathbf{h}_a(\tau)$ denote the symmetric and skew-symmetric part of $\mathbf{h}_v(\tau)$ and $\mathbf{W}_s(t-\tau)$ and $\mathbf{W}_a(t-\tau)$ denote the symmetric and skew-symmetric part of $\mathbf{W}(t-\tau)$ given by

$$\mathbf{h}_s(\tau) = \frac{1}{2}(\mathbf{h}_v(\tau) + \mathbf{h}_v(-\tau)) \quad (\text{B.25})$$

$$\mathbf{h}_a(\tau) = \frac{1}{2}(\mathbf{h}_v(\tau) - \mathbf{h}_v(-\tau))$$

$$\mathbf{W}_s(t-\tau) = \frac{1}{2}(\mathbf{W}(t-\tau) + \mathbf{W}(t+\tau)) \quad (\text{B.26})$$

$$\mathbf{W}_a(t-\tau) = \frac{1}{2}(\mathbf{W}(t-\tau) - \mathbf{W}(t+\tau))$$

The symmetric and skew-symmetric parts of $\mathbf{W}(\tau)$ are mutually independent white noise vector processes. Each input in $\mathbf{W}(t)$ is normally distributed with zero mean and variance $\sigma_v^2 = 2\pi\Delta t$, where Δt denotes the time step in the convolution integral. (B.24) can be written in discrete form as

$$\mathbf{v}(j) = \sum_{l=0}^{\infty} \mathbf{h}_s(l) \Delta \mathbf{W}_s(j-l) + \sum_{l=0}^{\infty} \mathbf{h}_a(l) \Delta \mathbf{W}_a(j-l) \quad (\text{B.27})$$

\mathbf{W}_s and $\mathbf{W}_a(j)$ are mutually independent, identical distributed zero mean M -dimensional Gaussian random vectors

$$E[\Delta \mathbf{W}_s(j) \Delta \mathbf{W}_s^T(k)] = E[\Delta \mathbf{W}_a(j) \Delta \mathbf{W}_a^T(k)] = \begin{cases} \mathbf{0} & , j \neq k \\ 4\pi \Delta t \mathbf{I} & , j = k \end{cases} \quad (\text{B.28})$$

Then (B.27) can be written in the following form

$$\mathbf{v}(j) = \sum_{l=0}^{\infty} \tilde{\mathbf{h}}(l) \Delta \check{\mathbf{W}}(j-l) \quad (\text{B.29})$$

where

$$\tilde{\mathbf{h}}(l) = [\mathbf{h}_s(l) \quad \mathbf{h}_a(l)] \quad (\text{B.30})$$

$$\Delta \check{\mathbf{W}}(j) = \begin{bmatrix} \Delta \mathbf{W}_s(j) \\ \Delta \mathbf{W}_a(j) \end{bmatrix} \quad (\text{B.31})$$

(B.29) may be interpreted as an equivalent causal filter with the impulse response matrix $\tilde{\mathbf{h}}(l)$ of dimension $M \times 2M$. $\check{\mathbf{W}}(j)$ is a zero mean normal vector with mutually independent random variables given as

$$E[\Delta \check{\mathbf{W}}(j) \Delta \check{\mathbf{W}}^T(k)] = \begin{cases} \mathbf{0} & , j \neq k \\ 4\pi \Delta t \mathbf{I} & , j = k \end{cases} \quad (\text{B.32})$$

To minimise the number of points, a grid described in angular and radial directions is used, see figure B.2. For each time step in the numerical integrator, the turbulence at a given point is determined by bilinear interpolation in the grid. No interpolation in the z_1 direction is performed, i.e. the structural part of the system that is affected by the turbulence is assumed to be positioned at $z_1 = 0$ at each time step cf. figure B.2.

For modelling the turbulence using the filter and the state space model the spectral density function (B.20) and the coherence function γ_s described in [Sichani et al., 2009] has been used

$$\gamma_s(\mathbf{r}, \omega) = \exp\left(-\frac{|\mathbf{r}|\omega}{V} d_1\right) \exp\left(i \frac{s(\mathbf{r})|\mathbf{r}|\omega}{V} d_2\right) \quad (\text{B.33})$$

where the sign function s is defined so that $s(r) = 1$ and $s(-r) = -1$. The parameters d_1 and d_2 are given as $d_1 \simeq 1.5$ and $d_2 \simeq 1.3$.

The model is very sensitive to the frequency resolution. If an insufficient frequency resolution is used, the turbulence calculated by the models does not converge towards the analytical autocovariance and covariance functions. To obtain convergence, the frequency response function should include more than $2^{11} = 2048$ frequency steps for each point in the grid if using a Δt of 0.1 s. The relatively high number of frequency steps mean that generation of 40-50 grid points at each time step requires extensive computational time. Turbulence simulation for FAST therefore requires an ARMA model or a state space representation of an ARMA model.

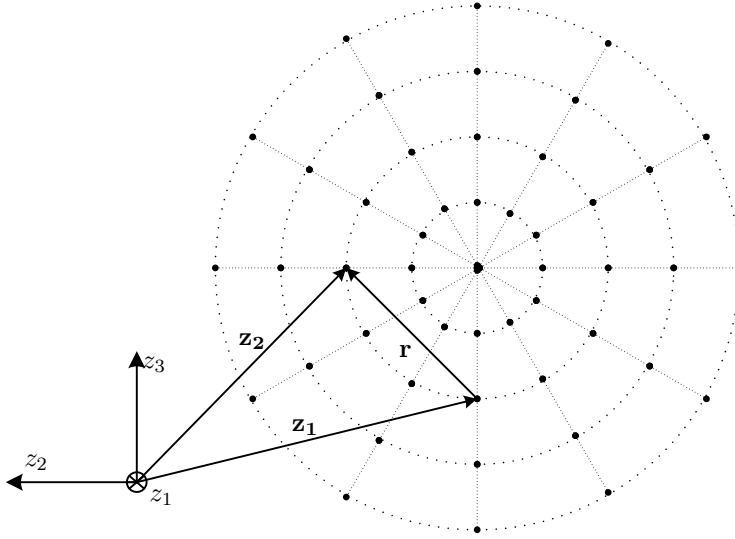


Figure B.2: Grid used in Moving Average model.

B.3 Turbulence simulation using state space ARMA model

The state space model is used for simulation of turbulence having only short memory. In addition the turbulence can be calculated simultaneously at each timestep while solving the structural system in e.g. FAST, which is a requirement for using the RR&S algorithm. The general formulation of the state space representation of an ARMA model is [Sichani et al., 2009]

$$\begin{aligned}\hat{\mathbf{x}}(j+1) &= \mathcal{A}\hat{\mathbf{x}}(j) + \mathcal{B}\Delta\mathbf{W}(j) \\ \mathbf{v}(j) &= \mathcal{C}\hat{\mathbf{x}}(j) + \mathcal{D}\Delta\mathbf{W}(j)\end{aligned}\tag{B.34}$$

where the state vector $\hat{\mathbf{x}}(j)$ has dimension $M \times 1$, $\Delta\mathbf{W}(j)$ is a stationary white noise vector process of dimension $N \times 1$. \mathcal{A} is a system matrix of dimension $M \times M$, \mathcal{B} is the Kalman gain matrix of dimension $M \times N$, \mathcal{C} is an observation matrix of dimension $N \times M$ and \mathcal{D} is an identity matrix of dimension $N \times N$.

The idea of the state space model is to estimate the matrices \mathcal{A} , \mathcal{B} , \mathcal{C} and \mathcal{D} so that the output process $\mathbf{v}(\mathbf{j})$ satisfy a given cross-covariance using a model order M sufficiently small to provide fast simulation of N coherent turbulence processes. An explanation of estimation of the matrices are out of the scope of this thesis - an explanation of the estimation technique is given in [Sichani et al., 2009].

For testing the RR&S algorithm a state space model for $N = 61$ spatial points in a radial grid and model of order $M = 175$ has been fitted for a mean wind speed at hub height of 15 m/s.

Appendix C

Description of 5MW reference wind turbine

The aeroelastic simulations in FAST are performed on a 5-MW reference wind turbine, the "NREL offshore 5-MW baseline wind turbine", designed by the National Renewable Energy Laboratory (NREL) on basis of the REpower 5M offshore wind turbine [Jonkman et al., 2009]. This wind turbine is used throughout the project to have a frame of reference for all calculations.

Data for the three-bladed, variable-speed, variable blade-pitch-to-feather-controlled wind turbine is given in table C.1.

Rating	5 MW
Rated Rotor Speed	12.1 rpm
Rated generator speed	1173.7 rpm
Rotor diameter	126 m
Blade lengths	61.5 m
Hub height	90 m
Cut-in, Rated, Cut-out wind speeds	5 m/s, 11.4 m/s, 25 m/s
Rated tip speed	80 m/s
Blade masses	17000 kg
Total rotor mass	90000 kg
Nacelle mass	240000 kg
Tower mass	347460 kg

Table C.1: Data for 5MW reference wind turbine [Jonkman et al., 2009].

The simulation in FAST includes 22 dofs distributed over the support platform, tower motions, nacelle motion, generator azimuth, compliance between generator and rotor and displacements of blades. The simulation assumes a fixed support at the tower bottom. The tower and blade motions are described by modal coordinates and corresponding mode shapes. The mode shapes for the tower and blades are shown in figure C.1 and C.2, respectively. The tower mode shape 1 and 2 for fore-aft and side-side motions are almost alike and can not be distinguished on the figure. The expressions for the modes are also given in table C.2.

Tower fore-aft mode 1	$\Phi_7(x) = 0.70x^2 + 2.19x^3 - 5.62x^4 + 6.22x^5 - 2.50x^6$
Tower fore-aft mode 2	$\Phi_8(x) = -70.53x^2 - 63.76x^3 + 289.73x^4 - 176.51x^5 + 22.07x^6$
Tower side-side mode 1	$\Phi_9(x) = 1.38x^2 - 1.76x^3 + 3.08x^4 - 2.23x^5 + 0.53x^6$
Tower side-side mode 2	$\Phi_{10}(x) = -121.20x^2 + 184.41x^3 - 224.90x^4 + 298.53x^5 - 135.83x^6$
Blade flap mode 1	$\Phi_{14}(x) = 0.06x^2 + 1.72x^3 - 3.24x^4 + 4.71x^5 - 2.25x^6$
Blade flap mode 2	$\Phi_{15}(x) = -0.58x^2 + 1.20x^3 - 15.53x^4 + 29.73x^5 - 13.82x^6$
Blade edge mode 1	$\Phi_{16}(x) = 0.36x^2 + 2.53x^3 - 3.57x^4 + 2.37x^5 - 0.69x^6$

Table C.2: Expressions for mode shapes of tower and blades. Numbering of the dofs are given in figure A.1.

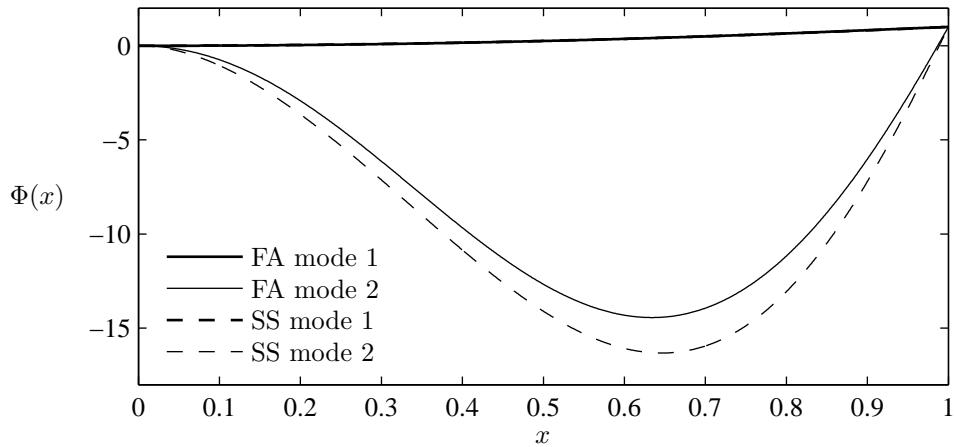


Figure C.1: Mode shapes for tower fore-aft (FA) and side-side (SS) motions.

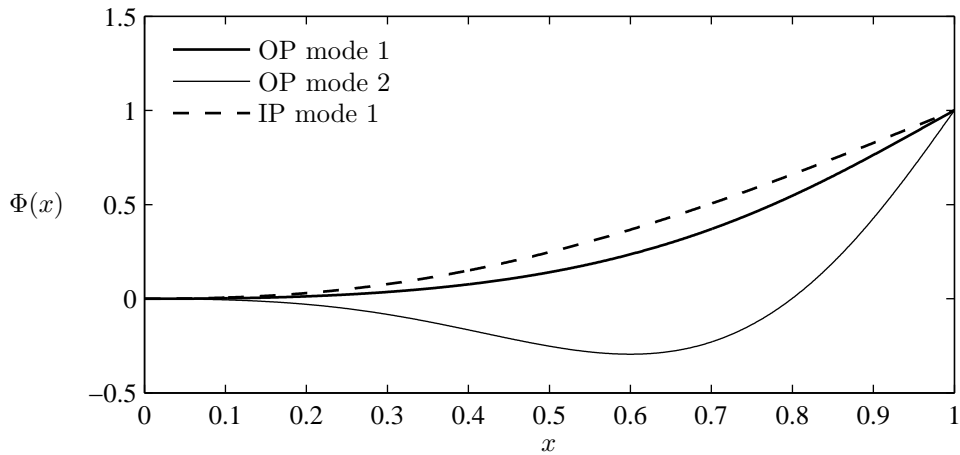


Figure C.2: Mode shapes for blade in-plane (IP) and out-of-plane (OP) motions.

The eigenfrequencies of the structural parts of the wind turbine are given in table C.3.

Mode	[rad/s]
Tower fore-aft mode 1	2.1
Tower fore-aft mode 2	19.2
Tower side-side mode 1	2.1
Tower side-side mode 2	19.2
Blade flap mode 1	4.6
Blade flap mode 2	12.7
Blade edge mode 1	7.0

Table C.3: Angular eigenfrequencies of modes.

The initial conditions for all simulations are set according to steady-state behavior as described in the definition paper of the wind turbine [Jonkman et al., 2009]. The initial conditions that can be

specified in the FAST input file are; blade pitch angles, blade out-of-plane displacement, tower top fore-aft displacement and rotor speed. For all simulations the total run time is set to 650 s of which the last 600 s are used for analysis to make sure that no influence from initial conditions is present.

The turbulence applied is simulated by TurbSim or the state space model described in appendices B.1 and B.3, respectively. The turbulence from Turbsim is simulated in a rectangular grid of 160×160 m using a total of 64 grid points - 8 grid points in both vertical and horizontal direction. The turbulence simulated using a state space model is simulated in a circular grid with diameter 125 m using a total of 61 grid points - 1 grid point in the hub center, 10 grid points in angular direction and 6 in radial direction.

Appendix D

Analysis of wind turbine response Gaussianity

In order to test the Gaussianity of the response from the wind turbine structural model, the statistical moments of the 1st order distribution are useful. For Gaussian random variables the following results for the normalised n 'th order statistical moment, m_n , apply [Nielsen, 2007b].

$$m_n = \frac{E[(M - \mu_M)^n]}{\sigma_M^n} = \begin{cases} 0 & , n \text{ odd} \\ (n-1)(n-3)\dots 3 \cdot 1 & , n \text{ even} \end{cases} \quad (\text{D.1})$$

This means that the 3rd order normalised central moment (skewness) should be 0 and the 4th order normalised central moment (kurtosis) should be 3. The sample data used are the data from the analysis in section 2.2. For different wind speed bins the skewness and kurtosis have been calculated. For all wind speed bins, except 13 – 15 m/s and 15 – 17 m/s, the skewness is in the interval -0.2 to 0.2 . For the 13 – 15 m/s and 15 – 17 m/s bins the skewnesses are 0.46 and 0.36 respectively which seems to be a relatively high deviation from the Gaussianity criteria. The largest deviations from the kurtosis for a Gaussian random variable occurs in the 11 – 13 m/s and 15 – 17 m/s bins having values of 2.59 and 3.2, respectively. Convergence of estimates of the skewness and kurtosis in the 13 – 15 m/s bin as a function of the sampling interval t is shown in figure D.1. The curves represent the mean values of the running ergodic estimates of 10 independent realisations. It seems that the response is not Gaussian and will neither be Gaussian for larger times series as m_3 and m_4 does not converge toward 0 and 3, respectively. The reason for the non-Gaussianity might be non-linearities in the control systems or non-linearities in the aerodynamic loads which consequently seems to be specific active in the 13 – 15 m/s bin. A description of the non-linearities included in the FAST model is given in appendix A.

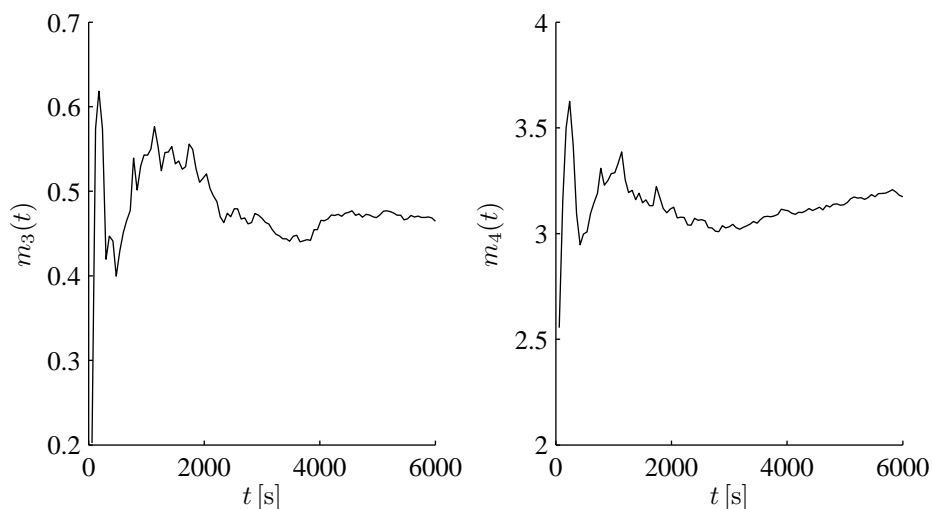


Figure D.1: Convergence of ergodic sampling of skewness and kurtosis for 13 – 15 m/s bin as a function of time. Mean values of 10 realisations.

Appendix E

Load extrapolation

E.1 Extrapolation results and observations by LE³

The load extrapolation requirements were introduced in the IEC61400-1 standard in 2005. Shortly after, the IEC decided to commission a subcommittee "Loads Extrapolation and Evaluation Exercise (LE³)" [Moriarty and Veers, 2008]. A part of the work by this subcommittee was the so-called LE³ meeting, which were held in April 2007. The meeting was based on the 2005 version of the IEC61400-1 standard (Annex F) which concerns determination of extreme responses for wind turbines. Several members of the wind turbine industry were invited to present results obtained on the same dataset from simulations of the "NREL offshore 5-MW baseline wind turbine". The participants presented results obtained by using the normal methods used in determining extreme responses in their organisation or company. The following description is based on [Moriarty, 2007]

The results obtained by the participants are listed in table E.1. The table lists methods used for data extraction, probability distribution function (CDF), the number of simulations used in each wind speed bin and the results obtained using the different methods. In the following, details of the methods and results from the different participants are shown.

Participant 1 tested both the global maxima method and the POT method using the 3-parameter Weibull probability distribution function and a minimum time separation of 5 s between maxima. It is seen that the global maxima and the POT methods provide significantly different extrapolated responses, even when utilising a large number of simulations in each bin. The participant suggests that a threshold is chosen by visual inspection of the probability distribution function of the maxima. The probability distribution function shows a sudden change of slope which makes the 3-parameter Weibull distribution function fit inferior. Instead the threshold is chosen as the value of the response where a change of slope occurs, see figure E.1

Participant 2 tested the global maxima method using 3 different candidate distribution functions; the generalised extreme value distribution function, the 3-parameter Weibull distribution function and the log-normal distribution function. The results obtained for the 3-parameter Weibull and the log-normal distribution functions seems to correspond well to the results obtained by participant 1, whereas the generalised extreme value distribution function seems to give considerable larger responses.

Participant 3 tested the generalised Pareto probability distribution function using a minimum time separation between maxima of 15 s. The participant concludes that at least 40 simulations in each bin are required to get a reliable extrapolation of responses corresponding to a 50 year recurrence period. Also, it is concluded that choosing the threshold providing the best fit is very difficult because the optimal short term fit in terms of average relative error does not necessarily lead to a "good" extrapolation.

Participant 4 tested the 3-parameter Weibull probability distribution function using maxima for every 100 s of the simulations. The out-of-plane bending moment corresponding to a 50 year recurrence period is estimated using different numbers of simulations - see figure E.2. The number of simulations seems to have a great influence on the confidence of the obtained response.

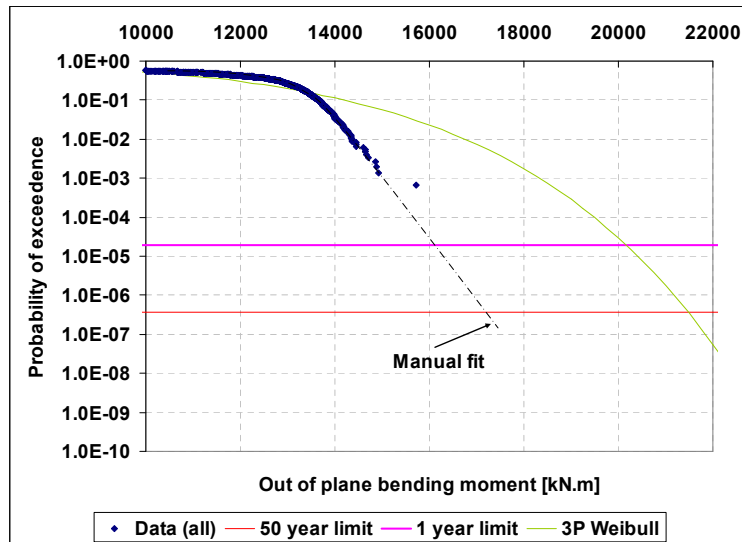


Figure E.1: Choice of threshold suggested by participant 1 [Moriarty, 2007].

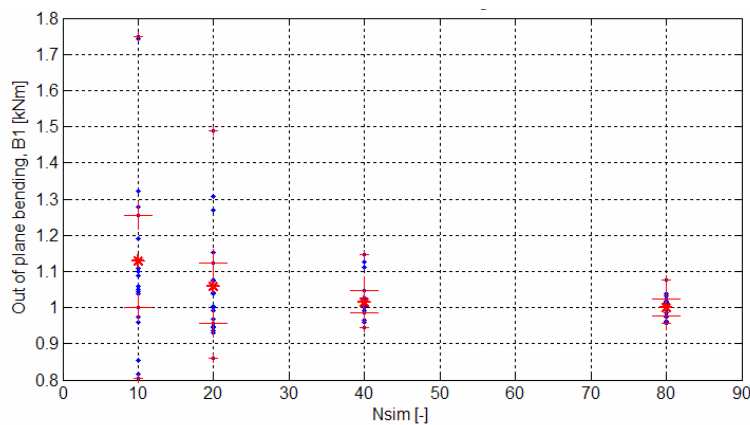


Figure E.2: Results obtained for different number of simulations in each wind speed bin using 3-parameter Weibull probability distribution function. The values on the ordinate are normalised with respect to the mean value obtained for 80 simulations/bin. The figure shows the estimates (dots), the mean value of the estimates (stars) and the confidence intervals (lines) [Moriarty, 2007].

Participant	Extraction	CDF	Sim./bin	Response [kNm]	
1	Global Maxima	3P Weibull	30	18750	
			100	17667	
			200	17500	
	POT - $\mu_M + 1.4\sigma_M$			30	22333
				30	22000
				30	22500
				Assembled	Variable
2	Global Maxima	GEV	30	21841	
		3P Weibull	30	17426	
		Log-normal	30	17723	
3	Top 175 or less	Pareto	200	19637	
4	Max in 100 sec.	3P Weibull	10	18324	
			20	18548	
			40	18411	
			80	18948	
5	Top 175 to Top 19	Pareto	10	27817	
			20	24665	
			40	22464	
		3P Weibull	80	21127	
			10	22078	
			20	20880	
			40	19625	
			80	18886	
			80	18886	
6	POT - $m+1.4sd$	Lexpol	10	16847	
			20	16744	
			40	16638	
			60	16582	
			80	16576	
			100	16552	
			200	16537	

Table E.1: Results obtained by participants at LE³Boulder meeting. The response shown is the blade out-of-plane moment. ¹Global peak over threshold for all bins. [Moriarty, 2007]

Participant 5 tested the Pareto and 3-parameter Weibull probability distribution functions using a minimum time separation of 7.5s in extracting maxima. The short term probability distribution functions are fitted using between 19 and 175 extreme values. The fits providing an average relative error above 5% are discarded and so are fits obtained using a large number of extreme values. The response is determined by the mean of the extrapolated responses of the remaining fits. The response obtained for the candidate probability distribution functions using different number of simulations in each bin is shown in figure E.3. In general it can be concluded that the 3-parameter Weibull probability distribution function is more stable than the Pareto probability distribution function for low number of seeds. However, it is also seen that a large number of simulations are needed to obtain convergence.

Participant 6 tested the commercial code Lexpol. No further comments will be given on the results obtained by this code as the methods behind the code is not fully publicly available.

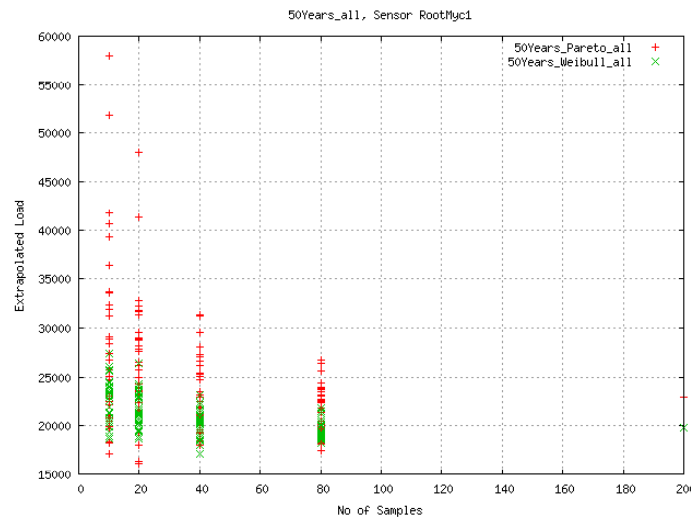


Figure E.3: Results obtained by 3-parameter Weibull and Pareto probability distribution functions for different number of simulations in each wind speed bin for participant 5 [Moriarty, 2007].

E.1.1 Conclusion

The meeting summary points out the problems and uncertainties found by the participants. Regarding extraction of maxima, the general observation is that by using the POT method one might lose important points and care should be taken that the extracted values are independent, e.g. by introducing a minimum time separation. Time separations between 5 s and 15 s have been used and it is concluded that a method of determining independence between maxima should be developed.

The contributors used different probability distribution functions in fitting the local probabilities in each wind speed bin. No conclusion was made on which probability distribution function to prefer. However, the 3-parameter Weibull probability distribution function was chosen by most participants and was also found to be more stable than the Pareto distribution function c.f. figure E.3.

The number of simulations to use in each bin for convergence is dependent on the choice of probability distribution function. It is concluded that using only 10 simulations in each bin, which was the case for most of the industry, is not sufficient. Instead some convergence criteria that can be easily employed has to be developed.

E.2 Amendment to IEC61400-1:2005 - draft for voting

Because of the problem and uncertainties described in appendix E.1, the IEC Technical Committee for Wind Turbines has prepared an amendment for the IEC61400-1:2005 [IEC Technical Committee 88, 2009]. This amendment clarifies and provides guidance to specific topics and issues in the standard. The load extrapolation method is clarified in the amendment by total rewriting the description of load extrapolation in Annex F. In the following a description of the overall changes in the extrapolation method are described.

The amendment suggest two general methods of extrapolating the extreme response:

1. Extract extreme values in each wind speed bin and determine probability distribution functions in each wind speed bin by fitting candidate distribution functions. The response corresponding to a 50-year recurrence period is determined by weighing the probability distribution functions

by the probability of occurrence of each wind speed bin.

2. Perform a given number of simulations in each wind speed bin. The number of simulations in each wind speed bin is determined by the wind speed probability distribution function. Aggregate all extracted maximum values and fit one global probability distribution function and determine the load from the global probability distribution function.

The amendment does not suggest use of the Gumbel and 3-parameter Weibull distribution functions as candidates. Instead it is now up to the designer to choose a suitable probability distribution function.

In the IEC61400-1:2005 standard extrapolation of maximum values is performed by the POT method by extracting values larger than the mean value plus 1.4 times the standard deviation. The amendment suggests use of one global maxima in each 10 minute time series or use of a block method, where e.g. the 10 minute time series are split into 10 time series of 1 minute and maxima in each block is extracted. When utilising one of the extraction methods a minimum time separation between successive maximas should be at least three response cycles to minimise dependence between maximum values. Also, different methods for testing independence between maximas are suggested in the amendment.

The minimum number of simulations to perform in each wind speed bin is set to 15 by the amendment. This is significantly larger than in the IEC61400-1:2005 where a minimum simulation time of 300s distributed over the significant wind conditions were suggested. Also, a convergence criteria is to be applied to the extracted maximas. Different methods are suggested to make sure that the extrapolated response is within a given confidence level.

Appendix F

Extremes of stationary Gaussian processes

Distribution of local maxima in stationary Gaussian processes

$\{X(t), t \in R\}$ is a stationary Gaussian process with the mean value function μ_X , the standard deviation σ_X , and the autocorrelation coefficient function $\rho_{XX}(\tau)$. Let $\{A_1, A_2, \dots, A_n\}$ denote the stationary stochastic sequence of the local maxima of the process in a given interval $[0, T]$. Further, if certain ergodicity properties are fulfilled the first order probability distribution function of the indicated sequence is given as [Nielsen, 2007b]

$$F_A(a) = 1 - \frac{\mu_a}{\mu_0} \quad (\text{F.1})$$

where μ_a and μ_0 denote the expected number of local maxima in the interval above the levels a and μ_X , respectively. If the process is at least twice differentiable, so the standard deviations $\sigma_{\dot{X}}$ and $\sigma_{\ddot{X}}$ exist, these become [Nielsen, 2007b]

$$\mu_0 = \frac{1}{2\pi} \frac{\sigma_{\ddot{X}}}{\sigma_{\dot{X}}} \quad (\text{F.2})$$

$$\mu_a = \frac{1}{\sqrt{2\pi}} \frac{\sigma_{\ddot{X}}}{\sigma_{\dot{X}}} \int_{\alpha}^{\infty} \varphi(u) \left(\int_{-\infty}^0 -\frac{w}{\sqrt{1-r^2}} \varphi\left(\frac{w-ru}{\sqrt{1-r^2}}\right) dw \right) du \quad (\text{F.3})$$

where $\varphi(\cdot)$ indicates the standardized normal probability density function, and

$$\alpha = \frac{a - \mu_X}{\sigma_X}, \quad r = -\frac{\sigma_{\dot{X}}^2}{\sigma_X \sigma_{\ddot{X}}} \quad (\text{F.4})$$

The innermost integral in (F.3) can be evaluated analytically in terms of the standardized normal probability density and distribution functions. r denotes the correlation coefficient between $X(t)$ and $\dot{X}(t)$, which is slightly above -1 for a narrow-banded process. In the extreme narrow-banded limit, as $r \rightarrow -1$, (F.1) reduces to the Rayleigh distribution [Nielsen, 2007b]

$$F_A(a) = 1 - \exp\left(-\frac{1}{2} \left(\frac{a - \mu_X}{\sigma_X}\right)^2\right) \quad (\text{F.5})$$

In the extreme broad-banded limit, as $r \rightarrow 0$, the distribution function becomes Gaussian [Nielsen, 2007b]

$$F_A(a) = 1 - \Phi\left(\frac{a - \mu_X}{\sigma_X}\right) \quad (\text{F.6})$$

where $\Phi(\cdot)$ indicates the standardized normal probability distribution function.

Distribution of extremes in stationary Gaussian processes

Let

$$A_{\max}(T) = \max(A_1, A_2, \dots, A_n) \quad (\text{F.7})$$

Further, assume that the local maxima of the process in the considered interval of the length T is stochastic independent and identical distributed random variables. Then, the distribution function of $A_{\max}(T)$ becomes

$$\begin{aligned} F_{A_{\max}(T)}(a) &= P(A_{\max}(T) \leq a) = P(A_1 \leq a \wedge A_2 \leq a \wedge \dots \wedge A_n \leq a) = \\ &= \prod_{j=1}^n F_{A_j}(a) = F_A^n(a) = \left(1 - \frac{\mu_a}{\mu_0}\right)^n = \exp\left(n \ln\left(1 - \frac{\mu_a}{\mu_0}\right)\right) \simeq \exp\left(-n \frac{\mu_a}{\mu_0}\right) \end{aligned} \quad (\text{F.8})$$

The last statement of (F.8) presumes that $\mu_a \ll \mu_0$. Let n denote the expected number of local maxima above μ_X during the interval T . Then, n is given as

$$n = T \mu_0 \quad (\text{F.9})$$

In turn this means that (F.8) reduces to

$$F_{A_{\max}(T)}(a) = \exp(-\mu_a T) \quad (\text{F.10})$$

Next, we are interested in the distribution function of the maximum local maxima during the interval T , on condition that the local maxima are above some threshold $a_0 > \mu_X$. The conditional distribution function becomes

$$F_A(a|A > a_0) = \frac{P(a_0 < A \leq a)}{P(a_0 < A)} = \frac{F_A(a) - F_A(a_0)}{1 - F_A(a_0)} = \frac{\frac{\mu_{a_0}}{\mu_0} - \frac{\mu_a}{\mu_0}}{\frac{\mu_{a_0}}{\mu_0}} = 1 - \frac{\mu_a}{\mu_{a_0}} \quad (\text{F.11})$$

The distribution function of the maximum local maxima on condition that the local maxima are above the threshold a_0 becomes, cf. (F.8)

$$F_{A_{\max}(T)}(a|A > a_0) = F_A^n(a|A > a_0) = \left(1 - \frac{\mu_a}{\mu_{a_0}}\right)^n \simeq \exp\left(-n \frac{\mu_a}{\mu_{a_0}}\right) \quad (\text{F.12})$$

where $\mu_a \ll \mu_0$ has been assumed in the last statement of (F.12). Now, let n denote the expected number of local maxima above a_0 during the interval T . Then, n is given as

$$n = T \mu_{a_0} \quad (\text{F.13})$$

In turn this means that (F.12) reduces to

$$F_{A_{\max}(T)}(a|A > a_0) = \exp(-\mu_a T) \quad (\text{F.14})$$

From (F.14) is concluding that the distribution function of the maximum local maxima during the interval on condition of maxima above a certain threshold a_0 is not depending on the threshold level. The result presumes Gaussianity of the underlying stochastic process, and that $\mu_a \ll \mu_{a_0}$.

First passage time distribution and recurrence period

Let b denote a critical upper barrier of the considered process, and let T_1 be the first-passage time of the process in relation to the thus defined safe domain. The probability distribution function of T_1 follows from

$$F_{T_1}(t) = P(T_1 \leq t) = P(A_{\max}(t) > b) = 1 - \exp(-\mu_b t) \quad (\text{F.15})$$

(F.15) shows that the hazard rate of the process is given by μ_b as calculated from (F.3) for $b = a$. The recurrence period $T_r = E[T_1]$ becomes

$$T_r = \frac{1}{\mu_b} \quad (\text{F.16})$$

For a given recurrence period the design value b_{cr} of the barrier function is obtained as the solution $b = b_{cr}$ to (F.15).

Appendix G

Modal analysis of plane n storey shear frame exposed to a horizontal earthquake excitation

Equations of Motion

The total horizontal displacements x_j of the storey beams relative to the ground surface are chosen as degree of freedom. This is inconsistent with the equation of motion given in chapter 4, but this allows to set up the system parameters on a simple analytical form. The damping ratios and eigenfrequencies of the system are independent of the reference frame, whereby the relative displacements are easily achieved. The absolute storey displacement is given as x_j and the relative storey displacement is denoted y_j .

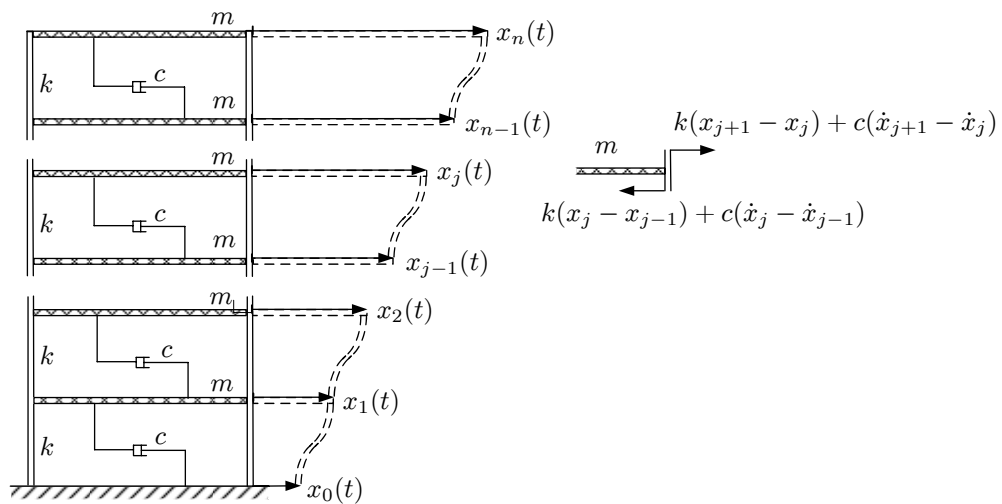


Figure G.1: Illustration of the absolute displacements and forces acting on the j th storey for a n storey shear frame.

The storeys are cut free from the columns and the damper elements, and Newton's 2nd law of motion is applied to each storey mass:

$$\left. \begin{aligned}
 m(\ddot{x}_0 + \ddot{x}_1) &= -k x_1 + k(x_2 - x_1) - c\dot{x}_1 + c(\dot{x}_2 - \dot{x}_1) \\
 \vdots \\
 m(\ddot{x}_0 + \ddot{x}_j) &= -k(x_j - x_{j-1}) + k(x_{j+1} - x_j) - c(\dot{x}_j - \dot{x}_{j-1}) + c(\dot{x}_{j+1} - \dot{x}_j) \quad , \quad j = 2, \dots, n-1 \\
 \vdots \\
 m(\ddot{x}_0 + \ddot{x}_n) &= -k(x_n - x_{n-1}) - c(\dot{x}_n - \dot{x}_{n-1})
 \end{aligned} \right\} \quad (G.1)$$

(G.1) may be stated in the following matrix format

$$\ddot{\mathbf{x}} + 2\zeta_0\omega_0 \mathbf{k} \dot{\mathbf{x}} + \omega_0^2 \mathbf{k} \mathbf{x} = -\mathbf{b}\ddot{x}_0(t) \quad (G.2)$$

where

$$\mathbf{x}(t) = \begin{bmatrix} x_1(t) \\ x_2(t) \\ \vdots \\ x_n(t) \end{bmatrix}, \quad \mathbf{k} = \begin{bmatrix} 2 & -1 & 0 & \cdots & 0 & 0 & 0 \\ -1 & 2 & -1 & \cdots & 0 & 0 & 0 \\ \vdots & \vdots & \vdots & \ddots & \vdots & \vdots & \vdots \\ 0 & 0 & 0 & \cdots & -1 & 2 & -1 \\ 0 & 0 & 0 & \cdots & 0 & -1 & 1 \end{bmatrix}, \quad \mathbf{b} = \begin{bmatrix} 1 \\ 1 \\ \vdots \\ 1 \end{bmatrix} \quad (G.3)$$

$$\omega_0 = \sqrt{\frac{k}{m}} \quad , \quad \zeta_0 = \frac{c}{2\sqrt{km}} \quad (G.4)$$

Eigenvibration Analysis

Given the following eigenvalue problem

$$(\mathbf{k} - \lambda \mathbf{I}) \Phi = \mathbf{0} \quad , \quad \lambda = \frac{\omega^2}{\omega_0^2} \quad , \quad \Phi = \begin{bmatrix} \Phi_1 \\ \Phi_2 \\ \vdots \\ \Phi_{n-1} \\ \Phi_n \end{bmatrix} \quad (G.5)$$

The homogeneous matrix equation (G.5) may be restated in terms of the following component equations

$$\left. \begin{aligned}
 2\Phi_1 - \Phi_2 - \lambda\Phi_1 &= 0 \quad , \quad j = 1 \\
 -\Phi_{j-1} + 2\Phi_j - \Phi_{j+1} - \lambda\Phi_j &= 0 \quad , \quad j = 2, \dots, n-1 \\
 -\Phi_{n-1} + \Phi_n - \lambda\Phi_n &= 0 \quad , \quad j = n
 \end{aligned} \right\} \quad (G.6)$$

A solution to (G.6) is searched on the form [Geradin and Rixen, 1997]

$$\Phi_j = \sin(j\mu) \quad , \quad j = 1, \dots, n \quad (\text{G.7})$$

μ and λ are next determined, so all n equations in (G.6) are fulfilled. Insertion into the equations for $j = 2, \dots, n - 1$ provides

$$\begin{aligned} -\sin((j-1)\mu) + 2\sin(j\mu) - \sin((j+1)\mu) - \lambda\sin(j\mu) &= 0 & \Rightarrow \\ -\sin(j\mu)\cos\mu + \cos(j\mu)\sin\mu + 2\sin(j\mu) - \sin(j\mu)\cos\mu - \cos(j\mu)\sin\mu - \lambda\sin(j\mu) &= 0 & \Rightarrow \\ -\sin(j\mu)(\cos\mu - 2 + \cos\mu + \lambda) &= 0 & (\text{G.8}) \end{aligned}$$

(G.8) is fulfilled for $\sin(j\mu) = \Phi_j = 0$, which corresponds to the trivial solutions. Hence, (G.7) represents non-trivial solutions, if the following relation is fulfilled between λ and μ

$$\lambda = 2(1 - \cos\mu) \quad (\text{G.9})$$

Upon insertion of (G.7) into the first equation in (G.6), it is seen that fulfillment of this equation again leads to the relation (G.9). Finally, insertion into the last equation of (G.6) provides

$$\begin{aligned} -\sin((n-1)\mu) + \sin(n\mu) - \lambda\sin(n\mu) &= 0 & \Rightarrow \\ -\sin(n\mu)\cos\mu + \cos(n\mu)\sin\mu + \sin(n\mu) - 2\sin(n\mu) + 2\sin(n\mu)\cos\mu &= 0 & \Rightarrow \\ -\sin(n\mu) + \sin(n\mu)\cos\mu + \cos(n\mu)\sin\mu &= 0 & \Rightarrow \\ \sin((n+1)\mu) = \sin(n\mu) = \sin(\pi - n\mu) & & (\text{G.10}) \end{aligned}$$

where (G.9) has been used to eliminate λ . (G.10) has the solutions

$$\left. \begin{aligned} (n+1)\mu = n\mu + 2\pi(l-1) & \Rightarrow \mu_l = 2\pi(l-1) \\ (n+1)\mu = \pi - n\mu + 2\pi(l-1) & \Rightarrow \mu_l = \frac{2l-1}{2n+1}\pi \end{aligned} \right\} \quad , \quad l = 1, 2, \dots, n \quad (\text{G.11})$$

The first solution implies that $\sin(j\mu_l) = 0$, and hence implies the trivial solution. The second solution determines the non-trivial solutions to the problem. The components of the l th eigenmode become

$$\Phi_j^{(l)} = \sin(j\mu_l) = \sin\left(j \frac{2l-1}{2n+1} \pi\right) \quad , \quad l = 1, 2, \dots, n \quad (\text{G.12})$$

The undamped angular eigenfrequencies follow from (G.9) and (G.11)

$$\omega_l = \omega_0 \sqrt{2(1 - \cos \mu_l)} = \omega_0 \sqrt{2 \left(1 - \cos \left(\frac{2l-1}{2n+1} \pi \right) \right)} \quad , \quad l = 1, 2, \dots, n \quad (G.13)$$

For a two storey frame (G.12) and (G.13) provides the results

$$\omega_l^2 = \begin{cases} \sqrt{2(1 - \cos(\pi/5))} \omega_0 & , \quad l = 1 \\ \sqrt{2(1 - \cos(3\pi/5))} \omega_0 & , \quad l = 2 \end{cases} \quad (G.14)$$

$$\Phi^{(l)} = \begin{cases} \begin{bmatrix} \sin(\pi/5) \\ \sin(2\pi/5) \end{bmatrix} & , \quad l = 1 \\ \begin{bmatrix} \sin(3\pi/5) \\ \sin(6\pi/5) \end{bmatrix} & , \quad l = 2 \end{cases} \quad (G.15)$$

Modal Masses

$$m_l = m \Phi^{(l)T} \mathbf{I} \Phi^{(l)} = m \sum_{j=1}^n \left(\Phi_j^{(l)} \right)^2 = m \sum_{j=1}^n \sin^2 (j\mu_l) = m \left(\frac{2n+1}{4} - \frac{1}{4} \frac{\sin((2n+1)\mu_l)}{\sin \mu_l} \right) = \frac{2n+1}{4} m \quad (G.16)$$

where it has been used that $\sin((2n+1)\mu_l) = \sin((2l-1)\pi) = 0$. Hence, the modal masses are identical for all modes.

Modal Damping Ratios

$$2 \zeta_l \omega_l m_l = \Phi^{(l)T} \mathbf{C} \Phi^{(l)} = \frac{c}{k} \Phi^{(l)T} \mathbf{K} \Phi^{(l)} = \frac{c}{k} \omega_l^2 m_l \Rightarrow \zeta_l = \frac{1}{2} \frac{c}{k} \omega_l = \zeta_0 \sqrt{2 \left(1 - \cos \left(\frac{2l-1}{2n+1} \pi \right) \right)} \quad , \quad l = 1, \dots, n \quad (G.17)$$

where \mathbf{C} and \mathbf{K} are the modal damping matrix and modal stiffness matrix, respectively.

Modal Loads

$$F_l(t) = -\Phi^{(l)T} \mathbf{b} \ddot{x}_0(t) \quad (G.18)$$

where

$$\begin{aligned} \Phi^{(l)T} \mathbf{b} &= \sum_{j=1}^n \Phi_j^{(l)} = \sum_{j=1}^n \sin(j\mu_l) = \\ \frac{1}{2} \frac{\cos\left(\frac{\mu_l}{2}\right) - \cos\left((2n+1)\frac{\mu_l}{2}\right)}{\sin\left(\frac{\mu_l}{2}\right)} &= \frac{1}{2} \frac{\cos\left(\frac{\mu_l}{2}\right)}{\sin\left(\frac{\mu_l}{2}\right)}, \quad l = 1, 2, \dots, n \end{aligned} \quad (\text{G.19})$$

where it has been used that $\cos\left((2n+1)\frac{\mu_l}{2}\right) = \cos\left((2l-1)\frac{\pi}{2}\right) = 0$.

Frequency Response Function of Relative Storey Displacements

Now, the frequency response function of the relative storey displacement is determined. The frequency response matrix of the system admits the following expansion in outer products of the eigenmodes [Nielsen, 2007b]

$$\mathbf{H}(z) = \left(\mathbf{I}z^2 + 2\zeta_0 \omega_0 \mathbf{k}z + \omega_0^2 \mathbf{k} \right)^{-1} = \sum_{l=1}^n \frac{\Phi^{(l)} \Phi^{(l)T}}{m_l (z^2 + 2\zeta_l \omega_l z + \omega_l^2)} \quad (\text{G.20})$$

The relative displacement between the $j-1$ th and j th storey is given as

$$y_j(t) = x_j(t) - x_{j-1}(t) = \mathbf{a}_j^T \mathbf{x}(t) \quad (\text{G.21})$$

where

$$\mathbf{a}_1 = \begin{bmatrix} 1 \\ \vdots \\ 0 \\ 0 \\ 0 \\ 0 \\ \vdots \\ 0 \end{bmatrix}, \quad \mathbf{a}_j = \begin{bmatrix} 0 \\ \vdots \\ 0 \\ -1 \\ 1 \\ 0 \\ \vdots \\ 0 \end{bmatrix} \leftarrow j\text{th component}, \quad j = 2, \dots, n \quad (\text{G.22})$$

A harmonically varying support point acceleration with the amplitude $\ddot{X}_0(z)$ causes a harmonically varying relative storey displacement with the amplitude $\ddot{Y}_j(z)$ given as

$$\ddot{Y}_j(z) = H_j(z) \ddot{X}_0(z) \quad (\text{G.23})$$

where

$$H_j(z) = -\mathbf{a}_j^T \mathbf{H}(z) \mathbf{b} = -\mathbf{a}_j^T \left(\sum_{l=1}^n \frac{\Phi^{(l)} \Phi^{(l)T}}{m_l (z^2 + 2\zeta_l \omega_l z + \omega_l^2)} \right) \mathbf{b} = \sum_{l=1}^n \frac{c_{jl}}{z^2 + 2\zeta_l \omega_l z + \omega_l^2} \quad (\text{G.24})$$

$$\begin{aligned}
 c_{jl} &= -\frac{1}{m_l} \mathbf{a}_j^T \Phi^{(l)} \Phi^{(l)T} \mathbf{b} = -\frac{4}{(2n+1)m} \left(\Phi_j^{(l)} - \Phi_{j-1}^{(l)} \right) \Phi^{(l)T} \mathbf{b} = \\
 &= -\frac{4}{(2n+1)m} \left(\sin(j\mu_l) - \sin((j-1)\mu_l) \right) \cdot \frac{1}{2} \frac{\cos\left(\frac{\mu_l}{2}\right)}{\sin\left(\frac{\mu_l}{2}\right)} = \\
 &= -\frac{4}{(2n+1)m} \cdot 2 \cos\left((2j-1)\frac{\mu_l}{2}\right) \sin\left(\frac{\mu_l}{2}\right) \cdot \frac{1}{2} \frac{\cos\left(\frac{\mu_l}{2}\right)}{\sin\left(\frac{\mu_l}{2}\right)} = \\
 &= -\frac{4}{(2n+1)m} \cos\left((2j-1)\frac{\mu_l}{2}\right) \cos\left(\frac{\mu_l}{2}\right)
 \end{aligned} \tag{G.25}$$

Upon assembling the terms within the summation in (G.24) with a common denominator the frequency response function may be written as the following rational function

$$H_j(z) = \frac{P_j(z)}{Q(z)} \tag{G.26}$$

$$P_j(z) = p_{j0}z^{2n-2} + p_{j1}z^{2n-3} + \dots + p_{j,2n-3}z + p_{j,2n-2} \quad , \quad j = 1, \dots, n \tag{G.27}$$

$$Q(z) = \prod_{k=1}^{2n} (z - z_k) \tag{G.28}$$

where the poles z_k are given as

$$\left. \begin{matrix} z_{2k-1} \\ z_{2k} \end{matrix} \right\} = \omega_k \left(-\zeta_k \pm \sqrt{1 - \zeta_k^2} \right) \quad , \quad k = 1, \dots, n \tag{G.29}$$

The function values of $P_j(z)$ can be evaluated from the relation

$$P_j(z) = H_j(z)Q(z) = \sum_{l=1}^n \frac{c_{jl}}{z^2 + 2\zeta_l \omega_l z + \omega_l^2} \cdot \prod_{k=1}^{2n} (z - z_k) \tag{G.30}$$

By entering $2n - 1$ different values of z (G.29) a linear system of equations may be formulated from which the coefficients $p_{j0}, p_{j1}, \dots, p_{j,2n-3}, p_{j,2n-2}$ in (G.27) may be determined. For $n=5, m = \omega_0 = 1, \zeta_0 = 0.01$ the following results are obtained for the 5 interstoreys

$$\begin{array}{c} \downarrow \\ j \end{array} \begin{array}{c} \rightarrow l = 0, \dots, 8 \\ \left| \begin{array}{ccccccccc} -1.0000 & -0.1600 & -8.0084 & -0.8402 & -21.0240 & -1.2002 & -20.0120 & -0.4000 & -5.0000 \\ -0.0000 & -0.0200 & -1.0024 & -0.2401 & -6.0120 & -0.6001 & -10.0096 & -0.3200 & -4.0000 \\ -0.0000 & 0.0000 & -0.0004 & -0.0400 & -1.0048 & -0.2401 & -4.0072 & -0.2400 & -3.0000 \\ 0.0000 & -0.0000 & 0.0000 & -0.0000 & -0.0012 & -0.0601 & -1.0048 & -0.1600 & -2.0000 \\ -0.0000 & 0.0000 & -0.0000 & 0.0000 & -0.0000 & -0.0000 & -0.0024 & -0.0800 & -1.0000 \end{array} \right| \end{array}$$

Table 1: Coefficients p_{jl} for the numerator polynomials in the frequency response function for the j th relative interstorey displacement $y_j(t)$ for a 5 storey shear frame. $m = 1$, $\zeta_0 = 0.01$, $\omega_0 = 1$.

As seen from the table the order of the numerator polynomials decrease with one for each storey above the surface. Hence, the response of these become increasingly smooth.

Appendix H

Assessments of the Broken Line Process

Some issues can occur when generating the broken line process which will be investigated in this appendix. Consider a random variable \tilde{O}_j of the broken line process randomly interpolated linearly between the two variables O_i and O_{i+1} cf. figure H.1. $O_1 \dots O_n$ are independent zero-mean normally distributed random variables with the variance σ_O^2 . The random variable \tilde{O}_j is obtained by

$$\tilde{O}_j = O_i + (O_{i+1} - O_i) \frac{\epsilon \Delta t_{bl}}{\Delta t_{bl}} \quad (\text{H.1})$$

where ϵ is a random uniformly distributed variable in the interval $[0, 1]$. Note that \tilde{O}_j is not Gaussian unless ϵ is deterministic. The reason for distinguishing between indices i and j on the O and \tilde{O} processes is that the number of interpolated time intervals for the \tilde{O} process is not equal to the number of original time steps for the O process.

Since ϵ is independent of O_i and O_{i+1} , the expectation of \tilde{O}_j becomes

$$\begin{aligned} \text{E} [\tilde{O}_j] &= \text{E} [O_i + (O_{i+1} - O_i) \epsilon] = \\ &= \text{E} [O_i] + \text{E} [O_{i+1} - O_i] \text{E} [\epsilon] = 0 \end{aligned} \quad (\text{H.2})$$

The variance of \tilde{O}_j is determined by

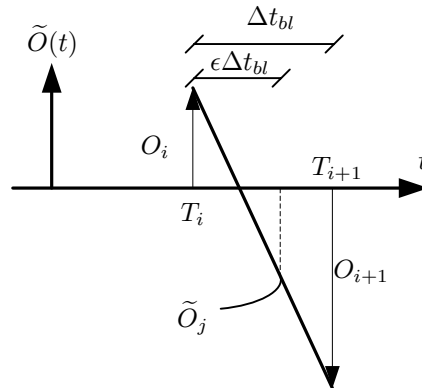


Figure H.1: Interpolation of the process \tilde{O}_j .

$$\begin{aligned}
 E[\tilde{O}_j \tilde{O}_j] &= E [O_i^2] + (E [O_{i+1}^2] + E [O_i^2] - 2E [O_i O_{i+1}]) E [\epsilon^2] \\
 &\quad + 2 (E [O_{i+1} O_i] - E [O_i O_i]) E [\epsilon] \\
 &= \sigma_O^2 + 2\sigma_O^2 E [\epsilon^2] - 2\sigma_O^2 E [\epsilon] \\
 &= \sigma_O^2 \left(1 + \frac{2}{3} - 1 \right) = \frac{2}{3} \sigma_O^2
 \end{aligned}
 \tag{H.3}$$

If ϵ is deterministic as shown on figure H.2 $\sigma_{\tilde{O}_j}^2$ is determined by

$$\sigma_{\tilde{O}_j}^2 = \sigma_O^2 (2\epsilon^2 - 2\epsilon + 1)
 \tag{H.4}$$

As seen in (H.4), $\sigma_{\tilde{O}_j}^2$ attains a value in the interval $[\frac{1}{2}\sigma_O^2, \sigma_O^2]$, whereby $\sigma_{\tilde{O}_j}^2$ is unambiguous. In cases where Δt_{bl} is an integer multiple r of Δt_I it corresponds to ϵ taking a sequence of r numbers in the interval $[0, 1]$. For $r \rightarrow \infty$ the analytical result is given by (H.3). By choosing the ratios $\frac{\Delta t_{bl}}{\Delta t_I}$ and $\frac{\Delta t_I}{\Delta t_{bl}}$ as irrational numbers a converging broken line process is achieved.

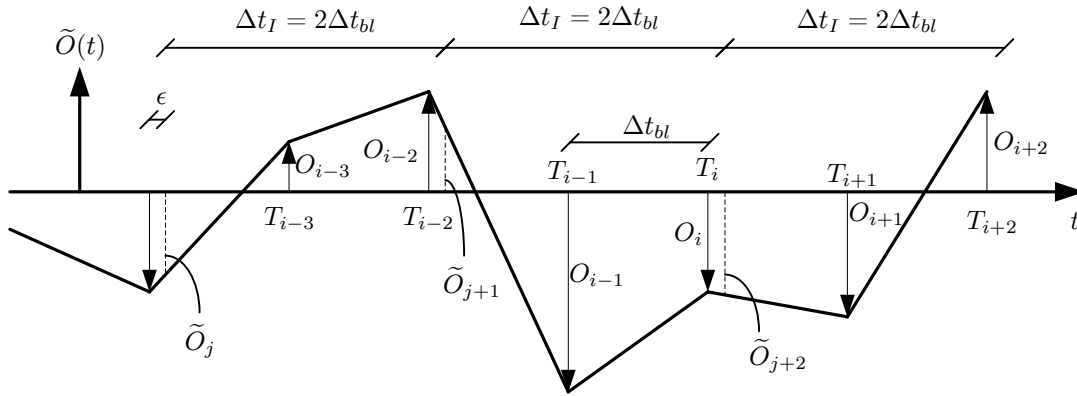


Figure H.2: Interpolation of the broken line process when the integration time step is an integer multiple of the broken line time step.

Appendix I

RR&S

I.1 Implementation on one dof oscillator

In the following the so-called Takens-Bogdanov single degree of freedom, non-linear oscillator used in [Pradlwarter and Schuëller, 1999] will be used for verification of the implementation of the method. The oscillator is given by the equation of motion

$$\ddot{x} = \lambda_1 + \lambda_2 x + x^2 + x\dot{x} + X(t) \quad \Rightarrow \quad \ddot{x} - \lambda_2 x - x^2 - x\dot{x} = \lambda_1 + X(t) \quad (\text{I.1})$$

where $X(t)$ is non-Gaussian noise bounded by ρ and given by

$$X(t) = \rho \cdot \sin(W(t))$$

where $W(t)$ denotes the standard Wiener process, i.e. $E[W^2(t)] = t$ for $t \geq 0$. To verify the RR&S algorithm the following values are used $(\lambda_1, \lambda_2) = (-0.3, -1.0)$. The used threshold values are $|x_c| = 1.5$ and $|\dot{x}_c| = 100$, where $|\cdot|$ denotes absolute value. For the given values of λ_1 and λ_2 (I.1) takes the form

$$\ddot{x} - x\dot{x} + x - x^2 = -0.3 + X(t) \quad (\text{I.2})$$

The barriers and initial conditions of the system are illustrated in figure I.1.

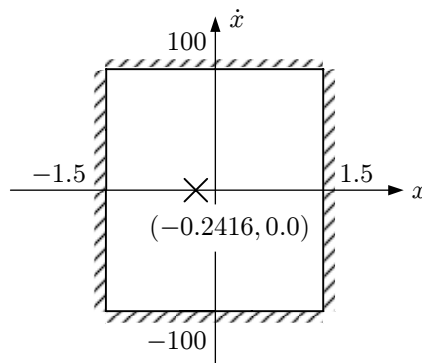


Figure I.1: Barriers and initial condition for Takens-Bogdanov oscillator.

According to [Pradlwarter and Schuëller, 1999], starting at time $t = 0$ with initial conditions $(x, \dot{x}) = (-0.2416, 0.0)$ the oscillator is unstable for $\rho > \rho_c = 0.0924$. This means that the oscillator will leave

the save domain within an infinite time for $\rho > \rho_c$. Using CMC simulation only few samples passing the threshold can be generated for $\rho_c < \rho < 0.20$. The first passage time probability distribution function for this range is investigated in [Pradlwarter and Schuëller, 1999] using the discrete values $\rho = [0.19, 0.18, 0.17, 0.16, 0.15]$. In the following only the first passage time probability distribution function for $\rho = 0.19$ is used for verification.

The state vector of the oscillator is $\mathbf{Z}(t) = [x(t), \dot{x}(t)]^T$. The interval widths used in the normalisation in (8.1) are set to $s_1 = s_2 = 1$.

The settings for the RR&S simulation are shown in table I.1.

N	ρ	$\Delta\tau$	η	P_0	w_{min}	K
200	0.19	1.0	0.5	0.4	$5 \cdot 10^{-5}$	6

Table I.1: Settings for the RR&S simulation in figure I.2.

The results of the CMC and RR&S simulation are shown in figure I.2.

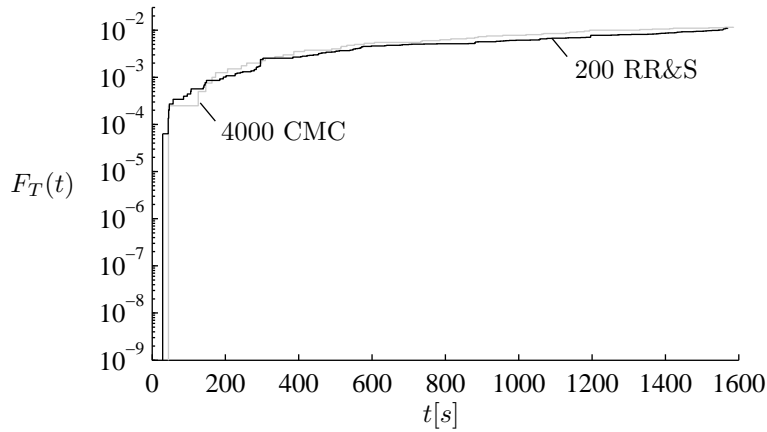


Figure I.2: First passage time distribution function for Takens-Bogdanov oscillator with settings as in table I.1.

The result shown in figure I.2 is comparable with the top most result in figure I.3. Figure I.3 is a copy of figure 4 in [Pradlwarter and Schuëller, 1999].

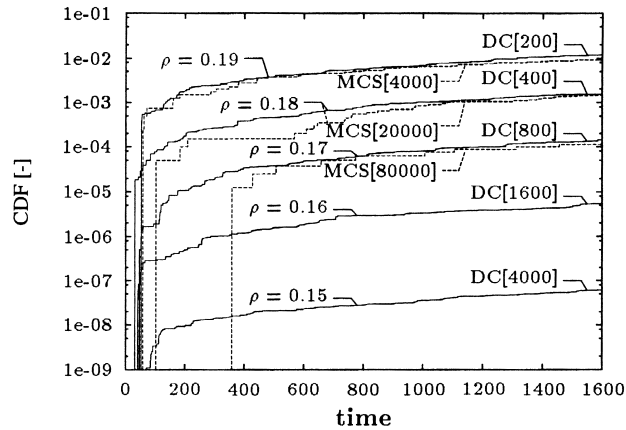


Figure I.3: Estimates of exit probabilities of Takens-Bogdanov oscillator for various excitation ranges ρ (DC[n]: distance controlled Monte Carlo (RR&S) using a sample size n ; MCS[n]: direct Monte Carlo Simulation using a sample size n). This figure corresponds to figure 4 in [Pradlwarter and Schuëller, 1999].

As the results in figure I.2 are comparable with results obtained by [Pradlwarter and Schuëller, 1999] it is verified that the RR&S algorithm has been correctly implemented to the one dof non-linear Takens-Bogdanov oscillator.

I.2 Implementation on two dof shear frame exposed to earthquake, static load & carrier wave

The implementation of the RR&S algorithm onto the earthquake exposed two dof shear frame is the first step toward implementing the algorithm on more complex systems. Before moving on to the three dof wind turbine and the 5MW reference wind turbine the two dof shear frame is tested with another set of loadings than just horizontal earthquake. The reason for this is a marked qualitative difference between the displacement response of the wind turbine tower and the two dof shear frame, see figure I.4.

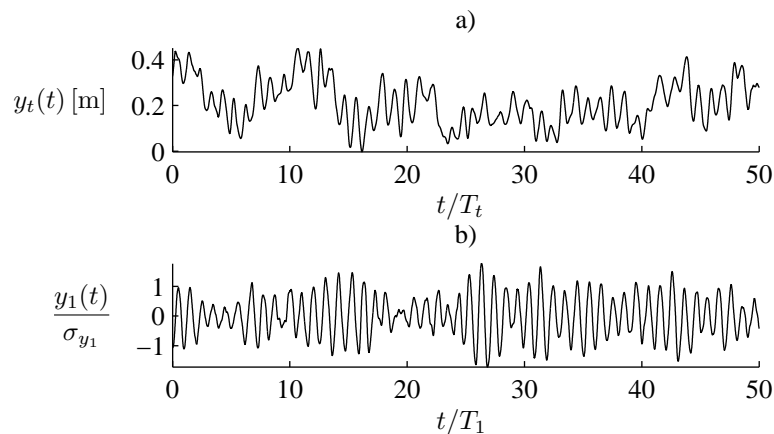


Figure I.4: a) Realisation of the tower fore-aft displacement response for the 5MW reference wind turbine. b) Normalised realisation of the displacement response for the first storey of the frame.

In figure I.4a a realisation of the tower fore-aft displacement obtained by the FAST program is shown and in figure I.4b a realisation of the displacement for the first storey of the frame is shown. The time has been normalised with respect to the eigenperiod. The eigenperiod for the tower is denoted T_t and the eigenperiod for the frame is denoted T_1 . The values of the eigenperiod of the tower is

$$T_t = \frac{2\pi}{\omega} = \frac{2\pi}{2.1} = 2.99 \text{ [seconds]} \quad (\text{I.3})$$

where ω is the angular eigenfrequency of the tower fore-aft mode 1 from table C.3.

As seen from the figures the displacement response of the frame is narrow banded and has a mean value zero whereas the fore-aft displacement response of the tower is broad banded and has a mean value different from zero. To assess what effect this has to the efficiency of the mechanical energy as distance variable, a set of loadings are constructed which causes the displacement response of the frame to imitate the main characteristics of the displacement response of the tower. The tower response has two characteristics, namely

- Static displacement
- Carrier wave

These characteristics arise due to the static and quasi-static nature of the wind load and it is shown in appendix I.4 that these characteristics introduce some disturbing oscillations in the mechanical energy.

I.2.1 Two storey frame with modified loading

Up to now, the shear frame has only been exposed to horizontal earthquake with zero mean. To resemble the characteristics from the wind turbine the shear frame is next exposed to an additional horizontal static wind load F_s and a horizontal carrier load on both storeys as shown in figure I.5. The static force, F_s is set to $F_s = 50 \text{ N}$. The carrier wave F_c is modelled as a harmonic varying load with amplitude 10 and the angular frequency $2\pi/30 \text{ rad/s}$

$$F_c = 10 \cos\left(\frac{2\pi}{30}t + \Phi_i\right) \text{ N} \quad (\text{I.4})$$

where Φ_i is a random phase associated with the i th realisation and uniformly distributed, $\Phi_i \sim U(0, 2\pi)$. The earthquake acceleration, \ddot{Y}_0 , is modelled as a bandlimited white noise with intensity $S_0 = 1$. As shown in figure I.5a the earthquake process \ddot{Y}_0 gives rise to the relative forces F_0 on the storeys when describing the system in relative coordinates. Since the storey masses are the same for both storeys F_0 is also the same for both storeys. The relative loads entering in the equation of motion in the case of relative coordinates are illustrated in figure I.5b.

A realisation of the load process and the corresponding relative displacement response for the first storey is shown in figure I.6.

I.2.2 Candidates for distance variable

In the following some candidate expressions for the distance variable are assessed to choose a distance variable to use when implementing the RR&S algorithm on FAST. The candidates are

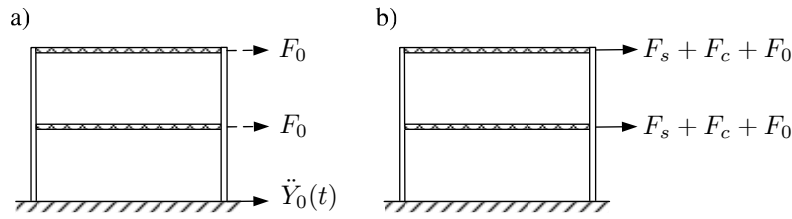


Figure I.5: a) Relative loads on shear frame due to \ddot{Y}_0 . b) All relative loads acting on shear frame.

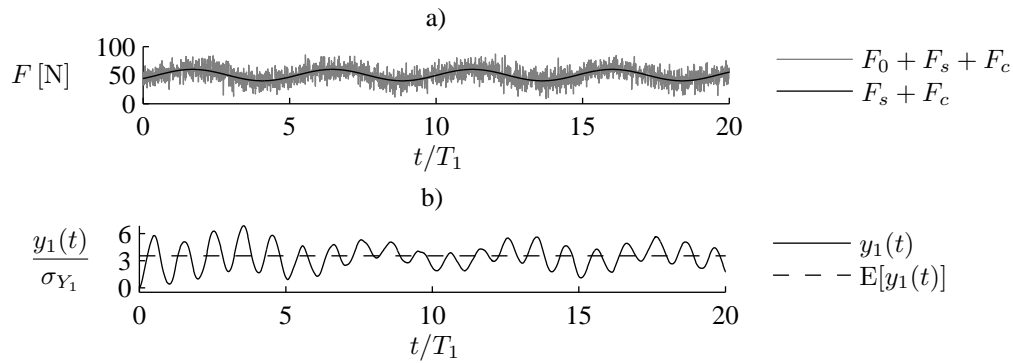


Figure I.6: a) Realisation of relative load process. b) Normalised realisation of displacement response relative to the ground surface of the first storey of the frame.

1. Candidate 1 - Mechanical energy (static displacement is subtracted).
2. Candidate 2 - Mechanical energy.
3. Candidate 3 - Sum of absolute normalised displacements and velocities. Normalised with respect to the maximum and minimum values.
4. Candidate 4 - Sum of absolute normalised displacements and velocities. Normalised with respect to barrier levels.
5. Candidate 5 - Maximum mechanical energy within 1 eigenperiod.
6. Candidate 6 - Average mechanical energy within 1 eigenperiod.
7. Candidate 7 - Pradlwarter and Schuëller's definition.

In the following the analytical expressions for the distance variables are given.

Candidate 1 is the mechanical energy, where the static displacement contribution has been subtracted before calculating the mechanical energy. According to the observation in appendix I.4 concerning oscillations in the mechanical energy due to a static displacement, this should be more efficient than using the total mechanical energy. However, in appendix I.4 it is also argued that the carrier wave introduces some oscillations in the same manner as the static displacement does. It is not possible to circumvent the oscillations due to the carrier wave and the carrier wave is therefore expected to have a negative influence on the efficiency of the mechanical energy as distance variable. The distance variable \bar{l} for candidate 1 is given by

$$\tilde{l} = \frac{1}{2}(\mathbf{y}(t) - \mathbf{y}_s(t))^T \mathbf{K}(\mathbf{y}(t) - \mathbf{y}_s(t)) + \frac{1}{2}\dot{\mathbf{y}}(t)^T \mathbf{M}\dot{\mathbf{y}}(t) \quad (\text{I.5})$$

where \mathbf{y}_s is the constant static displacement vector due to F_s given by $\mathbf{y}_s = [y_{s1}, y_{s2}]$ where y_{s1} and y_{s2} are the static displacement for the first and second storey, respectively. The static displacements are found by exposing the shear frame only to the static load.

Candidate 2 is the mechanical energy, without subtracting the static displacement contribution. Though, the observation in section I.4 does not favour this method, it is tested to verify the reduced efficiency compared to candidate 1. The distance variable \tilde{l} for candidate 2 is given by

$$\tilde{l} = \frac{1}{2}\mathbf{y}(t)^T \mathbf{K}\mathbf{y}(t) + \frac{1}{2}\dot{\mathbf{y}}(t)^T \mathbf{M}\dot{\mathbf{y}}(t) \quad (\text{I.6})$$

Candidate 3 is a weighting of the displacements and velocities. Each displacement and velocity component of the state vector $\mathbf{z}^T = [y_1, y_2, \dot{y}_1, \dot{y}_2]$ are mapped into the interval $[0, 1]$ as shown below. Furthermore, all displacements and velocities are weighted equally. The distance variable \tilde{l} for candidate 3 is given by

$$\tilde{l} = \tilde{z}_1 + \tilde{z}_2 + \tilde{z}_3 + \tilde{z}_4 \quad , \quad \tilde{z}_i^{(j)} = \frac{|z_i^{(j)}| - z_i^{min}}{z_i^{max} - z_i^{min}} \quad (\text{I.7})$$

where $|\cdot|$ denotes the absolute value, uppercase (j) denotes the j th realisation, z_i^{min} and z_i^{max} denotes the minimum and maximum value of $|z_i|$.

Candidate 4 is also a weighting of the displacements and velocities. In this case the displacements and velocities are normalised with respect to their outcrossing barrier. In this connection a velocity barrier is introduced. \tilde{l} for candidate 4 is given by

$$\tilde{l} = \frac{|y_1|}{y_{c,1}} + \frac{|y_2|}{y_{c,2}} + \frac{|\dot{y}_1|}{\dot{y}_{c,1}} + \frac{|\dot{y}_2|}{\dot{y}_{c,2}} \quad (\text{I.8})$$

where $y_{c,i}$ are displacements barriers, $\dot{y}_{c,i}$ are velocity barriers. $\dot{y}_{c,i}$ are calculated by assuming that failure happens at a specific value of mechanical energy. The needed mechanical energy for a storey to fail is then calculated as the potential energy the storey will have when reaching its displacement barrier $y_{c,i}$. The idea is then, to calculate the velocity barrier by putting the kinetic energy equal to the potential energy which is needed for the storey to fail, i.e.

$$\frac{1}{2}ky_{c,i}^2 = \frac{1}{2}m\dot{y}_{c,i}^2 \quad (\text{I.9})$$

where k and m are the stiffness and mass of the storeys.

Candidate 5. \tilde{l} is determined as the maximum value of the mechanical energy within the last eigenperiod. The mechanical energy is calculated in the same way as shown for candidate 1. The idea is to eliminate the effect of the oscillations by only using the maximum value within the last eigenperiod. In this way the troughs in the oscillations are disregarded.

Candidate 6. \tilde{l} is determined as the average value of the mechanical energy within the last eigenperiod. The mechanical energy is calculated in the same way as shown for candidate 1. The idea is to reduce the effects of the oscillations by performing an average over the last eigenperiod.

Candidate 7. \mathbf{l} is put equal to the state vector \mathbf{z} . $\tilde{\mathbf{l}}$ is then calculated by (8.1). This method is tested to see if it provides better results when distributing the realisations uniformly in the state space \mathbf{z} .

I.2.3 Assessment of candidates

In the following the candidates are compared pair-wise. The efficiency of the candidates are compared by the number of outcrossings they produce and the candidate which produces the most outcrossings is said to be the most efficient candidate. The comparison assumes that the parameter values of the RR&S algorithm is the same for all simulations. The used RR&S simulation parameters are given in table I.2.

α	$\Delta\tau/T_1$	β	P_0	w_{min}	K	N	T/T_1
6	0.1	0.8	0.5	$1 \cdot 10^{-9}$	10	2000	100

Table I.2: Parameter values for RR&S simulation in assessment of the distance variables candidate 1 to candidate 7.

The barriers y_{c_i} are determined by (6.7) using μ_{y_i} and σ_{y_i} where μ_{y_i} is determined by exposing the frame only to the static load F_s in both dofs and σ_{y_i} is determined by an ergodic sampling. The values of μ_{y_i} and σ_{y_i} are given by

$$\boldsymbol{\mu}_y = \begin{bmatrix} \mu_{y_1} \\ \mu_{y_2} \end{bmatrix} = \begin{bmatrix} 38.2 \\ 19.1 \end{bmatrix}, \quad \boldsymbol{\sigma}_y = \begin{bmatrix} \sigma_{y_1} \\ \sigma_{y_2} \end{bmatrix} = \begin{bmatrix} 10.7703 \\ 6.3797 \end{bmatrix} \quad (\text{I.10})$$

In the following the candidates are compared pair-wise. To show that candidate 1 seems to provide the best result, all candidates are compared to candidate 1. Candidate 1 seems to provide the most efficient distance measures, based on a visual judgement of the first passage time distribution function as well as on the number of outcrossings achieved. The number of outcrossings for each candidate is shown in the legends of the figures.

Comparison of candidate 1 and 2. The first passage time distribution functions for candidate 1 and 2 are shown in figure I.7a. Candidate 1 has produced 860 outcrossings, whereas candidate 2 has only produced 4. A realisation of \tilde{l} calculated by candidate 1 and 2 is shown in figure I.7c and I.7d, respectively. The poor result produced by candidate 2 is assumed to be due to the very periodic oscillations seen in \tilde{l} in figure I.7.

Comparison of candidate 1 and 3. The first passage time distribution functions for candidate 1 and 3 are shown in figure I.8a. Candidate 3 has produced 102 outcrossings. A realisation of \tilde{l} calculated by candidate 1 and 3 is shown in figure I.8c and I.8d, respectively. The poor result produced by candidate 3 is assumed to be due to the periodic troughs in \tilde{l} . When the displacement response is in a trough, the displacement has a local minimum and the velocity is zero. Therefore \tilde{l} , calculated by candidate 3, will have troughs at same time as the displacement response.

Comparison of candidate 1 and 4. The first passage time distribution functions for candidate 1 and 4 are shown in figure I.9a. Candidate 4 has produced 16 outcrossings. A realisation of \tilde{L} calculated by candidate 1 and 4 is shown in figure I.9c and I.9d, respectively. The poor result produced by candidate

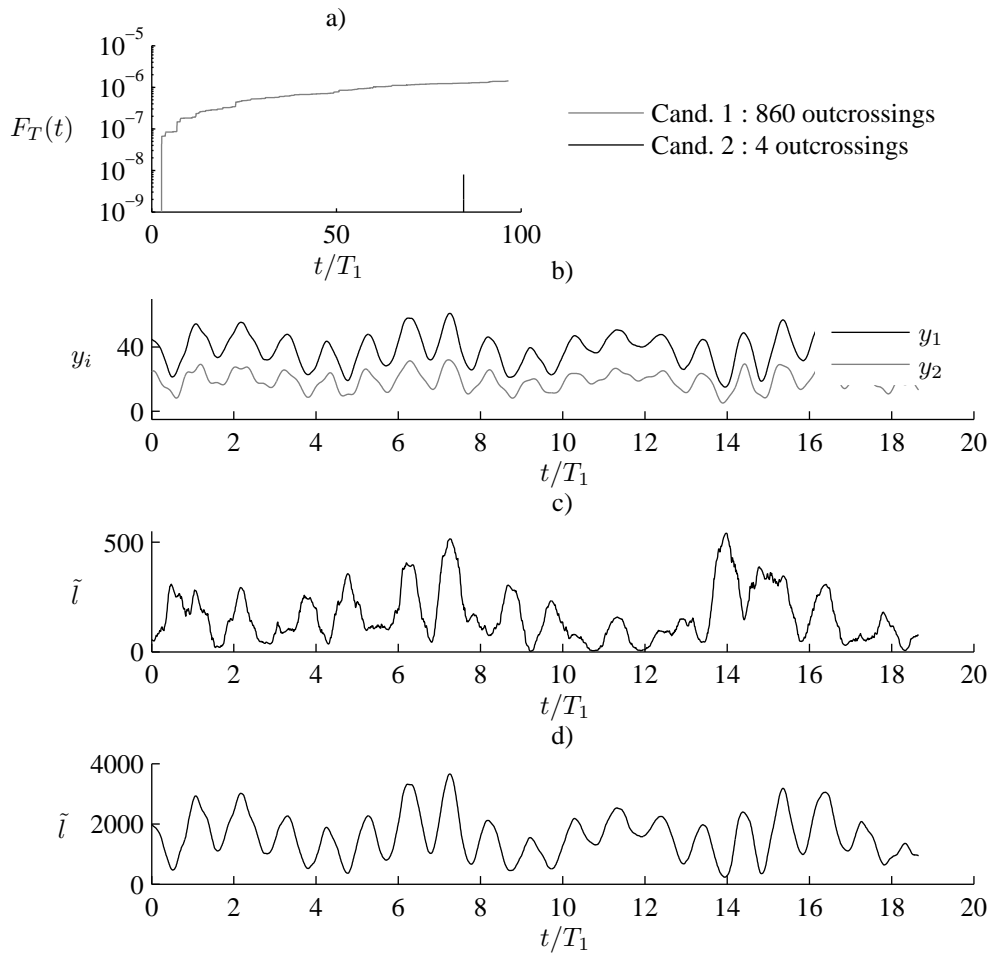


Figure I.7: a) Comparison of first passage distribution functions for candidate 1 and candidate 2. b) Realisations of relative displacement response. c) Realisation of \tilde{L} for candidate 1. d) Realisation of \tilde{L} for candidate 2.

4 is assumed to be due to same problem as described for candidate 3. When the displacement response is in a trough, a local minimum occurs in \tilde{l} for candidate 4.

Comparison of candidate 1 and 5. The first passage time distribution functions for candidate 1 and 5 are shown in figure I.10a. Candidate 5 has produced 326 outcrossings. A realisation of \tilde{L} calculated by candidate 1 and 5 is shown in figure I.10c and I.10d, respectively. It appears that the peak value of the mechanical energy within the latest eigenperiod is not a very good measure due to a too short memory.

Comparison of candidate 1 and 6. The first passage time distribution functions for candidate 1 and 6 are shown in figure I.11a. Candidate 6 has produced 97 outcrossings. A realisation of \tilde{L} calculated by candidate 1 and 6 is shown in figure I.11c and I.11d, respectively. Looking at \tilde{l} in figure I.11c and I.11d, it is seen that averaging the mechanical energy over the last eigenperiod delays the peaks in \tilde{l} . This is assumed to reduce the efficiency of candidate 6.

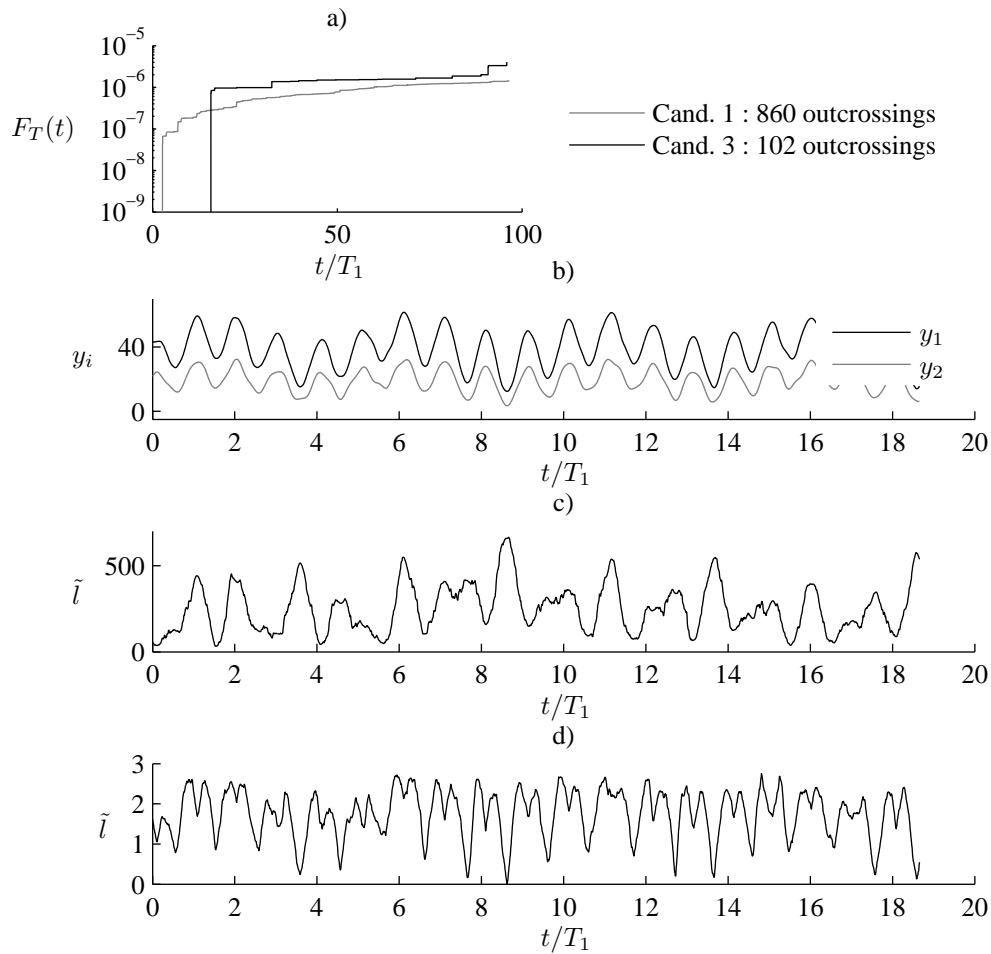


Figure I.8: a) Comparison of first passage distribution functions for candidate 1 and candidate 3. b) Realisation of relative displacement response. c) Realisation of \tilde{L} for candidate 1. d) Realisation of \tilde{L} for candidate 3.

Comparison of candidate 1 and 7. The first passage time distribution functions for candidate 1 and 7 are shown in figure I.12. Candidate 7 has produced 16 outcrossings. As $\tilde{\mathbf{I}}$ calculated by candidate 7 is not a scalar, no plots of $\tilde{\mathbf{I}}$ is made. Candidate 7 works toward a uniformly distribution of realisation in state space \mathbf{Z} which is seen to be less efficient than distributing realisations in the mechanical energy space.

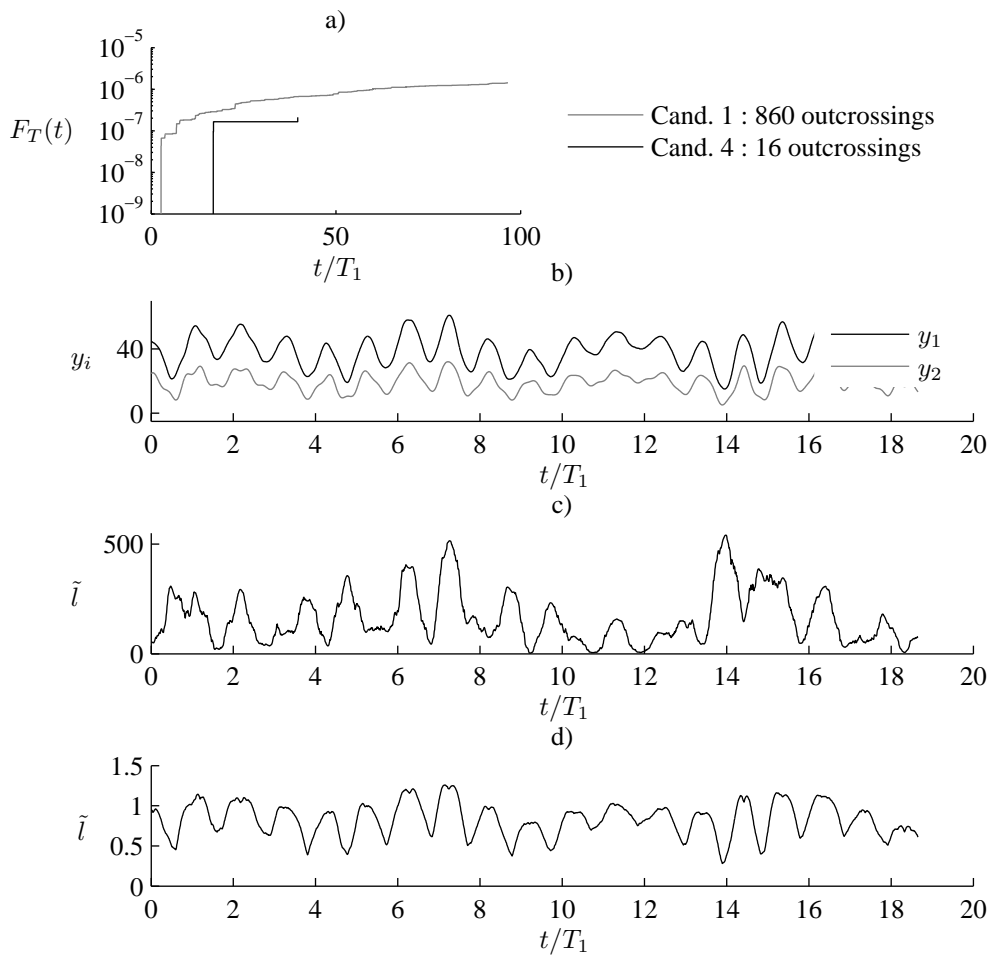


Figure I.9: a) Comparison of first passage distribution functions for candidate 1 and candidate 4. b) Realisation of relative displacement response. c) Realisation of \tilde{L} for candidate 1. d) Realisation of \tilde{L} for candidate 4.

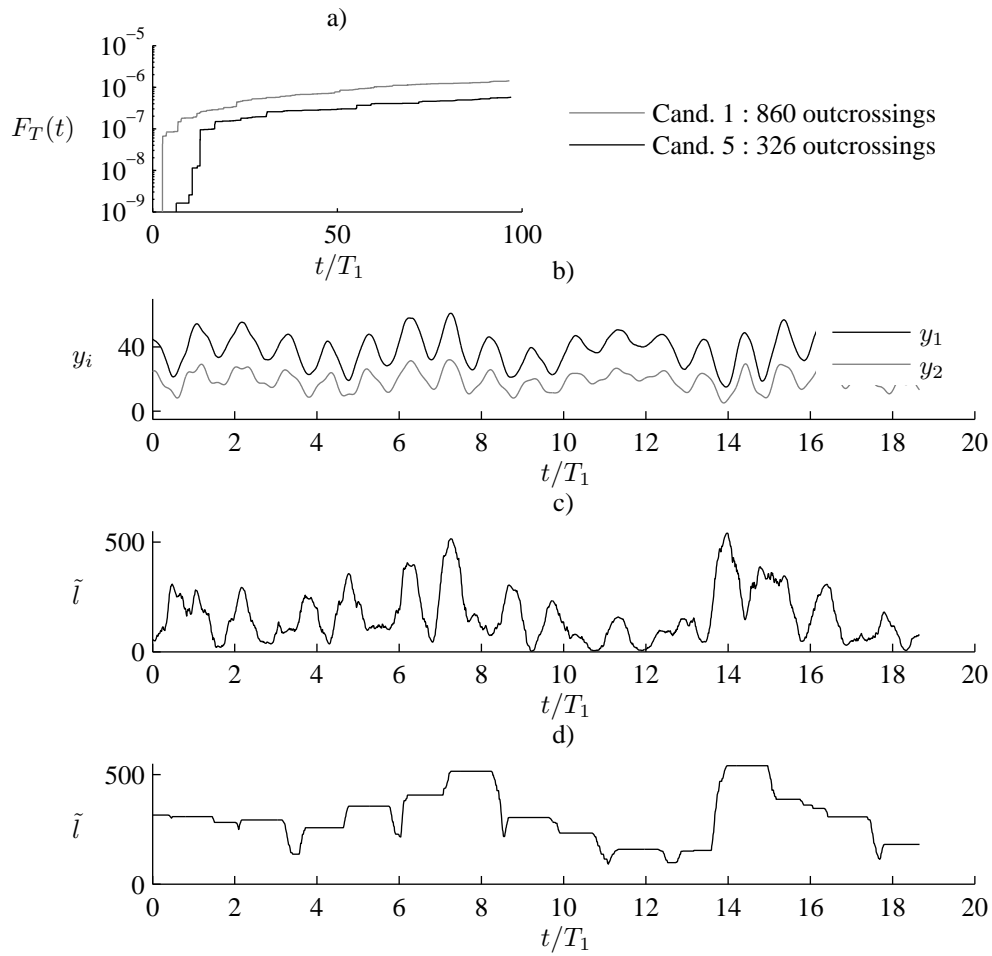


Figure I.10: a) Comparison of first passage distribution functions for candidate 1 and candidate 5. b) Realisation of relative displacement response. c) Realisation of \tilde{L} for candidate 1. d) Realisation of \tilde{L} for candidate 5.

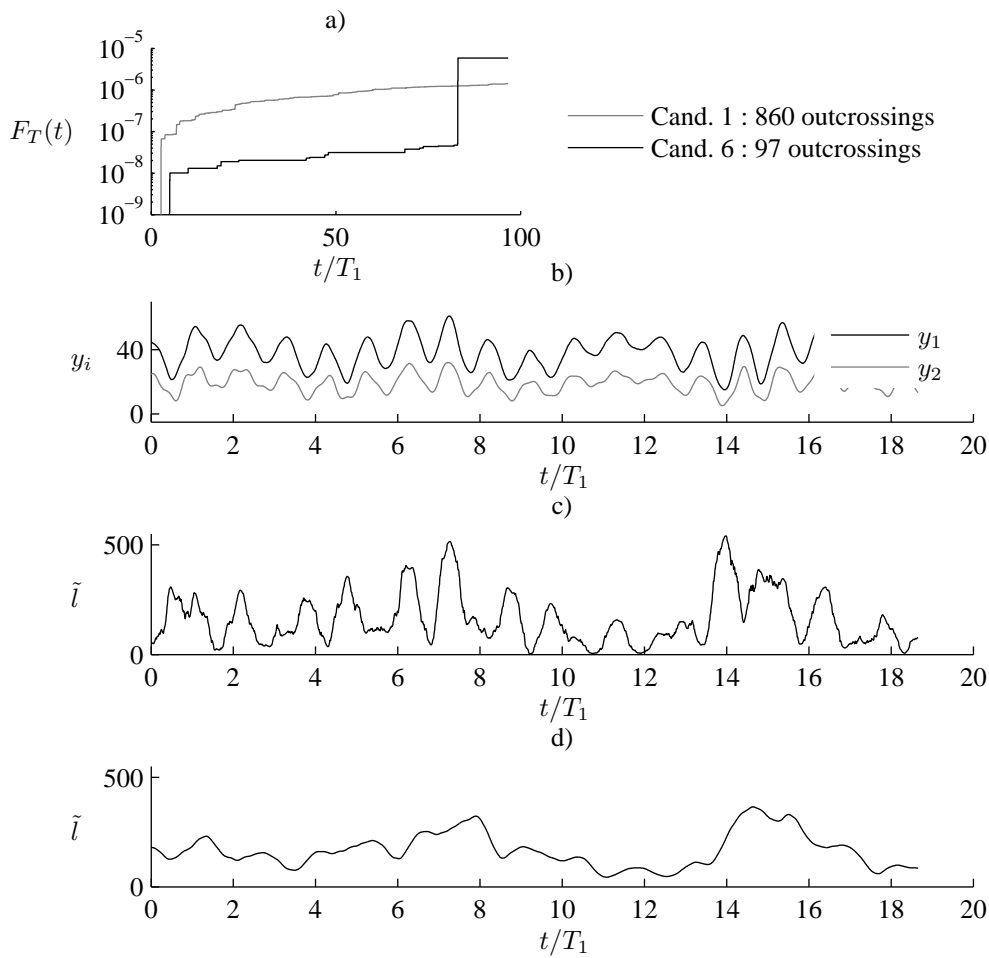


Figure I.11: a) Comparison of first passage distribution functions for candidate 1 and candidate 6. b) Realisation of relative displacement response. c) Realisation of \tilde{L} for candidate 1. d) Realisation of \tilde{L} for candidate 6.

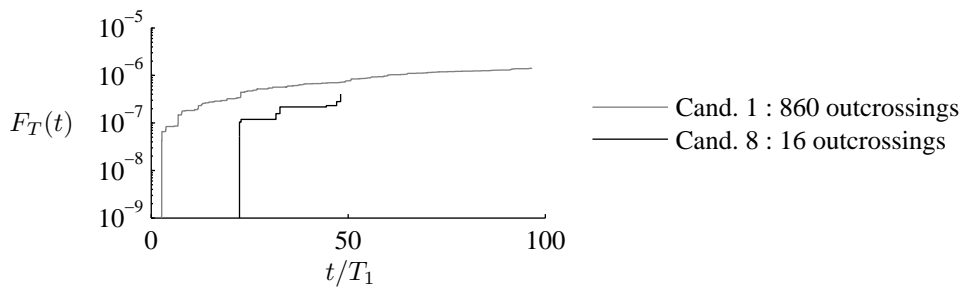


Figure I.12: Comparison of first passage distribution functions for candidate 1 and candidate 7.

I.2.4 Conclusion

The conclusion from figure I.7 to I.12 is that candidate 1 is the most efficient of the candidates for estimating the first passage times for the two dof shear frame exposed to the set of relative loadings shown in figure I.5. A ranking of the candidates according to the produced number of outcrossings is provided in table I.3.

Rank	Candidate	Outcrossings
1	1	860
2	5	326
3	3	102
4	6	97
5	4	16
5	7	16
6	2	4

Table I.3: Rank of candidate 1-7 based on the produced number of outcrossings.

Candidate 5 is the 2nd most efficient candidate. It seems that the attempt to smoothen candidate 1 by choosing the largest peak value within the last eigenperiod do not improve the efficiency, on the contrary it reduces it. A problem with candidate 5 is that its efficiency depends on the displacement response having a certain memory which it may not have. To illustrate the problem, consider figure I.10d at the time $t/T_1 \approx 7.2$ where candidate 5 takes the value of the peak in figure I.10c at the same time $t/T_1 \approx 7.2$. Now, candidate 5 maintains this value for the next eigenperiod as no other peaks occur which exceeds this peak value. This implies that the realisation is equally important within this eigenperiod, which it may not actually be. This issue seems to reduce the efficiency compared to candidate 1.

Candidate 3 is the 3rd most efficient candidate. A problem with candidate 3 is that when the displacement response enters a trough, the displacement has a minimum and the velocity is zero. Therefore, \tilde{l} is bound to experience a trough as well. These periodic troughs seems to reduce the efficiency of \tilde{l} calculated by candidate 3.

Candidate 6 is the 4th most efficient candidate. Candidate 6 is another method to smoothen candidate 1. A problem with candidate 6 is that it displaces the peaks in candidate 1. This can be seen in figure I.11d by considering the peak at $t/T_1 \approx 7.9$. Comparing the location of this peak with the response in figure I.11b it is seen that the smoothening of candidate 1 displace the peak in time. Therefore, when the peak at $t/T_1 \approx 7.9$ in figure I.11 occurs, the displacement response has already past its peak, and is therefore no longer as important as candidate 6 implies that it is.

Candidate 4 and 7 both produced 16 outcrossings and is therefore considered equally inefficient. They rank as the 5th most efficient candidates. What is noticed about candidate 4 is that it only produced approximately 15% of the outcrossings achieved by candidate 3. This implies that how the displacements and velocities are weighted has a significant influence on the efficiency.

The poor result produced by candidate 7 may be explained from figure I.13. Figure I.13a is a copy of figure 8.7a from section 8.2 where it was argued that realisations which oscillates harmonically will be well separated when distributed in the velocity displacement space. By considering figure I.13b it can be argued that this is also the case when the realisations has a static displacement y_s as this only displaces the circles by y_s .

However, if the realisations are influenced by a carrier wave, their quasi static displacements may not be the same. In this case the realisations may have quasi static displacements $y_{s,a}$ and $y_{s,b}$ as

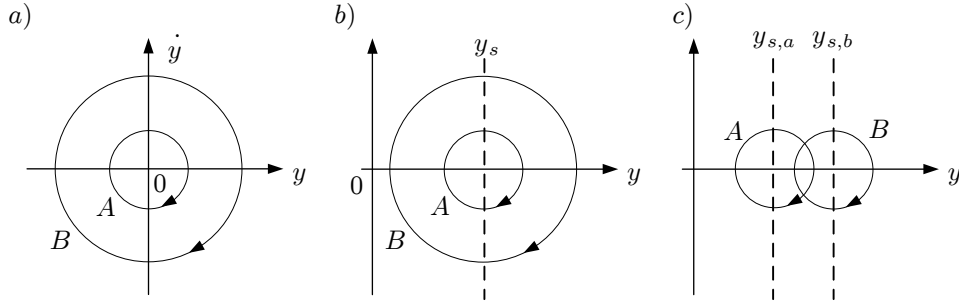


Figure I.13: a) Illustration of A and B in the velocity and displacement space. b) Illustration of A and B in the velocity and displacement space in case of a static displacement. c) Illustration of A and B in the velocity and displacement space in the case of a static displacement and carrier wave.

illustrated by figure I.13c. This implies that the realisations are no longer well separated.

Candidate 2 ranks as number 6 and is thereby the less efficient candidate. The problem with candidate 2 is the static displacement, which in section I.4 is argued to introduce oscillations in the mechanical energy. These oscillations have the effect that realisations close to failure are no longer well separated from realisations far from failure in the mechanical energy space. The investigation of the distance variables shows that candidate 1 is the most efficient of the 7 investigated candidates and candidate 1 is therefore used in the implementation onto the simple three dof turbine.

I.3 Non-uniform distribution of realisations

The suggested distance measure (8.3) works towards a uniform distribution in the D -space. A uniform distribution is approached because the distance measure depends on the distance between neighbouring realisations. Hereby, realisations with large distance measure implies that the density of realisations should be increased in this area. In this way the whole range of the probability density function for L is described equally well. When simulating first passage times at high barriers, it is as such of no importance to have a description of the whole probability density function. A correct description is only needed for the part of the probability density function where the outcrossings occur.

Therefore an alternative distance measure which increases the density of realisations in the failure area of the probability density function is suggested. The distance measure which is proposed assumes that the distance variable is a scalar which means that no difference is made between the normalised and unnormalised distance variable, whereby $l = \tilde{l}$.

The idea is to make the distance measure depend on the distance from origo instead of the relative distance to neighbouring realisations. In this way, realisations far away from origo, and thereby close to failure will be considered more important and thereby be splitted.

The difference between the distance measure (8.3) and (I.11) is illustrated by figure I.14. The distance measure (8.3) is calculated as illustrated by figure I.14a where the distance measure $d_{\tau}^{(j)}$ is calculated as a weighted sum of distances to the neighbouring realisations.

In figure I.14b it is seen that the distance measure (I.11) will be given directly by the distance variable as

$$d_{\tau_i}^{(j)} = l_{\tau_i}^{(j)} \quad (\text{I.11})$$

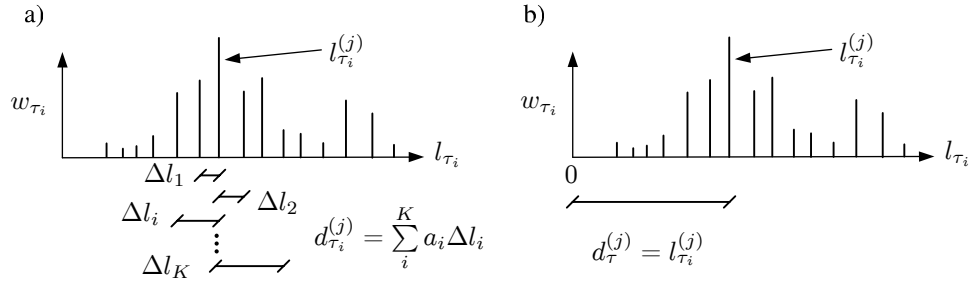


Figure I.14: a) Distance measure given by (8.3). b) Distance measure given by (I.11).

Using (I.11) as distance measure, implies that realisations with large $l_{\tau_i}^{(j)}$ will be considered important. Hereby the realisation density will increase for high values of $l_{\tau_i}^{(j)}$ and decrease for low values of $l_{\tau_i}^{(j)}$. This is illustrated in figure I.15 where the realisation density is low towards zero and high towards high values of l_{τ_i} .

The alternative distance measure (I.11) have been assessed by using it for simulation of the first passage time probability distribution function for the 2-dof shear frame exposed to horizontal earthquake. The parameter settings for the RR&S algorithm is given in table I.4.

α	$\Delta\tau/T_1$	η	P_0	w_{min}	K	N	$T [T_1]$
6	0.1	0.8	0.5	$1 \cdot 10^{-9}$	10	2000	100

Table I.4: Parameter settings for RR&S algorithm for assessment of distance measure given by (I.11).

The first passage time distribution function produced by (8.3) and (I.11) have been compared in figure I.15.

It can be concluded by a visual judgement of figure I.15 that the distance measure (I.14) produces a very poor estimate. The reason for the poor result is sought in the approximation of the probability density function of L . Therefore an approximation of the probability density function by CMC simulation and RR&S simulation is made. The approximations are seen in figure I.17 where 200 realisations have been used to approximate the probability density function of L . In figure I.17a the probability density function is approximated by a CMC simulation. It is seen that only the high probability area of the probability density function is represented.

In figure I.17b the probability density function is represented by a RR&S simulation using the distance measure (8.3). It is seen that the weights have been adjusted and a larger range of the probability density function is described.

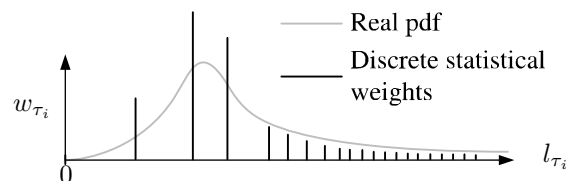


Figure I.15: Distribution of realisations when using distance measure by (I.11).

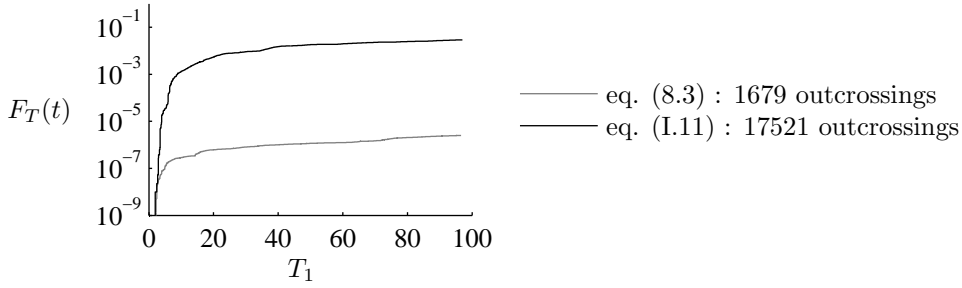


Figure I.16: First passage distribution functions estimated by RR&S simulation using the two distance measures (I.11) and (8.3).

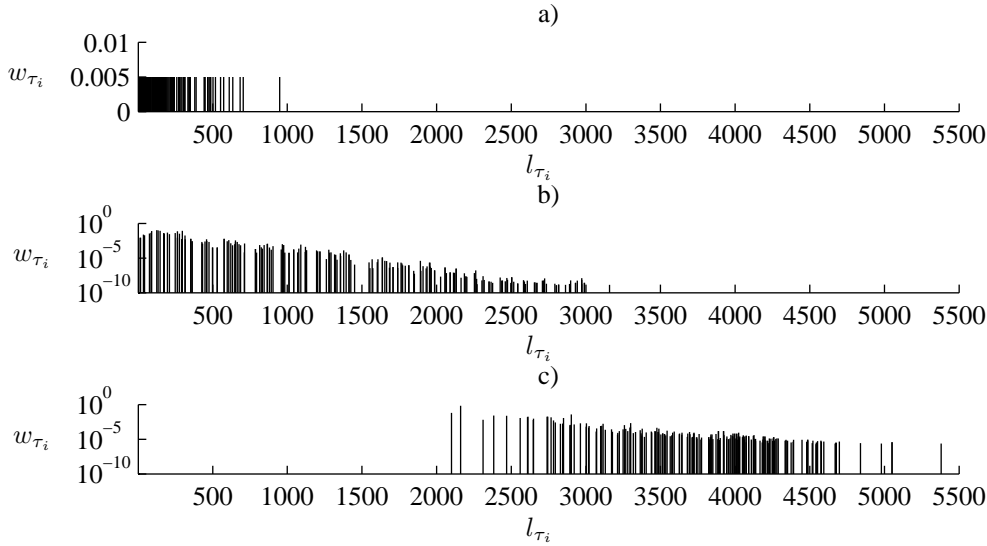


Figure I.17: a) Approximation of probability density function by CMC simulation. b) Approximation of probability density function by RR&S simulation using (8.3) as distance measure. c) Approximation of probability density function by RR&S simulation using (I.11) as distance measure.

In figure I.17c the probability density function is described by a RR&S simulation using the distance measure (I.11). It seems that the RR&S algorithm with this distance measure and using $N = 200$ does not represent the probability density function at all in the range $l_{\tau_i} = [0, 2000]$. This has the effect that the statistical mass which actually belongs to the interval $l_{\tau_i} = [0, 2000]$ is wrongly distributed across the interval $l_{\tau_i} = [2000, 5500]$. This has the effect that the associated with the realisations which crosses out are too high. Looking at samples around $l_{\tau_i} = 3000$ it is seen that the weights given by figure I.17b are far below 10^{-5} whereas weights in figure I.17c are above 10^{-5} . Therefore $F_T(t)$ is poorly estimated.

The conclusion is that distributing the realisations differently than uniform may lead to a larger statistical uncertainty on the estimates. It is thus important that areas with large statistical mass is described properly which is best obtained by distributing the realisations uniformly. The distance measure (I.11) is disregarded and (8.3) will be used in the further work.

I.4 Mechanical energy oscillations

It is shown in the following that the kind of loading which the wind turbine experiences introduces some oscillations in the mechanical energy which disturb the separation of the realisations according to their closeness to failure. Thus, the realisations are no longer well separated as illustrated by figure 8.7c. This is assumed to reduce the efficiency of the distance variable.

To illustrate the problem a single dof system with stiffness $k = 1$ and mass $m = 1$ is considered. The system is undamped and performs harmonic eigen vibrations around a static displacement y_s with the amplitude A and the angular frequency ω . Then,

$$y(t) = A\cos(\omega t) + y_s \quad , \quad T = \frac{2\pi}{\omega} \quad (\text{I.12})$$

where T is the eigenperiod. The mechanical energy of the system is given by

$$e_m(t) = \frac{1}{2}k(y_s + A\cos(\omega t))^2 + \frac{1}{2}m(-A\omega\sin(\omega t))^2 \quad (\text{I.13})$$

$$= \frac{1}{2}(k + m\omega^2)A^2 + \frac{1}{2}ky_s^2 + ky_sA\cos(\omega t) \quad (\text{I.14})$$

The term $ky_sA\cos(\omega t)$ introduces oscillations in the mechanical energy as shown in figure I.18b where $y_s/A = 0.05$ has been used.

The oscillations in the mechanical energy disturb the distance measure as the displacement response in figure I.18a should be equally important over the range $t/T = [0, 3]$. To emphasise the problem, consider the case where the static displacement y_s is equal to zero. In this case the mechanical energy is constant, which implies that the response is equally important no matter what instant of time it is observed. Now, adding a static displacement to the response should not change the importance of the realisation. If y_s is known it is possible to subtract this in (I.12) whereby a distance measure which do not oscillate still can be obtained. It therefore seems possible to circumvent the problem concerning the static load.

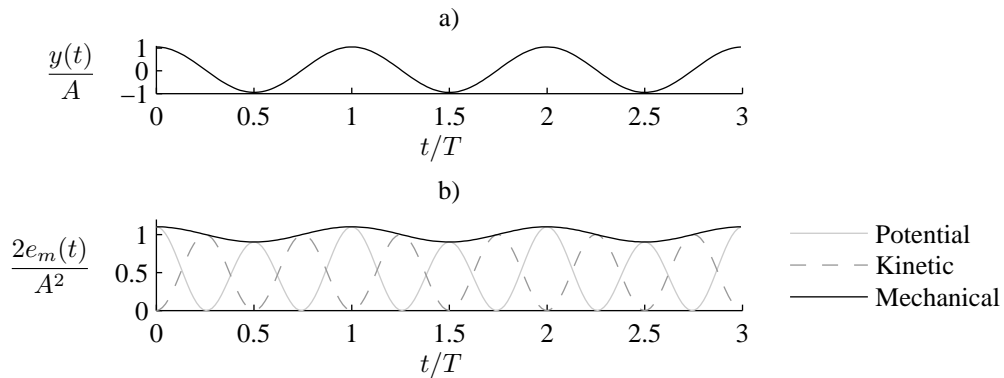


Figure I.18: a) Normalised displacement of (I.12). b) Normalised potential, kinetic and mechanical energy for oscillation in figure I.18a.

Low frequency load

The second characteristic in the loading of the wind turbine is the low frequency component in the wind load, a so-called carrier wave. A carrier wave introduces a quasi-static displacement on the system which introduces oscillations in the mechanical energy in quite the same way as seen for the static load above. Since the carrier wave consists of low frequency oscillations only a negligible contribution to the kinetic energy appears.

To illustrate the effect of a carrier wave a harmonic oscillation with a lower frequency is added to (I.12). The harmonic oscillation is given by

$$y_c(t) = \frac{A}{2} \cos\left(\frac{\omega}{10}t\right) \quad (\text{I.15})$$

The displacements $y + y_c$ and y_c are shown in figure I.19a. The corresponding variation in mechanical energy is shown in figure I.19b. It is seen that oscillations due to the carrier wave arise.

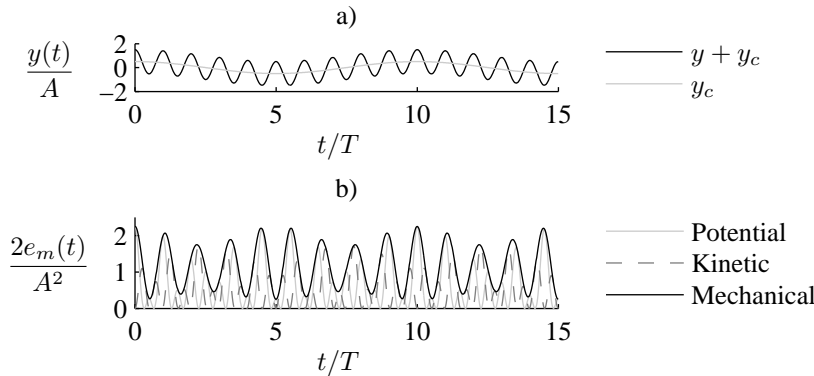


Figure I.19: a) Normalised displacement. b) Normalised potential, kinetic and mechanical energy for oscillation in figure I.19a.

When implementing RR&S on the wind turbine a distance variable which is effected as little as possible by this type of carrier waves should be chosen. As this type of carrier waves are a part of the wind load it can not be circumvented in the same way as for the static load.

I.5 Parameter analysis

In this section the influence of the parameters of the RR&S algorithm is investigated to evaluate how sensitive the parameters are to variations. The assessment is performed on the two dof shear frame exposed to horizontal earthquake and the mechanical energy is utilised for the distance variable. The parameters are assessed by considering their influence on the estimated mean value $\mu_{\hat{F}_T(600)}$ and standard deviation $\sigma_{\hat{F}_T(600)}$ of the first passage time distribution function $F_T(t)$ at $t = 600$, denoted $F_T(600)$. The reference for the assessment is the estimation of $F_T(600)$ for the barrier level $\alpha = 5$ using $N = 200$. $\mu_{\hat{F}_T(600)}$ and $\sigma_{\hat{F}_T(600)}$ are calculated from 50 estimates of $F_T(600)$ by

$$\mu_{\hat{F}_T(600)} = \frac{1}{50} \sum_{i=1}^{50} \hat{F}_T^{(i)}(600) \quad (\text{I.16})$$

$$\sigma_{\hat{F}_T(600)} = \frac{1}{50} \sum_{i=1}^{50} (\hat{F}_T^{(i)}(600) - \mu_{\hat{F}_T(600)})^2 \quad (\text{I.17})$$

where uppercase (i) denotes the i th estimate of $F_T(600)$. For comparison a reference mean value $\mu_{F_T(600)}^{\text{ref}}$ for $F_T(600)$ has been calculated using a CMC simulation with $N = 10^6$. The reference value is simulated to

$$\mu_{F_T(600)}^{\text{ref}} = 3.87 \cdot 10^{-4} \quad (\text{I.18})$$

The assessed parameters are the time step between the evaluation points $\Delta\tau$, the minimum allowable weight of samples w_{min} , the exponent in the imperical expression for the importance measure η , the number of neighbouring samples K to use for calculating the distance measure and the killing rate parameter P_0 .

Assessment of $\Delta\tau$

In this section the timestep between each evaluation point, $\Delta\tau$, is assessed to see if any arbitrary low value can be chosen without making the method unstable. Furthermore it is investigated if some optimal $\Delta\tau$ seems to occur. The optimal $\Delta\tau$ is considered as the value of $\Delta\tau$ which provides the correct mean value with the smallest variance.

Generally the evaluation time step $\Delta\tau$ needs to be larger than the integration time step Δt . Some overall considerations when choosing $\Delta\tau$ is firstly made according to: 1) the order of the failure probability which is to be estimated. 2) the rate of change in the mechanical energy.

1) The order of the failure probability: What is noticed here, is that a certain number of splittings are necessary in order to bring the weights down from the start weights to weights which as a minimum are smaller than the failure probability. Consider as an example the case where 10 time series are used to estimate a failure probability of 1%. As the start weights will be 1/10, 4-5 splittings are needed in order to achieve weights of the order of 1%. However, as the weights are modified and normalised during the RR&S algorithm, the necessary number of evaluation points are not found as simple as in the example.

2) The rate of change in the mechanical energy: What is noticed here is that it seems reasonable not to choose values of $\Delta\tau$ which would give rise to peaks in the energy arising and disappearing within $\Delta\tau$. This is not preferable as a splitting of these peaks will increase the probability of an outcrossing.

In figure I.20 a realisation of the displacement response $Y_1(t)$ of the first storey relative to the ground surface and a realisations of the mechanical energy $E_m(t)$ response of both storeys are shown. As the response of the two storeys are rather afine only the displacement of the first storey is shown. What is noticed about the mechanical energy response is that it is not as smooth as the displacement response. The fuzziness of e_m is due to the equivalent white noise used as load, which makes the velocity process non-differentiable.

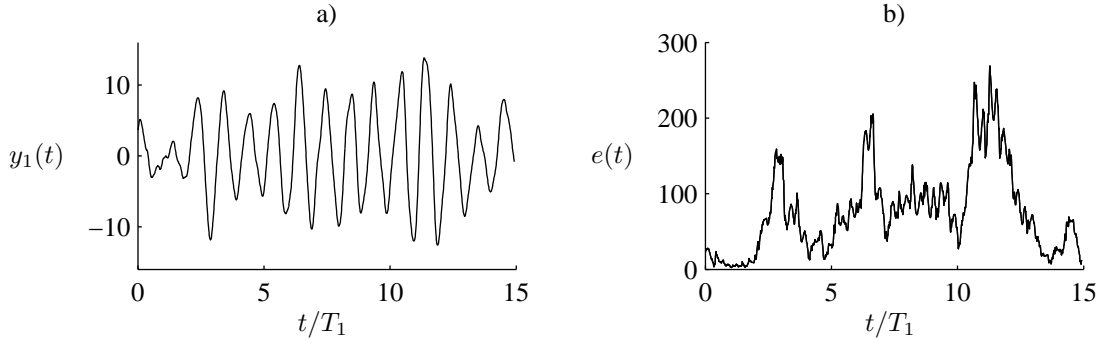


Figure I.20: a) Realisation of the displacement response Y_1 . b) Realisation of the mechanical energy E_m of the two storey frame.

Next, it is investigated if arbitrary small values of $\Delta\tau$ will provide unbiased failure estimates. The results are given in figure I.21, where the RR&S parameters used to produce the results are given in table I.5.

N	α	$\Delta\tau/T_1$	η	P_0	w_{min}	K	T [s]
200	5	[0.1, 10]	0.8	0.5	$1 \cdot 10^{-7}$	10	600

Table I.5: Parameter values for RR&S simulation in figure I.21.

Figure I.21a shows the mean value $\mu_{\hat{F}_T(600)}$ as a function of $\Delta\tau$ and figure I.21b shows the standard deviation $\sigma_{\hat{F}_T(600)}$ as a function of $\Delta\tau$. From figure I.21b it is seen that the standard deviation decreases when $\Delta\tau$ decreases. This implies that the variance of an estimate by RR&S simulation can be reduced simply by lowering $\Delta\tau$. But, decreasing the value of $\Delta\tau$ also has a negative effect. From figure I.21a it is seen that the algorithm produces a bias on the estimate of $F_T(600)$ when $\Delta\tau$ goes toward zero. It is suggested that this bias occur when the evaluation time step becomes so small that a splitted realisation and its copy do not have enough time to develop into independent realisations before the next evaluation time occurs. This means that the outcrossings are no longer independent and a bias may be expected. By increasing $\Delta\tau$ the variance is seen to increase and the mean value is fluctuating around $\mu_{F_T(600)}^{ref}$.

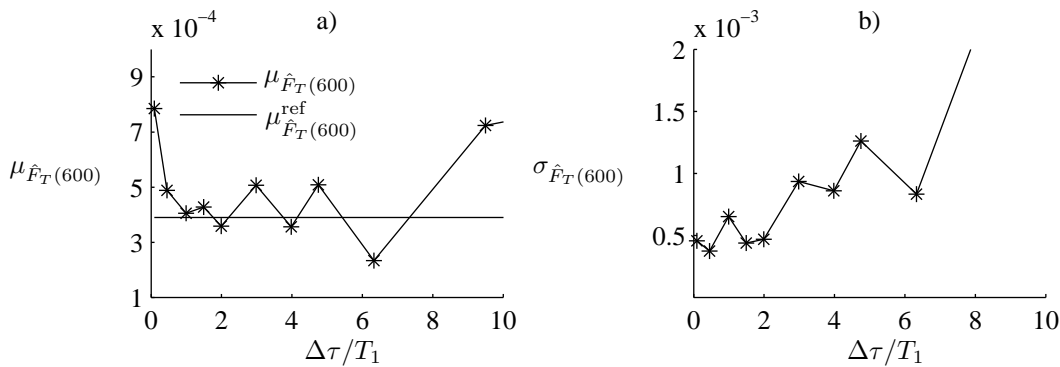


Figure I.21: a) Mean value of failure estimates as a function of $\Delta\tau$. b) Standard deviation of failure estimates as a function of $\Delta\tau$.

Figure I.21 is produced using the number of realisations $N = 200$. If $N = 50$ is used instead, the same tendency is seen, i.e. increasing bias for $\Delta\tau < T_1$. But, for increasing N the bias seems to converge toward zero. This indicates that it is not a bias but a statistical uncertainty. Table I.6 shows results for $\mu_{\hat{F}_T(600)}$ and $\sigma_{\hat{F}_T(600)}$ for varying N and $\Delta\tau$. It thus seems possible to use values of $\Delta\tau$ smaller than T_1 and still produce unbiased results of $\mu_{\hat{F}_T(600)}$.

N	RR&S ($\Delta\tau = 0.1T_1$)		RR&S ($\Delta\tau = T_1$)	
	$\mu_{\hat{F}_T(600)}$ [10^{-4}]	$\sigma_{\hat{F}_T(600)}$ [10^{-4}]	$\mu_{\hat{F}_T(600)}$ [10^{-4}]	$\sigma_{\hat{F}_T(600)}$ [10^{-4}]
50	13.5	17.2688	7.50	18.5851
200	7.85	4.5595	4.10	4.6858
500	5.19	3.0499	3.91	2.8456
1.000	4.33	1.2144	4.52	3.5138
2.000	4.10	0.9202	4.05	1.3669

Table I.6: Estimates of $F_T(600)$ produced by RR&S simulation with two different values for $\Delta\tau$ and five different values of N .

The obtained gain when decreasing $\Delta\tau$ is illustrated in figure I.22. Figure I.22a shows 50 estimates of $F_T(t)$ which are produced using $\Delta\tau = T_1$ and figure I.22b shows 50 estimates of $F_T(t)$ which are produced using $\Delta\tau = 0.1T_1$. It is seen that the variance of the estimates of $F_T(t)$ are reduced in figure I.22b compared to figure I.22a.

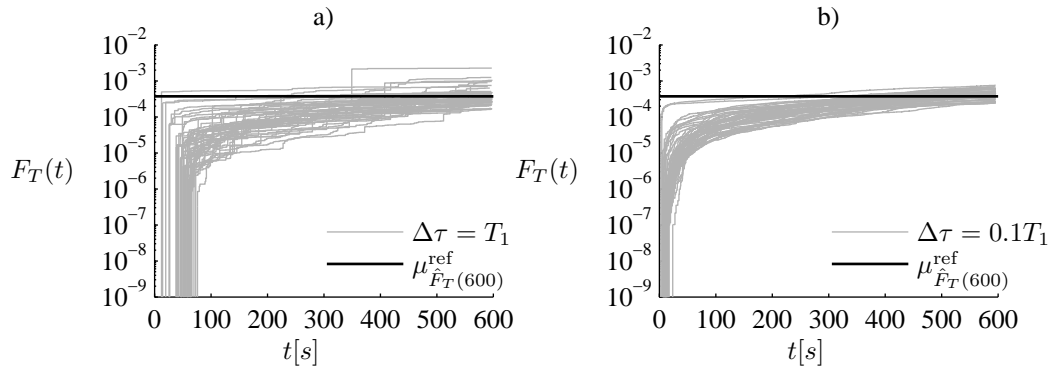


Figure I.22: a) 50 realisations of $F_T(600)$ for $\alpha = 5.0$ using $N = 1000$ and $\Delta\tau \approx T_1$. b) 50 realisations of $F_T(600)$ for $\alpha = 5.0$ using $N = 1000$ and $\Delta\tau = 0.1T_1$.

The conclusion from the investigation of $\Delta\tau$ is that it seems reasonable to use values of $\Delta\tau$ in the interval $\Delta\tau = [0.1T_1, T_1]$.

Assessment of w_{min}

w_{min} is the minimum allowable statistical weight of a realisation. [Pradlwarter and Schuëller, 1999] states that it must be selected small enough to assess the failure domain, but not too small as it will lead to an increased variance of the reliability estimation. As example is mentioned, that if a failure probability of the order 10^{-5} is to be estimated, then $w_{min} = 10^{-5}$ is too large and $w_{min} = 10^{-9}$ is too small, whereas $w_{min} = 10^{-7}$ would be more appropriate.

In figure I.23 the mean value $\mu_{\hat{F}_T(600)}$ and standard deviation $\sigma_{\hat{F}_T(600)}$ is shown as a function of w_{min} . The parameters used for the RR&S simulations are shown in table I.7.

From figure I.23 it seems that the value of w_{min} is less critical compared to $\Delta\tau$. Increasing w_{min} towards 10^{-4} shows a slight divergence from $\mu_{\hat{F}_T(600)}^{ref}$. However, when w_{min} is increased, the number of outcrossings are reduced and therefore the divergence in figure I.23a is believed not to be a bias, but rather due to random fluctuations around $\mu_{\hat{F}_T(600)}^{ref}$. In figure I.23b it is seen that the standard deviation seems rather insensible to w_{min} . Values of w_{min} close to $\mu_{\hat{F}_T(600)}^{ref}$ shows an increase in the variance. Lowering w_{min} several orders of magnitude below $\mu_{\hat{F}_T(600)}^{ref}$ seems only to lower the variance of $\mu_{\hat{F}_T(600)}$. The increase in variance, which [Pradlwarter and Schuëller, 1999] have indicated to occur when decreasing w_{min} too much is not seen in this assessment.

The most significant effect when varying w_{min} is the number of outcrossing which is experienced. This is clearly seen on figure I.24. Figure I.24a shows 50 estimates of $F_T(t)$ using $w_{min} = 10^{-4}$ and figure I.24b shows 50 estimates of $F_T(t)$ using $w_{min} = 10^{-7}$.

The conclusion from the assessment of w_{min} is that it seems reasonable to use values of w_{min} at least a few orders of magnitude below the failure probability which is simulated. As indicated by [Pradlwarter and Schuëller, 1999] then $w_{min} = 10^{-5}$ is a too low value of w_{min} for simulation of failure probabilities around 10^{-5} . No significant difference in the variance is experienced when using values of w_{min} 2-4 orders of magnitude lower than the simulated failure probability.

Assessment of η

η is the exponent in the imperical expression for the importance measure. It determines the influence of the weight to the distance measure. The importance measure is defined by [Pradlwarter and Schuëller, 1999] as

N	α	$\Delta\tau/T_1$	η	P_0	w_{min}	K	T
200	5	1	0.8	0.5	$[10^{-9}, 10^{-4}]$	10	600

Table I.7: Parameter values for RR&S simulations in figure I.23.

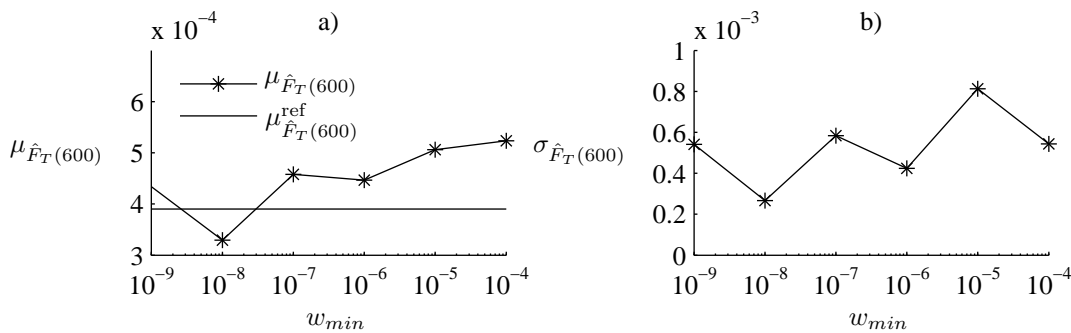


Figure I.23: a) Mean value of failure estimates as a function of w_{min} . b) Standard deviation of failure estimates as a function of w_{min} .

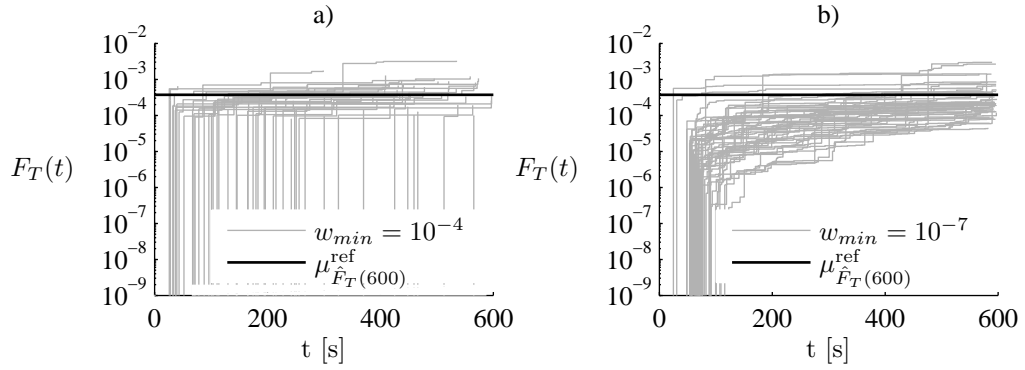


Figure I.24: a) 50 realisations of $F_T(t)$ for $\alpha = 5.0$ using $N = 200$ and $w_{min} = 5 \cdot 10^{-4}$. b) 50 realisations of $F_T(t)$ for $\alpha = 5.0$ using $w_{min} = 10^{-7}$.

$$c_\tau^{(j)} = \frac{d_\tau^{(j)}}{1 + \left(\ln\left(v_\tau^{(j)}\right)\right)^\eta} \quad (\text{I.19})$$

where $c_\tau^{(j)}$ is the importance measure, $d_\tau^{(j)}$ is the distance measure and $v_\tau^{(j)}$ is the weight measure.

In figure I.25 the importance measure from (I.19) has been normalised with respect to the distance measure $d_\tau^{(j)}$ and it is seen how the weights are suppressed faster if η is low. Using $\eta = 0$ means that the weights no longer have any influence on the importance measure.

In figure I.26 $\mu_{\hat{F}_T(600)}$ and $\sigma_{\hat{F}_T(600)}$ is shown as a function of η . In figure I.26 it is seen that $\mu_{\hat{F}_T(600)}$ fluctuates as η goes towards zero. Furthermore, $\sigma_{\hat{F}_T(600)}$ increases as η goes towards zero.

The parameters for the RR&S algorithm used to produce figure I.26 are shown in table I.8.

The conclusion from the assessment of η is that it seems reasonable to use values of η around 0.8-1.5. In [Pradlwarter and Schuëller, 1999] values of η between 0.5-0.8 is used. The choice of η is therefore not unambiguous.

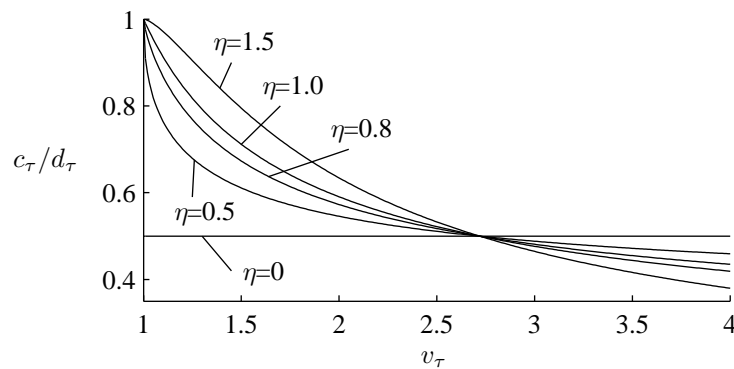


Figure I.25: Normalised importance measure as a function of the weight measure.

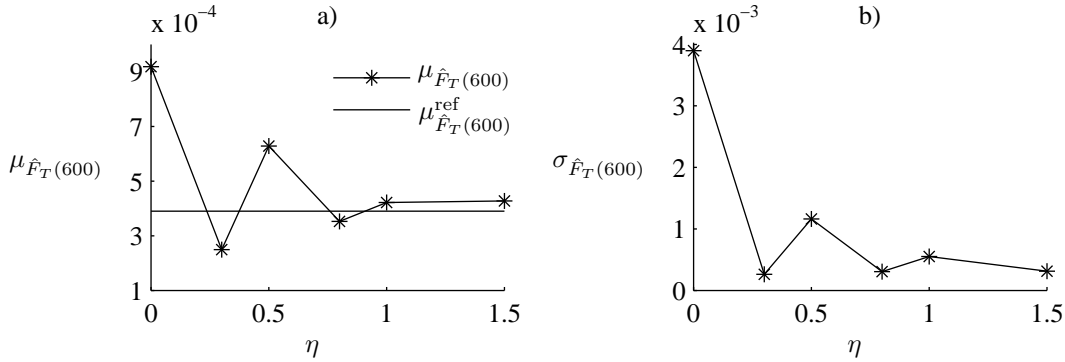


Figure I.26: a) Mean value of failure estimates as a function of η . b) Standard deviation of failure estimates as a function of η .

N	α	$\Delta\tau/T_1$	η	P_0	w_{min}	K
200	5	1	[0,1.5]	0.5	$1 \cdot 10^{-7}$	10

Table I.8: Parameter values for RR&S in figure I.26.

Assessment of K

K is the number of neighbouring realisations which are included in the calculation of the distance and weight measure. [Pradlwarter and Schuëller, 1999] suggests the following expression for how the K neighbouring realisations should be weighted. This expression is given by

$$a_i = 2^{1-i} \quad , \quad i = 1, \dots, K \quad (\text{I.20})$$

Where a_i is the weight given to the i th closest realisation. By (I.20) the closest neighbouring realisations have an influence on the distance measure, whereas other realisations have negligible influence. As figure I.27 shows then values of K above 10 seems unnecessary.

Assessment of a_i

The weights a_i are used in the expressions for calculating the distance measure (8.2) and weights measure (8.5). [Pradlwarter and Schuëller, 1999] suggests to use an expression for a_i given by

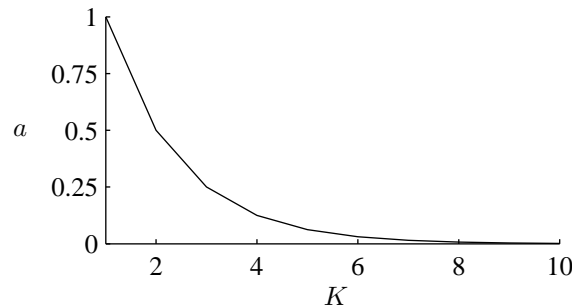


Figure I.27: Weights a as a function of K .

$$a_i = 2^{1-i} \quad (\text{I.21})$$

To assess the effect of the weights a_i , $\mu_{\hat{F}_T(600)}$ and $\sigma_{\hat{F}_T(600)}$ are first calculated by RR&S simulation using (I.21). These results are compared with results for $\mu_{\hat{F}_T(600)}$ and $\sigma_{\hat{F}_T(600)}$ calculated by RR&S simulation using the constant values of the weights a_i given by

$$a_i = 1 \quad (\text{I.22})$$

The parameter values for the RR&S algorithm is given in table I.9.

N	α	$\Delta\tau/T_1$	η	P_0	w_{min}	K
200	5	1	0.8	0.5	$1 \cdot 10^{-7}$	10

Table I.9: Parameter values for RR&S algorithm used to produce results in table I.10.

The results are shown in table I.10. It is seen that no significant difference is seen in neither $\mu_{\hat{F}_T(600)}$ or $\sigma_{\hat{F}_T(600)}$.

a_i	$\mu_{\hat{F}_T(600)}$	$\sigma_{\hat{F}_T(600)}$
2^{1-i}	$5.18 \cdot 10^{-4}$	$7.38 \cdot 10^{-4}$
1	$4.62 \cdot 10^{-4}$	$7.99 \cdot 10^{-4}$

Table I.10: Two estimates of $\mu_{F_T(600)}$ and $\sigma_{F_T(600)}$ using (I.21) and (I.22) for a_i .

The conclusion from the assessment of a_i is that no significant difference is seen in $\mu_{\hat{F}_T(600)}$ or $\sigma_{\hat{F}_T(600)}$ when using the expression (I.22) instead of (I.21).

Assessment of P_0

P_0 controls the rate of killing of "unimportant" realisations. [Pradlwarter and Schuëller, 1999] suggests the following expression for the killing probability

$$p_\tau^{(j)} = \begin{cases} 1 & \text{if } \hat{c}_\tau^{(j)} \geq 1 \\ 1 - P_0(1 - \hat{c}_\tau^{(j)}) & \text{if } \hat{c}_\tau^{(j)} < 1 \end{cases}$$

$\hat{c}_\tau^{(j)}$ is the normalised importance measure, where $\hat{c}_\tau^{(j)} > 1$ characterises the j th realisation as important and $\hat{c}_\tau^{(j)} < 1$ as unimportant. The survival probability, of the unimportant realisations will then be in the interval $[1 - P_0, 1]$. Setting P_0 too high can then have the effect that more realisations are to be killed than the amount of important realisations available to split. If this happens the algorithm will start to split unimportant realisations which have survived Russian Roulette. If the algorithm runs out of realisations to split it aborts. The conclusion is that P_0 should be set as high as possible as this will imply the largest possible interchange between important and unimportant realisations. Decreasing P_0 will simply mean that fewer important realisation are splitted as fewer unimportant realisations are killed.

Conclusion

The conclusion of the parameter analysis is that the most crucial parameter is $\Delta\tau$ as this parameter has great influence on the variance of the estimate of $F_T(t)$. The optimal value seems to be somewhere in the range $[0.1T_1, T_1]$ eigenperiods. w_{min} increases the variance if it is set to high and the value of w_{min} should therefore be around two orders of magnitude smaller than the simulated failure probability. The choice of η was not unambiguous but the assessment shows that $\eta = 0.8$ is a reasonable value. P_0 should be chosen as high as possible, but setting P_0 too high will make the algorithm abort. The value of P_0 is therefore not unambiguous but a value of $P_0 = 0.5$ has been used in all the RR&S simulations performed in this section. The weights a_i does not seem to have any significant influence and it can be chosen to put them constant $a_i = 1$. However, in all simulations performed in the thesis the weights $a_i = 2^{1-i}$ is used.

Appendix J

Importance Sampling

J.1 Stochastic differential equations

Itô Stochastic Differential Equations

The standard form of a one-dimensional stochastic differential equation for the unknown response process $\{X(t), t \in [0, T]\}$ is given as [Arnold, 1974]

$$\left. \begin{aligned} dX(t) &= \mu(X(t), t) dt + \sigma(X(t), t) dW(t) \quad , \quad t > 0 \\ X(0) &= X_0 \end{aligned} \right\} \quad (\text{J.1})$$

The indicated equation is referred to as an *Itô stochastic differential equation* after the mathematician who at first presented the theory on a rigorous footing. $\{W(t), t \in [0, T]\}$ is a unit Wiener process, which is defined below. X_0 is the initial value, which may be a stochastic variable. $\mu(X(t), t)$ and $\sigma(X(t), t)$ are denoted the *drift term* and *diffusion term*, respectively. It is shown below, that the drift and diffusion terms control the mean value function $E[X(t)]$ and the variance of $\{X(t), t \in [0, T]\}$, respectively. For an unloaded system with deterministic start $x(0) = x_0$, Eq. (J.1) reduces to

$$\left. \begin{aligned} \frac{dx(t)}{dt} &= \mu(x(t), t) \quad , \quad t > 0 \\ x(0) &= x_0 \end{aligned} \right\} \quad (\text{J.2})$$

Hence, in a generalized multi-dimensional version the drift term determines the non-linear eigenvibration of the system. Correspondingly, the drift and diffusion terms represent the internal and external forces in a non-linear discretized model of the structure on state vector form.

$dX(t) = X(t+dt) - X(t)$ indicates the increment of the response process during the interval $]t, t+dt]$. Similarly, $dW(t) = W(t+dt) - W(t)$ indicates the increment in the same interval of the unit Wiener process $\{W(t) \mid t \in [0, T]\}$, which is a continuous, non-differential, Gaussian process fulfilling the properties [Nielsen, 2007b]

$$\left. \begin{aligned} W(0) &= 0 \\ E[W(t)] &= 0 \\ E[W(t_1)W(t_2)] &= \min(t_1, t_2) \\ E[(W(t_2) - W(t_1))(W(t_4) - W(t_3))] &= 0 \quad , \quad t_1 < t_2 < t_3 < t_4 \end{aligned} \right\} \quad (\text{J.3})$$

As a consequence, the increment $dW(t)$ becomes normal distributed with the mean value 0 and the variance dt , i.e. $dW(t) \sim N(0, dt)$. Further, the increment $dW(t_1)$ and $dW(t_2)$ belonging to different

intervals are mutual independent, and independent of the initial value X_0 . In turn, this means that $\sigma(X(t), t)$ and $dW(t)$ becomes independent random variables. This implies that the evolution of the mean value function is obtained from

$$\begin{aligned} E[dX(t)] &= dE[X(t)] = E[\mu(X(t), t) dt] + E[\sigma(X(t), t) dW(t)] = \\ E[\mu(X(t), t)] dt + E[\sigma(X(t), t)] E[dW(t)] &= E[\mu(X(t), t)] dt \Rightarrow \\ \frac{d}{dt} E[X(t)] &= E[\mu(X(t), t)] \end{aligned} \quad (\text{J.4})$$

(J.4) is solved with the initial value $E[X(0)] = E[X_0]$. Hence, the evolution of the mean value function is controlled by the mean of the drift term and the mean of the initial value X_0 .

Assume that $X(t)$ realizes the value $X(t) = x$ at the time t . Then, $dX(t)$ becomes normal distributed with the mean value $\mu(x, t) dt$ and the variance $\sigma^2(x, t) dt$, i.e. $dX(t) \sim N(\mu(x, t) dt, \sigma^2(x, t) dt)$. The indicated distribution should be interpreted as the distribution of $dX(t)$ on condition of $X(t) = x$. The essential point is that $dX(t) = X(t + dt) - x$ only depends on $dW(t) = W(t + dt) - W(t)$ and the latest realized value x . More generally, on condition that $X(t_1) = x_1$ is known, the response $X(t_2)$ at a later time t_2 only depends on the sub-Wiener process $\{W(t), t \in [t_1, t_2]\}$ and x_1 , whereas realizations previous to t_1 of the response process and the Wiener process are of no importance. Such a process with restricted memory is denoted a *Markov process*.

Stochastic Differential Equations in Engineering

The engineering interpretation of (J.1) is given as

$$\left. \begin{aligned} \frac{d\tilde{X}(t)}{dt} &= \mu(\tilde{X}(t), t) + \sigma(\tilde{X}(t), t) \tilde{w}(t) \quad , \quad t > 0 \\ X(0) &= X_0 \end{aligned} \right\} \quad (\text{J.5})$$

where $\{\tilde{w}(t), t \in [0, T]\}$ is a broad-banded stationary zero-mean Gaussian process with finite variance, for which the double-sided auto-spectral density function attains the value $S_0 = \frac{1}{2\pi}$ over a sufficiently broad frequency range encompassing all significant eigenfrequencies of the structure. As the bandwidth of the excitation process $\{\tilde{w}(t), t \in [0, T]\}$ is extended beyond limits it is assumed that the process may be replaced by a unit white noise process $\{\tilde{w}(t), t \in [0, T]\}$, i.e. a Gaussian process with the properties

$$\left. \begin{aligned} E[\tilde{w}(t)] &= 0 \\ E[\tilde{w}(t_1)\tilde{w}(t_2)] &= \delta(t_2 - t_1) \end{aligned} \right\} \quad (\text{J.6})$$

where $\delta(\cdot)$ denotes the Dirac delta function. Despite the Wiener process is not differentiable, $w(t)$ is interpreted as the formal derivative $\frac{dW(t)}{dt}$ of a unit Wiener process in engineering. If this derivative is inserted for $\tilde{w}(t)$ in (J.5), Eq. (J.1) is formally recovered. The problem is whether the response process $\{\tilde{X}(t), t \in [0, T]\}$ obtained from (J.5) in the limit as the band-width goes to infinity is the same response process as obtained from (J.1). Unfortunately, the answer to this question is no. Instead the limit process is obtained as the solution to the so-called *Stratonovich stochastic differential equation* given as

$$\left. \begin{aligned} d\tilde{X}(t) &= \mu\left(\tilde{X}\left(t + \frac{1}{2}dt\right), t + \frac{1}{2}dt\right) dt + \sigma\left(\tilde{X}\left(t + \frac{1}{2}dt\right), t + \frac{1}{2}dt\right) dW(t) \quad , \quad t > 0 \\ \tilde{X}(0) &= X_0 \end{aligned} \right\} \quad (\text{J.7})$$

The essential difference to Eq. (J.1) is that the drift- and diffusion terms are now evaluated in the midst of the interval $]t, t+dt]$. This is of no importance for the drift term. However, $\sigma\left(\tilde{X}\left(t + \frac{1}{2}dt\right), t + \frac{1}{2}dt\right)$ and $dW(t)$ are no longer mutual independent, so the expectation of $\sigma\left(\tilde{X}\left(t + \frac{1}{2}dt\right), t + \frac{1}{2}dt\right) dW(t)$ does not vanishes, but causes a net drift of system. In order to calculate this net contribution the following first order Taylor expansion is considered

$$\begin{aligned} \sigma\left(\tilde{X}\left(t + \frac{1}{2}dt\right), t + \frac{1}{2}dt\right) &= \sigma\left(\tilde{X}(t), t\right) + \frac{\partial\sigma\left(\tilde{X}(t), t\right)}{\partial t} \frac{1}{2}dt + \\ &\frac{\partial\sigma\left(\tilde{X}(t), t\right)}{\partial X} \left(\tilde{X}\left(t + \frac{1}{2}dt\right) - \tilde{X}(t)\right) = \\ \sigma\left(\tilde{X}(t), t\right) + \frac{\partial\sigma\left(\tilde{X}(t), t\right)}{\partial t} \frac{1}{2}dt + \\ &\frac{\partial\sigma\left(\tilde{X}(t), t\right)}{\partial X} \left(\mu\left(\tilde{X}(t), t\right) \frac{1}{2}dt + \sigma\left(\tilde{X}(t), t\right) \left(W\left(t + \frac{1}{2}dt\right) - W(t)\right)\right) \end{aligned} \quad (\text{J.8})$$

Then,

$$\begin{aligned} E\left[\sigma\left(\tilde{X}\left(t + \frac{1}{2}dt\right), t + \frac{1}{2}dt\right) dW(t)\right] &= \\ E\left[\frac{\partial\sigma\left(\tilde{X}(t), t\right)}{\partial X} \sigma\left(\tilde{X}(t), t\right) \left(W\left(t + \frac{1}{2}dt\right) - W(t)\right) \left(W(t+dt) - W(t)\right)\right] &= \\ E\left[\frac{\partial\sigma\left(\tilde{X}(t), t\right)}{\partial X} \sigma\left(\tilde{X}(t), t\right)\right] E\left[\left(W\left(t + \frac{1}{2}dt\right) - W(t)\right) \left(W(t+dt) - W(t)\right)\right] &= \\ E\left[\frac{\partial\sigma\left(\tilde{X}(t), t\right)}{\partial X} \sigma\left(\tilde{X}(t), t\right)\right] E\left[\left(W\left(t + \frac{1}{2}dt\right) - W(t)\right)^2\right] &= \\ E\left[\frac{\partial\sigma\left(\tilde{X}(t), t\right)}{\partial X} \sigma\left(\tilde{X}(t), t\right)\right] \frac{1}{2}dt & \end{aligned} \quad (\text{J.9})$$

This suggests the equivalence of (J.7) with the following Itô differential equation

$$\left. \begin{aligned} d\tilde{X}(t) &= \left(\mu\left(\tilde{X}(t), t\right) + \frac{1}{2} \frac{\partial\sigma\left(\tilde{X}(t), t\right)}{\partial X} \sigma\left(\tilde{X}(t), t\right)\right) dt + \sigma\left(\tilde{X}(t), t\right) dW(t) \quad , \quad t > 0 \\ \tilde{X}(0) &= X_0 \end{aligned} \right\} \quad (\text{J.10})$$

Actually, the validity of (J.7) can be proven. The indicated correction of the drift term is known as the *Wong-Zakai correction*. [Wong and Zakai, 1965]

J.1.1 Girsanov's Theorem

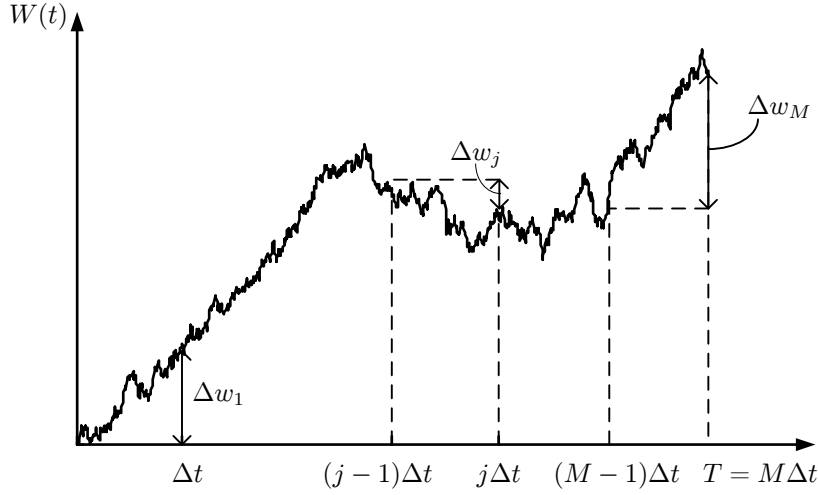


Figure J.1: Increments of a unit Wiener process.

Let the interval $[0, T]$ be divided into m subintervals each of the length $\Delta t = \frac{T}{M}$. Then, a unit Wiener process $\{W(t), t \in [0, T]\}$ is discretized into an M -dimensional vector

$$\Delta \mathbf{W}^T = [\Delta W_1, \Delta W_2, \dots, \Delta W_M] \quad (\text{J.11})$$

where ΔW_j denotes the increment in the j th subinterval, cf. figure J.1.

$$\Delta W_j = W(j\Delta t) - W((j-1)\Delta t) \quad , \quad j = 1, \dots, M \quad (\text{J.12})$$

The random variables ΔW_j are mutually independent and identical distributed normal random variables with zero mean and variance Δt , i.e. the probability density function is given as

$$f_{\Delta W_j}(\Delta w_j) = \frac{1}{(2\pi\Delta t)^{1/2}} \exp\left(-\frac{\Delta w_j^2}{2\Delta t}\right) \quad (\text{J.13})$$

Then, the joint probability density function of $\Delta \mathbf{W}$ becomes

$$f_{\Delta \mathbf{w}}(\Delta \mathbf{w}) = \prod_{j=1}^M f_{\Delta W_j}(\Delta w_j) = \frac{1}{(2\pi\Delta t)^{M/2}} \exp\left(-\frac{\sum_{j=1}^M \Delta w_j^2}{2\Delta t}\right) \quad (\text{J.14})$$

Next, consider an auxiliary stochastic process $\{\tilde{W}(t), t \in [0, T]\}$, where

$$\tilde{W}(t) = W(t) + \int_0^t u(s) ds \quad (\text{J.15})$$

where $u(t)$ is a suitable chosen function. (J.15) is known as the Girsanov transformation.[Girsanov, 1960]
 $\{\tilde{W}(t) , t \in [0, T]\}$, is discretized in the same way as $\{W(t) , t \in [0, T]\}$ into an n -dimensional vector

$$\Delta \tilde{\mathbf{W}}^T = [\Delta \tilde{W}_1, \Delta \tilde{W}_2, \dots, \Delta \tilde{W}_M] \quad (\text{J.16})$$

where $\Delta \tilde{W}_j$ denotes the increment of $\{\tilde{W}(t) , t \in [0, T]\}$ in the j th subinterval

$$\Delta \tilde{W}_j = \tilde{W}(j\Delta t) - \tilde{W}((j-1)\Delta t) \simeq \Delta W_j + u_j \Delta t \quad , \quad j = 1, \dots, n \quad (\text{J.17})$$

and $u_j = u(j\Delta t)$. The random variables $\Delta \tilde{W}_j$ are mutually independent normal random variables with mean value $u_j \Delta t$ and variance Δt , i.e. the probability density function is given as

$$f_{\Delta \tilde{W}_j}(\Delta \tilde{w}_j) = \frac{1}{(2\pi \Delta t)^{1/2}} \exp\left(-\frac{(\Delta \tilde{w}_j - u_j \Delta t)^2}{2\Delta t}\right) \quad (\text{J.18})$$

The joint probability density function of $\Delta \tilde{\mathbf{W}}$ becomes

$$f_{\Delta \tilde{\mathbf{W}}}(\Delta \tilde{\mathbf{w}}) = \prod_{j=1}^M f_{\Delta \tilde{W}_j}(\Delta \tilde{w}_j) = \frac{1}{(2\pi \Delta t)^{M/2}} \exp\left(-\frac{\sum_{j=1}^M (\Delta \tilde{w}_j - u_j \Delta t)^2}{2\Delta t}\right) \quad (\text{J.19})$$

Hence, the Radon-Nikodym derivative of the measure $P_{\Delta \mathbf{W}}(\Delta \tilde{\mathbf{w}})$ with respect to the measure $P_{\Delta \tilde{\mathbf{W}}}(\Delta \tilde{\mathbf{w}})$ at the sample point $\Delta \tilde{\mathbf{w}}$ becomes

$$\frac{dP_{\Delta \mathbf{W}}(\Delta \tilde{\mathbf{w}})}{dP_{\Delta \tilde{\mathbf{W}}}(\Delta \tilde{\mathbf{w}})} = \frac{f_{\Delta \mathbf{W}}(\Delta \tilde{\mathbf{w}})}{f_{\Delta \tilde{\mathbf{W}}}(\Delta \tilde{\mathbf{w}})} = \exp\left(\sum_{j=1}^M u_j \Delta \tilde{w}_j - \frac{1}{2} \sum_{j=1}^M u_j^2 \Delta t\right) \quad (\text{J.20})$$

Let $M \rightarrow \infty$. Then, $\Delta \mathbf{W}$ and $\Delta \tilde{\mathbf{W}}$ converge to the stochastic processes $\{dW(t) , t \in [0, T]\}$ and $\{d\tilde{W}(t) , t \in [0, T]\}$. Let $P_{\{dW\}}$ and $P_{\{d\tilde{W}\}}$ denote the probability measures of the infinite many stochastic variables contained in the indicated processes. Then, the Radon-Nikodym derivative of $P_{\{dW\}}[d\tilde{w}(t)]$ with respect to $P_{\{d\tilde{W}\}}[d\tilde{w}(t)]$ evaluated at increments of the same sample curve $\tilde{w}(t)$ of $\{\tilde{\mathbf{W}}(t) , t \in [0, T]\}$ follows from the limit of (J.20)

$$\frac{dP_{\{dW\}}[d\tilde{w}(t)]}{dP_{\{d\tilde{W}\}}[d\tilde{w}(t)]} = \exp\left(\int_0^T u(t)d\tilde{w}(t) - \frac{1}{2}\int_0^T u^2(t)dt\right) \quad (\text{J.21})$$

We search the realizations $\tilde{x}_j(t)$ of the process $\{\tilde{X}(t), t \in [0, T]\}$, obtained when the Wiener unit process in (J.1) is replaced by the process $\{\tilde{W}(t), t \in [0, T]\}$, i.e.

$$\left. \begin{aligned} d\tilde{X}(t) &= \mu(\tilde{X}(t), t) dt + \sigma(\tilde{X}(t), t) d\tilde{W}(t) \quad , \quad t > 0 \\ \tilde{X}(0) &= X_0 \end{aligned} \right\} \quad (\text{J.22})$$

From (J.15) follows

$$d\tilde{W}(t) = dW(t) + u(t) dt \quad (\text{J.23})$$

Then, (J.21) and (J.22) may be rewritten in the form

$$\frac{dP_{\{dW\}}[d\tilde{w}(t)]}{dP_{\{d\tilde{W}\}}[d\tilde{w}(t)]} = \exp\left(-\int_0^T u(t)dw(t) - \frac{1}{2}\int_0^T u^2(t)dt\right) \quad (\text{J.24})$$

$$\left. \begin{aligned} d\tilde{X}(t) &= \left(\mu(\tilde{X}(t), t) + \sigma(\tilde{X}(t), t)u(t)\right) dt + \sigma(\tilde{X}(t), t) dW(t) \quad , \quad t > 0 \\ \tilde{X}(0) &= X_0 \end{aligned} \right\} \quad (\text{J.25})$$

In (J.25) $\{W(t), t \in [0, T]\}$ denotes a unit Wiener process, and $dw(t)$ in (J.24) represents the increments of a given realization $w(t)$ of this process.

Let $w_1(t), \dots, w_N(t)$ denote N realizations of $\{W(t), t \in [0, T]\}$, and let $\tilde{x}_1(t), \dots, \tilde{x}_N(t)$ be the corresponding realizations of $\{\tilde{X}(t), t \in [0, T]\}$, obtained by numerical integration of the differential equation of (J.25). Then, an unbiased estimate of the failure probability is given as

$$\begin{aligned} \hat{P}_f &= \frac{1}{N} \sum_{j=1}^N I[\tilde{x}_j(t)] \frac{dP_{\{dW\}}[d\tilde{w}_j(t)]}{dP_{\{d\tilde{W}\}}[d\tilde{w}_j(t)]} = \\ &= \frac{1}{N} \sum_{j=1}^N I[\tilde{x}_j(t)] \exp\left(-\int_0^T u(t)dw_j(t) - \frac{1}{2}\int_0^T u^2(t)dt\right) \end{aligned} \quad (\text{J.26})$$

$I[\tilde{x}_j]$ denotes an indicator functional, which is 1, if the realization $\tilde{x}_j(t)$ causes failure, and 0, if $\tilde{x}_j(t)$ remains in the safe domain throughout the interval $[0, T]$. It should be emphasized that (J.26) provides an unbiased estimate of the failure probability no matter which function $u(t)$ is used. However,

should the method be efficient it is of importance that the function, which is referred to as the sample control function, will induce failure in approximated half of the realization. In turn this means that the Radon-Nikodym derivative $\frac{dP_{\{d\mathbf{W}\}}[d\tilde{\mathbf{w}}(t)]}{dP_{\{d\tilde{\mathbf{w}}\}}[d\tilde{\mathbf{w}}(t)]}$ should attain a small value.

The Itô stochastic differential equation an n -dimensional dynamic response process $\{\mathbf{X}(t), t \in [0, T]\}$ is given as

$$\left. \begin{aligned} d\mathbf{X}(t) &= \boldsymbol{\mu}(\mathbf{X}(t), t) dt + \boldsymbol{\sigma}(\mathbf{X}(t), t) d\mathbf{W}(t) \quad , \quad t > 0 \\ \mathbf{X}(0) &= \mathbf{X}_0 \end{aligned} \right\} \quad (\text{J.27})$$

$$\left. \begin{aligned} \mathbf{X}(t) &= \begin{bmatrix} X_1(t) \\ X_2(t) \\ \vdots \\ X_n(t) \end{bmatrix} \quad , \quad \mathbf{W}(t) = \begin{bmatrix} W_1(t) \\ W_2(t) \\ \vdots \\ W_n(t) \end{bmatrix} \quad , \quad \boldsymbol{\mu}(\mathbf{X}(t), t) = \begin{bmatrix} \mu_1(\mathbf{X}(t), t) \\ \mu_2(\mathbf{X}(t), t) \\ \vdots \\ \mu_n(\mathbf{X}(t), t) \end{bmatrix} \\ \boldsymbol{\sigma}(\mathbf{X}(t), t) &= \begin{bmatrix} \sigma_{11}(\mathbf{X}(t), t) & \sigma_{12}(\mathbf{X}(t), t) & \cdots & \sigma_{1m}(\mathbf{X}(t), t) \\ \sigma_{21}(\mathbf{X}(t), t) & \sigma_{22}(\mathbf{X}(t), t) & \cdots & \sigma_{2m}(\mathbf{X}(t), t) \\ \vdots & \vdots & \ddots & \vdots \\ \sigma_{n1}(\mathbf{X}(t), t) & \sigma_{n2}(\mathbf{X}(t), t) & \cdots & \sigma_{nm}(\mathbf{X}(t), t) \end{bmatrix} \end{aligned} \right\} \quad (\text{J.28})$$

The n -dimensional vector $\boldsymbol{\mu}(\mathbf{X}(t), t)$ and the $n \times m$ dimensional matrix $\boldsymbol{\sigma}(\mathbf{X}(t), t)$ are referred to as the *drift vector* and the *diffusion matrix*, respectively. $\{W_j(t), t \in [0, T]\}$, $j = 1, \dots, m$ are independent unit Wiener processes fulfilling the properties, cf. (J.3)

$$\left. \begin{aligned} E[W_j(t)] &= 0 \\ E[W_j(t_1)W_k(t_2)] &= \delta_{jk} \min(t_1, t_2) \end{aligned} \right\} \quad (\text{J.29})$$

where δ_{jk} signifies the Kronecker's delta. In analogy to (J.15) an auxiliary vector process $\{\tilde{\mathbf{W}}(t), t \in [0, T]\}$ is introduced with increments given by

$$d\tilde{\mathbf{W}}(t) + d\mathbf{W}(t) + \mathbf{u}(t) dt \quad (\text{J.30})$$

The components of the m -dimensional vector $\mathbf{u}(t)$ represents the control functions on each of the M input Wiener processes. The Radon-Nikodym derivative of $P_{\{d\mathbf{W}\}}[d\tilde{\mathbf{w}}(t)]$ with respect to $P_{\{d\tilde{\mathbf{w}}\}}[d\tilde{\mathbf{w}}(t)]$ evaluated at increments of the same sample curve $\tilde{\mathbf{w}}(t)$ of $\{\tilde{\mathbf{W}}(t), t \in [0, T]\}$ follows from the limit of (J.20)

$$\frac{dP_{\{d\mathbf{W}\}}[d\tilde{\mathbf{w}}(t)]}{dP_{\{d\tilde{\mathbf{w}}\}}[d\tilde{\mathbf{w}}(t)]} = \exp \left(- \sum_{j=1}^m \int_0^T u_j(t) dw_j(t) - \sum_{j=1}^m \frac{1}{2} \int_0^T u_j^2(t) dt \right) \quad (\text{J.31})$$

$$\left. \begin{aligned} d\tilde{\mathbf{X}}(t) &= \left(\boldsymbol{\mu}(\tilde{\mathbf{X}}(t), t) - \boldsymbol{\sigma}(\tilde{\mathbf{X}}(t), t) \mathbf{u}(t) \right) dt + \boldsymbol{\sigma}(\tilde{\mathbf{X}}(t), t) d\mathbf{W}(t) \quad , \quad t > 0 \\ \tilde{\mathbf{X}}(0) &= \mathbf{X}_0 \end{aligned} \right\} \quad (\text{J.32})$$

In (J.31) $\{W(t), t \in [0, T]\}$ denotes a unit Wiener process, and $dw(t)$ in (J.32) represents the increments of a given realization $w(t)$ of this process.

Let $\mathbf{w}_1(t), \dots, \mathbf{w}_N(t)$ denote N realizations of $\{\mathbf{W}(t), t \in [0, T]\}$, and let $\tilde{\mathbf{x}}_1(t), \dots, \tilde{\mathbf{x}}_N(t)$ be the corresponding realizations of $\{\tilde{\mathbf{X}}(t), t \in [0, T]\}$, obtained by numerical integration of (J.32). Then, an unbiased estimate of the failure probability is given as

$$\begin{aligned} \hat{P}_f &= \frac{1}{N} \sum_{j=1}^N I[\tilde{\mathbf{x}}_j(t)] \frac{dP_{\{d\mathbf{W}\}}[d\tilde{\mathbf{w}}(t)]}{dP_{\{d\tilde{\mathbf{W}}\}}[d\tilde{\mathbf{w}}(t)]} = \\ &= \frac{1}{N} \sum_{j=1}^N I[\tilde{\mathbf{x}}_j(t)] \exp \left(- \sum_{j=1}^m \int_0^T u_j(t) dw_j(t) - \sum_{j=1}^m \frac{1}{2} \int_0^T u_j^2(t) dt \right) \end{aligned} \quad (\text{J.33})$$

J.2 Multi-modal sampling simulation methods

In conventional IS methods, samples are generated in the failure domain with relative high probability density. Since the nature of oscillating systems provide wide spread failure domain, it is not sufficient to generate samples in the region with the largest probability density. A way to overcome this problem is by using the so-called *multi-modal sampling density*, which generates samples around a number of points in the failure domain, but emphasizes the region around a point in proportion to the probability density at that point. Let $\{\Delta\tilde{\mathbf{w}}^{(1)}, \Delta\tilde{\mathbf{w}}^{(2)}, \dots, \Delta\tilde{\mathbf{w}}^{(M)}\}$ be a set of points in the failure region, which are used to construct the multi-modal sampling density, which is given by [Karamchandani, 1990]

$$h_{\Delta\tilde{\mathbf{W}}}(\Delta\tilde{\mathbf{w}}^{(l)}) = \sum_{i=1}^M \mathcal{W}_i f_{\Delta\tilde{\mathbf{W}}}^{(i)}(\Delta\tilde{\mathbf{w}}^{(l)}) \quad (\text{J.34})$$

where $f_{\Delta\tilde{\mathbf{W}}}(\Delta\tilde{\mathbf{w}}^{(l)})$ is determined by (J.19), upper index (l) corresponds to the control function $u^{(l)}$ and \mathcal{W} are the weights estimated by

$$\mathcal{W}_i = \frac{\Phi(-\beta^{(i)})}{\sum_{j=1}^M \Phi(-\beta^{(j)})} \quad (\text{J.35})$$

An auxiliary fraction is introduced as

$$\mathcal{R}_i^{(l)} = \frac{f_{\Delta\tilde{\mathbf{W}}}(\Delta\tilde{\mathbf{w}}^{(l)})}{f_{\Delta\tilde{\mathbf{W}}}(\Delta\tilde{\mathbf{w}}^{(l)})} \quad (\text{J.36})$$

by inserting (J.14), (J.19) and (J.17) the following emerge

$$\begin{aligned}
\mathcal{R}_i^{(l)} &= \exp \left(\frac{-1}{2\Delta t} \sum_{j=1}^M \left((\Delta \tilde{w}_j^{(l)} - u_j^{(i)} \Delta t)^2 - \Delta \tilde{w}_j^{(l)} \right) \right) \\
&= \exp \left(\frac{-1}{2\Delta t} \sum_{j=1}^M \left((u_j^{(i)})^2 \Delta t^2 - 2\Delta \tilde{w}_j^{(l)} u_j^{(i)} \Delta t \right) \right) \\
&= \exp \left(\frac{-1}{2\Delta t} \sum_{j=1}^M \left((u_j^{(i)})^2 \Delta t^2 - 2\Delta u_j^{(i)} \Delta t (u_j^{(l)} \Delta t + \Delta w_j) \right) \right) \\
&= \exp \left(\frac{-1}{2\Delta t} \sum_{j=1}^M \left(u_j^{(i)} \Delta t (u_j^{(i)} \Delta t - 2u_j^{(l)} \Delta t) - 2u_j^{(i)} \Delta w_j \Delta t \right) \right) \\
&= \exp \left(\sum_{j=1}^M u_j^{(i)} \Delta w_j + \frac{1}{2} \sum_{j=1}^M u_j^{(i)} (2u_j^{(l)} - u_j^{(i)}) \Delta t \right) \tag{J.37}
\end{aligned}$$

The Radon-Nikodym derivative is then given by

$$\frac{1}{\mathcal{R}^{(l)}} = \frac{h_{\Delta \tilde{\mathbf{W}}}(\Delta \tilde{\mathbf{w}}^{(l)})}{f_{\Delta \mathbf{W}}(\Delta \tilde{\mathbf{w}}^{(l)})} = \sum_{i=1}^M \mathcal{W}_i \mathcal{R}_i^{(l)} \tag{J.38}$$

whereby an estimate of the failure probability is determined from

$$\hat{P}_f = \frac{1}{N} \sum_{s=1}^N I(\tilde{\mathbf{w}}_s) \mathcal{R}^{(l)} \tag{J.39}$$

Upper index (l) corresponds to the design point $\beta^{(l)}$ and is a random integer in the interval $[1M]$ generated from the \mathcal{W} distribution.

J.3 Scalar diffusion with a constant drift

In the following the IS method is verified for a simple dynamic system. The example which is taken from [Tanaka, 1998] takes its basis in the scalar Itô differential equation

$$dX(t) = \mu dt + \sigma dW(t) \quad , \quad t \in [0, T] \tag{J.40}$$

where the drift and diffusion term μ and σ are constants and $W(t)$ is a unit Wiener process $W(t) \sim N(0, t)$.

Utilising the Girsanov transformation a drift is introduced into the diffusion process $X(t)$ via the excitation process $\tilde{W}(t)$ with increments given as

$$d\tilde{W}(t) = u(t)dt + dW(t) \quad (\text{J.41})$$

The control function $u(t)$ is specified so $X(t)$ reaches the critical level x_c at the design time $t^* = T$. The failure function is then given by

$$g(x) = x_c - x \quad (\text{J.42})$$

By using the Euler time integration, the failure function $g(x(T))$ is described by the stochastic safety margin \mathcal{M} which in the standard normal distributed space is given by

$$\mathcal{M}(\Xi) = x_c - x_0 - M\Delta t - \sigma\sqrt{\Delta t} \sum_{i=1}^M \Xi_i \quad (\text{J.43})$$

where $X(0) = x_0$ is the deterministic initial value, M is the number of discretisations given by $M = \frac{T}{\Delta t}$ and $\Xi_i = \frac{\Delta W_i}{\sqrt{\Delta t}}$. By using the FORM notation, (J.43) can be written as

$$\mathcal{M} = \beta - \sum_{i=1}^M \alpha_i \Xi_i \quad , \quad i = 1, 2, \dots, M \quad (\text{J.44})$$

where

$$\beta(t) = \frac{x_c - x_0 - \mu t}{\sigma\sqrt{t}} \quad , \quad \alpha_i = \frac{-1}{\sqrt{M}}$$

The optimal load process driving the response process to failure at the design time $t^* = T$ is in the standard normal distributed space given by

$$\Xi_i^* = \beta(t_M)\alpha_i = \frac{-x_c + x_0 + \mu T}{M\sigma\sqrt{\Delta t}} \quad (\text{J.45})$$

(J.45) is transformed back to the original space by a requirement of variance consistence of (J.41).

$$u_i = \frac{x_c - x_0 - \mu T}{\sigma T} \quad (\text{J.46})$$

From (J.46) it emerge that the control function is constant. Realisations of the process $\tilde{X}(t)$ is obtained as a solution to (J.40), where (J.41) is used.

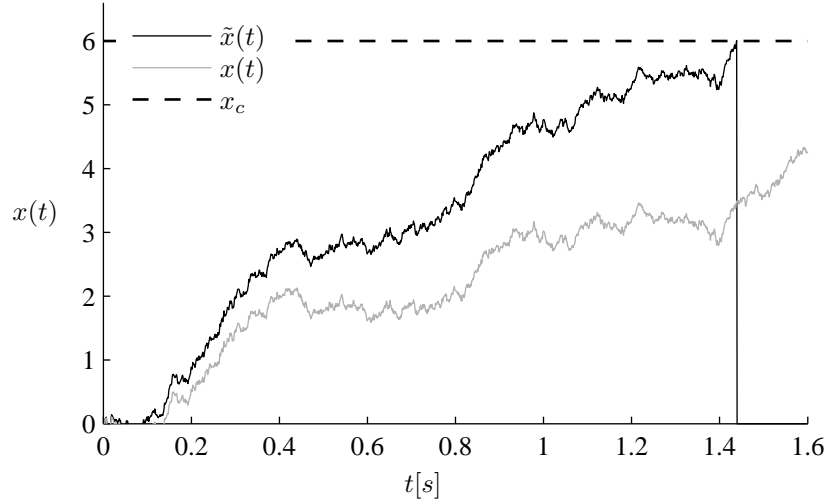


Figure J.2: Realisation of $x(t)$ and $\tilde{x}(t)$.

Utilizing the parameters $\mu = 2$, $\sigma = 1$, $\Delta t = 1.0 \cdot 10^{-4}$, $T = 1.6$, $x_0 = 0$ and $x_c = 6$, realisations of $X(t)$ exposed to $\tilde{W}(t)$ and $W(t)$ is shown in figure J.2.

As seen, the control function $u(t)$ gives a contribution to the drift term which in average drives the process to failure.

The estimated first passage probability distribution function $F_T(t)$ determined by IS method as shown in figure J.3, along with the analytical solution to (J.40) which is obtained by, [Tanaka, 1998]

$$F_T(t) = \int_0^\tau \frac{x_c - x_0}{\sigma\sqrt{2\pi\tau^3}} \cdot \exp\left[-\frac{(x_c - x_0 - \mu\tau)^2}{2\sigma^2\tau}\right] dt \quad (\text{J.47})$$

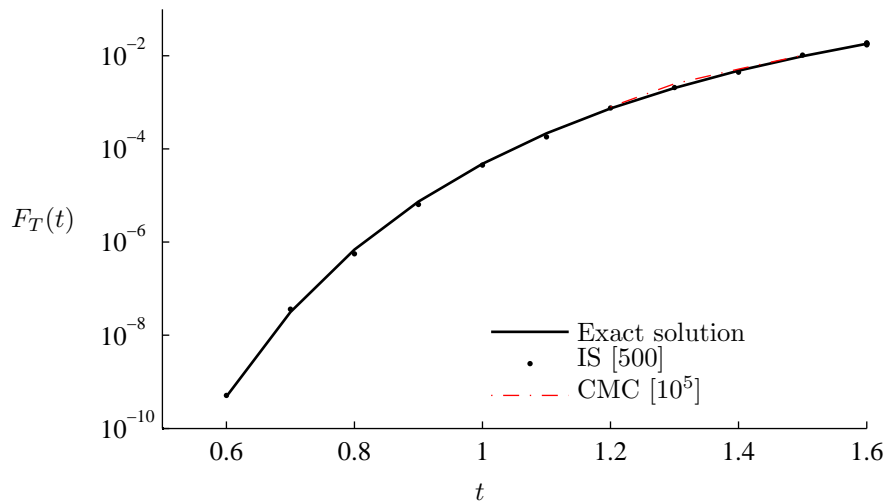


Figure J.3: Estimated first passage time probability distribution function.

As seen in figure J.3 the IS method produce very good result with a relative few number of simulations, even for high failure probabilities. Regarding the CMC simulation it is in this case not practical possible to simulate failure probabilities lower than 10^{-5} .

J.4 Importance sampling applied to a single dof linear oscillator

In the following example the failure probability for a single dof linear oscillator will be determined by means of the multi-modal sampling simulation method. The equation of motion is given as

$$\ddot{Y}(t) + 2\zeta\dot{Y}(t) + Y(t) = \sqrt{4\zeta}\dot{W}(t), \quad Y(0) = \dot{Y}(0) = 0 \quad (\text{J.48})$$

where $\dot{W}(t)$ is a zero-mean unit Gaussian white noise and ζ is the damping ratio. The displacement $Y(t)$ and the velocity $\dot{Y}(t)$ have been normalised to a unit stationary variance. The equation is written in a state vector form, as

$$\begin{aligned} \frac{d}{dt}\mathbf{Z}(t) &= \mathbf{A}\mathbf{Z}(t) + \mathbf{c}\dot{W}(t) \\ \mathbf{Z}(t) &= \begin{bmatrix} \mathbf{Y}(t) \\ \dot{\mathbf{Y}}(t) \end{bmatrix}, \quad \mathbf{A} = \begin{bmatrix} 0 & 1 \\ -1 & -2\zeta \end{bmatrix}, \quad \mathbf{c} = \begin{bmatrix} 0 \\ \sqrt{4\zeta} \end{bmatrix} \end{aligned} \quad (\text{J.49})$$

Equation (J.49) is reformulated to the following Itô-differential equation

$$d\mathbf{Z} = \mathbf{A}\mathbf{Z}(t)dt + \mathbf{c}dW(t) \quad (\text{J.50})$$

For quiescent initial conditions, the response process $\{Y(t), t \in [0 T]\}$ is determined by the Duhamel-integral

$$Y(t) = \sqrt{4\zeta} \int_0^t h(t-\tau)dW(\tau) \quad (\text{J.51})$$

where h is the impulse response function given by

$$h(t) = \frac{\exp(-\zeta t)}{\sqrt{1-\zeta^2}} \sin \sqrt{1-\zeta^2}t \quad (\text{J.52})$$

By means of an Euler iteration scheme (J.51) becomes

$$Y(i) = \sqrt{4\zeta} \sum_{j=1}^i h(i-j)\Xi(j)\sqrt{\Delta t}, \quad (\text{J.53})$$

where $Y(i) = Y(i\Delta t)$, $h(i-j) = h((i-j)\Delta t)$, $\Delta W(j) = \sqrt{\Delta t} \Xi(j)$ and $\Xi \sim N(0, 1)$. Failure occurs when the response process is greater than the deterministic barrier function y_c , thus the linear safety margin at $t = i$ is given as

$$\mathcal{M}(Y(i)) = y_c - Y(i) = y_c - \sqrt{4\zeta} \sum_{j=1}^i h(i-j) \Xi(j) \sqrt{\Delta t} \quad (\text{J.54})$$

The mean value and standard deviation of the linear safety margin is given as

$$\mu_{\mathcal{M}} = y_c \quad , \quad \sigma_{\mathcal{M}} = \sqrt{4\zeta \Delta t \sum_{j=1}^i (h(i-j))^2} \quad (\text{J.55})$$

The minimal distance $\beta^{(i)}$ and the normal vector to the failure surface at the design time $t = i$ is then determined as

$$\beta^{(i)} = \frac{\mu_{\mathcal{M}}}{\sigma_{\mathcal{M}}} = \frac{y_c}{\sqrt{4\zeta \Delta t \sum_{j=1}^i (h(i-j))^2}} \quad , \quad \alpha^{(i)}(j) = \frac{-\sqrt{4\zeta \Delta t} h(i-j)}{\sqrt{4\zeta \Delta t \sum_{j=1}^i (h(i-j))^2}} \quad (\text{J.56})$$

whereby the design point becomes

$$\xi^{(i)*}(j) = \beta^{(i)} \alpha^{(i)}(j) = \frac{-y_c h(i-j)}{\sqrt{4\zeta \Delta t \sum_{j=1}^i (h(i-j))^2}} \quad (\text{J.57})$$

The sample control function $u(t)$ corresponding to the design point ξ_i^* in the original space is determined by (7.15) as

$$u^{(i)}(j) = \frac{y_c}{\sqrt{4\zeta} \sum_{j=1}^i (h(j-i))^2 \Delta t} h(i-j) \quad (\text{J.58})$$

As mentioned earlier $u^{(i)}(t)$ is merely an underlying process that drives the response process to failure at $t^* = i$. As it emerge from (J.58), $u(t)$ is a time inverted impulse response function as shown in figure J.4 for different design points.

The sample paths is generated by inserting (7.10) into (J.53), thus

$$\tilde{y}(i) = \sqrt{4\zeta} \sum_{j=1}^i h_{ij} (u_j^{(l)} \Delta t + \Delta w_j), \quad (\text{J.59})$$

where $u^{(l)}$ corresponds to the minimal distance $\beta^{(l)}$ at the design time $t^* = l$. A Realisation of the response process $\tilde{Y}(t)$ and $Y(t)$ generated from the incremental Wiener process series $[\Delta w_1, \dots, \Delta w_M]$

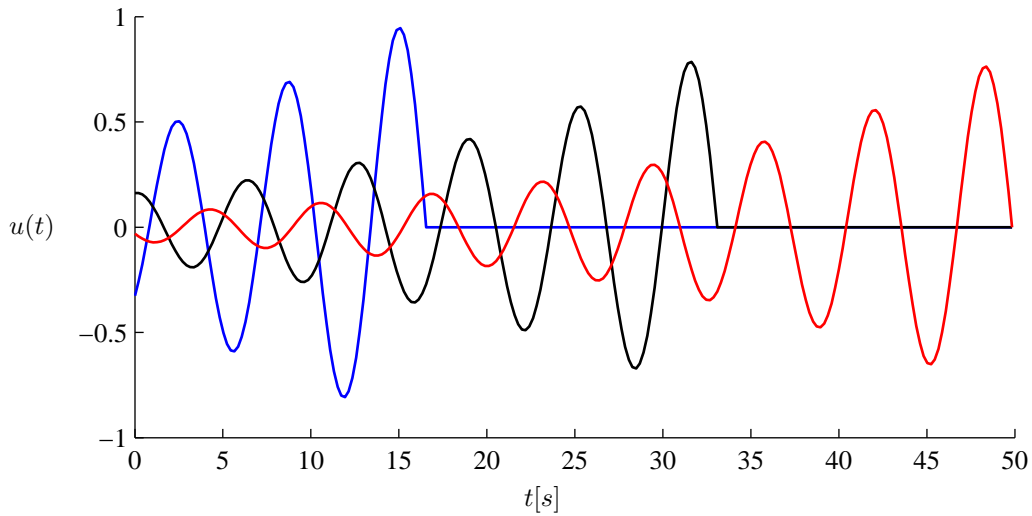


Figure J.4: Sample control function $u^{(l)}(t)$ for different values of (l)

is shown in figure J.5. Only small differences in the trajectories can be observed in the first part of the time interval, however the control function $u^{(l)}(t)$ becomes dominant and affects the oscillator in its eigenmode.

As seen in figure J.6 the sample control function with the highest likelihood of $Y(t) \in \mathcal{F}$ is found at the design time $t^* = T$. It is evident that $\beta(t)$ for $t \in [15, T]$ is almost constant which indicates that the failure probability is not dominated by a single exit time and thereby a single design time.

To validate the first passage time probability density function approximation $\mathcal{W}(t)$ given by (7.19) a CMC simulation is performed cf. figure J.7.

As seen in figure J.7 $\mathcal{W}(t)$ is a rather good approximation of $f_T(t)$ and thereby suitable for weighting

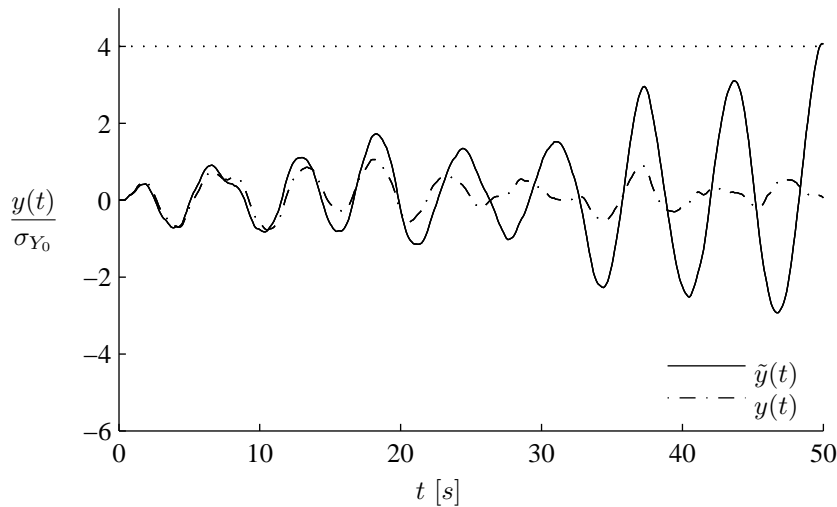


Figure J.5: Realisation of the response process with and without the control function $u^*(t)$

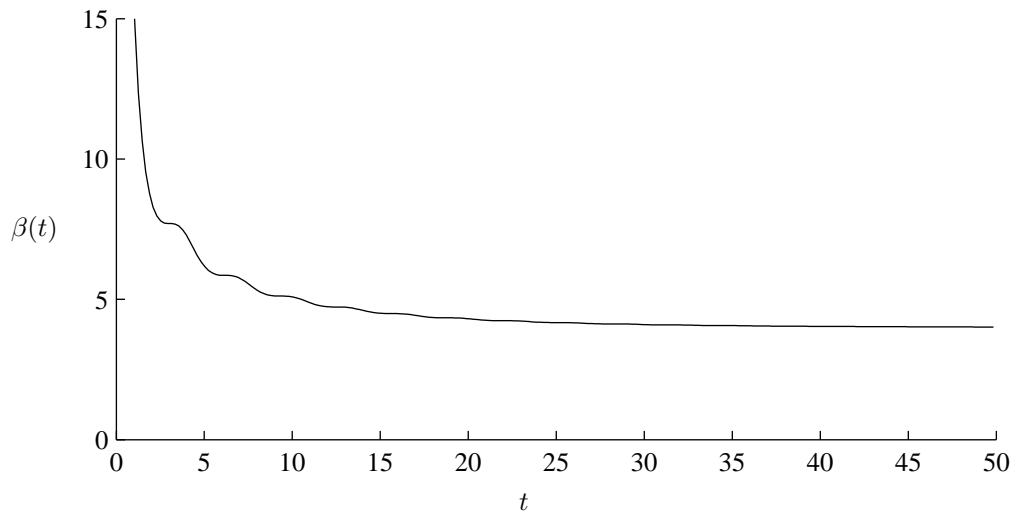


Figure J.6: Reliability index $\beta(t)$ for for the barrier $y_c = 4$.

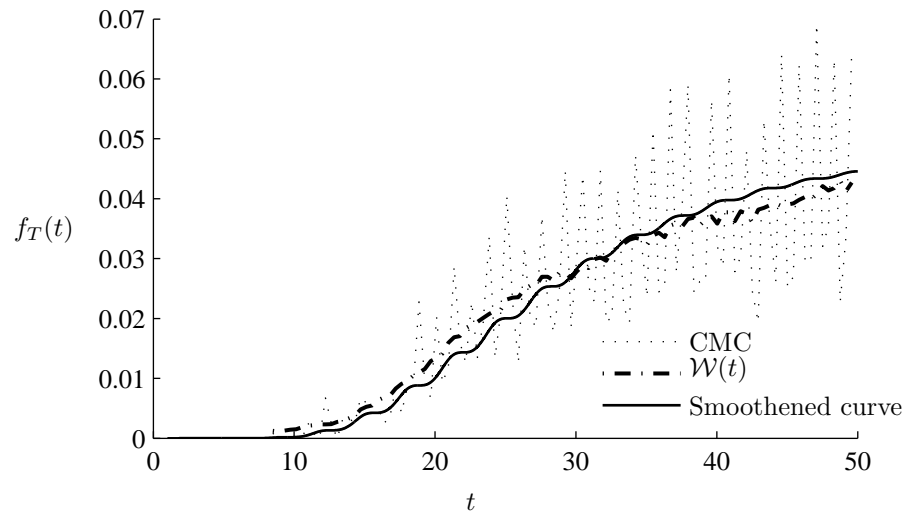


Figure J.7: First passage probability density function.

the control function corresponding to different exit times. The failure probability for different exit times is shown in figure J.8

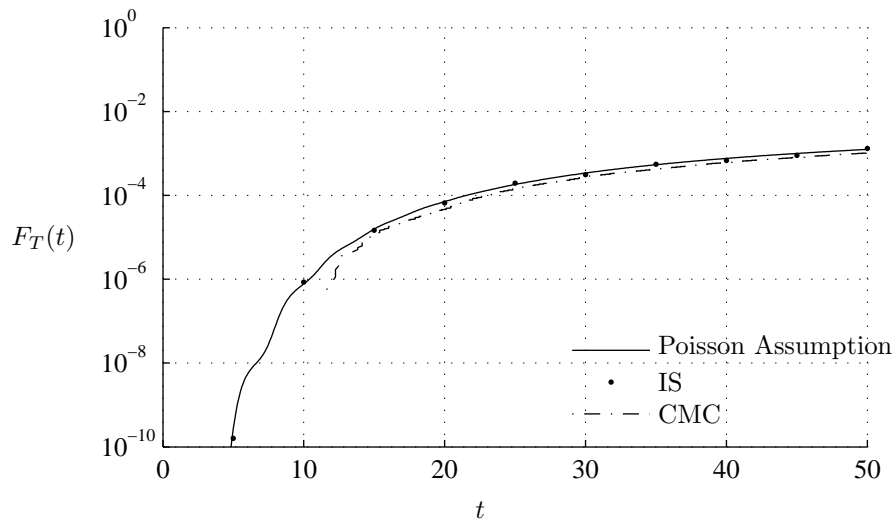


Figure J.8: Failure probability estimated by the IS method ($N = 500$), Poisson approximation and by a CMC simulation ($N = 10^6$).

The Poisson assumption shown in figure J.8 is determined in appendix K. As seen in figure J.8 the IS method is very effective and the required number of simulations are independent of the threshold.

Appendix K

Poisson approximation

Poisson approximation to the first passage time probability density function. Consider a linear sdof oscillator exposed to a stationary white noise acceleration

$$\left. \begin{aligned} \ddot{X} + 2\zeta\omega_0\dot{X} + \omega_0^2X &= \frac{1}{m}\dot{W}(t) \quad , \quad t > 0 \\ X(0) = x_0 \quad , \quad \dot{X} &= \dot{x}_0 \end{aligned} \right\} \quad (\text{K.1})$$

m is the mass, ω_0 is the undamped angular frequency and ζ is the damping ratio. The oscillator starts at the deterministic initial values $(X(0), \dot{X}(0)) = (x_0, \dot{x}_0)$. $\{\dot{W}(t), t \in \mathbb{R}\}$ is a stationary zero mean white noise process with the double sided auto spectral density S_0 .

The stationary auto-covariance function of the response process $\{X(t), t \in \mathbb{R}\}$ is given as [Nielsen, 2007b]

$$\kappa_{XX}(\tau) = \sigma_{X_0}^2 \rho(\tau) \quad (\text{K.2})$$

$$\sigma_{X_0}^2 = \frac{\pi S_0}{2\zeta\omega_0^3 m^2} \quad (\text{K.3})$$

$$\rho(\tau) = e^{-\zeta\omega_0|\tau|} \left(\cos(\omega_d\tau) + \frac{\zeta}{\sqrt{1-\zeta^2}} \sin(\omega_d|\tau|) \right) \quad (\text{K.4})$$

where

$$\omega_d = \omega_0 \sqrt{1-\zeta^2} \quad (\text{K.5})$$

The 1st and 2nd derivative of the auto correlation coefficient function become

$$\rho'(\tau) = -\frac{\omega_0}{\sqrt{1-\zeta^2}} e^{-\zeta\omega_0|\tau|} \sin(\omega_d\tau) \quad (\text{K.6})$$

$$\rho''(\tau) = -\omega_0^2 e^{-\zeta\omega_0|\tau|} \left(\cos(\omega_d\tau) - \frac{\zeta}{\sqrt{1-\zeta^2}} \sin(\omega_d\tau) \right) \quad (\text{K.7})$$

The joint probability density function of $(X(t), \dot{X}(t))$ on condition of $(X(0), \dot{X}(0)) = (x_0, \dot{x}_0)$ becomes, [Nielsen, 2007b]

$$f_{(\mathbf{X}|\mathbf{x}_0)}(\mathbf{x}|\mathbf{x}_0) = \frac{1}{2\pi|\mathbf{C}_{\mathbf{X}|\mathbf{x}_0}|} \exp\left(-\frac{1}{2}(\mathbf{x} - \mu_{\mathbf{x}|\mathbf{x}_0})^T \mathbf{C}_{\mathbf{X}|\mathbf{x}_0}^{-1} (\mathbf{x} - \mu_{\mathbf{x}|\mathbf{x}_0})\right) \quad (\text{K.8})$$

where

$$\mathbf{X}(t) = \begin{bmatrix} X(t) \\ \dot{X}(t) \end{bmatrix}, \quad \mathbf{X}_0(t) = \begin{bmatrix} X(0) \\ \dot{X}(0) \end{bmatrix} \quad (\text{K.9})$$

$\mu_{\mathbf{X}|\mathbf{x}_0}(t)$ and $\mathbf{C}_{\mathbf{X}|\mathbf{x}_0}(t)$ denote the mean value function and covariance matrix of $\mathbf{X}(t)$ on condition of $\mathbf{X}(0) = \mathbf{x}_0 = [x_0, \dot{x}_0]^T$. These are given as

$$\mu_{\mathbf{X}|\mathbf{x}_0}(t) = \begin{bmatrix} \mu_X(t) \\ \mu_{\dot{X}}(t) \end{bmatrix} = \begin{bmatrix} \rho(t)x_0 - \rho'(t)\frac{\dot{x}_0}{\omega_0^2} \\ \rho'(t)x_0 - \rho''(t)\frac{\dot{x}_0}{\omega_0^2} \end{bmatrix} \quad (\text{K.10})$$

$$\mathbf{C}_{\mathbf{X}|\mathbf{x}_0}(t) = \sigma_{X_0}^2 \begin{bmatrix} 1 - \rho^2(t) - \frac{(\rho'(t))^2}{\omega_0^2} & -\rho'(t)\left(\rho(t) + \frac{\rho''(t)}{\omega_0^2}\right) \\ -\rho'(t)\left(\rho(t) + \frac{\rho''(t)}{\omega_0^2}\right) & \omega_0^2 - (\rho'(t))^2 - \frac{(\rho''(t))^2}{\omega_0^2} \end{bmatrix} \quad (\text{K.11})$$

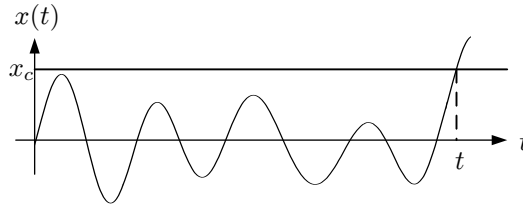


Figure K.1: Single barrier problem with constant upper barrier.

Consider a single barrier reliability problem with a constant upper barrier x_c , figure K.1. The out-crossing rate $f_1(t)$ on condition of deterministic start at the state $\mathbf{X}_0 = \mathbf{x}_0$ is given by Rice's formula

$$f_1(t) = \int_0^\infty \dot{x} f_{\mathbf{X}|\mathbf{x}_0}(x_c, \dot{x}|\mathbf{x}_0) d\dot{x} \quad (\text{K.12})$$

$\mathbf{C}_{\mathbf{X}|\mathbf{x}_0}(t)$ can be written

$$\mathbf{C}_{\mathbf{X}|\mathbf{x}_0}(t) = \begin{bmatrix} \sigma_X^2 & \sigma_X \sigma_{\dot{X}} r(t) \\ \sigma_X \sigma_{\dot{X}} r(t) & \sigma_{\dot{X}}^2 \end{bmatrix} \quad (\text{K.13})$$

$$\sigma_{\dot{X}}^2(t) = \sigma_{\dot{X}_0}^2 \left(1 - \rho^2(t) - \frac{(\rho'(t))^2}{\omega_0^2} \right) \quad (\text{K.14})$$

$$\sigma_X^2(t) = \omega_0^2 \sigma_{X_0}^2 \left(1 - \frac{(\rho'(t))^2}{\omega_0^2} - \frac{(\rho''(t))^2}{\omega_0^4} \right) \quad (\text{K.15})$$

$$r(t) = \frac{2\zeta}{\omega_0} \frac{\sigma_{\dot{X}_0}^2}{\sigma_X \sigma_{\dot{X}}} (\rho'(t))^2 \quad (\text{K.16})$$

In (K.16) the relation $\rho''(t) + \omega_0^2 \rho(t) = -2\zeta \omega_0 \rho'(t)$ is used, cf. [Nielsen, 2007b]. $\sigma_X(t)$, $\sigma_{\dot{X}}(t)$ and $r(t)$ denote the standard deviations of $X(t)$ and $\dot{X}(t)$, and the correlation coefficient between $X(t)$ and $\dot{X}(t)$ on condition of $\mathbf{X}(0) = \mathbf{x}_0$. Then $f_{\mathbf{X}|\mathbf{x}_0}(x_c, \dot{x}|\mathbf{x}_0)$ can be written as

$$f_{\mathbf{X}|\mathbf{x}_0}(x_c, \dot{x}|\mathbf{x}_0) = f_X(x_c) f_{\dot{X}|X}(\dot{x}) \quad (\text{K.17})$$

where

$$f_X(x_c) = \frac{1}{\sqrt{2\pi}\sigma_X(t)} \exp\left(-\frac{1}{2} \frac{(x_c - \mu_X(t))^2}{\sigma_X^2(t)}\right) \quad (\text{K.18})$$

$$f_{\dot{X}|X}(\dot{x}) = \frac{1}{\sqrt{2\pi}\sigma(t)} \exp\left(-\frac{1}{2} \frac{(\dot{x} - \mu(t))^2}{\sigma^2(t)}\right) \quad (\text{K.19})$$

where

$$\mu(t) = \mu_{\dot{X}}(t) + r(t) \frac{\sigma_{\dot{X}}(t)}{\sigma_X(t)} (x_c - \mu_X(t)) \quad (\text{K.20})$$

$$\sigma(t) = \sigma_{\dot{X}}(t) \sqrt{1 - r^2(t)} \quad (\text{K.21})$$

where $\mu_X(t)$ and $\mu_{\dot{X}}(t)$ are given by (K.10). Inserting (K.17), (K.18) and (K.19) into (K.12) provides

$$f_1(t) = \frac{1}{\sigma_X} \varphi\left(\frac{x_c - \mu_X}{\sigma_X}\right) \int_0^\infty \frac{\dot{x}}{\sqrt{2\pi}\sigma} \exp\left(-\frac{1}{2} \frac{(\dot{x} - \mu)^2}{\sigma^2}\right) d\dot{x} \quad (\text{K.22})$$

The integral in (K.22) is evaluated as

$$\int_0^\infty \frac{\dot{x}}{\sqrt{2\pi}\sigma} \exp\left(-\frac{1}{2} \frac{(x-\mu)^2}{\sigma^2}\right) dx = \quad (\text{K.23})$$

$$\sigma \int_{-\frac{\mu}{\sigma}}^\infty \frac{u}{\sqrt{2\pi}} \exp\left(-\frac{1}{2}u^2\right) du + \mu \int_{-\frac{\mu}{\sigma}}^\infty \frac{1}{\sqrt{2\pi}} \exp\left(-\frac{1}{2}u^2\right) du = \quad (\text{K.24})$$

$$\sigma\varphi\left(\frac{\mu}{\sigma}\right) + \mu\Phi\left(\frac{\mu}{\sigma}\right) \quad (\text{K.25})$$

Hence, the final result for $f_1(t)$ becomes

$$f_1(t) = \frac{1}{\sigma_X(t)} \varphi\left(\frac{x_c - \mu_X(t)}{\sigma_X(t)}\right) \left(\sigma(t)\varphi\left(\frac{\mu(t)}{\sigma(t)}\right) + \mu(t)\Phi\left(\frac{\mu(t)}{\sigma(t)}\right) \right) \quad (\text{K.26})$$

Assuming stochastic independent outcrossings of the barrier x_c (the "Poisson assumption") the approximation for the first passage probability density function reads, [Nielsen, 2007b].

$$f_T(t) \approx f_1(t) = \exp\left(-\int_0^t f_1(\tau) d\tau\right) \quad (\text{K.27})$$